

UNDERWATER GLIDERS: DYNAMICS, CONTROL AND DESIGN

Joshua Grady Graver

A DISSERTATION
PRESENTED TO THE
FACULTY OF PRINCETON UNIVERSITY
IN CANDIDACY FOR THE DEGREE
OF DOCTOR OF PHILOSOPHY

RECOMMENDED FOR ACCEPTANCE BY THE
DEPARTMENT OF
MECHANICAL AND AEROSPACE ENGINEERING

May, 2005

© Copyright by Joshua Grady Graver, 2005. All rights reserved.

Abstract

This dissertation concerns modelling the dynamics of underwater gliders and application of the model to analysis of glider dynamics, control, navigation, and design. Underwater gliders are a novel type of autonomous underwater vehicle that glide by controlling their buoyancy and attitude using internal actuators. We develop a first principles based model of the dynamics of a general underwater glider, including hydrodynamic forces, buoyancy and added mass effects, and the nonlinear coupling between glider and moving internal masses. This model is applicable to a wide range of gliders, as opposed to being vehicle specific. Development of a model of the dynamics of a general underwater glider is necessary for systematic model based control and design of this class of vehicles. This work builds on existing aircraft and underwater vehicle theory and facilitates application of existing techniques in dynamics and controls to this new type of vehicle.

The glider model is applied to an analysis of the dynamics of underwater gliders, identifying gliding equilibria and their stability in a longitudinal, vertical-plane model, in a simplified dynamic model based on Lanchesters phugoid assumptions, and in full three dimensional gliding.

In addition to modelling a class of vehicles, our model can be tailored to a specific glider for the purpose of predicting performance, developing improved control and navigation algorithms, and design analysis. We adapt the glider model to model the Slocum electric glider. Experimental data from trials at sea using a Slocum glider and reference data are used to identify the buoyancy trim and hydrodynamic coefficients of the experimental glider.

The general glider model is applied to study control of gliders using buoyancy control, internal mass actuators, and external surfaces. A controller and observer for steady gliding and inflections between glides is designed. Control systems on operational gliders are described and analyzed. Controller induced limit cycles are analyzed.

An analysis of glider design begins with a comparison of underwater gliders and sailplanes in the air. The glider model is then applied to analysis of glider design and glide speed, glider and ballast sizing, and alternate glider designs, including flying wings.

To Ann and Clare

Acknowledgements

This dissertation is a product of my research work done at the Dynamical Control Systems Lab at Princeton University. I want to express my warmest gratitude and admiration to my advisor and the director of that lab, Professor Naomi E. Leonard. I began my work in her lab one summer as a Princeton undergraduate, designing and building a laboratory-scale underwater glider. Now I have been able to complete my doctoral research on this interesting and exciting topic. I owe Professor Leonard a debt of gratitude for her advice and instruction during my time in the lab, and for the opportunity to work with her on such fascinating research. I consider the opportunity to work with her a great privilege. I also thank her for all of her work advising my research and for her extensive help in editing this dissertation.

I thank my dissertation readers, Professors Luigi Martinelli and Clancy Rowly of Princeton University's Mechanical and Aerospace Engineering (MAE) Department, for their time and advice. I would also like to thank my good friend Professor Craig Woolsey of Virginia Tech for his thoughtful comments and for his collaboration in this research. I thank Craig and Professor Lex Smits of Princeton MAE for serving as my Ph.D. examiners.

In the Dynamical Control Systems Laboratory, I want to thank Pradeep Bhatta for reviewing my dissertation with special attention to the equations, and also thank him and Ralf Bachmayer for their collaboration in my research on underwater gliders. Thanks also to Eddie Fiorelli for his collaboration in research and especially for his technical help. I am lucky to count all of these people among my friends and colleagues.

I also thank the other students in the Dynamical Control Systems Laboratory and the faculty, students and post-docs in my department, whose comments and discussions have helped my research. These include Phil Holmes and Howard Curtiss, for our interesting

discussions on glider dynamics. Thanks also to all of the administrators and staff members in the MAE department who have helped me over the years.

I would also like to thank the many scientists and engineers who work on underwater gliders and who have collaborated with me on research. I thank Clayton Jones, Dan Webb and Douglas C. Webb from Webb Research Corporation and Tom Campbell from Dinkum Software for their expertise and help in all areas related to the Slocum gliders and for the many helpful discussions we had. I also thank David M. Fratantoni from WHOI for the opportunity to join the glider test cruise on board the *RV Walton Smith* in January 2003 and for providing the gliders and assistance in performing the glider flight tests. I also thank the other members of the WHOI glider lab, including John Lund, Paul "Luigi" Fucile and David Sutherland. Thanks also to the captain and crew of the *RV Walton Smith* for their help and support.

I would also like to acknowledge the Office of Naval Research for supporting this research under grants N00014-98-1-0649 and N00014-02-1-0861.

Most of all, I thank my mother Ann and my sister Clare for their love, support, advice and encouragement. I also thank my wonderful girlfriend Bridget and all of my great friends from Princeton throughout my graduate and undergraduate years for their company, encouragement and friendship.

Contents

0.1	Definition of Variables	xvii
1	Introduction	1
1.1	Underwater Gliders	3
1.1.1	Characteristics and Design	3
1.1.2	Application in Oceanography	5
1.2	Motivation for Study	8
1.2.1	Technical Aspects	8
1.2.2	Applications	10
1.2.3	The Excitement of a New Vehicle System	11
1.3	Contributions and Outline of Remaining Chapters	12
2	A Brief Survey of Underwater Gliders	14
2.1	History and Development of Underwater Gliders	14
2.1.1	From Floats to Gliders	15
2.1.2	The Slocum Concept and “The Slocum Mission”	19
2.1.3	Other Glider Concepts	22
2.1.4	Modern Gliders and Programs	23
2.1.5	Glider Research at Princeton	26

2.2	Existing Underwater Glider Designs	26
2.2.1	Features of Existing Glider Designs	28
2.2.2	Slocum	29
2.2.3	Spray	30
2.2.4	Seaglider	31
2.2.5	ALBAC	33
2.2.6	STERNE	34
2.2.7	The ROGUE Laboratory Glider	35
2.3	Literature Review	37
3	Modelling of Gliders	42
3.1	Glider Model: Kinematics	45
3.1.1	Frames of Reference	45
3.1.2	Currents	47
3.1.3	Wind Frame	48
3.2	Glider Model: Dynamics	51
3.2.1	Vehicle Model	52
3.2.2	Restoring Forces: Buoyancy and Gravity	55
3.2.3	Glider Equations of Motion	57
3.2.4	Change of States and Controls to Point mass Accelerations	70
3.2.5	Glider Dynamic Equations With Point Mass Acceleration Control	74
3.2.6	Glider Dynamic Equations With Acceleration Control and Simplified Internal Masses	77
3.2.7	Glider Model Hydrodynamic Terms: Lift, Drag, Moment	82

4	Glider Dynamics	86
4.1	Longitudinal Model	88
4.1.1	Equations of Motion in the Vertical Plane	89
4.1.2	Gliding Equilibria	94
4.1.3	Linearization	99
4.1.4	Equilibrium Glides for ROGUE	102
4.1.5	Stability of Equilibrium Glides	104
4.1.6	Example: Sawtooth Gliding in The Vertical Plane	107
4.2	The Phugoid Mode for Underwater Gliders	110
4.2.1	Lanchester’s Assumptions and the Phugoid Equations	112
4.2.2	Phugoid Dynamics for $\alpha \neq 0$	116
4.2.3	Lateral Dynamics	120
4.3	Gliding in Three Dimensions	125
4.3.1	Steady Glides	125
4.3.2	Spiral Glides	128
4.3.3	Turning	135
4.3.4	Static Mis-trim	139
4.3.5	Rudder-roll coupling	142
4.4	Chapter Summary	144
5	Modelling The Slocum Glider and Parameter Identification from Experiments at Sea	147
5.1	Slocum Glider Model	149
5.1.1	Slocum Glider	149
5.1.2	Experiments with Slocum	152

5.1.3	Slocum Model Planar Equilibrium Equations	156
5.2	Parameter Identification	161
5.2.1	Lift	164
5.2.2	Drag	165
5.2.3	Pitch Moment	171
5.2.4	Identifying Unsteady Parameters	176
5.3	Remarks on These Methods	177
6	Glider Controller Design and Analysis	181
6.1	Controlled Planar Gliding	184
6.1.1	Controllability	185
6.1.2	Observability	187
6.1.3	Design of a Controller with Observer	189
6.1.4	Simulation: Controlled Planar Gliding	192
6.1.5	Simulation: Controlled Gliding with Inflections	194
6.2	Control Systems on Operational Gliders	196
6.2.1	Existing Glider Pitch and Heading Control Systems	197
6.2.2	Slocum Control Experiments at Sea	198
6.3	Other Control Applications of the Glider Model	209
6.3.1	Adaptation and Parameter Identification	209
6.3.2	Control of Inflections	210
6.3.3	Intermittent Control and Deadbands	213
6.3.4	Controller Induced Limit Cycles: Describing Function Analysis	214
6.4	Chapter Summary	221

7	Glider Design	224
7.1	Glidors vs. Sailplanes	227
7.2	Glider Design and Steady Glide Speed	229
7.2.1	Glide Speed vs. Ballast Load and Energy	231
7.2.2	Glide Speed vs. Angle	234
7.2.3	Speed vs. Volume and Ballast Fraction	236
7.3	Preliminary Glider Design	238
7.3.1	Glider Hydrodynamic Design	240
7.4	Conventional and Alternate Glider Designs	243
7.4.1	Symmetrical Designs	244
7.4.2	Flying Wing vs. Conventional Glider Designs	245
8	Conclusions	248
A	Appendix	256
A.1	Rotation Matrices and Parameterizations:	
	Euler Angles and Quaternions	256
A.1.1	Properties of Rotation Matrices	256
A.1.2	Euler angles	257
A.1.3	Quaternions	260

List of Figures

2.1	Experimental, laboratory-scale underwater glider ROGUE.	35
2.2	ROGUE with hull open.	36
3.1	Frame assignment on underwater glider.	46
3.2	Glider position and orientation variables	47
3.3	Wind frame and aerodynamic angles relative to body frame [89].	49
3.4	Glider mass definitions.	53
4.1	Sawtooth Gliding in the Vertical Plane.	88
4.2	Glider with simplified internal masses.	91
4.3	Lift and drag on glider confined to the vertical plane.	92
4.4	Planar gliding controlled to a line.	93
4.5	Family of possible movable mass locations for a steady glide.	98
4.6	Glide path in the vertical plane. From simulation.	107
4.7	Vertical Plane States.	108
4.8	Internal mass position, accelerations, and net buoyancy and pumping rate.	109
4.9	Phugoid Flight Paths.	114
4.10	Phugoid Phase Plane. Level Sets of A.	116
4.11	Flight Paths for $\alpha = 5$	118

4.12	Phase Trajectories for $\alpha = 5$, Same Initial Conditions.	119
4.13	A vs. Time along Phugoid Trajectories. $\alpha = 5$, Same Initial Conditions. . .	120
4.14	Energy vs. Time along Phugoid Trajectories. $\alpha = 5$, Same Initial Conditions.	121
4.15	Lateral forces and states (shown with glider in xy plane).	122
4.16	Simulation Euler Angles.	127
4.17	Simulation Aerodynamic Angles.	128
4.18	A steady spiral glide.	128
4.19	Steady Spiral Simulation. Glider inflects at maximum depth.	131
4.20	Glider path projected onto xz , yz and xy planes.	132
4.21	Position and orientation. Heading, pitch, roll in Euler angles.	133
4.22	Angular and linear velocities expressed in the glider body frame.	134
4.23	Internal mass positions and controls.	134
4.24	Roll and roll moment, viewed from rear. Shown with e_1 aligned with i . . .	136
4.25	Slocum Glider Test Vert 18. Heading, depth, pitch and roll.	143
4.26	Slocum Glider Test Vert 18. Pitch, ballast, mass position, and depth. . . .	144
5.1	A Slocum Glider.	149
5.2	Slocum Electric Glider Layout [77].	151
5.3	Slocum Data from Flight Test Vert 21.	154
5.4	Slocum Data from Flight Test Vert 21.	155
5.5	Glider mass definitions.	158
5.6	Lift and drag on glider.	159
5.7	Equilibrium glides using lift and drag estimated from reference data.	161
5.8	Equilibrium speed using lift, drag, estimated from reference data.	162
5.9	C_D computed from equilibrium glide data assuming no buoyancy trim offset.	167

5.10	C_D computed from equilibrium glide data assuming buoyancy trim offset of -73 grams.	169
5.11	Equilibrium glides using Lift, Drag fit to glide data	172
5.12	Equilibrium speed using Lift, Drag fit to glide data.	173
5.13	$C_{M_{total}}$ computed from equilibrium glide data.	175
6.1	Planar gliding controlled to a line.	184
6.2	Simulation of glide path from 45° downward to 30° downward.	193
6.3	Simulation of position and velocity variables.	194
6.4	Simulation of movable mass, variable mass and control inputs.	194
6.5	Vertical Plane States.	195
6.6	Internal mass position, accelerations, and net buoyancy and pumping rate. .	196
6.7	Typical controller block diagram. Pitch shown as example, [2].	197
6.8	Glider WEO1 test run before control modifications. Bahamas, January 2003 (see Chapter 5).	200
6.9	Slocum pitch response with high gain, no sliding mass clipping. Spring 2003, glider deployment from CFAV Quest, [2].	201
6.10	Slocum WE01 pitch response after controller tuning. Bahamas, January 2003 (see Chapter 5).	202
6.11	Slocum WE01 heading performance, test VERT 22 Segment 5. Bahamas, January 2003 (see Chapter 5).	204
6.12	Slocum WE01 heading performance, test 55 Segment 36. Bahamas, January 2003 (see Chapter 5).	205
6.13	Slocum heading in upwards vs. downwards glides, Buzzards Bay 2/23/02. [1]. Data courtesy of David Fratantoni, WHOI.	206

6.14	Heading, roll and rudder ($\div 6$) in upwards vs. downwards glides , Buzzards Bay 2/23/02. [1]. Data courtesy of David Fratantoni, WHOI.	208
6.15	System with describing function.	215
6.16	Nyquist Diagram.	217
6.17	Nonlinearities, describing functions, and plots on Nyquist plane.	220
6.18	Comparison of describing functions. Note scaling of saturator/limiter with DB is different than other describing functions shown.	221
7.1	Minimum glide path angle vs. maximum lift/drag ratio.	230
7.2	Conventional glider design speed vs glide path angle.	232
7.3	Component of Horizontal Glide Speed Equation, $\cos \xi (\sin \xi)^{(1/2)}$	235
7.4	Maximum horizontal velocity vs glider size and ballast fraction.	238
7.5	Lift/drag ratio vs wing reference area for conventional glider at fixed angle of attack.	246

0.1 Definition of Variables

Table 1: Table of Symbols

Name	Description
α	angle of attack, $\cos \alpha = v_1 / \sqrt{v_1^2 + v_3^2}$
\mathbf{b}	vehicle position vector from inertial frame
β	sideslip angle
CB	center of buoyancy and origin of body frame
CG	center of gravity
D	drag force
D_f	added mass cross term
$\mathbf{e}_1, \mathbf{e}_2, \mathbf{e}_3$	unit vectors along body frame 1, 2, 3 axes
$\bar{\mathbf{F}}$	total force in body coordinates
\mathbf{F}_{ext}	external force on vehicle in body coordinates
\mathbf{f}_{ext}	external force on vehicle in inertial coordinates
\mathcal{I}	identity matrix
\mathbf{I}	total mass/inertia matrix of vehicle/fluid system
$\mathbf{i}, \mathbf{j}, \mathbf{k}$	unit vectors in x, y, z directions
\mathbf{J}_f	added inertia matrix
\mathbf{J}_h	inertia of the hull (excludes inertia due \bar{m}, m_w)
\mathbf{J}_s	inertia of stationary mass, $\mathbf{J}_s = \mathbf{J}_h - m_w \hat{\mathbf{r}}_w \hat{\mathbf{r}}_w - m_b \hat{\mathbf{r}}_b \hat{\mathbf{r}}_b$
\mathbf{J}	$\mathbf{J}_s + \mathbf{J}_f$
J_i	i th diagonal element of \mathbf{J}
L	lift force
\mathbf{M}	sum of body and added mass, $\mathbf{M} = m_s \mathcal{I} + \mathbf{M}_f$
\mathbf{M}_f	added mass matrix
M_{DL}	viscous moment
m	mass of displaced fluid
\bar{m}	movable point mass
m_b	variable ballast mass located at CB
m_{fi}	i th diagonal element of \mathbf{M}_f
m_i	i th diagonal element of \mathbf{M}
m_h	uniformly distributed hull mass
m_s	stationary body mass, $m_s = m_h + m_w + m_b$
m_v	total vehicle mass, $m_v = m_s + \bar{m}$
m_w	point mass for nonuniform hull mass distribution
m_0	excess mass, $m_0 = m_v - m$

Continued on following page

Name	Description
Ω	angular velocity in body coordinates
Ω_i	i th component of Ω
\mathbf{P}	total linear momentum in body coordinates
\mathbf{P}_b	linear momentum of m_b in body coordinates
\mathbf{P}_p	linear momentum of \bar{m} in body coordinates
\mathbf{P}_w	linear momentum of m_w in body coordinates
\mathbf{p}	total linear momentum in inertial coordinates
\mathbf{p}_b	linear momentum of m_b in inertial coordinates
\mathbf{p}_p	linear momentum of \bar{m} in inertial coordinates
\mathbf{p}_w	linear momentum of m_w in inertial coordinates
$\mathbf{\Pi}$	total angular momentum (body frame)
$\boldsymbol{\pi}$	total angular momentum (inertial frame)
ϕ	roll angle
ψ	yaw/heading angle
\mathbf{R}	rotation matrix for vehicle orientation
\mathbf{R}_{BW}	rotation matrix from body frame to wind frame
\mathbf{R}_{WB}	rotation matrix from wind frame to body frame
\mathbf{R}_α	rotation matrix about body axis \mathbf{w}_2 by angle α
\mathbf{R}_β	rotation matrix about wind axis \mathbf{w}_3 by angle β
\mathbf{r}_b	position vector from CB to m_b
\mathbf{r}_p	position of movable mass \bar{m} in body coordinates
r_{pi}	i th component of \mathbf{r}_p
\mathbf{r}_s	position vector from CB to center of mass m_s
\mathbf{r}_w	position vector from CB to m_w
SF	side force (from hydrodynamics)
sm	subscript designates simplified internal mass arrangement
θ	pitch angle
$\bar{\mathbf{T}}$	total torque in body coordinates
\mathbf{T}_{ext}	total external torque in body coordinates
$\boldsymbol{\tau}_{ext}$	pure external torque in inertial coordinates
T	total kinetic energy, $T = T_s + T_p + T_f$
T_b	kinetic energy of ballast mass m_b
T_f	kinetic energy of fluid
T_p	kinetic energy of movable point mass
T_s	kinetic energy of stationary body mass m_s
T_w	kinetic energy of mass m_w

Continued on following page

Name	Description
\mathbf{u}	vector of control inputs
$\bar{\mathbf{u}}$	$(u_1, u_2, u_3)^T$, control force on sliding point mass, $\bar{\mathbf{u}} = \dot{P}_p$
\mathbf{u}_b	$(u_{b1}, u_{b2}, u_{b3})^T$, control force on ballast mass, $\mathbf{u}_b = \dot{P}_b$
$u_{ballast_rate}$	controlled variable mass rate, $u_{ballast_rate} = \dot{m}_b$
u_4	same as $u_{ballast_rate}$
\mathbf{u}_w	$(u_{w1}, u_{w2}, u_{w3})^T$, control force on mass m_w , $\mathbf{u}_w = \dot{P}_w$
V	speed in vertical plane, $V = \sqrt{(v_1^2 + v_3^2)}$
V_d	desired speed in vertical plane
V_r	speed of glider relative to fluid, $V_r = \mathbf{v}_r $
\mathbf{v}	velocity in body coordinates
v_i	i th component of \mathbf{v}
\mathbf{v}_c	velocity of current (relative to inertial frame)
\mathbf{v}_r	velocity of glider relative to fluid
\mathbf{w}	vector of accelerations of internal masses (in body frame)
\mathbf{w}_p	vector of accelerations of mass \bar{m} (in body frame), $\mathbf{w}_p = \ddot{\mathbf{r}}_p$
\mathbf{w}_b	vector of accelerations of mass m_b (in body frame), $\mathbf{w}_b = \ddot{\mathbf{r}}_b$
\mathbf{w}_w	vector of accelerations of mass m_w (in body frame), $\mathbf{w}_w = \ddot{\mathbf{r}}_w$
x, y, z	components of vehicle position vector \mathbf{b}
ξ	glide path angle, $\xi = \theta - \alpha$
ξ_d	desired glide path angle
z'	perpendicular distance to desired glide path

Chapter 1

Introduction

Underwater gliders constitute a new class of autonomous underwater vehicles. With wings and tail, they glide through the ocean, controlling their buoyancy and attitude using internal actuators. Gliders have many useful applications, notably in oceanographic sensing and data collection. In this application they are attractive because of their low cost, autonomy, and capability for long-range, extended-duration deployments. The last five years have seen the first ocean deployments of underwater gliders, and there is a need for improved understanding and modelling of their dynamics to further capitalize on the unique advantages of underwater gliders. This dissertation details the development of a model of the dynamics of underwater gliders. The model is then applied to analysis of glider dynamics, glider control and glider design.

There are two main themes within this work:

1. *Modelling the dynamics of underwater gliders and application of the model to analysis of the dynamics, control and design of underwater gliders.* We develop a first-principles based model of the dynamics of a general underwater glider, including hydrodynamic forces, buoyancy and added mass effects, and the nonlinear coupling

between glider and moving internal masses. This model is applicable to a wide range of gliders, as opposed to being vehicle specific. We apply the model to study of glider dynamics, control, navigation, and design. Our work builds on existing aircraft and underwater vehicle theory and facilitates application of existing techniques in dynamics and controls to this new type of vehicle.

Development of a model of the dynamics of a general underwater glider is necessary for systematic model based control and design of this class of vehicles. In addition to modelling a class of vehicles, our model can be tailored to a specific glider for the purpose of predicting performance, developing improved control and navigation algorithms, and design analysis.

2. *Development of both the technical and intuitive understanding of glider dynamics through analogy with aircraft and sailplanes.* In simple terms, what does it mean to put a sailplane in the water? In exploring the differences and similarities between underwater gliders and sailplanes, we help to apply existing understanding of sailplanes to underwater gliders. The principal differences between sailplanes and underwater gliders arise from the fact that sailplanes are much more dense than the air through which they fly, while gliders are designed to be close to neutrally buoyant and have the same density as water. The same hydrodynamic laws govern the fluid flow and forces on both vehicles, but because of the high relative density of water (800 times greater than air), additional effects including buoyancy and added mass are significant in the dynamics of underwater gliders. Our glider dynamic model, and other simplified models derived from it, are used to illustrate the differences in dynamics and forces acting on an underwater glider in comparison to a sailplane. We discuss how these lead to differences in the design and control of the two types of vehicles.

In this introduction, we describe the attributes of underwater gliders (Section 1.1.1) and the application of gliders (Section 1.1.2).

Section 1.2 details the motivation for the study of glider dynamics and control. Section 1.3 describes new contributions within this work and outlines the chapters of this dissertation.

1.1 Underwater Gliders

1.1.1 Characteristics and Design

Underwater gliders are a class of Autonomous Underwater Vehicles (AUVs) that glide by controlling their buoyancy using internal tanks and pumps. Existing gliders have fixed external wings and tails and control their attitude by moving internal masses and using external control surfaces such as a rudder. Gliders travel from place to place by concatenating a series of upwards and downwards glides. Characteristic glider motions include upwards and downwards straight glides in a sawtooth pattern, turning, and gliding in a vertical spiral.

Gliding flight is buoyancy driven, and does not use thrusters or propellers. Thus, gliders must change depth to glide. They glide downwards and upwards in the ocean by controlling their buoyancy to make themselves negatively and positively buoyant. Gliders may also hold their position by gliding against the current, make themselves neutrally buoyant and drift with the current, or rest on the bottom.

Through their use of buoyancy propulsion systems and low power designs, gliders are capable of long-range and high-endurance deployments. With careful design, buoyancy-driven gliders are quiet and use little power. Housing vehicle actuators within the hull

shields them from the hostile ocean environment and makes gliders more durable.

Existing oceanographic gliders are designed for long deployments and ranges and very low power consumption. In comparison to other AUVs they are relatively slow, travelling at about one half knot (.25 m/s), but have much longer ranges, on the order of hundreds or thousands of kilometers, and much longer deployment periods, on the order of weeks or months. As an example of present capabilities, the Atlantic ocean is about 2000 miles across, and Seaglider has completed missions over 1000 miles and has an expected range above 1500 miles [14].

The concept of underwater gliders is simple and elegant. Gliders may potentially make use of currents and internal waves in the ocean for more efficient, faster and longer range flight. Through careful planning they may make use of horizontal ocean currents to aid their travel [18]. Like sailplanes gliding on thermal updrafts in the air, they have the potential to make use of vertical flows in the ocean.

Gliders may also derive their propulsive energy from the ocean itself. One concept in development at Webb Research Corporation (WRC) is a thermally driven buoyancy engine that is driven by the differences in temperature across the ocean thermocline [80]. Use of such an engine would allow the glider to get the energy for propulsion from the ocean, leading to extremely long ranges and deployment. Such a glider would need battery power for its electronics and sensors only. In more standard glider designs eighty percent of vehicle power or more may be used for ballast pumping [32]. If this pumping energy were supplied by a thermal engine so the battery power used for pumping instead supported the vehicle electronics, the glider's range would increase by a factor of five. Vehicle range and endurance would be limited only by available electrical power for the vehicle hotel load. This could give gliders ranges above thirty thousand kilometers [32].

Because of their propulsion and design, gliders are relatively inexpensive in comparison to other AUVs, and they are much less expensive than ships. This makes gliders very attractive for many applications, including oceanography. “ The operational cost of making a section [for scientific data collection], including launch, recovery, refurbishment, and telemetry is as low as \$2 per km... Gliders can be operated for a year for the cost of a single day of research vessel operation. Fabrication cost is equivalent to the cost of 2-4 days of ship time” [13].

1.1.2 Application in Oceanography

Gliders have application in remote sensing for physical, chemical and biological oceanography. Other possible applications include use as communications gateways or navigation aids and military applications such as tactical oceanography and maritime reconnaissance. Attractive glider characteristics include autonomous operation, high endurance and range, and low cost. Gliders are well suited to extended missions such as collecting sensor data while traversing a chosen path or maintaining position. Gliders can operate autonomously individually or in a group, and may adaptively adjust their missions according to remote instruction or according to observed sensor information.

The first application of underwater gliders, and the inspiration for their design, has been oceanographic data collection. Use of gliders in a distributed fleet is a part of the original vision for their use in oceanography. The importance of understanding the oceans and their role in the planet’s ecosystem cannot be overstated. Progress in oceanography depends in part on the gathering of scientific data from the oceans. Because of the distributed nature of ocean dynamics, data is needed over a wide temporal and spatial range. Collection of data at any one point in space and time is of much less scientific use than collection of data

over large regions. Gliders offer a flexible and elegant platform to meet this need.

Underwater gliders have a variety of advantages over existing methods of ocean sampling. They are inexpensive, they offer superior scientific sampling, with greater spatial density of measurements over a longer period of time, and they are much more flexible than existing platforms. They may also be operated in coordinated groups. Other methods for gathering data include the use of ships, fixed moorings and drifters. Ships are expensive to operate and are limited in number and availability. Fixed moorings give data about only one location, while drifters cannot choose their path through the ocean. By their design and nature, gliders overcome many of these difficulties.

The characteristic sawtooth motion gliders make is also well suited to oceanographic sampling. Variations of ocean water properties are generally much stronger in the vertical than horizontal directions, making vertical sampling important in oceanographic applications. For this reason, propeller driven AUVs and towed arrays are often flown in a vertical sawtooth pattern for data collection.

The concept of underwater gliders for oceanographic sensing, described by Henry Stommel in “The Slocum Mission” [68], has motivated the development of three operational gliders, including the Slocum glider [80], the Spray glider [63] and the Seaglider [14]. Their development and designs are described further in Section 2.2.

These existing autonomous underwater gliders are designed to collect science data during extended ocean deployments. Their designs carefully conserve power and glide relatively slowly. Typical missions include repeatedly surveying an area of the ocean over a long period or maintaining their position against a current.

During a typical deployment for oceanographic sensing, a glider is deployed from a small boat and goes through a brief systems-check dive. The glider then travels autonomously to

its assigned survey area, gliding in a sawtooth pattern. It surfaces periodically to obtain a GPS fix and communicate using satellite telephony. The glider's mission can be updated or changed via satellite at any of these communication points by a controller anywhere on earth. The glider then continues through its assigned mission, traversing a survey route for a few weeks and periodically returning data, including water conductivity, temperature and depth, via satellite. Estimated currents are also reported. Gliders may carry additional sensors for chemical and optical measurements, such as dissolved oxygen sensors, Chlorophyll fluorescence, optical backscatter sensors, and photosynthetic active radiation (PAR) sensors to measure light available for photosynthesis at depth. At mission's end, the glider travels autonomously to its retrieval point. A glider could even be deployed and retrieved from shore at locations with waters deep enough for gliding.

Oceanographic sampling also calls for the deployment of groups of gliders. In Summer 2003, as part of the Autonomous Oceanographic Sampling Network II (AOSN II) experiment, seventeen gliders were deployed in the Monterey Bay, California, over a six-week period [11]. Twelve Slocum gliders were deployed in varying intervals by Woods Hole Oceanographic Institution (WHOI), and five Spray gliders from Scripps Institution of Oceanography (SIO) operated in the bay for the duration of the experiment. AOSN-II is a multi-institutional collaborative research program sponsored by the Office of Naval Research (ONR). As part of the experiment, the network of gliders performed adaptive sampling missions for purposes including updating and evaluating forecast models. This application made use of the gliders as a re-configurable sensor array and took advantage of the available data from the sampling network to plan glider trajectories [11].

Other Applications

Gliders also have application in a variety of military roles, some quite different from the oceanographic science for which they were invented. They may be employed for remote sensing missions similar to those described above, such as in tactical oceanography and reconnaissance, surveillance, etc.

Gliders can operate in both deep ocean and littoral (coastal) environments. Operations could involve gliders loitering in an area of interest for long periods, transiting undetected between areas, or waiting on the bottom for long periods before beginning a mission. Because they do not have thrusters and use internal actuators, gliders are quiet. This is an attractive feature for military applications because quieter vehicles are more difficult to detect.

1.2 Motivation for Study

Our study of the dynamics of underwater gliders is motivated by three principal elements. The first is an interest in the dynamics and technical challenges that arise with this new type of underwater vehicle incorporating an internal actuation system. Second, the applications of underwater gliders are scientifically important and will benefit from an improved understanding of their dynamics and the resulting improvements in design and control. Third, underwater gliders are exciting on a popular, nontechnical level because of their autonomy, actuation, and role in understanding the oceans.

1.2.1 Technical Aspects

“Modelling the dynamics of underwater gliders will allow for improvements in the control and design of existing and future gliders and corresponding improvements in their utility in

applications. In order for the advantages in ocean sampling using underwater gliders to be fully realized, an accurate and reliable glider control system should be developed. Most importantly, the use of feedback control provides robustness to uncertainty and disturbances. Development of such systems requires modelling of glider dynamics” [42].

Analysis of the dynamics of underwater gliders is challenging and new. Glider dynamics are both elegant and complex. They bring together areas of aerospace and marine engineering in interesting ways for a new application. The science and understanding of aircraft, aerodynamics and hydrodynamics is well developed. There is a great deal of existing research on the design, dynamics and control of aircraft, sailplanes and submarines. Underwater gliders bring together elements of these including hydrodynamic design and active control of buoyancy, and add to them the use of moving internal mass actuators.

The use of internal mass actuators is novel. Few aircraft (save hang-gliders) or submarines make use of such a system. In addition to being robust and shielded from the ocean, internal mass actuators may offer improved performance in some flight regimes, for example in very slow flight. The use of internal mass actuators introduces new and non-linear dynamics into the system. There is a need to model their role in the dynamics and control of gliders in order to best make use of this new technology.

Development of “a model-based feedback control design methodology is intended to improve upon the currently implemented glider control strategies. A systematic design methodology that provides control in the full state-space is expected to make it possible to design glider controllers that require less experimentation and tuning and provide more robustness to fouling, payload changes and other uncertainties as compared to current techniques. Additionally, with a model-based approach, a dynamic observer can be designed to estimate states such as glider velocity. These estimated states could then be used to de-

termine horizontal glider motion instead of the current methods which rely on assumptions of constant angle of attack. A model-based approach may also prove useful in determining optimal glider motions” [42].

1.2.2 Applications

The scientific applications of gliders are important. Their use in Autonomous Ocean Sampling Networks has the potential to open a new era in oceanography, giving scientists access to ocean data on a previously unseen scale. The importance of the ocean to the global environment is immense. Among other things it plays a great role in global weather and food production.

Our research effort is also motivated by recent studies on the full possible range of glider performance, design and applications, see e.g., [32]. Only within the past five years have the first gliders been deployed on full missions in the ocean. Gliders show great potential for future application and design improvements, an effort aided by development of a glider model as described in this dissertation.

The existing gliders, Slocum, Spray and Seaglider, are all designed for extended range and duration missions, and of necessity are relatively slow moving vehicles designed to conserve power. Their maximum speeds are on the order of half a knot, relatively slow compared to other AUVs. Gliders need not be slow, however. The speed and energy use of a glider is a design choice. Some applications may call for a faster vehicle, and in these cases it is possible to design gliders capable of speeds on the order of several knots. This is discussed further in Chapter 7.

1.2.3 The Excitement of a New Vehicle System

Aside from technical interests, the idea of gliders is captivating and exciting. Gliders capture the popularity of flight, exploration and science. People also find the autonomous and extended operation of gliders intriguing, as well as their application in exploring and understanding the oceans and world environment.

Watching a glider operate in a test tank or the ocean is a unique experience, as the glider moves through the water seemingly without any moving parts or driving mechanism. “What makes it go?” is a typical question. People are even more fascinated upon hearing a simple explanation, that the glider is propelled completely through internal actuators to control buoyancy and move internal mass.

While aboard ship one day to recover and deploy gliders in the Monterey Bay during AOSN II, it was possible to see five Slocum gliders in the water, all alternately drifting on the surface and diving to keep station against the current. Their bright yellow tails could be seen rising from the water for communication and GPS fixes. As each glider drifted beyond a set distance from its assigned position, it would slip silently beneath the surface, reappearing later after gliding to its assigned location. Over the course of AOSN II, the gliders continued on to perform their appointed sampling missions, periodically surfacing to communicate their data. That information was analyzed and examined by scientists sitting in a control room on shore, not far from the beach, but which could have been anywhere on earth. This and other glider experiments show the prescience of Henry Stommel’s vision in “The Slocum Mission” [68], described in Section 2.1, and how close gliders may soon come to fulfilling it.

1.3 Contributions and Outline of Remaining Chapters

A summary of the contributions in this work and an outline of the remaining chapters follows.

Chapter 2 presents some background on underwater gliders, a survey of existing glider designs and their special features, and a literature review.

Chapter 3 develops a general, first-principles based model of the dynamics of an underwater glider. This model is widely applicable as opposed to vehicle specific. It includes the major design elements of underwater gliders, including buoyancy control, wings and external control surfaces, and the nonlinear coupling between the glider and internal mass actuators.

Chapter 4 applies the glider model to analysis of the dynamics of underwater gliders, identifying gliding equilibria and their stability in a longitudinal, vertical-plane model, in a simplified dynamic model based on Lanchester's phugoid assumptions, and in full three dimensional gliding. Steady glides include straight glides and vertical spiral glides.

Chapter 5 adapts the glider model to model the Slocum electric glider. Experimental data from trials at sea using a Slocum glider, reference hydrodynamic data, and computational fluid dynamics reference data are used to identify the buoyancy trim and hydrodynamic coefficients of the experimental glider.

Chapter 6 applies the general glider model to study control of gliders using buoyancy control, internal mass actuators, and external surfaces. A controller and observer for steady gliding and inflections between glides is designed. Control systems on

operational gliders are described and analyzed using the glider model. Controller induced limit cycles, observed during experimental trials at sea, are analyzed using describing function analysis.

Chapter 7 applies the glider model to analysis of glider design. This begins with a comparison of underwater gliders and sailplanes in the air, with the aim of developing an intuitive and technical understanding of glider dynamics by building upon the existing understanding of sailplanes. The glider model is then applied to analysis of glider design and glide speed, glider and ballast sizing, and alternate glider designs, including flying wings.

Chapter 8 includes conclusions and suggestions for future work.

Chapter 2

A Brief Survey of Underwater Gliders

In this chapter, Section 2.1 briefly reviews the history and development of underwater gliders. Section 2.2 describes existing glider designs and some design features of interest. Section 2.3 contains a brief literature review, including previous work on underwater gliders.

2.1 History and Development of Underwater Gliders

The concept for oceanographic underwater gliders grew from the need for oceanographic sampling and work on oceanographic floats. The need to track currents and bodies of water in the ocean, and later to provide distributed and economical collection of such data, was first filled with oceanographic floats. Work on profiling floats played a role in the development of the Slocum glider concept, which led to work on the three existing oceanographic gliders: Slocum, Spray and Seaglider. References central to this review include [10, 13, 82, 21, 32, 63, 67, 68, 69, 76, 78, 79, 80, 81, 38, 75].

2.1.1 From Floats to Gliders

One of the great difficulties in oceanography is collecting science data in the ocean. Science data such as temperature, salinity/conductivity and currents are of great importance to understanding the ocean and its dynamics. Data on conditions as a function of depth are very important, as the vertical variation of these quantities plays a vital role in ocean dynamics and is much stronger, i.e. occurs on much shorter length scales, than the horizontal variation. Because of this, oceanographic studies often require a series of temperature, salinity, and current profiles by depth in many locations, spaced throughout the region of study.

Because of the physics of seawater, measurement of these quantities requires sensors on-site. The ocean absorbs light, radiation, and thermal energy in a relatively short distance. Acoustic sensing is one of the few technologies available for remote sensing in the ocean. The difficulty involved in sensing anything in the ocean is one reason that nuclear submarines are able to avoid detection.

The study of ocean dynamics is in many ways analogous to the study of the atmospheric dynamics and the weather. In the case of the atmosphere, a great amount of science data is available from weather stations all over the world, satellites, aircraft, weather balloons and other sensors. Because of the physical properties of air, it is possible to gather much information using remote sensing such as radar, visual imaging, and infra-red imaging. Data acquisition is also aided by the ability to communicate through the atmosphere via radio. It is also possible for a few satellites to provide coverage over most of the globe.

The problems of ocean sensing are more difficult. In the case of oceanographic sensing, remote sensing technologies (such as satellite based sensors) can only collect data about the surface layers of the ocean. Acquiring data at depth requires fixed moorings, floats, drifters,

or ships dragging equipment and sensors. The work is further hampered by the difficulties of communicating through the ocean with sensors deployed at depth.

This technical challenge led to the extensive use of surface drifters and submerged floats in oceanography. “The concept of a neutrally buoyant float to measure subsurface ocean currents was developed simultaneously and independently in the mid-1950s by Henry Stommel [67] in the USA and by John Swallow [69] in the UK” [21]. Early floats were developed to track ocean currents and did not carry other science instruments. The Swallow float, developed by John Swallow in the 1950’s, was a neutrally buoyant float equipped with an acoustic source. It was deployed to a chosen depth where it circulated with the water and could be tracked by a following ship.

Following the development of the Swallow float came the SOFAR float, developed by Doug Webb and Tim Rossby in the 1960’s. The float makes use of the ocean’s “deep sound channel”, or Sound Fixing and Ranging (SOFAR) Layer, discovered by Maurice Ewing and J. L. Worzel at Columbia University in 1943. This acoustic feature of the ocean occurs because of changes in the speed of sound in water with temperature and pressure. Low frequency sound in this layer of the ocean is trapped and refracted about the depth region of minimum sound velocity, travelling thousands of kilometers horizontally with little loss of signal.

The SOFAR float was designed to be neutrally buoyant at a given depth and to carry a sound source made with a metal pipe about 25 feet long. This transmits sound into the SOFAR layer at fixed time intervals. These signals were picked up by autonomous receivers at fixed locations in the ocean, which recorded time of arrival of the signals. After a period of study (perhaps as long as a year), the sources could be retrieved and the path of the float determined by comparing the signals’ times of arrival. A later version of the system, the

RAFOS system (SOFAR spelled backwards), placed the acoustic sources at fixed locations and placed hydrophones on the floats. The floats would then record times of arrival of the acoustic signals and then, after a period of operation, come to the surface by dropping a weight and communicate their data via satellite. Note that these systems predate GPS, and that their designs incorporated new technologies such as satellite communication as they became available.

Further developments led to design of the bobber float, so called because it could control its depth to cycle up and down. These floats control their buoyancy and depth using an electrically powered pump to move oil between an internal reservoir and an external bladder.

While working in the late 1980's at Webb Research Corporation (WRC) on this ballast system, Doug Webb developed the idea of using a thermally powered buoyancy engine [76]. Such an engine would make use of the ocean's thermocline, differences in temperature with depth, to power the float's travel between relatively warm surface water and the colder depths. This would extend the number of possible dive cycles to thousands, in comparison with a hundred or so cycles when powered by electric batteries. This engine concept is described further in [80]. A central idea is that, during ascent from cold depths to the relatively warm surface, the increase in temperature is used to warm and expand a working fluid. This expansion is used to charge the buoyancy system for the next ascent from depth.

The possibility of deriving the energy for pumping from the ocean and the resulting increase in endurance led Webb to extend his idea to the use of the thermal engine in an underwater glider. Such a vehicle would utilize the up and down vertical profiling motion of a float to also give control of the vehicle's horizontal position. This insight led to the development of the Slocum glider concept, described below.

Floats in the SOFAR and RAFOS systems were limited in their deployment area and

range by the acoustic systems involved. This was overcome by development of the ALACE (Autonomous Lagrangian Circulation Explorer) and PALACE (Profiling ALACE) floats, which communicate by satellite. The ALACE system was developed in the late 1980's by Russ E. Davis's group at Scripps Institute of Oceanography (SIO) and Doug Webb at WRC. ALACE uses an electric buoyancy pump to control its buoyancy. Upon deployment at sea it maintains a set depth and drifts with the current for a given period before surfacing to obtain a GPS fix and communicate via satellite. The PALACE design included conductivity, temperature and depth sensors (CTD) to take profile data when surfacing. The floats have battery power for about 100 depth cycles, 150 in the newer APEX designs. A typical mission might involve drifting for as much as five years at up to 2000 m depth, surfacing periodically for communications until battery power is expended.

These types of floats have seen extensive use in oceanography, including in the large-scale experiments such as the World Ocean Circulation Experiment (WOCE) in the 1990's [21]. To date, thousands of these types of floats have been deployed in oceanography experiments all over the world. New designs including the APEX float are based on ALACE. They incorporate new design elements and have higher endurance. In November 2004 more than 1450 active profiling floats transmitted ocean data as part of the Argo global sensor array [21].

Each innovation in float design has provided significant new scientific data and has led to significant new scientific results and advances in the understanding of the oceans. This shows how new technologies can drive the advancement of the oceanographic sciences. Underwater gliders may lead to further advances in this manner.

Technology and concepts from the ALACE float design appear in several gliders. For example, ALACE uses the ARGOS satellite system, which appears in some glider designs.

The Leduc ballast pump design used in ALACE was modified and augmented for use in the Spray and Seaglider ballast systems.

2.1.2 The Slocum Concept and “The Slocum Mission”

The underwater glider concept and its application to oceanography originated in the 1980’s with Doug Webb and Henry Stommel in Woods Hole and Falmouth, MA. Both had worked at WHOI, and Webb had started his own company, Webb Research Corporation, in Falmouth. Stommel was a world-renowned oceanographer. Webb is known for, among many other things, his innovative work in ocean engineering and instrumentation for oceanography, as well as his extensive work on drifters for oceanographic sampling.

Stommel was both a friend and mentor to Webb, the two having worked together during their time at WHOI. Stommel was known for developing insightful and uncomplicated explanations for complex phenomena, including an explanation of the jet stream as a product of the Coriolis force [96]. He has been described as “probably the most original and important physical oceanographer of all time, (he) was in large measure the creator of the modern field of dynamical oceanography” [96]. Among his extensive body of work is the development of the modern concept of ocean circulation. It is interesting that both Stommel and Webb had reputations for developing simple and novel explanations and approaches for complex phenomena and problems in their fields. The underwater glider can be seen as a product of this method.

Webb’s ideas for oceanographic gliders grew from work on oceanographic floats and buoyancy systems. Floats were being designed to move up and down in the water, and were moving towards autonomous designs. The thermal engine would mean they could perform thousands of vertical cycles. Electric floats were limited by on-board power storage to a

few hundred cycles. Webb reasoned that a glider with wings and tail could make use of this vertical motion to glide horizontally and control its position as well as depth. The thermal ballast engine would give the glider tremendous range and endurance, provided ocean conditions had the required thermal differences. By moving a battery or some other mass around inside the hull, the glider could control its pitch and roll. By pitching, the glider could control its glide angle, and by rolling the glider could turn and control its heading. Gliders could not only move up and down like a float, drifting with the current, but could also choose their path to travel anywhere in the ocean. This opened up tremendous possibilities for glider applications.

Beginning in 1988, Webb described to Stommel his idea for the thermally powered glider, and the two began work on the Slocum glider concept [34, 13]. Stommel proposed the name Slocum, after the New Englander Joshua Slocum. Slocum was the first man to circumnavigate the globe alone, a feat he accomplished in his small boat *Spray* and chronicled in his book *Around the World Alone*. “On April 24, 1895, at the age of 51, he departed Boston in his tiny sloop *Spray* and sailed around the world single-handed, a passage of 46,000 miles, returning to Newport, Rhode Island on June 27, 1898. This historic achievement made him the patron saint of small-boat voyagers, navigators and adventurers all over the world” [82].

In April 1989 “The Slocum Mission”, a science fiction article by Henry Stommel, appeared in the journal *Oceanography* [68]. Written from the perspective of an oceanographer in 2021, working at the world headquarters for the Slocum oceanographic project, the article envisions a fleet of one thousand thermally powered Slocum gliders continuously collecting science data throughout the world’s oceans. The gliders would “migrate vertically through the ocean by changing ballast, and they can be steered horizontally by gliding on wings

at about a 35 degree angle. They generally broach the surface six times a day to contact Mission Control via satellite. During brief moments at the surface, they transmit their accumulated data and receive instructions telling them how to steer through the ocean while submerged. Their speed is generally about half a knot” [68]. Stommel envisioned 480 “Sentinel Slocums” continuously traversing a series of tracks in the ocean to collect data and sending it back to headquarters for standard weather analysis. The balance of the glider fleet would be flexibly assigned to programs of scientific interest directed by academic investigating scientists.

At the time Stommel wrote the article, these same tracks were being surveyed by ship as part of the World Ocean Circulation Experiment (WOCE), and were covered only once every year. Stommel’s article described the same track being covered monthly by the fleet of sentinel Slocums. The article presents a detailed picture for the oceanographic use of underwater gliders and gives a picture of their design that is still accurate today. Stommel’s article also envisioned gliders crossing the Atlantic and an international round-the world race (in 1996!) by autonomous gliders from the USA, Australia and France. It also pointed out the important advantages of gliders including low cost, autonomy, range and endurance, and potential for distributed and coordinated operation.

Working together, Webb and Stommel continued to developed the Slocum idea and design. In 1990 they were awarded a contract by the Office of Naval Technology to develop a battery powered prototype. The prototype Slocum design used an electrically powered buoyancy system with a piston type ballast pump and a moving internal mass for pitch and roll. The electric glider would be used to develop the glider vehicle technology, while work on its thermal buoyancy engine was continued in a profiling float, to be integrated into the glider later in the design process.

In that same year, 1990, the first autonomous ALACE floats, developed by Russ E. Davis at SIO and Doug Webb at WRC, entered service in the ARGO float program. The floats were also deployed extensively in almost every part of the ocean for the World Ocean Circulation Experiment during the 1990's. As of 2003, thousands of autonomous floats have been built and they have been deployed by more than 25 labs in nine countries [21].

In January 1991 WRC performed the first tests of the Slocum electric glider, conducting 29 dives to depths up to 20 m at Wakulla Springs in Florida. In November of that year, operating from a small boat, they tested the glider at Lake Seneca, New York. At the same time they tested the thermal buoyancy engine in a float. Testing was conducted at Lake Seneca because it has sufficient depth and temperature gradient for the thermal engine. The Slocum Electric Prototype tested at that time had all the main characteristics seen in today's underwater gliders, with an electric buoyancy pump, fixed wings and tail, and a moving internal mass to control pitch and roll.

Henry Stommel passed away on January 17, 1992. Stommel's life, career and research are described in [96, 28], and in [74], a volume of personal notes and contributed essays by friends and colleagues.

2.1.3 Other Glider Concepts

Two separate early projects on underwater gliders are of note. Possibly unrelated to the development of gliders for oceanography, they appeared in the 1960's and 1970's. The first set of references includes two internal technical reports on "Project Whisper", a program at General Dynamics to develop a buoyancy propelled gliding swimmer delivery vehicle for use by the Navy. Project Whisper's name may be assumed to refer to the acoustics of gliding. The second reference is a paper in the ASME Transactions, "Optimum Design and Control

of Underwater Gliders” [3], which looks at a simplified kinematic model of a glider and examines choices of glidepath. This work apparently did not lead to further application, design or construction.

The use of gliding for efficient travel also has biological inspirations. This is a relatively recent discovery. Many marine mammals, including seals, dolphins and whales, use gliding to conserve energy during deep dives, allowing them to make longer and deeper dives. At depth, the bodies and lungs of these mammals compress enough that they become negatively buoyant. They can then rest while gliding downwards for extended periods, and then swim to ascend [84, 85].

Sperm whales use an even more sophisticated system to conserve energy. The head of a sperm whale, comprising one third of the animal’s length, is mostly taken up by a huge cavity of oil known as spermaceti. Using a specialized system of organs connected to its blow-hole and running around this reservoir, the whale can heat and cool the oil by circulating warm blood or cold seawater around it. In this manner the whale is able to control the volume of the cavity and change its buoyancy [9].

2.1.4 Modern Gliders and Programs

It is an exciting time in the development of underwater gliders. The second half of the 1990’s saw increasing funding and support of the glider concept from the Office of Naval Research, in part as an element of the AOSN initiative. This led to three programs to design and develop oceanographic gliders: the Slocum glider at WRC, Seaglider at University of Washington, and Spray at SIO. Within the last ten years, these groups have developed these underwater gliders and deployed them in large-scale oceanography projects. These three glider designs are now approaching the end of their development phase [34, 13]. Gliders

also show great potential in other applications. Recent studies show exciting possibilities for glider performance and future designs [32].

The year 2002 saw the first commercial sales of gliders. These electric Slocum gliders sold by WRC to WHOI are the first to be operated by a group that had not built the glider themselves. Early operations by the WHOI Glider Lab took place in Buzzards Bay, off Cape Cod, MA. In January 2003 that lab, directed by David Fratantoni, deployed three Slocum Electric gliders in operations from a vessel in the Bahamas. Tests of a thermally driven Slocum glider were conducted by WRC concurrently.

Some dates of interest in the development of oceanographic gliders are:

1989 “The Slocum Mission” appears in *Oceanography* [68].

1990 Office of Naval Technology (ONT) awards WRC contract for Slocum prototype.

1991 Tests of Slocum prototype and thermal engine, Wakulla Springs FL and Lake Seneca, NY.

1992 First deployment of the ALBAC glider, a shuttle type glider developed at the University of Tokyo in the lab of Tamaki Ura. The ALBAC design uses a drop weight to drive the glider in a single dive cycle between deployment and recovery from ship. It uses a moving internal mass to control pitch and roll [35]. ALBAC is described further in Section 2.2.

1993 Autonomous Oceanographic Sampling Networks paper appears in *Oceanography* [10].

1999 Slocum gliders tested at LEO-15 Observatory, NJ. Slocum glider continue to be used there for ocean sampling through 2005.

1999 Autonomous Ocean Sampling Network (AOSN) I conducted in Monterey Bay, CA.

Gliders are used to make oceanographic surveys. A prototype Spray operates for 11 days. Three Seagliders were also deployed in the bay. [63, 14]

2000 By this time all three glider programs, Spray, Slocum and Seaglider, have completed 10 day missions.

2001 Spray glider makes 280 km section from San Diego [63, 13].

2002 Seaglider travels 1000+ km off Washington Coast. Another Seaglider is deployed for month in storms off shelf near Seward Alaska.

2003 January. Deployments of three Slocum Gliders in the Bahamas by WHOI. Trials of prototype thermal Slocum conducted by WRC on same cruise.

2003 February. SPAWAR and the Canadian Navy conduct tests in the Gulf of Mexico of three Slocum Electric gliders equipped with acoustic modems.

2003 August - September. AOSN II conducted in Monterey Bay, CA. Gliders are used to make extensive oceanographic surveys over a six week period. Twelve Slocum and five Spray gliders are deployed during the experiment, to date the most gliders deployed for one project.

2004 September - November. A Spray glider travels across the Gulf Stream, beginning about 100 miles south of Nantucket, MA and arriving near Bermuda about one month later [54]. The glider travels 600 miles, at a speed of about .5 miles per hour or 12 miles per day. Spray is the first AUV to cross the gulf stream underwater.

2.1.5 Glider Research at Princeton

At Princeton University, Professor Naomi Leonard’s Dynamical Control Systems Lab conducts research on the dynamics and control of underwater vehicles, underwater gliders, groups of vehicles, and more general nonlinear systems (and many other topics). The motivation for this group’s work on gliders comes from a control design and mechanics perspective. One aim is to exploit the natural dynamics of these, and other complex systems, for improved control. Work on underwater gliders grew from initial theoretical and experimental studies of the stability of rigid bodies in water.

The group’s theoretical and experimental work on underwater gliders first considered wingless gliders including lifting bodies and flying wings, as well as possibilities for control and operational flexibility due to those geometries (some of which are symmetrical front-to-back). Experimental work includes the construction of several laboratory-scale underwater gliders and other vehicles, including ROGUE (described below), a glider which uses multiple internal ballast tanks in place of an actuated internal mass.

Some of this group’s related research and publications are described further in Section 2.3 and in Chapter 1.

2.2 Existing Underwater Glider Designs

As of 2003, three buoyancy driven autonomous underwater gliders, Slocum, Spray, and Seaglider, have been developed and deployed by programs in the U.S. Spray, from SIO, and Seaglider, from UW, are designed for deep-sea use at depths up to 1500 m. Electric Slocum is designed for shallow or littoral applications at depths to 200 m. Thermal Slocum is designed for deep-sea use and is under development. All grew from the initial Slocum glider

concept. As of 2003, multiple gliders of each type have been manufactured and deployed in large-scale oceanography projects. Work continues to adjust their design and software to move them towards maximum performance. Their many useful features include low operational and capital costs, high range and endurance due to minimal power consumption, durability due to design and protection of actuator mechanisms within the hull, low noise and vibration, and autonomous operation. They are of increasing oceanographic utility. New sensors for physical, chemical and biological oceanography have been added since the gliders' first deployment or are under development. The gliders carry sensors such as CTD's, fluorometers (for optical backscatter and chlorophyll measurements), dissolved oxygen sensors, PAR sensors, biological and other sensors. Integration of a sensor into the gliders often involves adjustments of the sensor and packaging to meet the power, space, and hydrodynamic requirements of the gliders. The gliders surface to obtain GPS position fixes and communicate via satellite or radio.

The three glider designs are of similar dimensions, have fixed wings and tail, and use internal mass actuators to control attitude. All use electrically driven buoyancy systems and internal moving mass actuators (the thermally driven Slocum is under development and prototype testing). These gliders are all designed for extended autonomous operation for oceanographic sensing. They have mission durations of weeks or months, have ranges in the hundreds or thousands of km, and travel relatively slowly - about 0.25 m/s (.5 knot). This speed is sufficient for many science applications. Glider range and speed vary with factors such as glide angle, speed, depth, and sensor load (see Chapter 4). The Seaglider has an estimated range of 6000 km or 900 cycles to 1000 m depth with a speed of 25 cm/s. Spray's range is estimated as 4000 km when travelling at 35 cm/s.

Spray and Seaglider use ballast systems derived from that used in the ALACE float,

which uses a Leduc pump to move oil between an internal reservoir and an external bladder. The Leduc pump is a hydraulic axial pump, and the glider pump designs use boost pumps and redesigned compression ratios to allow operation of the pump in various attitudes and to prevent un-priming of the pump due to air bubbles. These pumps are more efficient at deeper depths. This plays an important role in glider range because most of the glider energy budget goes to pumping work.

The Spray, Seaglider, and Thermal Slocum designs move internal masses to control both pitch and roll. They control yaw and heading through roll, which produces a yaw. The Electric Slocum controls pitch using an internal mass and yaw using a rudder. Its roll is set by static weight distribution. The design difference for yaw control, use of a rudder instead of roll, is due to the number and frequency of inflections at shallower operating depths and the resulting number of rolling motions required to steer. Newer Slocum Thermal prototypes also make use of a rudder. Steering is discussed in Chapter 4.

Internationally, two glider designs have been developed: ALBAC [35], at University of Tokyo, and STERNE [45], at Ecole Nationale Supérieure D'Ingenieurs (ENSIETA) in Brest, France. These designs are described below. They share many features with the three oceanographic gliders, but have different applications and have several unusual design features. The ALBAC glider is driven by a drop weight instead of a ballast system, and the STERNE glider is a hybrid design with both ballast control and a thruster.

2.2.1 Features of Existing Glider Designs

In this section we describe the designs of existing gliders. This is intended to show the present state of the art in underwater gliders and to guide the development of our dynamic model and its application to glider control and design.

These designs have several features of interest in the design and dynamics of underwater gliders, including:

- Ballast systems to control buoyancy.
- A design without a buoyancy system, propelled by a drop weight.
- Moving internal masses to control attitude, using one or two masses.
- Symmetrical designs with fixed wings for gliding both up and down.
- Wings of varying size, location and geometry.
- External surfaces for control, including a rudder.
- Tail surfaces that change angle at inflection from downwards to upwards glides.
- Use of low-drag hull shapes, including use of laminar flow shapes.
- Use of an internal pressure hull with an external hydrodynamic shroud.
- Use of an isopycnal hull (that has the same compressibility as seawater) to reduce pumping work.
- A hybrid glider design using both buoyancy and a thruster for propulsion.
- Design of a large (1000 kg) glider.

2.2.2 Slocum

There are two types of Slocum Gliders, electrically powered gliders operating to 200 m depths using a syringe type ballast pump, and thermally powered Slocums operating to depths of 1500 m. As of 2003, the Thermal Slocum design is still in prototype testing,

while Electric Slocums are a working vehicle. More than 21 Electric Slocums have been manufactured and sold to groups including WHOI, SPAWAR, the Canadian Navy, Rutgers University, and Scientific Fisheries.

The Electric Slocum is 1.8 m long. It glides to depths up to 200 m at speeds around 0.5 m/s. The hull is 1.5 m long and 54 cm in diameter. The tail is 0.3 m long. Slocum uses a syringe type ballast pump with 500 cc volume capacity, housed immediately behind the nose of the glider. Pitch is controlled by moving a battery pack, also located in the front section of the hull. Roll is trimmed statically. Slocum has fixed wings, swept to avoid fouling by seaweed or the like, with one meter span. The wing sections are flat plates. Slocum has a vertical tail with a rudder. The tail also houses the antenna for GPS and communication [80]. The Slocum glider is described further in Chapter 5 and in [78, 79].

2.2.3 Spray

The Spray oceanographic glider, developed at SIO, is two meters long and has a mass of 50 kg. Russ Davis's research group at Scripps designed and operates the Spray gliders. Note that Davis played a leading role in the development of the ALACE floats. Spray, named after Joshua Slocum's ship, is described in [63], which details the design, construction and early operation of the glider.

Spray has a range in the thousands of kilometers, depending on speed, sensing, communications and other energy use. It uses lithium batteries, which have better energy density and performance than alkaline batteries. [63] gives a table of estimated ranges for Spray - one example is 4000 km at .35 m/s horizontal speed.

Spray has a cylindrical pressure hull with two wings and a vertical tail. A flooded fairing forms the rear of the hull and houses the external oil-filled bladder for the ballast

system. The hydraulic ballast pump is derived from the ALACE pump and uses an improved design including an added priming pump and a greater compression ratio. These design improvements make the pump more suitable for use in a glider by allowing it to operate in different orientations and to avoid losing pump priming due to bubble formation in the pumped fluid.

The Spray design uses two internal moving masses, one for pitch and one for roll. This is different than the designs of Slocum and Seaglider, which move a single battery pack. The roll actuator is a battery pack located in the nose of the vehicle and can rotate 360 degrees. The pitch actuator is a battery pack moved by a rack and pin actuation system driven by DC motors. The pitch battery has a range of travel of 10 cm, moving the vehicle center of gravity (CG) up to 17 mm. For pitch control, Spray uses a proportional control with a low gain, giving a desired overdamped response in pitch. The vehicle heading control uses a proportional-integral loop, with a “fading memory” or “leaky” integrator. Glider control is discussed in Chapter 6.

Spray’s antenna is located inside one of the wings, and the vehicle rolls on its side to extend this wing above the surface for GPS and Orbcomm communication. The wing aerodynamic center is located behind the vehicle CG, placing the vehicle center of lift 10 cm behind the CG and CB for stability. Stability of gliding motions is discussed in Chapter 4.

2.2.4 Seaglider

Seaglider, from The University of Washington Applied Physics Lab, is designed for extended oceanographic sampling missions. It has a range of roughly 6000 km, or 900 dives to 1000 m depth. It has a mass of 52 kg and its hull is made up of an internal pressure hull

and an external fairing. The fairing is 1.8 m long with 30 cm maximum diameter and is free flooding.

Seaglider is designed to dive as deep as 1500 m. Deeper dives increase the Seaglider pump's efficiency. The internal pressure hull is unusual in that it is designed to be isopycnal, i.e., to have the same compressibility as seawater. Density layers in the ocean have a strong effect on the pumping work required to propel a glider or float. The isopycnal hull reduces the ballast pumping requirements. By matching the compressibility of seawater, "this feature extends vehicle range by as much as fifty percent over a conventional stiff hull" [14].

The Seaglider external fairing uses a different design than other gliders. Its shape is derived from a low drag laminar flow shape used by the Navy in target drones. The shape is designed to reduce pressure drag by developing a favorable pressure gradient at the rear of the vehicle.

Seaglider has a fixed wing with a one meter span and vertical tail fins located above and below the body. The location of Seaglider's wings near the rear of the vehicle causes a reversal in the usual sense of coupling between roll and yaw. This is discussed further in Chapter 4.

Pitch and roll are controlled by moving an internal battery pack. The system moves the battery pack fore and aft to control pitch and rotates it to roll the glider. Seaglider uses proportional and proportional-integral-derivative (PID) control loops to maintain pitch and heading. Currents are estimated using a Kalman filter that includes tides and diurnal cycles. To conserve power by reducing the vehicle hotel load, on-board systems including the control system are powered down during steady glides. In this mode the pitch and yaw controllers are turned on as little as every 500 seconds.

2.2.5 ALBAC

Deployed and tested in 1992 in Sugura Bay, Japan, The ALBAC glider was developed at the University of Tokyo in the lab of Tamaki Ura [35]. This design is notable because it is a shuttle type glider designed to conduct dives from a ship and does not have a buoyancy control system. ALBAC is driven by a drop weight which it carries on one downward glide and then releases to ascend back to the surface, conducting a single trip to depth between deployment and retrieval.

ALBAC has fixed wings and a vertical and horizontal tail. It is 1.4 m long, weighs 45 kg, and can dive to depths of 300 m at speeds of one to two knots (.5 to 1.0 m/s). It has horizontal tail fins which change angle at inflection from downwards to upwards gliding, a feature not present in other gliders. The wings and tail are larger in comparison to the body than on Slocum, Spray or Seaglider. ALBAC moves a battery pack internally to control pitch and yaw in the same manner as Seaglider. Because it has no ballast pump, ALBAC carries batteries to power only its instruments and actuators.

ALBAC carries flight sensors including compass, depth, pitch, roll, and a propeller-type velocity meter. Note that Slocum, Spray and Seaglider do not carry velocity meters, in order to conserve power and because of the difficulty of accurately sensing velocity at glider operating speeds.

The paper describing ALBAC also describes an interesting glider phenomenon. “Because of small misalignment of tail and wings, the vehicle rolls a little even if weight hasn’t been moved” [35]. This phenomenon of dynamic roll occurs in all gliders and is discussed further in Chapter 4.

2.2.6 STERNE

The STERNE glider is under development at the Ecole Nationale Supérieure D'Ingenieurs (ENSIETA), in Brest, France. It is designed for long endurance missions and surveys close to the seabed [45]. It is notable for its large size, use of a thruster, and relatively high power use. STERNE is 4.5 m long, 0.6 m in diameter, and has a mass of about 990 kg. This is significantly larger than the three oceanographic gliders (ten times by mass). STERNE is designed to conduct surveys by gliding or by flying level using its thruster, located at the rear of the vehicle behind the tail. Range is estimated as 120 miles. Its estimated speed is 2.5 knots (1.3 m/s) when gliding and 3.5 knots (1.8 m/s) when flying level with the thruster. The thruster may also be used to power the glider during inflections in gliding flight.

The STERNE glider has a ballast tank with 40 liter (4000 cc) capacity, proportionally slightly smaller than in the Slocum electric glider. A large battery pack is actuated to control pitch. STERNE has two fixed wings. The design makes use of external control surfaces, including two actuated horizontal tail fins and a vertical tail with rudder.

The use of a propeller makes the STERNE design a hybrid between a glider and a more conventional AUV. Hybrid designs are discussed further in [32]. When using a thruster, such a vehicle sacrifices much of the low power, long range and endurance of other glider designs, but may be better suited to some applications. Surveying, mine detection and countermeasures are examples of a military application that may involve level controlled flight. (ENSIETA is administered under the French Ministry for Defense.)

Design of the STERNE glider also involved construction and testing of a 1/3 scale model, which itself is the size of the existing oceanographic gliders. The model is 1.8 m long, 50 kg, and has a ballast range of +/- 630 grams (positive or negatively buoyant), much larger than in the oceanographic gliders and more than twice as large as the Slocum Electric's



Figure 2.1: Experimental, laboratory-scale underwater glider ROGUE.

ballast tank.

2.2.7 The ROGUE Laboratory Glider

The ROGUE vehicle is an example of a glider design that is smaller and built for a different purpose than the operational ocean-going gliders. ROGUE (Figure 2.1) is a laboratory-scale gliding vehicle designed for experiments in glider dynamics and control [23, 25, 24, 42]. The vehicle consists of a water-tight body, modular wings and tail, internal ballast actuators, and on-board electronics and batteries. Using its on-board computer and sensors the vehicle is capable of autonomous or remote operation. Buoyancy and pitch and roll are controlled by differentially actuating the four internal ballast tanks.

ROGUE’s ellipsoidal body has axes of length 18, 12 and 6 inches. The vehicle body contains the vehicle actuators, power, computer and sensors, and has mounts for the modular vehicle wings and tail. Different sets of wings and tail can be attached to perform experiments with different vehicle hydrodynamic profiles. We note that the body and wings have not been designed for optimal gliding performance but rather in consideration of available facilities and other manufacturing constraints. Experiments are currently planned using the ROGUE vehicle in our twenty-one-foot diameter laboratory tank and in an olympic sized pool at Princeton University.

In the configuration shown in Figure 2.2, each wing has span of 28 inches with aspect ratio 9.3. The wings use symmetric Selig airfoils designed for low Reynolds number flight.

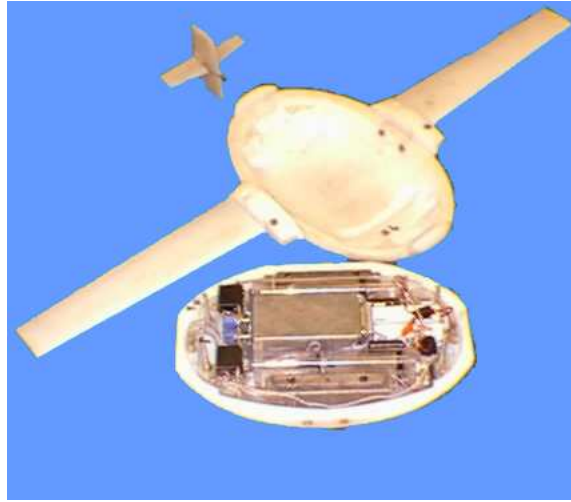


Figure 2.2: ROGUE with hull open.

The vertical tail is designed to give yaw stability in forward glides and is modular, allowing tail volume to be changed. The glider body, wings and tail are all machined from UHMW (ultra-high molecular weight) plastic. In Figure 4.2 the top half of the vehicle is separated from the bottom so the internal components are visible. The metal box at the center of the vehicle contains the vehicle on-board computer. Two syringe-type ballast tanks are visible, one on each side of the computer housing. Visible to the left of each ballast tank is its driving servo (they appear as black squares). To the right of the computer housing are two white battery packs.

2.3 Literature Review

Here we present a brief review of published work on gliders and research in related areas, grouped by topic.

Aircraft

A significant body of work exists on the design, aerodynamics and control of aircraft. Some of this work is applicable to analysis of glider hydrodynamics and control. Differences between aircraft and underwater gliders are discussed in Section 7.1. Thorough texts on aircraft and their dynamics include [15, 48, 43, 56] (as well as many others). References on the aerodynamics of aircraft and their component shapes, and much else, are useful in evaluating the hydrodynamics of gliders. Comprehensive references on aerodynamics and hydrodynamics include [27, 26, 60, 37, 46]. References on aircraft design include [52]. Evaluation of aircraft aerodynamics is included in [8, 55, 62, 61]. Aircraft control and dynamics are covered in [57, 58, 44, 7].

Also of relevance to underwater gliders is research on the dynamics of blimps [53] and other lighter-than-air craft. These share with gliders the properties of buoyancy and apparent or added mass. These effects become significant when a vehicle moves through a fluid of the same order density as the vehicle. Apparent mass effects are also important in ultralight aircraft and in aggressive aircraft maneuvers.

Gliders share many characteristics with sailplanes, which are unpowered aircraft designed for extended flight. Sailplanes are designed principally for maximum aerodynamic gliding performance and very high lift/drag ratios. They use thermally driven updrafts to gain altitude and extend their flight. Path planning for sailplanes involves choices between flight inside thermals to gain altitude, flight at minimum vertical sink rate, and higher

speed flight during transits between thermal updrafts. The goal of such planning is often maximum time aloft or maximum range, problems similar to those of underwater gliders. In addition to the aircraft literature, references on sailplanes include [95, 93, 94]. Path planning for sailplanes is addressed in [33, 31], among others.

Marine Vehicles and AUVs

There is a significant body of work on the hydrodynamics, dynamics and control of ships, submarines and underwater vehicles. Along with sharing the hydrodynamics literature mentioned above, dynamics of marine vehicles are covered specifically in [17, 16, 59]. Fossen [17] covers modelling of dynamics and control for ships and underwater vehicles including AUV's. Other references on underwater vehicles include [29, 41].

Newman [46], Lamb [39] and Hopkins [30] address hydrodynamics, including added mass effects and phenomena specific to marine vehicles.

Internal Mass Control

Vehicle attitude control using actuated internal masses is a novel concept and still the subject of active research. It has been proposed for applications in control of aerospace vehicles such as satellites and reentry warheads. Use of reaction wheels to control satellite attitudes is used in some existing satellites. [51, 70, 83] address use of moving masses in aerospace vehicles, including missile warheads during atmospheric re-entry. They investigate use of actuators including internal masses and strap-down mass actuator units. Control in these applications makes use of the aerodynamics and spinning motion of the vehicle, and the coupling between the internal mass actuator and the vehicle dynamics.

Leonard and Woolsey address the use of internal mass actuators in underwater vehicles

[87, 41, 90, 91, 86, 92, 88]. This work includes use of internal moving masses and spinning rotors for stabilization and control of underwater vehicles.

Underwater Gliders

A number of glider references are already described in Section 2.1.

Papers by Webb and others working on the Slocum vehicle [79, 80] are some of the earliest on the underwater glider dynamics and optimization. They discuss use of glider steady state glide equations to choose glide path angle, speed, and ballast loading.

“Autonomous Oceanographic Sampling Networks” [10], by Curtin, Bellingham, Catipovic and Webb, appeared in *Oceanography* in 1989. In it they propose use of a network of ships, moorings, floats, and AUV’s, including gliders, for oceanographic sampling.

An *IEEE Journal of Ocean Engineering* 2001 special issue on AUVs includes papers on the design and deployment of Seaglider [14], Spray [63] and Slocum [80]. These include discussion of hydrodynamic and mechanical design of the gliders, on-board electronics and sensors, choice of glidepaths, energy use and ranges, and navigation and control. These papers include analysis of the equilibrium performance of the gliders and results from in-water tests and deployments. Discussion of the design choices of hydrodynamic hull shapes, ballast systems, control systems, sensors, and much else provide valuable insight into issues in underwater glider dynamics and control.

Work on glider dynamics and control by Leonard and Graver [42], incorporated in this dissertation, also appeared in this JOE special issue. Other papers on this research include [25, 24, 22]. Related work by Leonard and Bhatta [5] extends this work to control of multiple gliders.

“Guidance and Control of an Autonomous Underwater Glider” [45] by Moitie and Seube,

appeared in 2001 and uses a model of a glider in the vertical plane, adapted from an aircraft gust model, to design glider controllers. The model includes use of ballast control and is used to look at inflection performance and stability. A controller for angle of attack and a sliding mode control for following a reference trajectory are presented. The paper also contains a brief description of the STERNE glider design.

“Optimal Path Planning and High Level Control of an Autonomous Gliding Underwater Vehicle” [18], an MIT master’s thesis by Anna Galea, describes methods for path planning for gliders travelling in a known current field. It models a glider, based on the Slocum design, navigating through a current field, and presents several computational methods for generating energy efficient paths between waypoints.

“Optimization Criteria and Hierarchy of Mathematical Models of an Underwater Gliding Vehicle” [72], by Russian author Ulanov A. Vladimirovich, presents a model of the longitudinal dynamics of a vesoplan (underwater glider) with two ballast tanks and an internal mass actuators. The model is used to develop a control law for glide stabilization.

“Technology and Applications of Autonomous Underwater Vehicles”, published in 2003, surveys the developments and technologies of AUVs. It contains a chapter on gliders, “Autonomous Buoyancy-driven Underwater Gliders”, written by Russ E. Davis (SIO), Charles C. Ericksen (UW), and Clayton Jones (WRC), three principals in the existing oceanographic glider programs.

A recent report for ONR, “Underwater Glider System Study” [32], contains work by all of the research groups currently working on glider design in the U.S. It presents analysis of the three existing oceanographic gliders, analysis of the maximum possible performance envelope of gliding underwater vehicles, parametric design studies, and proposals for future glider applications including military use. It includes analysis of the hydrodynamics and

flight of their gliders as well as a flying wing design. The report discussed maximum possible ranges, sizes and speeds for underwater gliders, the effect of scaling and ballast size, and more. Future applications of gliders and sensors are discussed. A discussion of alternative glider geometries such as blended wing bodies and flying wings is included. Also see Chapter 7.

Chapter 3

Modelling of Gliders

This chapter develops a model of the dynamics of an underwater glider. The glider has a body with fixed wings and tail, ballast control, controlled internal moving mass, and external control surfaces such as a rudder. The dynamic model is developed from first principles and is intended to include the important elements of glider dynamics without unnecessary complexity. The main elements in the model are glider configuration and geometry, the forces of gravity and buoyancy, the effects of added mass and inertia due to motion in a dense fluid, hydrodynamic forces including lift, drag and moment, and the control of moving internal masses and ballast. Provisions are included to account for external control surfaces such as a rudder and ailerons. The model includes the nonlinear coupling between the moving internal mass and the glider dynamics.

The model presented here expands on the glider model presented by Leonard and Graver, [42] and [24]. The development here follows along the lines of those papers and adds elements to model additional internal masses and external control surfaces. This produces a more detailed glider model and allows the model to be adapted in Chapter 5 to model an existing glider.

As described in the Introduction, applications of the model include analysis of glider dynamics, control and navigation, design, among others. Development and application of the model is intended to complement other work on gliders and glider dynamics, including work on Slocum, Spray and Seaglider. With this in mind, a widely applicable approach is emphasized, rather than one that is vehicle-specific. The model development takes into account the design of existing gliders and incorporates elements, including the number and location of internal masses and ballast tanks, allowing it to be tailored to a specific glider. In this chapter the model is adapted to match the Slocum glider. Chapter 5 details parameter identification from flight tests of a Slocum glider. Simplified versions of the model are used for analysis of glider dynamics, Chapter 4, and control analysis, Chapter 6, as well as in the analysis of glider design and scaling, Chapter 7.

This chapter is arranged as follows: Section 3.1 introduces the glider kinematics to track the glider's orientation, position and motion. The inertial and body-fixed frames of reference and conversions between them are introduced. The wind frame is introduced to track the relative velocity of the glider through the water. Provisions are made to account for currents.

Section 3.2 develops the dynamic model of the glider, including the three dimensional equations of motion. Section 3.2.1 describes the model of the vehicle body and internal masses. The model includes three internal masses: a ballast mass with fixed position and variable controlled mass, a moving mass whose position is controlled and whose mass is fixed, and a static offset mass whose position and mass are fixed. The dynamic model includes the coupling between these masses and the glider motion. Section 3.2.2 adds forces due to buoyancy and gravity.

In Section 3.2.3, the glider equations of motion in three dimensions with a controlled

internal moving mass and ballast mass are derived from first principles. The control on the internal moving mass is the force on the mass, and the ballast control is the ballast pumping rate. Section 3.2.4 introduces a change of states and a control transformation, making the moving mass control the acceleration of the moving internal mass. This provides a ‘suspension system’ for the internal masses. It allows the internal masses to be fixed in place within the glider and improves the stability of glides (discussed in Chapter 4). It is also more consistent with the implementation of the internal masses in existing gliders. Section 3.2.5 presents the glider equations after the state and control transformation, where the control is the point mass acceleration and the ballast rate. This model is simplified in Section 3.2.6 by restricting the arrangement of the internal masses. The ballast mass is fixed at the center of the body-fixed frame and the static offset mass is eliminated. This reduces the complexity of the model terms while preserving the principal elements of the glider model. This facilitates the study of glider dynamics and control in later chapters and should be useful in future work. This ‘simplified mass’ arrangement is used in [42] and [24].

Section 3.2.7 introduces model terms for hydrodynamic lift, drag and moment on the glider. These terms are left in a general form to be specified at the level of detail required for a specific application. The model may include the effects of hydrodynamic control surfaces. Some analysis in later chapters uses a coefficient-based, quasi-steady hydrodynamic model briefly introduced here.

3.1 Glider Model: Kinematics

3.1.1 Frames of Reference

Inertial Frame

Consider an inertially fixed, non-rotating reference frame $\boldsymbol{x}\boldsymbol{y}\boldsymbol{z}$. For marine vehicles this may be taken to be an earth-fixed frame and accelerations may be neglected. Let the \boldsymbol{x} and \boldsymbol{y} inertial axes lie in the horizontal plane, perpendicular to gravity. The \boldsymbol{z} axis lies in the direction of the gravity vector and is positive downwards. Let \boldsymbol{i} , \boldsymbol{j} , \boldsymbol{k} be the unit vectors in the \boldsymbol{x} , \boldsymbol{y} , \boldsymbol{z} directions, respectively, as shown in Figure 3.1. This choice of inertial frame is consistent with the underwater vehicle literature, as in [17] and others. The inertial frame may be chosen such that $\boldsymbol{z} = 0$ coincides with the ocean's surface, in which case \boldsymbol{z} is depth.

Body-Fixed Frame and Kinematics

Assign a coordinate frame fixed to the glider vehicle body with its origin at the glider center of buoyancy (CB) and its axes aligned with the principal axes of the glider. Let body axis 1 lie along the long axis of the vehicle (positive in the direction of the glider's nose), let body axis 2 lie in the plane of the wings and body axis 3 point in the direction orthogonal to the wings as shown in Figure 3.1.

The orientation of the glider is given by the rotation matrix \boldsymbol{R} . \boldsymbol{R} maps vectors expressed with respect to the body frame into inertial frame coordinates. \boldsymbol{R} may be parameterized using Euler angles or quaternion parameters. See Appendix A or [20, 66, 17]. The XYZ, or yaw, pitch, roll convention, is the standard Euler angle convention in aircraft and underwater vehicle dynamics and is utilized here. The rotation from inertial to body reference frame is parameterized by three angles: yaw ψ , pitch θ and roll ϕ . Yaw ψ is defined as positive

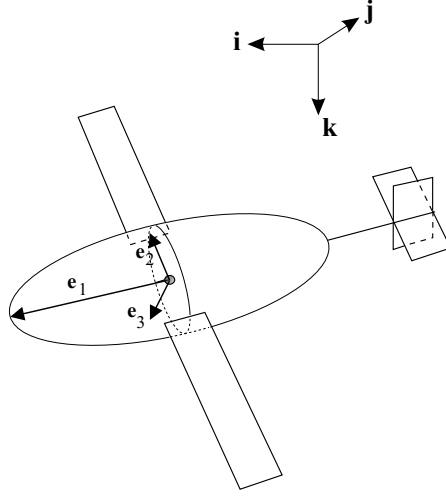


Figure 3.1: Frame assignment on underwater glider.

right (clockwise) when viewed from above, pitch θ is positive nose-up, and roll ϕ is positive right-wing down. Rotation matrices are given in Appendix A.

The position of the glider, $\mathbf{b} = (x, y, z)^T$, is the vector from the origin of the inertial frame to the origin of the body frame as shown in Figure 3.2. The vehicle moves with translational velocity $\mathbf{v} = (v_1, v_2, v_3)^T$ relative to the inertial frame and angular velocity $\mathbf{\Omega} = (\Omega_1, \Omega_2, \Omega_3)^T$, both expressed in the body frame. (Note that we have diverged from the notation typical of the submarine literature where $\mathbf{v} = (u, v, w)^T$ and $\mathbf{\Omega} = (p, q, r)^T$. The notation that we use here is taken from texts in classical mechanics such as [20] and is more convenient for the derivation and analysis.)

Define the operator $\hat{\cdot}$ so that for a vector $\mathbf{x} = (x_1, x_2, x_3)^T$,

$$\hat{\mathbf{x}} = \begin{pmatrix} 0 & -x_3 & x_2 \\ x_3 & 0 & -x_1 \\ -x_2 & x_1 & 0 \end{pmatrix}.$$

Then, for vector $\mathbf{y} = (y_1, y_2, y_3)^T$,

$$\hat{\mathbf{x}}\mathbf{y} = \begin{pmatrix} 0 & -x_3 & x_2 \\ x_3 & 0 & -x_1 \\ -x_2 & x_1 & 0 \end{pmatrix} \begin{pmatrix} y_1 \\ y_2 \\ y_3 \end{pmatrix} = \mathbf{x} \times \mathbf{y},$$

i.e., the operator $\hat{\cdot}$ maps a vector \mathbf{x} to the (skew-symmetric) matrix representation of the vector cross product operator.

In this notation, the kinematics of the glider are given by

$$\dot{\mathbf{R}} = \mathbf{R}\hat{\Omega} \tag{3.1}$$

$$\dot{\mathbf{b}} = \mathbf{R}\mathbf{v}. \tag{3.2}$$

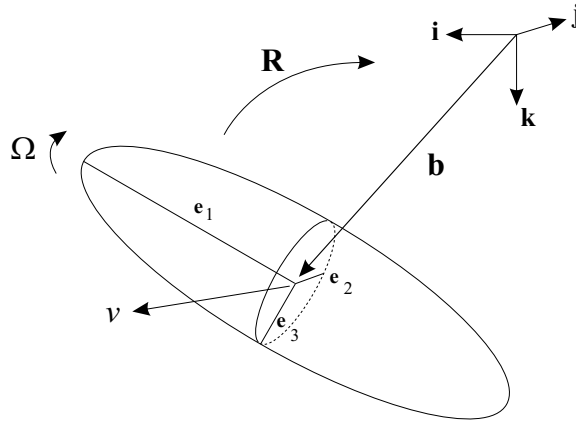


Figure 3.2: Glider position and orientation variables

3.1.2 Currents

Glider operation may occur in the presence of currents, where the fluid is in motion relative to the inertial reference frame. Here any variation in currents will be modelled as occurring

over length scales several orders of magnitude greater than the glider’s length. Therefore, wind shearing effects may be neglected. This is a common assumption in aircraft and underwater vehicle literature. For treatment of wind shear effects when this assumption does not hold, see [15] and [17].

Let \mathbf{v}_r be the velocity of the glider relative to the fluid, expressed in the body frame. Let $\mathbf{V}_c = (V_{cx}, V_{cy}, V_{cz})$ be the velocity of the fluid relative to the inertial frame as expressed in the inertial frame. Then

$$\mathbf{v}_r = \mathbf{v} - \mathbf{R}^T \mathbf{V}_c$$

and

$$\dot{\mathbf{b}} = \mathbf{R}\mathbf{v} = \mathbf{R}\mathbf{v}_r + \mathbf{V}_c$$

Note that the hydrodynamic forces on the vehicle are a function of \mathbf{v}_r . Except when specified otherwise, this dissertation takes currents \mathbf{V}_c to be zero, i.e., $\mathbf{v} = \mathbf{v}_r$. Note that in much of the analysis this assumption does not change the glider’s dynamics. The difference between many gliding motions with or without currents is simply the superposition of the current velocities onto the glider motion without currents. Navigation with respect to the inertial frame must account for the effect of currents. It should also be noted that in oceanographic applications the ability of gliders to determine the local current is important for both navigation and scientific data collection. Sensors capable of doing this include acoustic doppler current profilers (ADCPs) and doppler velocity logs (DVLs).

3.1.3 Wind Frame

The hydrodynamic forces on an underwater vehicle depend on the velocity and orientation of the vehicle relative to the fluid through which it moves. The velocity of the glider relative

to the fluid is \mathbf{v}_r as specified above. In the absence of currents, i.e. when the fluid is at rest with respect to the inertial frame of reference, \mathbf{v}_r is equal to glider velocity \mathbf{v} . Assign a wind reference frame to track the glider orientation with respect to the glider's relative velocity through the water, \mathbf{v}_r .

As is standard in aircraft literature [15, 66, 48], the orientation of the wind frame relative to the body frame will be described by two aerodynamic angles, the angle of attack α and the sideslip angle β . The wind reference frame is defined such that one axis is aligned with \mathbf{v}_r . The aerodynamic angles are defined as

$$\alpha = \tan^{-1} \left(\frac{v_{r3}}{v_{r1}} \right) \quad \text{and} \quad \beta = \tan^{-1} \left(\frac{v_{r2}}{\|\mathbf{v}_r\|} \right).$$

These angles are well-defined for nonzero velocities with use of the four-quadrant arctangent.

Angle of attack α is the angle from the body \mathbf{e}_1 axis to the vector $(v_{r1}, 0, v_{r3})^T$, the projection of the \mathbf{v} vector onto the $\mathbf{e}_1 - \mathbf{e}_3$ plane. The sideslip angle β is defined as the angle from the projection of \mathbf{v}_r on the $\mathbf{e}_1 - \mathbf{e}_3$ plane to the vector \mathbf{v}_r . Angles α and β and their positive directions are shown in Figure 3.3.

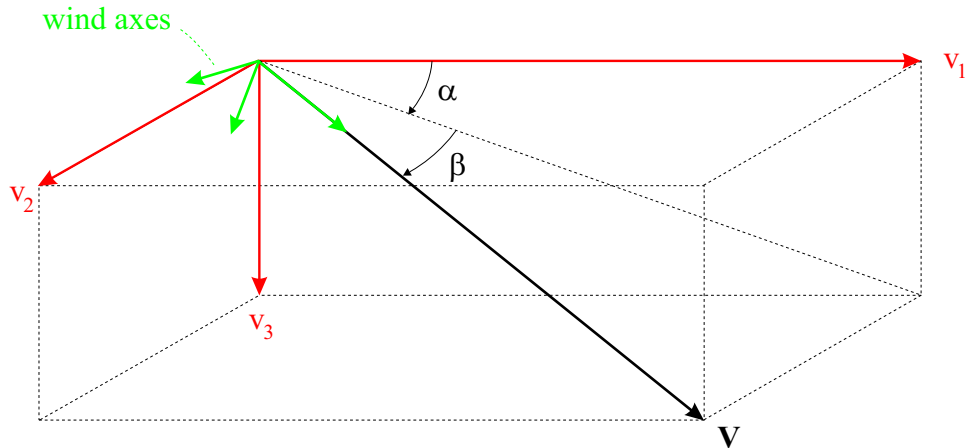


Figure 3.3: Wind frame and aerodynamic angles relative to body frame [89].

Define the wind frame to have its origin at the glider center of buoyancy (CB) and its

orientation defined by the velocity of the glider through the water as follows. Let wind axis \mathbf{w}_1 point in the direction of \mathbf{v}_r , the glider velocity relative to the water. The orientation of wind axes \mathbf{w}_2 and \mathbf{w}_3 are defined by the following sequence of rotations:

1. Begin with the wind frame coincident with the body frame, with wind axes \mathbf{w}_1 , \mathbf{w}_2 , \mathbf{w}_3 aligned with body axes \mathbf{e}_1 , \mathbf{e}_2 , \mathbf{e}_3 , respectively.
2. Rotate about wind axis \mathbf{w}_2 by angle α . Positive α is shown in Figure 3.3. Note that this is opposite the normal positive direction as given by the right-hand rule. Let $\mathbf{R}_\alpha(\alpha)$ represent this rotation.
3. Rotate about wind axis \mathbf{w}_3 by angle β . This rotation is written as $\mathbf{R}_\beta(\beta)$ and follows the normal sense of rotation, as shown in the figure.

Note that the wind axis \mathbf{w}_3 lies in the body \mathbf{e}_1 - \mathbf{e}_3 plane. Rotation from the body frame to the wind frame is then given by $\mathbf{R}_{BW}(\alpha, \beta) = \mathbf{R}_\beta \mathbf{R}_\alpha$.

$$\mathbf{R}_\alpha(\alpha) = \begin{pmatrix} \cos \alpha & 0 & \sin \alpha \\ 0 & 1 & 0 \\ -\sin \alpha & 0 & \cos \alpha \end{pmatrix}, \quad \mathbf{R}_\beta(\beta) = \begin{pmatrix} \cos \beta & \sin \beta & 0 \\ -\sin \beta & \cos \beta & 0 \\ 0 & 0 & 1 \end{pmatrix}. \quad (3.3)$$

$$\mathbf{R}_{BW}(\alpha, \beta) = \mathbf{R}_\beta \mathbf{R}_\alpha = \begin{pmatrix} \cos \alpha \cos \beta & \sin \beta & \sin \alpha \cos \beta \\ -\cos \alpha \sin \beta & \cos \beta & -\sin \alpha \sin \beta \\ -\sin \alpha & 0 & \cos \alpha \end{pmatrix} \quad (3.4)$$

The inverse rotation from wind to body frame is simply the transpose,

$$\mathbf{R}_{WB}(\alpha, \beta) = (\mathbf{R}_\alpha)^T (\mathbf{R}_\beta)^T = \begin{pmatrix} \cos \alpha \cos \beta & -\cos \alpha \sin \beta & -\sin \alpha \\ \sin \beta & \cos \beta & 0 \\ \sin \alpha \cos \beta & -\sin \alpha \sin \beta & \cos \alpha \end{pmatrix}$$

\mathbf{R}_{WB} maps vectors expressed with respect to the wind frame into body frame coordinates. Writing the body relative velocities in terms of relative speed $V_r = |\mathbf{v}_r|$ and aerodynamic angles α and β gives

$$\mathbf{v}_r = \begin{pmatrix} v_{r1} \\ v_{r2} \\ v_{r3} \end{pmatrix} = \begin{pmatrix} V_r \cos \beta \cos \alpha \\ V_r \sin \beta \\ V_r \cos \beta \sin \alpha \end{pmatrix}.$$

3.2 Glider Model: Dynamics

In this section the glider equations of motion are derived from first principles, using a computation of the total system energy to determine the vehicle momenta and then applying Newton's laws. The derivation of the model follows the lines of the glider model derived in [42] and adds additional elements. Related references by Woolsey and Leonard on underwater vehicle dynamics with internal mass actuators include [41, 86, 87, 91, 92, 88]. These include Newtonian and Hamiltonian analysis of the dynamics of underwater vehicles with moving internal masses or internal rotors, as well as work on stabilization and control of those vehicles. There is an extensive body of research on underwater vehicle dynamics, including [17, 39, 59]. In [42], the ballast system is fixed at the glider CB and the only point mass offset from the CB is the controlled moving mass. The model presented here has

additional terms to account for an offset location of the glider ballast system, an additional fixed mass offset from the CB, and external control surfaces such as a rudder.

The choice of internal masses in the vehicle takes into account the designs of existing oceanographic gliders. In these gliders the ballast systems are located at the nose or tail of the vehicle in order to provide a pitching moment from a change of ballast. Their moving internal masses are located according to the vehicle geometry and space limitations and have a fixed range of travel. In the case of the Slocum glider, for example, both the ballast system and the sliding mass are located in the nose of the vehicle, well forward of the glider CB. The offset static mass is included in the model in order to properly model the static balance and CG location of the vehicle. Adjusting the parameters corresponding to the static mass make it possible to match the static balance and inertia of the oceanographic gliders. Simplified versions of the model are used for analysis and control purposes, considered in Chapters 4 and 6.

3.2.1 Vehicle Model

The glider dynamics model derived here describes a glider with general body and wing shape. We model the underwater glider as a rigid body, immersed in a fluid, with fixed wings and tail. The glider has buoyancy control and a controlled internal moving mass. The body-fixed coordinate frame has its origin at the vehicle CB and its axes aligned with the principal axes of the vehicle as described in Section 3.1.1.

The total stationary mass of the glider m_s , also referred to as body mass, is the sum of three terms: $m_s = m_h + m_w + m_b$. Hull mass m_h is a fixed mass that is uniformly distributed throughout the body of the glider. Three internal point masses are included in the model. This allows the model to be tailored to model existing glider designs, such as

Slocum (see Chapter 5). m_w is a fixed point mass that may be offset from the CB. m_b is the variable ballast point mass, which may also be offset from the CB. The moving internal point mass is \bar{m} . The internal masses and position vectors are illustrated in Figure 3.4.

The total mass of the vehicle is then

$$m_v = m_h + m_w + m_b + \bar{m} = m_s + \bar{m}.$$

The positions, in the body frame, of point masses m_w and m_b are given by the vectors \mathbf{r}_w and \mathbf{r}_b from the CB to the respective masses. The vector $\mathbf{r}_p(t)$ describes the position of the moving mass \bar{m} in the body-fixed frame at time t .

The static mass parameters m_w and \mathbf{r}_w may be set to balance the pitching and rolling moment on the glider from the other point masses and to set the vehicle inertia. Model parameter identification is discussed in Chapter 5.

The mass of the fluid displaced by the vehicle is denoted m . Define the net buoyancy to be $m_0 = m_v - m$ so that the vehicle is negatively (positively) buoyant if m_0 is positive (negative).

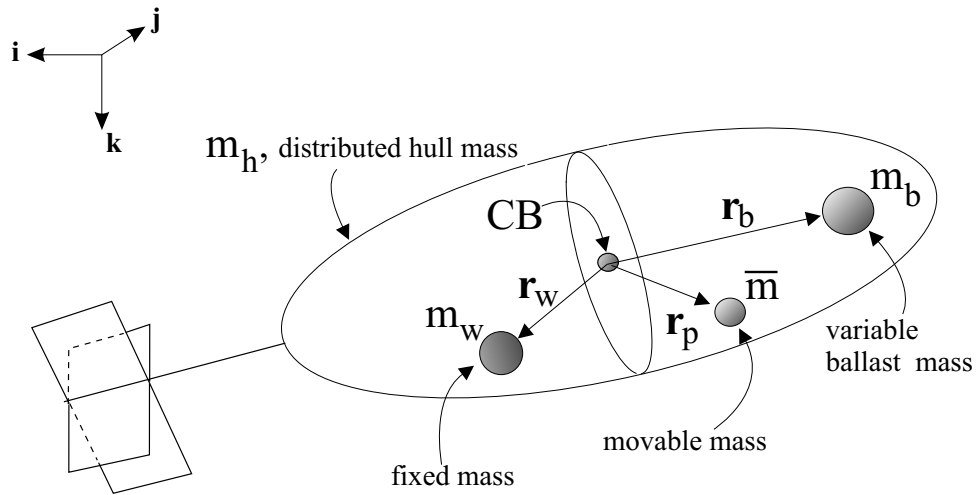


Figure 3.4: Glider mass definitions.

Let \mathbf{J}_h denote the inertia matrix, with respect to the body frame, for the uniformly distributed hull mass m_h . The inertia matrix for the stationary (body) mass expressed with respect to body frame coordinates is

$$\mathbf{J}_s = \mathbf{J}_h - m_w \hat{\mathbf{r}}_w \hat{\mathbf{r}}_w - m_b \hat{\mathbf{r}}_b \hat{\mathbf{r}}_b.$$

Modelling Different Ballast Systems

As mentioned above, the choice of internal masses for the model is motivated by the geometry of the Slocum, Seaglider and Spray gliders. In the Slocum design, ballast mass m_b and moving internal mass \bar{m} are both well forward of the glider CB (as described in Chapter 2). In Seaglider and Spray the ballast systems are located in the tails of the vehicles, aft of the vehicle CB. In the Slocum glider the ballast system is a syringe-type ballast tank which takes in water to become negatively buoyant. The placement of the ballast system in the nose gives a nose-down moment from the ballast when the vehicle is negatively buoyant.

The Spray and Seaglider designs control ballast using an external oil-filled bladder. This is a balloon connected through a pump to an oil reservoir inside the hull. Pumping oil into the external bladder displaces water with (less dense) oil and increases buoyancy, while pumping oil from the external bladder to the in-hull reservoir reduces buoyancy. This also results in a moment on the vehicle, whose magnitude and direction depend on the location and volume of the internal and external reservoirs.

Ballast systems of this type may be analyzed using the model presented here. The volume of the fully inflated external bladder may be treated as a control volume, and the corresponding mass within that volume modelled as a ballast point mass. When the external bladder is inflated, the ballast mass is the mass of the inflated bladder and oil.

When the bladder is deflated, the ballast mass is equal to the mass of water in the control volume. The internal oil reservoir may be modelled as a separate ballast mass, or the internal and external ballast reservoirs may be approximated by one point mass located at an intermediate position. The choice of whether to model this system with one or two ballast masses will depend on the distance between the two reservoirs, the relative magnitude of the moments they exert on the glider at different ballast states, and the desired level of detail in the model.

Controlled Internal Masses

Control is applied to two point masses inside the vehicle: the ballast mass has variable mass m_b but fixed position \mathbf{r}_b , while moving point mass \bar{m} has fixed mass but variable position \mathbf{r}_p . Control input \dot{m}_b specifies the rate of change of the ballast mass and another control input vector corresponds to the force applied to the movable mass.

The Spray glider design has two moving masses, one mass actuated in the roll direction and the other in the pitch direction. To model this, a second controlled moving mass may be added to the model given below. Adding a second moving mass to the derivation below is a straightforward operation. Additional masses will appear as terms similar to those of \bar{m} , m_b and m_w .

3.2.2 Restoring Forces: Buoyancy and Gravity

Underwater gliders are subject to the forces of gravity and buoyancy. In underwater vehicle terminology these are referred to as *restoring forces*. The gravitational force on the vehicle, $m_v g$, acts in the positive (downwards) inertial \mathbf{k} direction at the vehicle center of gravity

(CG). The CG is the mass-weighted centroid of the vehicle. Its position is given by

$$\mathbf{r}_{CG} = \frac{\int \mathbf{r}\rho(\mathbf{r})dV}{\int \rho(\mathbf{r})dV}.$$

Where $\rho(\mathbf{r})$ is density, dV is a volume element and the integration is performed over the vehicle volume. For the glider masses defined here,

$$\mathbf{r}_{CG} = \frac{\sum_i m_i \mathbf{r}_i}{\sum m_i} = \frac{m_h \mathbf{r}_h + m_w \mathbf{r}_w + m_b \mathbf{r}_b + \bar{m} \mathbf{r}_p}{m_h + m_w + m_b + \bar{m}}. \quad (3.5)$$

Note that both internal controlled masses, m_b and \bar{m} , appear in this equation. Also, \mathbf{r}_h , the position in body coordinates of the centroid of the hull mass, is always zero because the hull mass is modelled as uniformly distributed. Therefore, the CG of the uniformly distributed hull mass always coincides with the CB of the glider (which is the origin of the body frame), so $\mathbf{r}_h = \mathbf{0}$.

The buoyant force on the glider is due to displacement of the fluid by the glider volume, as determined by Archimedes' Principle. This force results from the net pressure exerted by the fluid on the vehicle surface. The glider center of buoyancy (CB) is the centroid of the displaced volume. The net buoyant force acts at the CB and is equal to mg , where m is the mass of the displaced fluid. The buoyant force acts in the negative (upward) \mathbf{k} direction. The net buoyancy force is $m_0g = (m_v - m)g$, so that the vehicle is negatively (positively) buoyant if m_0 is positive (negative). Expressed in the body frame, the gravitational and buoyant forces are $\mathbf{f}_{gravity} = m_v g (\mathbf{R}^T \mathbf{k})$ and $\mathbf{f}_{buoyancy} = -mg (\mathbf{R}^T \mathbf{k})$. The CG is offset from the CB by vector \mathbf{r}_{CG} and the resulting gravitational torque on the vehicle, written

in the body frame, is

$$\boldsymbol{\tau}_{gravity} = \mathbf{r}_{CG} \times m_v g (\mathbf{R}^T \mathbf{k}) = m_v g \hat{\mathbf{r}}_{CG} (\mathbf{R}^T \mathbf{k}).$$

Because the origin of the body-fixed frame is defined as coincident with the vehicle centroid (and CB), torques due to the buoyancy of the vehicle (which acts at the CB) are zero in the body frame. From 3.5,

$$m_v \mathbf{r}_{CG} = m_w \mathbf{r}_w + m_b \mathbf{r}_b + \bar{m} \mathbf{r}_p.$$

and so the net torque is equivalently

$$\boldsymbol{\tau}_{gravity} = (\bar{m} \hat{\mathbf{r}}_p + m_w \hat{\mathbf{r}}_w + m_b \hat{\mathbf{r}}_b) g (\mathbf{R}^T \mathbf{k}).$$

The restoring torque on the glider provides a righting moment. It will be shown in later sections that the equilibrium orientation of the neutrally buoyant glider at rest, with $m_0 = 0$ and $\mathbf{v}_r = 0$, has the CG and CB along the same line in the vertical (\mathbf{k}) direction, so that the torque due to gravity is zero. Stability of equilibria will depend on whether the CG is above the CB (unstable) or below the CG (stable). See also [41].

3.2.3 Glider Equations of Motion

The glider equations of motion are derived here by computing momenta from the total vehicle-fluid system energy and applying Newton's laws.

Let \mathbf{p} represent the total translational momentum of the vehicle-fluid system and $\boldsymbol{\pi}$ the total angular momentum of the system about the inertial coordinate origin, all expressed

with respect to the inertial frame. Let \mathbf{p}_p represent the total momentum of the movable point mass \bar{m} with respect to the inertial frame. Likewise, \mathbf{p}_b and \mathbf{p}_w represent the total momentum of the ballast mass m_b and the offset point mass m_w with respect to the inertial frame. Then Newton's laws state that

$$\begin{aligned}
\dot{\mathbf{p}} &= \sum_{i=1}^I \mathbf{f}_{ext_i}, \\
\dot{\boldsymbol{\pi}} &= \sum_{i=1}^I (\mathbf{x}_i \times \mathbf{f}_{ext_i}) + \sum_{j=1}^J \boldsymbol{\tau}_{ext_j}, \\
\dot{\mathbf{p}}_p &= \bar{m}g\mathbf{k} + \sum_{k=1}^K \mathbf{f}_{int_pointmass_k}, \\
\dot{\mathbf{p}}_b &= m_b g\mathbf{k} + \sum_{l=1}^L \mathbf{f}_{int_ballast_l}, \\
\dot{\mathbf{p}}_w &= m_w g\mathbf{k} + \sum_{n=1}^N \mathbf{f}_{int_w_n},
\end{aligned} \tag{3.6}$$

where \mathbf{k} is the unit vector pointing in the direction of gravity, \mathbf{f}_{ext_i} is an external force applied to the system and $\boldsymbol{\tau}_{ext_j}$ is a pure external torque. All vectors are expressed with respect to the inertial frame. The vector \mathbf{x}_i locates the point of application of the force \mathbf{f}_{ext_i} with respect to the inertial coordinate frame. These external forces and torques include those due to gravity and buoyancy; however, gravity is included explicitly in the last three equations as it is the only external force acting on these point masses. The force $\mathbf{f}_{int_pointmass_k}$ is a force applied from the vehicle body onto the point mass. This will be used as a control force. The forces $\mathbf{f}_{int_ballast_l}$ and $\mathbf{f}_{int_w_n}$ are the forces applied from the vehicle body onto the ballast and offset point masses, m_b and m_w . These two masses are fixed in place in the vehicle (see Section 3.2.4). The equations in (3.6) corresponding to the fixed internal mass m_w and ballast mass m_b have the same form as the equation corresponding to \bar{m} . Because m_w and m_b have fixed positions within the vehicle, the

internal forces on them are considered to be constraint forces and not controls. These constraint forces will be determined by the motion of the glider.

Let \mathbf{P} be the momentum (with respect to the inertial frame) of the vehicle-fluid system expressed with respect to the body frame. Let $\mathbf{\Pi}$ be the total angular momentum about the origin of the body frame, also in body coordinates. Note that these terms include the momentum of the glider internal masses. Let \mathbf{P}_p represent the point mass momentum expressed in the body frame. \mathbf{P}_b and \mathbf{P}_w represent the ballast mass and offset point mass momenta in the body frame:

$$\begin{aligned}
\mathbf{p} &= \mathbf{R}\mathbf{P}, \\
\boldsymbol{\pi} &= \mathbf{R}\mathbf{\Pi} + \mathbf{b} \times \mathbf{p}, \\
\mathbf{p}_p &= \mathbf{R}\mathbf{P}_p, \\
\mathbf{p}_b &= \mathbf{R}\mathbf{P}_b, \\
\mathbf{p}_w &= \mathbf{R}\mathbf{P}_w.
\end{aligned} \tag{3.7}$$

Differentiating Equations (3.7) with respect to time and using the kinematic expressions (3.2) and (3.1) gives

$$\begin{aligned}
\dot{\mathbf{p}} &= \mathbf{R}(\dot{\mathbf{P}} + \hat{\boldsymbol{\Omega}}\mathbf{P}), \\
\dot{\boldsymbol{\pi}} &= \mathbf{R}(\dot{\mathbf{\Pi}} + \hat{\boldsymbol{\Omega}}\mathbf{\Pi}) + \mathbf{R}\mathbf{v} \times \mathbf{p} + \mathbf{b} \times \dot{\mathbf{p}}, \\
\dot{\mathbf{p}}_p &= \mathbf{R}(\dot{\mathbf{P}}_p + \hat{\boldsymbol{\Omega}}\mathbf{P}_p), \\
\dot{\mathbf{p}}_b &= \mathbf{R}(\dot{\mathbf{P}}_b + \hat{\boldsymbol{\Omega}}\mathbf{P}_b), \\
\dot{\mathbf{p}}_w &= \mathbf{R}(\dot{\mathbf{P}}_w + \hat{\boldsymbol{\Omega}}\mathbf{P}_w).
\end{aligned} \tag{3.8}$$

Substituting (3.6) into (3.8) for the rate of change of inertial momenta gives the following dynamic equations in body coordinates:

$$\dot{\mathbf{P}} = \mathbf{P} \times \boldsymbol{\Omega} + \mathbf{R}^T \sum_{i=1}^I \mathbf{f}_{ext_i}, \quad (3.9)$$

$$\begin{aligned} \dot{\boldsymbol{\Pi}} &= \boldsymbol{\Pi} \times \boldsymbol{\Omega} + \mathbf{P} \times \mathbf{v} \\ &+ \mathbf{R}^T \left(\sum_{i=1}^I (\mathbf{x}_i - \mathbf{b}) \times \mathbf{f}_{ext_i} \right) + \mathbf{R}^T \sum_{j=1}^J \boldsymbol{\tau}_{ext_j}, \end{aligned} \quad (3.10)$$

$$\dot{\mathbf{P}}_p = \mathbf{P}_p \times \boldsymbol{\Omega} + \bar{m}g(\mathbf{R}^T \mathbf{k}) + \mathbf{R}^T \sum_{k=1}^K \mathbf{f}_{int_pointmass_k}, \quad (3.11)$$

$$\dot{\mathbf{P}}_b = \mathbf{P}_b \times \boldsymbol{\Omega} + m_b g(\mathbf{R}^T \mathbf{k}) + \mathbf{R}^T \sum_{l=1}^L \mathbf{f}_{int_ballast_l}, \quad (3.12)$$

$$\dot{\mathbf{P}}_w = \mathbf{P}_w \times \boldsymbol{\Omega} + m_w g(\mathbf{R}^T \mathbf{k}) + \mathbf{R}^T \sum_{n=1}^N \mathbf{f}_{int_w_n}, \quad (3.13)$$

where $\mathbf{R}^T \sum_{k=1}^K \mathbf{f}_{int_pointmass_k}$ is the internal force acting on the point mass \bar{m} in body coordinates. Let

$$\bar{\mathbf{u}} = \begin{pmatrix} \bar{u}_1 \\ \bar{u}_2 \\ \bar{u}_3 \end{pmatrix} = \mathbf{P}_p \times \boldsymbol{\Omega} + \bar{m}g(\mathbf{R}^T \mathbf{k}) + \mathbf{R}^T \sum_{k=1}^K \mathbf{f}_{int_pointmass_k} \quad (3.14)$$

so that

$$\dot{\mathbf{P}}_p = \bar{\mathbf{u}}.$$

Note that $\bar{\mathbf{u}}$ is not the internal force on the point mass because the centrifugal and gravi-

tational forces on \bar{m} have been included in the expression for $\bar{\mathbf{u}}$ Likewise, let

$$\mathbf{u}_b = \begin{pmatrix} u_{b1} \\ u_{b2} \\ u_{b3} \end{pmatrix} = \mathbf{P}_b \times \boldsymbol{\Omega} + m_b g (\mathbf{R}^T \mathbf{k}) + \mathbf{R}^T \sum_{l=1}^L \mathbf{f}_{int_ballast_l} \quad (3.15)$$

and

$$\mathbf{u}_w = \begin{pmatrix} u_{w1} \\ u_{w2} \\ u_{w3} \end{pmatrix} = \mathbf{P}_w \times \boldsymbol{\Omega} + m_w g (\mathbf{R}^T \mathbf{k}) + \mathbf{R}^T \sum_{n=1}^N \mathbf{f}_{int_w_n} \quad (3.16)$$

so that

$$\dot{\mathbf{P}}_b = \mathbf{u}_b$$

and

$$\dot{\mathbf{P}}_w = \mathbf{u}_w.$$

The viscous hydrodynamic forces and torques on the glider, included in $\sum_{i=1}^I \mathbf{f}_{ext_i}$ and $\sum_{j=1}^J \boldsymbol{\tau}_{ext_j}$, depend on states \mathbf{v} and $\boldsymbol{\Omega}$. Therefore Equations (3.9)-(3.13) will not be used as the glider equations of motion and will instead be written in terms of a new set of states which include \mathbf{v} and $\boldsymbol{\Omega}$. To derive expressions for \mathbf{P} , $\boldsymbol{\Pi}$, \mathbf{P}_p , \mathbf{P}_b and \mathbf{P}_w , we determine the total kinetic energy of the glider-fluid system. The kinetic energy T_s of a rigid body with total mass m_s , CG position \mathbf{r}_s in the body frame (equal to \mathbf{r}_{CG}) and inertia matrix \mathbf{J}_s is

$$T_s = \frac{1}{2} \begin{pmatrix} \mathbf{v} \\ \boldsymbol{\Omega} \end{pmatrix} \cdot \begin{pmatrix} m_s \mathcal{I} & -m_s \hat{\mathbf{r}}_s \\ m_s \hat{\mathbf{r}}_s & \mathbf{J}_s \end{pmatrix} \begin{pmatrix} \mathbf{v} \\ \boldsymbol{\Omega} \end{pmatrix},$$

where \mathcal{I} is the 3×3 identity matrix.

Let \mathbf{v}_p be the absolute velocity of the movable point mass \bar{m} expressed in body coordinates. Given that the velocity of \bar{m} relative to the body frame is $\dot{\mathbf{r}}_p$, we compute

$$\mathbf{v}_p = \mathbf{v} + \dot{\mathbf{r}}_p + \boldsymbol{\Omega} \times \mathbf{r}_p . \quad (3.17)$$

The kinetic energy T_p of the movable point mass is then computed to be

$$T_p = \frac{1}{2} \bar{m} \|\mathbf{v}_p\|^2 = \frac{1}{2} \begin{pmatrix} \mathbf{v} \\ \boldsymbol{\Omega} \\ \dot{\mathbf{r}}_p \end{pmatrix} \cdot \begin{pmatrix} \bar{m}\mathcal{I} & -\bar{m}\hat{\mathbf{r}}_p & \bar{m}\mathcal{I} \\ \bar{m}\hat{\mathbf{r}}_p & -\bar{m}\hat{\mathbf{r}}_p\hat{\mathbf{r}}_p & \bar{m}\hat{\mathbf{r}}_p \\ \bar{m}\mathcal{I} & -\bar{m}\hat{\mathbf{r}}_p & \bar{m}\mathcal{I} \end{pmatrix} \begin{pmatrix} \mathbf{v} \\ \boldsymbol{\Omega} \\ \dot{\mathbf{r}}_p \end{pmatrix} .$$

The kinetic energies of the ballast and offset point masses are computed in the same manner. The constraints fixing their positions in the body frame will be applied in the following section. Let \mathbf{v}_b and \mathbf{v}_w be the absolute velocity of m_b and m_w expressed in body coordinates. Their kinetic energies are then

$$T_b = \frac{1}{2} m_b \|\mathbf{v}_b\|^2 = \frac{1}{2} \begin{pmatrix} \mathbf{v} \\ \boldsymbol{\Omega} \\ \dot{\mathbf{r}}_b \end{pmatrix} \cdot \begin{pmatrix} m_b\mathcal{I} & -m_b\hat{\mathbf{r}}_b & m_b\mathcal{I} \\ m_b\hat{\mathbf{r}}_b & -m_b\hat{\mathbf{r}}_b\hat{\mathbf{r}}_b & m_b\hat{\mathbf{r}}_b \\ m_b\mathcal{I} & -m_b\hat{\mathbf{r}}_b & m_b\mathcal{I} \end{pmatrix} \begin{pmatrix} \mathbf{v} \\ \boldsymbol{\Omega} \\ \dot{\mathbf{r}}_b \end{pmatrix} .$$

and

$$\begin{aligned} T_w &= \frac{1}{2} m_w \|\mathbf{v}_w\|^2 \\ &= \frac{1}{2} \begin{pmatrix} \mathbf{v} \\ \boldsymbol{\Omega} \\ \dot{\mathbf{r}}_w \end{pmatrix} \cdot \begin{pmatrix} m_w\mathcal{I} & -m_w\hat{\mathbf{r}}_w & m_w\mathcal{I} \\ m_w\hat{\mathbf{r}}_w & -m_w\hat{\mathbf{r}}_w\hat{\mathbf{r}}_w & m_w\hat{\mathbf{r}}_w \\ m_w\mathcal{I} & -m_w\hat{\mathbf{r}}_w & m_w\mathcal{I} \end{pmatrix} \begin{pmatrix} \mathbf{v} \\ \boldsymbol{\Omega} \\ \dot{\mathbf{r}}_w \end{pmatrix} . \end{aligned}$$

Kirchhoff [39] showed that the kinetic energy of an unbounded volume of ideal fluid due to the motion of an immersed rigid body takes the form

$$T_f = \frac{1}{2} \begin{pmatrix} \mathbf{v} \\ \boldsymbol{\Omega} \end{pmatrix} \cdot \begin{pmatrix} \mathbf{M}_f & \mathbf{D}_f^T \\ \mathbf{D}_f & \mathbf{J}_f \end{pmatrix} \begin{pmatrix} \mathbf{v} \\ \boldsymbol{\Omega} \end{pmatrix},$$

where \mathbf{M}_f is the added mass matrix, \mathbf{J}_f is the added inertia matrix and \mathbf{D}_f is the added cross term. These matrices depend upon the external shape of the body and the density of the fluid. The fluid is assumed to be inviscid, incompressible, irrotational and motionless at infinity.

Viscous effects such as lift and drag will be included in the model as external forces and torques.

The total vehicle fluid kinetic energy $T = T_s + T_p + T_f + T_b + T_w$ is computed to be

$$T = \frac{1}{2} \begin{pmatrix} \mathbf{v} \\ \boldsymbol{\Omega} \\ \dot{\mathbf{r}}_p \\ \dot{\mathbf{r}}_b \\ \dot{\mathbf{r}}_w \end{pmatrix} \cdot \mathbf{I} \begin{pmatrix} \mathbf{v} \\ \boldsymbol{\Omega} \\ \dot{\mathbf{r}}_p \\ \dot{\mathbf{r}}_b \\ \dot{\mathbf{r}}_w \end{pmatrix},$$

where

$$\mathbf{I} = \begin{pmatrix} (m_s + \bar{m})\mathcal{I} + \mathbf{M}_f & -\bar{m}\hat{\mathbf{r}}_p - m_b\hat{\mathbf{r}}_b - m_w\hat{\mathbf{r}}_w + \mathbf{D}_f^T & & & & \\ \bar{m}\hat{\mathbf{r}}_p + m_b\hat{\mathbf{r}}_b + m_w\hat{\mathbf{r}}_w + \mathbf{D}_f & \mathbf{J}_h - \bar{m}\hat{\mathbf{r}}_p\hat{\mathbf{r}}_p - m_b\hat{\mathbf{r}}_b\hat{\mathbf{r}}_b - m_w\hat{\mathbf{r}}_w\hat{\mathbf{r}}_w + \mathbf{J}_f & & & & \\ \bar{m}\mathcal{I} & & -\bar{m}\hat{\mathbf{r}}_p & & & \\ m_b\mathcal{I} & & & -m_b\hat{\mathbf{r}}_b & & \\ m_w\mathcal{I} & & & & -m_w\hat{\mathbf{r}}_w & \\ & & & & & \bar{m}\mathcal{I} & m_b\mathcal{I} & m_w\mathcal{I} \\ & & & & & \bar{m}\hat{\mathbf{r}}_p & m_b\hat{\mathbf{r}}_b & m_w\hat{\mathbf{r}}_w \\ & & & & & \bar{m}\mathcal{I} & 0 & 0 \\ & & & & & 0 & m_b\mathcal{I} & 0 \\ & & & & & 0 & 0 & m_w\mathcal{I} \end{pmatrix}. \quad (3.18)$$

We can then compute momenta as

$$\begin{aligned} \mathbf{P} = \frac{\partial T}{\partial \mathbf{v}} &= (m_s\mathcal{I} + \mathbf{M}_f)\mathbf{v} + \mathbf{D}_f^T\boldsymbol{\Omega} + \bar{m}(\mathbf{v} + \boldsymbol{\Omega} \times \mathbf{r}_p + \dot{\mathbf{r}}_p) \\ &\quad + m_b(\mathbf{v} + \boldsymbol{\Omega} \times \mathbf{r}_b + \dot{\mathbf{r}}_b) + m_w(\mathbf{v} + \boldsymbol{\Omega} \times \mathbf{r}_w + \dot{\mathbf{r}}_w), \end{aligned} \quad (3.19)$$

$$\begin{aligned} \boldsymbol{\Pi} = \frac{\partial T}{\partial \boldsymbol{\Omega}} &= \mathbf{D}_f\mathbf{v} + (\mathbf{J}_h + \mathbf{J}_f)\boldsymbol{\Omega} + \bar{m}\hat{\mathbf{r}}_p(\mathbf{v} + \boldsymbol{\Omega} \times \mathbf{r}_p + \dot{\mathbf{r}}_p) \\ &\quad + m_b\hat{\mathbf{r}}_b(\mathbf{v} + \boldsymbol{\Omega} \times \mathbf{r}_b + \dot{\mathbf{r}}_b) + m_w\hat{\mathbf{r}}_w(\mathbf{v} + \boldsymbol{\Omega} \times \mathbf{r}_w + \dot{\mathbf{r}}_w), \end{aligned} \quad (3.20)$$

$$\mathbf{P}_p = \frac{\partial T}{\partial \dot{\mathbf{r}}_p} = \bar{m}(\mathbf{v} + \boldsymbol{\Omega} \times \mathbf{r}_p + \dot{\mathbf{r}}_p), \quad (3.21)$$

$$\mathbf{P}_b = \frac{\partial T}{\partial \dot{\mathbf{r}}_b} = m_b(\mathbf{v} + \boldsymbol{\Omega} \times \mathbf{r}_b + \dot{\mathbf{r}}_b), \quad (3.22)$$

$$\mathbf{P}_w = \frac{\partial T}{\partial \dot{\mathbf{r}}_w} = m_w(\mathbf{v} + \boldsymbol{\Omega} \times \mathbf{r}_w + \dot{\mathbf{r}}_w). \quad (3.23)$$

Consider first the case where the vehicle geometry leads to diagonal added mass and inertia matrices. This occurs when the vehicle has three planes of symmetry. This could

correspond to a simple vehicle shape such as an ellipsoid or a more complex glider shape with wings mounted symmetrically. Then \mathbf{M}_f and \mathbf{J}_f are diagonal and $\mathbf{D}_f = \mathbf{0}$. Let $\mathbf{M}_f = \text{diag}(m_{f1}, m_{f2}, m_{f3})$ and $\mathbf{J}_f = \text{diag}(J_{f1}, J_{f2}, J_{f3})$. Define

$$\mathbf{M} = m_h \mathbf{I} + \mathbf{M}_f, \quad (3.24)$$

$$\mathbf{J} = \mathbf{J}_h + \mathbf{J}_f \quad (3.25)$$

where \mathbf{I} is the 3×3 identity matrix. Then,

$$\begin{pmatrix} \mathbf{P} \\ \mathbf{\Pi} \\ P_p \\ P_b \\ P_w \end{pmatrix} = \mathbf{I} \begin{pmatrix} v \\ \Omega \\ \dot{r}_p \\ \dot{r}_b \\ \dot{r}_w \end{pmatrix}, \quad (3.26)$$

where

$$\mathbf{I} = \begin{pmatrix} \mathbf{M} + (\bar{m} + m_b + m_w) \mathbf{I} & -\bar{m} \hat{\mathbf{r}}_p - m_b \hat{\mathbf{r}}_b - m_w \hat{\mathbf{r}}_w & \bar{m} \mathbf{I} & m_b \mathbf{I} & m_w \mathbf{I} \\ \bar{m} \hat{\mathbf{r}}_p + m_b \hat{\mathbf{r}}_b + m_w \hat{\mathbf{r}}_w & \mathbf{J} - \bar{m} \hat{\mathbf{r}}_p \hat{\mathbf{r}}_p - m_b \hat{\mathbf{r}}_b \hat{\mathbf{r}}_b - m_w \hat{\mathbf{r}}_w \hat{\mathbf{r}}_w & \bar{m} \hat{\mathbf{r}}_p & m_b \hat{\mathbf{r}}_b & m_w \hat{\mathbf{r}}_w \\ \bar{m} \mathbf{I} & -\bar{m} \hat{\mathbf{r}}_p & \bar{m} \mathbf{I} & 0 & 0 \\ m_b \mathbf{I} & -m_b \hat{\mathbf{r}}_b & 0 & m_b \mathbf{I} & 0 \\ m_w \mathbf{I} & -m_w \hat{\mathbf{r}}_w & 0 & 0 & m_w \mathbf{I} \end{pmatrix}.$$

Inverting the relationships (3.26) then gives the body velocities in terms of the body mo-

menta:

$$\begin{pmatrix} v \\ \Omega \\ \dot{r}_p \\ \dot{r}_b \\ \dot{r}_w \end{pmatrix} = I^{-1} \begin{pmatrix} P \\ \Pi \\ P_p \\ P_b \\ P_w \end{pmatrix}, \quad (3.27)$$

$$I^{-1} = \begin{pmatrix} M^{-1} & 0 & -M^{-1} & -M^{-1} & -M^{-1} \\ 0 & J^{-1} & -J^{-1}\hat{r}_p & -J^{-1}\hat{r}_b & -J^{-1}\hat{r}_w \\ -M^{-1} & \hat{r}_p J^{-1} & I^{-1}(3,3) & I^{-1}(3,4) & I^{-1}(3,5) \\ -M^{-1} & \hat{r}_b J^{-1} & I^{-1}(4,3) & I^{-1}(4,4) & I^{-1}(4,5) \\ -M^{-1} & \hat{r}_w J^{-1} & I^{-1}(5,3) & I^{-1}(5,4) & I^{-1}(5,5) \end{pmatrix},$$

where

$$I^{-1}(3,3) = M^{-1} - \hat{r}_p J^{-1} \hat{r}_p + \frac{1}{\bar{m}} \mathcal{I},$$

$$I^{-1}(3,4) = M^{-1} - \hat{r}_p J^{-1} \hat{r}_b,$$

$$I^{-1}(3,5) = M^{-1} - \hat{r}_p J^{-1} \hat{r}_w,$$

$$I^{-1}(4,3) = M^{-1} - \hat{r}_b J^{-1} \hat{r}_p,$$

$$I^{-1}(4,4) = M^{-1} - \hat{r}_b J^{-1} \hat{r}_b + \frac{1}{m_b} \mathcal{I},$$

$$I^{-1}(4,5) = M^{-1} - \hat{r}_b J^{-1} \hat{r}_w$$

$$I^{-1}(5,3) = M^{-1} - \hat{r}_w J^{-1} \hat{r}_p$$

$$I^{-1}(5,4) = M^{-1} - \hat{r}_w J^{-1} \hat{r}_b$$

$$I^{-1}(5,5) = M^{-1} - \hat{r}_w J^{-1} \hat{r}_w + \frac{1}{m_w} \mathcal{I}.$$

To get the equations of motion in terms of body velocities, we differentiate (3.27) with respect to time. This introduces terms related to ballast pumping rate \dot{m}_b . We assume that ballast is pumped in such a way that there is negligible associated thrust or moment on the glider. Therefore these \dot{m}_b terms are eliminated from the following equations.

Such ballast rate dependent forces would be equivalent to the thrust from the ejection of mass from a rocket. This is expected to be a negligible force on existing gliders. In existing oceanographic gliders, ballast masses are very small in comparison to the mass of the glider. Ballast pumping rates are very slow and ballast is ejected at a very low relative velocity (i.e. in the vehicle frame). Pumping occurs only at discrete intervals, during transitions from upwards to downwards glides, so \dot{m}_b is zero during most of the time of glider operation and does not affect steady glides. In cases where the ballast masses are of a comparable order of magnitude to the glider mass, or when ballast exit velocities are significant, glider designs are possible where buoyancy is changed in a symmetric way (e.g., ballast is pumped on and off board in streams with the appropriate symmetry) so that there is negligible associated thrust or moment on the glider.

One may also consider some radical glider designs where the ballast mass is of the same order of magnitude as the vehicle mass, or the ballast is ejected from the glider in a high speed jet. Also possible are glider operations or control systems that involve constantly changing ballast at high mass rates and exit velocities. In such cases, the resulting thrusts and moments should be accounted for by including \dot{m}_b terms in the following equations.

Let the ballast control input $u_{ballast_rate}$ be defined as

$$u_{ballast_rate} = \dot{m}_b \tag{3.28}$$

Differentiating (3.27) then gives

$$\begin{pmatrix} \dot{v} \\ \dot{\Omega} \\ \ddot{r}_p \\ \ddot{r}_b \\ \ddot{r}_w \end{pmatrix} = I^{-1} \begin{pmatrix} \dot{P} \\ \dot{\Pi} \\ \dot{P}_p \\ \dot{P}_b \\ \dot{P}_w \end{pmatrix} + \frac{d}{dt}(I^{-1}) \begin{pmatrix} P \\ \Pi \\ P_p \\ P_b \\ P_w \end{pmatrix} \quad (3.29)$$

where

$$\frac{d}{dt}I^{-1} = \begin{pmatrix} 0 & 0 & 0 & 0 & 0 \\ 0 & 0 & -J^{-1}\hat{r}_p & -J^{-1}\hat{r}_b & -J^{-1}\hat{r}_w \\ 0 & \hat{r}_p J^{-1} & \frac{d}{dt}I^{-1}(3,3) & \frac{d}{dt}I^{-1}(3,4) & \frac{d}{dt}I^{-1}(3,5) \\ 0 & \hat{r}_b J^{-1} & \frac{d}{dt}I^{-1}(4,3) & \frac{d}{dt}I^{-1}(4,4) & \frac{d}{dt}I^{-1}(4,5) \\ 0 & \hat{r}_w J^{-1} & \frac{d}{dt}I^{-1}(5,3) & \frac{d}{dt}I^{-1}(5,4) & \frac{d}{dt}I^{-1}(5,5) \end{pmatrix}. \quad (3.30)$$

since $\frac{d}{dt}M^{-1} = 0$, $\frac{d}{dt}J^{-1} = 0$, and

$$\begin{aligned} \frac{d}{dt}I^{-1}(3,3) &= -\hat{r}_p J^{-1} \hat{r}_p - \hat{r}_p J^{-1} \hat{r}_p, \\ \frac{d}{dt}I^{-1}(3,4) &= -\hat{r}_p J^{-1} \hat{r}_b - \hat{r}_p J^{-1} \hat{r}_b, \\ \frac{d}{dt}I^{-1}(3,5) &= -\hat{r}_p J^{-1} \hat{r}_w - \hat{r}_p J^{-1} \hat{r}_w, \\ \frac{d}{dt}I^{-1}(4,3) &= -\hat{r}_b J^{-1} \hat{r}_p - \hat{r}_b J^{-1} \hat{r}_p, \\ \frac{d}{dt}I^{-1}(4,4) &= -\hat{r}_b J^{-1} \hat{r}_b - \hat{r}_b J^{-1} \hat{r}_b, \\ \frac{d}{dt}I^{-1}(4,5) &= -\hat{r}_b J^{-1} \hat{r}_w - \hat{r}_b J^{-1} \hat{r}_w, \\ \frac{d}{dt}I^{-1}(5,3) &= -\hat{r}_w J^{-1} \hat{r}_p - \hat{r}_w J^{-1} \hat{r}_p \end{aligned}$$

$$\begin{aligned}\frac{d}{dt}\mathbf{I}^{-1}(5, 4) &= -\hat{\mathbf{r}}_w\mathbf{J}^{-1}\hat{\mathbf{r}}_b - \hat{\mathbf{r}}_w\mathbf{J}^{-1}\hat{\mathbf{r}}_b \\ \frac{d}{dt}\mathbf{I}^{-1}(5, 5) &= -\hat{\mathbf{r}}_w\mathbf{J}^{-1}\hat{\mathbf{r}}_w - \hat{\mathbf{r}}_w\mathbf{J}^{-1}\hat{\mathbf{r}}_w.\end{aligned}$$

These $\frac{d}{dt}\mathbf{I}^{-1}(i, j)$ terms are generally small in existing gliders. $\dot{\mathbf{r}}_w$ and $\dot{\mathbf{r}}_b$ are zero. $\dot{\mathbf{r}}_p$ is zero at equilibrium glides and is small during transitions between equilibria (due to the glider's actuator speeds). The magnitudes of elements of \mathbf{J} are generally large compared to those of elements of $\mathbf{r}_p, \mathbf{r}_b$ and \mathbf{r}_w (see Tables 4.2 and 4.3). These terms may be significant in very large or small glider designs or in gliders with fast internal mass actuators.

With the substitution into (3.29) of (3.9)-(3.16) for the derivatives $\dot{\mathbf{P}}, \dot{\mathbf{\Pi}}, \dot{\mathbf{P}}_p, \dot{\mathbf{P}}_b$ and $\dot{\mathbf{P}}_w$, (3.30) for $d/dt(\mathbf{I}^{-1})$ and (3.26) for the relationship between momenta and velocity, the complete equations of motion for the underwater glider moving in three-dimensional space are

$$\begin{pmatrix} \dot{\mathbf{R}} \\ \dot{\mathbf{b}} \\ \dot{\mathbf{\Omega}} \\ \dot{\mathbf{v}} \\ \dot{\mathbf{r}}_p \\ \dot{\mathbf{r}}_b \\ \dot{\mathbf{r}}_w \\ \dot{\mathbf{P}}_p \\ \dot{\mathbf{P}}_b \\ \dot{\mathbf{P}}_w \\ \dot{m}_b \end{pmatrix} = \begin{pmatrix} \mathbf{R}\hat{\mathbf{\Omega}} \\ \mathbf{R}\mathbf{v} \\ \mathbf{J}^{-1}\bar{\mathbf{T}} \\ \mathbf{M}^{-1}\bar{\mathbf{F}} \\ \frac{1}{m}\mathbf{P}_p - \mathbf{v} - \mathbf{\Omega} \times \mathbf{r}_p \\ \frac{1}{m_b}\mathbf{P}_b - \mathbf{v} - \mathbf{\Omega} \times \mathbf{r}_b \\ \frac{1}{m_w}\mathbf{P}_w - \mathbf{v} - \mathbf{\Omega} \times \mathbf{r}_w \\ \bar{\mathbf{u}} \\ \mathbf{u}_b \\ \mathbf{u}_w \\ u_{ballast_rate} \end{pmatrix}, \quad (3.31)$$

where

$$\begin{aligned}
\bar{\mathbf{T}} &= (\mathbf{J}\boldsymbol{\Omega} + \hat{\mathbf{r}}_p \mathbf{P}_p + \hat{\mathbf{r}}_b \mathbf{P}_b + \hat{\mathbf{r}}_w \mathbf{P}_w) \times \boldsymbol{\Omega} + (\mathbf{M}\mathbf{v} \times \mathbf{v}) \\
&\quad + (\boldsymbol{\Omega} \times \mathbf{r}_p) \times \mathbf{P}_p + (\boldsymbol{\Omega} \times \mathbf{r}_b) \times \mathbf{P}_b + (\boldsymbol{\Omega} \times \mathbf{r}_w) \times \mathbf{P}_w + (\bar{m}\hat{\mathbf{r}}_p + m_b\hat{\mathbf{r}}_b + m_w\hat{\mathbf{r}}_w)g\mathbf{R}^T\mathbf{k} \\
&\quad + \mathbf{T}_{ext} - \hat{\mathbf{r}}_p\bar{\mathbf{u}} - (\hat{\mathbf{r}}_b\mathbf{u}_b + \hat{\mathbf{r}}_w\mathbf{u}_w) \\
\bar{\mathbf{F}} &= (\mathbf{M}\mathbf{v} + \mathbf{P}_p + \mathbf{P}_b + \mathbf{P}_w) \times \boldsymbol{\Omega} + m_0g\mathbf{R}^T\mathbf{k} + \mathbf{F}_{ext} - \bar{\mathbf{u}} - (\mathbf{u}_b + \mathbf{u}_w).
\end{aligned}$$

Here,

$$\begin{aligned}
\mathbf{F}_{ext} &= \mathbf{R}^T \sum \mathbf{f}_{ext_i} \\
\mathbf{T}_{ext} &= \mathbf{R}^T \sum (\mathbf{x}_i - \mathbf{b}) \times \mathbf{f}_{ext_i} + \mathbf{R}^T \sum \boldsymbol{\tau}_{ext_j},
\end{aligned}$$

where \mathbf{x}_i is the point in the inertial frame where \mathbf{f}_{ext_i} acts, represent external forces and moments including lift, drag, and associated hydrodynamic moments with respect to the body frame.

$\bar{\mathbf{u}}$ is a control force on $\bar{\mathbf{m}}$, and \mathbf{u}_b and \mathbf{u}_w are the internal forces on masses m_b and m_w .

They will be constraint forces when those masses are fixed in place.

One could imagine a glider with a moving ballast mass, or one with two moving point masses such as Spray. In that case the \mathbf{u}_b and \mathbf{u}_w could be used as controls. It is also possible to modify the model to represent a glider with a moving ballast tank and an arbitrary number of point masses.

3.2.4 Change of States and Controls to Point mass Accelerations

In this section, in order to more accurately model general glider designs and existing glider designs such as Slocum, we perform control transformation and a change of variables and

control inputs to change the state vector from $\mathbf{z} = (\mathbf{R}, \mathbf{b}, \boldsymbol{\Omega}, \mathbf{v}, \mathbf{r}_p, \mathbf{r}_b, \mathbf{r}_w, \mathbf{P}_p, \mathbf{P}_b, \mathbf{P}_w, \dot{m}_b)^T$ to $\mathbf{x} = (\mathbf{R}, \mathbf{b}, \boldsymbol{\Omega}, \mathbf{v}, \mathbf{r}_p, \mathbf{r}_b, \mathbf{r}_w, \dot{\mathbf{r}}_p, \dot{\mathbf{r}}_b, \dot{\mathbf{r}}_w, \dot{m}_b)^T$. This control transformation changes the control vector from

$$\mathbf{u} = \begin{pmatrix} \bar{\mathbf{u}} \\ \mathbf{u}_b \\ \mathbf{u}_w \end{pmatrix} = \begin{pmatrix} \dot{\mathbf{P}}_p \\ \dot{\mathbf{P}}_b \\ \dot{\mathbf{P}}_w \end{pmatrix}, \quad (3.32)$$

corresponding to the forces on the internal point masses \bar{m} , m_b , and m_w , into control vector

$$\mathbf{w} = \begin{pmatrix} \mathbf{w}_p \\ \mathbf{w}_b \\ \mathbf{w}_w \end{pmatrix} = \begin{pmatrix} \ddot{\mathbf{r}}_p \\ \ddot{\mathbf{r}}_b \\ \ddot{\mathbf{r}}_w \end{pmatrix}, \quad (3.33)$$

the vector of the accelerations of the internal point masses. The state variables corresponding to the internal masses are changed from the positions and momenta of the masses in the body frame to the positions and accelerations, in the body frame, of the internal masses. This was presented in [5] for a glider model confined to the longitudinal plane, with $m_w = 0$ and with m_b fixed at the glider CB.

The control transformation and change of states and controls described here produces a number of benefits in modelling the glider's dynamics and control. The transformation effectively provides a suspension system for the glider's internal masses. This prevents those masses from moving within the glider in response to vehicle motion. Control of the acceleration of the internal masses more closely approximates the moving mass systems of existing gliders. It also allows for the point masses to be fixed in place in the glider frame by setting the corresponding velocities and accelerations to zero. Doing so allows the static stability of the glider to be examined. This formulation also allows us to solve for the

constraint forces on the masses when they are fixed in place. Most importantly, this control feedback transformation affects the stability of the glider, as will be explained further in Chapter 6. By preventing the internal masses from moving in the body frame in response to vehicle motion, the control transformation improves the stability of steady glides and improves the performance of the glider's switching between steady glides.

Now consider the transformation from control \mathbf{u} , the original set of force inputs, to control \mathbf{w} , the new set of acceleration inputs. Differentiating Equation (3.31) for $\dot{r}_p, \dot{r}_b, \dot{r}_w$ and substituting from (3.31) gives the accelerations of the point masses in terms of the new state vector \mathbf{x} and controls \mathbf{u} . The resulting equations for the point mass accelerations $\ddot{\mathbf{r}}$ may be written in the form

$$\ddot{\mathbf{r}} = \mathbf{Z}(\mathbf{x}) + \mathbf{F}(\mathbf{x})\mathbf{u}, \quad (3.34)$$

where $\mathbf{Z} = (\mathbf{Z}_p(\mathbf{x}), \mathbf{Z}_b(\mathbf{x}), \mathbf{Z}_w(\mathbf{x}))^T$. In the new state variables \mathbf{x} , $\mathbf{Z}(\mathbf{x})$ is the drift vector field and $\mathbf{F}(\mathbf{x})$ is the control vector field. Now, let $\mathbf{H} = \mathbf{F}^{-1}$ and set $\mathbf{u} = \mathbf{H}(-\mathbf{Z} + \mathbf{w})$, where $\mathbf{w} = (\mathbf{w}_p, \mathbf{w}_b, \mathbf{w}_w)^T$. Substituting this into Equation (3.34) gives $\ddot{\mathbf{r}} = \mathbf{w}$.

\mathbf{F} is computed, from Equations (3.29) and (3.31), to be

$$\begin{aligned} \mathbf{F} &= \begin{pmatrix} I^{-1}(3,3) & I^{-1}(3,4) & I^{-1}(3,5) \\ I^{-1}(4,3) & I^{-1}(4,4) & I^{-1}(4,5) \\ I^{-1}(5,3) & I^{-1}(5,4) & I^{-1}(5,5) \end{pmatrix} \\ &= \begin{pmatrix} M^{-1} - \hat{r}_p \mathbf{J}^{-1} \hat{r}_p + \frac{1}{m} \mathcal{I} & M^{-1} - \hat{r}_p \mathbf{J}^{-1} \hat{r}_b & M^{-1} - \hat{r}_p \mathbf{J}^{-1} \hat{r}_w \\ M^{-1} - \hat{r}_b \mathbf{J}^{-1} \hat{r}_p & M^{-1} - \hat{r}_b \mathbf{J}^{-1} \hat{r}_b + \frac{1}{m_b} \mathcal{I} & M^{-1} - \hat{r}_b \mathbf{J}^{-1} \hat{r}_w \\ M^{-1} - \hat{r}_w \mathbf{J}^{-1} \hat{r}_p & M^{-1} - \hat{r}_w \mathbf{J}^{-1} \hat{r}_b & M^{-1} - \hat{r}_w \mathbf{J}^{-1} \hat{r}_w + \frac{1}{m_w} \mathcal{I} \end{pmatrix}. \end{aligned} \quad (3.35)$$

The determinant of \mathbf{F} is always greater than zero, so $\mathbf{H} = \mathbf{F}^{-1}$ is always defined (given the properties of the vehicle masses and inertias already described, for example \mathbf{M} and \mathbf{J} are positive definite). $\mathbf{Z} = (\mathbf{Z}_p, \mathbf{Z}_b, \mathbf{Z}_w)^T$ is found by differentiating the equations for $\dot{\mathbf{r}}$ in (3.31) and making substitutions from (3.31). This gives

$$\begin{aligned}
\mathbf{Z}_p &= -\mathbf{M}^{-1}[(\mathbf{M}\mathbf{v} + \mathbf{P}_p + \mathbf{P}_b + \mathbf{P}_w) \times \boldsymbol{\Omega} + m_0 g \mathbf{R}^T \mathbf{k} + \mathbf{F}_{ext}] - \boldsymbol{\Omega} \times \dot{\mathbf{r}}_p \\
&\quad - \mathbf{J}^{-1}[(\mathbf{J}\boldsymbol{\Omega} + \hat{\mathbf{r}}_p \mathbf{P}_p + \hat{\mathbf{r}}_b \mathbf{P}_b + \hat{\mathbf{r}}_w \mathbf{P}_w) \times \boldsymbol{\Omega} + (\mathbf{M}\mathbf{v} \times \mathbf{v}) + \mathbf{T}_{ext} \\
&\quad + (\boldsymbol{\Omega} \times \mathbf{r}_p) \times \mathbf{P}_p + (\boldsymbol{\Omega} \times \mathbf{r}_b) \times \mathbf{P}_b + (\boldsymbol{\Omega} \times \mathbf{r}_w) \times \mathbf{P}_w \\
&\quad + (\bar{m}\hat{\mathbf{r}}_p + m_b \hat{\mathbf{r}}_b + m_w \hat{\mathbf{r}}_w) g \mathbf{R}^T \mathbf{k}] \times \mathbf{r}_p \\
\mathbf{Z}_b &= -\mathbf{M}^{-1}[(\mathbf{M}\mathbf{v} + \mathbf{P}_p + \mathbf{P}_b + \mathbf{P}_w) \times \boldsymbol{\Omega} + m_0 g \mathbf{R}^T \mathbf{k} + \mathbf{F}_{ext}] - \boldsymbol{\Omega} \times \dot{\mathbf{r}}_b \\
&\quad - \mathbf{J}^{-1}[(\mathbf{J}\boldsymbol{\Omega} + \hat{\mathbf{r}}_p \mathbf{P}_p + \hat{\mathbf{r}}_b \mathbf{P}_b + \hat{\mathbf{r}}_w \mathbf{P}_w) \times \boldsymbol{\Omega} + (\mathbf{M}\mathbf{v} \times \mathbf{v}) + \mathbf{T}_{ext} \\
&\quad + (\boldsymbol{\Omega} \times \mathbf{r}_p) \times \mathbf{P}_p + (\boldsymbol{\Omega} \times \mathbf{r}_b) \times \mathbf{P}_b + (\boldsymbol{\Omega} \times \mathbf{r}_w) \times \mathbf{P}_w \\
&\quad + (\bar{m}\hat{\mathbf{r}}_p + m_b \hat{\mathbf{r}}_b + m_w \hat{\mathbf{r}}_w) g \mathbf{R}^T \mathbf{k}] \times \mathbf{r}_b \\
\mathbf{Z}_w &= -\mathbf{M}^{-1}[(\mathbf{M}\mathbf{v} + \mathbf{P}_p + \mathbf{P}_b + \mathbf{P}_w) \times \boldsymbol{\Omega} + m_0 g \mathbf{R}^T \mathbf{k} + \mathbf{F}_{ext}] - \boldsymbol{\Omega} \times \dot{\mathbf{r}}_w \\
&\quad - \mathbf{J}^{-1}[(\mathbf{J}\boldsymbol{\Omega} + \hat{\mathbf{r}}_p \mathbf{P}_p + \hat{\mathbf{r}}_b \mathbf{P}_b + \hat{\mathbf{r}}_w \mathbf{P}_w) \times \boldsymbol{\Omega} + (\mathbf{M}\mathbf{v} \times \mathbf{v}) + \mathbf{T}_{ext} \\
&\quad + (\boldsymbol{\Omega} \times \mathbf{r}_p) \times \mathbf{P}_p + (\boldsymbol{\Omega} \times \mathbf{r}_b) \times \mathbf{P}_b + (\boldsymbol{\Omega} \times \mathbf{r}_w) \times \mathbf{P}_w \\
&\quad + (\bar{m}\hat{\mathbf{r}}_p + m_b \hat{\mathbf{r}}_b + m_w \hat{\mathbf{r}}_w) g \mathbf{R}^T \mathbf{k}] \times \mathbf{r}_w
\end{aligned} \tag{3.36}$$

For the control transformation to make control \mathbf{w} the acceleration of the point masses, set

$$\begin{pmatrix} \bar{\mathbf{u}} \\ \mathbf{u}_b \\ \mathbf{u}_w \end{pmatrix} = \mathbf{H} \begin{pmatrix} -\mathbf{Z}_p + \mathbf{w}_p \\ -\mathbf{Z}_b + \mathbf{w}_b \\ -\mathbf{Z}_w + \mathbf{w}_w \end{pmatrix} = \begin{pmatrix} H_{11}(-\mathbf{Z}_p + \mathbf{w}_p) + H_{12}(-\mathbf{Z}_b + \mathbf{w}_b) + H_{13}(-\mathbf{Z}_w + \mathbf{w}_w) \\ H_{21}(-\mathbf{Z}_p + \mathbf{w}_p) + H_{22}(-\mathbf{Z}_b + \mathbf{w}_b) + H_{23}(-\mathbf{Z}_w + \mathbf{w}_w) \\ H_{31}(-\mathbf{Z}_p + \mathbf{w}_p) + H_{32}(-\mathbf{Z}_b + \mathbf{w}_b) + H_{33}(-\mathbf{Z}_w + \mathbf{w}_w) \end{pmatrix}, \tag{3.37}$$

where H_{ij} is the (i, j) th component of \mathbf{H} .

Now implement the change of states along with the control transformation. Recall that, from (3.21)-(3.23),

$$\begin{aligned}\mathbf{P}_p &= \bar{m}(\mathbf{v} + \boldsymbol{\Omega} \times \mathbf{r}_p + \dot{\mathbf{r}}_p), \\ \mathbf{P}_b &= m_b(\mathbf{v} + \boldsymbol{\Omega} \times \mathbf{r}_b + \dot{\mathbf{r}}_b), \\ \mathbf{P}_w &= m_w(\mathbf{v} + \boldsymbol{\Omega} \times \mathbf{r}_w + \dot{\mathbf{r}}_w).\end{aligned}$$

3.2.5 Glider Dynamic Equations With Point Mass Acceleration Control

Writing the glider dynamic equations in terms of state vector $\mathbf{x} = (\mathbf{R}, \mathbf{b}, \boldsymbol{\Omega}, \mathbf{v}, \mathbf{r}_p, \mathbf{r}_b, \mathbf{r}_w, \dot{\mathbf{r}}_p, \dot{\mathbf{r}}_b, \dot{\mathbf{r}}_w, \dot{m}_b)^T$ and using control vector (3.37) gives

$$\begin{pmatrix} \dot{\mathbf{R}} \\ \dot{\mathbf{b}} \\ \dot{\boldsymbol{\Omega}} \\ \dot{\mathbf{v}} \\ \dot{\mathbf{r}}_p \\ \dot{\mathbf{r}}_b \\ \dot{\mathbf{r}}_w \\ \ddot{\mathbf{r}}_p \\ \ddot{\mathbf{r}}_b \\ \ddot{\mathbf{r}}_w \\ \dot{m}_b \end{pmatrix} = \begin{pmatrix} \mathbf{R}\hat{\boldsymbol{\Omega}} \\ \mathbf{R}\mathbf{v} \\ \mathbf{J}^{-1}\tilde{\mathbf{T}} \\ \mathbf{M}^{-1}\tilde{\mathbf{F}} \\ \dot{\mathbf{r}}_p \\ \dot{\mathbf{r}}_b \\ \dot{\mathbf{r}}_w \\ \mathbf{w}_p \\ \mathbf{w}_b \\ \mathbf{w}_w \\ u_{ballast_rate} \end{pmatrix}, \quad (3.38)$$

where

$$\begin{aligned}
\tilde{\mathbf{T}} &= [\mathbf{J}\boldsymbol{\Omega} + \hat{\mathbf{r}}_p(\bar{m}(\mathbf{v} + \boldsymbol{\Omega} \times \mathbf{r}_p + \dot{\mathbf{r}}_p))] \\
&\quad + \hat{\mathbf{r}}_b(m_b(\mathbf{v} + \boldsymbol{\Omega} \times \mathbf{r}_b + \dot{\mathbf{r}}_b)) + \hat{\mathbf{r}}_w(m_w(\mathbf{v} + \boldsymbol{\Omega} \times \mathbf{r}_w + \dot{\mathbf{r}}_w))] \times \boldsymbol{\Omega} \\
&\quad + (\mathbf{M}\mathbf{v} \times \mathbf{v}) + (\boldsymbol{\Omega} \times \mathbf{r}_p) \times (\bar{m}(\mathbf{v} + \boldsymbol{\Omega} \times \mathbf{r}_p + \dot{\mathbf{r}}_p)) + (\boldsymbol{\Omega} \times \mathbf{r}_b) \times (m_b(\mathbf{v} + \boldsymbol{\Omega} \times \mathbf{r}_b + \dot{\mathbf{r}}_b)) \\
&\quad + (\boldsymbol{\Omega} \times \mathbf{r}_w) \times (m_w(\mathbf{v} + \boldsymbol{\Omega} \times \mathbf{r}_w + \dot{\mathbf{r}}_w)) + (\bar{m}\hat{\mathbf{r}}_p + m_b\hat{\mathbf{r}}_b + m_w\hat{\mathbf{r}}_w)g\mathbf{R}^T\mathbf{k} \\
&\quad + \mathbf{T}_{ext} - \hat{\mathbf{r}}_p[H_{11}(-\tilde{\mathbf{Z}}_p + \mathbf{w}_p) + H_{12}(-\tilde{\mathbf{Z}}_b + \mathbf{w}_b) + H_{13}(-\tilde{\mathbf{Z}}_w + \mathbf{w}_w)] \\
&\quad - \hat{\mathbf{r}}_b[H_{21}(-\tilde{\mathbf{Z}}_p + \mathbf{w}_p) + H_{22}(-\tilde{\mathbf{Z}}_b + \mathbf{w}_b) + H_{23}(-\tilde{\mathbf{Z}}_w + \mathbf{w}_w)] \\
&\quad - \hat{\mathbf{r}}_w[H_{31}(-\tilde{\mathbf{Z}}_p + \mathbf{w}_p) + H_{32}(-\tilde{\mathbf{Z}}_b + \mathbf{w}_b) + H_{33}(-\tilde{\mathbf{Z}}_w + \mathbf{w}_w)], \tag{3.39}
\end{aligned}$$

$$\begin{aligned}
\tilde{\mathbf{F}} &= [\mathbf{M}\mathbf{v} + \bar{m}(\mathbf{v} + \boldsymbol{\Omega} \times \mathbf{r}_p + \dot{\mathbf{r}}_p) + m_b(\mathbf{v} + \boldsymbol{\Omega} \times \mathbf{r}_b + \dot{\mathbf{r}}_b) + m_w(\mathbf{v} + \boldsymbol{\Omega} \times \mathbf{r}_w + \dot{\mathbf{r}}_w)] \times \boldsymbol{\Omega} \\
&\quad + m_0g\mathbf{R}^T\mathbf{k} + \mathbf{F}_{ext} \\
&\quad - [H_{11}(-\tilde{\mathbf{Z}}_p + \mathbf{w}_p) + H_{12}(-\tilde{\mathbf{Z}}_b + \mathbf{w}_b) + H_{13}(-\tilde{\mathbf{Z}}_w + \mathbf{w}_w)] \\
&\quad - [H_{21}(-\tilde{\mathbf{Z}}_p + \mathbf{w}_p) + H_{22}(-\tilde{\mathbf{Z}}_b + \mathbf{w}_b) + H_{23}(-\tilde{\mathbf{Z}}_w + \mathbf{w}_w)] \\
&\quad - [H_{31}(-\tilde{\mathbf{Z}}_p + \mathbf{w}_p) + H_{32}(-\tilde{\mathbf{Z}}_b + \mathbf{w}_b) + H_{33}(-\tilde{\mathbf{Z}}_w + \mathbf{w}_w)], \tag{3.40}
\end{aligned}$$

where $\tilde{\mathbf{Z}}$ is \mathbf{Z} with the appropriate states (given below) and,

$$\begin{aligned}
\mathbf{F}_{ext} &= \mathbf{R}^T \sum \mathbf{f}_{ext_i} \\
\mathbf{T}_{ext} &= \mathbf{R}^T \sum (\mathbf{x}_i - \mathbf{b}) \times \mathbf{f}_{ext_i} + \mathbf{R}^T \sum \boldsymbol{\tau}_{ext_j}
\end{aligned}$$

Substituting for \mathbf{P}_p , \mathbf{P}_b and \mathbf{P}_w in equations (3.39)-(3.40) above for \mathbf{Z} gives $\tilde{\mathbf{Z}} = (\tilde{\mathbf{Z}}_p, \tilde{\mathbf{Z}}_b, \tilde{\mathbf{Z}}_w)^T$ in terms of the new state vector:

$$\tilde{\mathbf{Z}}_p = -\mathbf{M}^{-1}[[\mathbf{M}\mathbf{v} + \bar{m}(\mathbf{v} + \boldsymbol{\Omega} \times \mathbf{r}_p + \dot{\mathbf{r}}_p) + m_b(\mathbf{v} + \boldsymbol{\Omega} \times \mathbf{r}_b + \dot{\mathbf{r}}_b)$$

3.2.6 Glider Dynamic Equations With Acceleration Control and Simplified Internal Masses

In the case when m_b and m_w are fixed in place within a glider, the glider dynamic equations may be reduced by setting $\dot{\mathbf{r}}_b = \dot{\mathbf{r}}_w = \mathbf{w}_b = \mathbf{w}_w = 0$. The equations may be further simplified by setting $m_w = 0$ to eliminate the offset fixed mass, and by fixing the ballast mass m_b at the CB, $\mathbf{r}_b = 0$. This produces a simplified glider model, with ballast control, where the sliding internal mass is the only offset mass. Substituting $\mathbf{r}_b = \dot{\mathbf{r}}_b = \dot{\mathbf{r}}_w = \mathbf{w}_b = \mathbf{w}_w = 0$ and $m_w = 0$ into equation (3.38) gives the glider dynamics for this simplified glider model. Leonard and Graver, [42], describe the glider model with this mass arrangement where control vector $\bar{\mathbf{u}} = \dot{P}_p$ is the force on the moving internal mass \bar{m} . In this section the control \mathbf{w}_p is the acceleration of \bar{m} . Control u_4 is the ballast pumping rate $u_{ballast_rate}$. Note that in [42], m_b is included in the mass matrix \mathbf{M} , while here it is separate. The dynamics of the glider model with an internal sliding mass \bar{m} , m_b fixed at the CB, and $m_w = 0$ are

$$\begin{pmatrix} \dot{R} \\ \dot{b} \\ \dot{\Omega} \\ \dot{v} \\ \dot{r}_p \\ \ddot{r}_p \\ \dot{m}_b \end{pmatrix} = \begin{pmatrix} R\hat{\Omega} \\ Rv \\ J^{-1}\tilde{\mathbf{T}}_{sm} \\ M^{-1}\tilde{\mathbf{F}}_{sm} \\ \dot{r}_p \\ \mathbf{w}_p \\ u_4 \end{pmatrix}, \quad (3.42)$$

where $\tilde{\mathbf{T}}_{sm}$ and $\tilde{\mathbf{F}}_{sm}$ denote the torques and forces in this ‘simplified masses’ model.

They are

$$\begin{aligned}\tilde{\mathbf{T}}_{sm} = & [\mathbf{J}\boldsymbol{\Omega} + \hat{\mathbf{r}}_p(\bar{m}(\mathbf{v} + \boldsymbol{\Omega} \times \mathbf{r}_p + \dot{\mathbf{r}}_p))] \times \boldsymbol{\Omega} + (\mathbf{M}\mathbf{v} \times \mathbf{v}) + (\boldsymbol{\Omega} \times \mathbf{r}_p) \times (\bar{m}(\mathbf{v} + \boldsymbol{\Omega} \times \mathbf{r}_p + \dot{\mathbf{r}}_p)) \\ & + \bar{m}\hat{\mathbf{r}}_p g \mathbf{R}^T \mathbf{k} + \mathbf{T}_{ext} - \hat{\mathbf{r}}_p [H_{11}(-\tilde{\mathbf{Z}}_p + \mathbf{w}_p) + H_{12}(-\tilde{\mathbf{Z}}_b)]\end{aligned}$$

$$\begin{aligned}\tilde{\mathbf{F}}_{sm} = & [(\mathbf{M} + m_b \mathcal{I})\mathbf{v} + \bar{m}(\mathbf{v} + \boldsymbol{\Omega} \times \mathbf{r}_p + \dot{\mathbf{r}}_p)] \times \boldsymbol{\Omega} + m_0 g \mathbf{R}^T \mathbf{k} + \mathbf{F}_{ext} \\ & - [H_{11}(-\tilde{\mathbf{Z}}_p + \mathbf{w}_p) + H_{12}(-\tilde{\mathbf{Z}}_b)] - [H_{21}(-\tilde{\mathbf{Z}}_p + \mathbf{w}_p) + H_{22}(-\tilde{\mathbf{Z}}_b)].\end{aligned}$$

\mathbf{F}_{ext} and \mathbf{T}_{ext} are the external force and torques defined as before. Substituting $m_w = 0$ and $\mathbf{r}_b = \dot{\mathbf{r}}_b = \dot{\mathbf{r}}_w = \mathbf{w}_b = \mathbf{w}_w = 0$ into Equation 3.2.5 for $\tilde{\mathbf{Z}}$, dropping $\tilde{\mathbf{Z}}_w$ since $m_w = 0$, gives $\tilde{\mathbf{Z}}_{sm} = (\tilde{\mathbf{Z}}_{p_{sm}}, \tilde{\mathbf{Z}}_{b_{sm}})^T$ where

$$\begin{aligned}\tilde{\mathbf{Z}}_{p_{sm}} = & -\mathbf{M}^{-1}[(\mathbf{M} + m_b \mathcal{I})\mathbf{v} + \bar{m}(\mathbf{v} + \boldsymbol{\Omega} \times \mathbf{r}_p + \dot{\mathbf{r}}_p)] \times \boldsymbol{\Omega} \\ & + m_0 g \mathbf{R}^T \mathbf{k} + \mathbf{F}_{ext}] - \boldsymbol{\Omega} \times \dot{\mathbf{r}}_p \\ & - \mathbf{J}^{-1}[(\mathbf{J}\boldsymbol{\Omega} + \hat{\mathbf{r}}_p(\bar{m}(\mathbf{v} + \boldsymbol{\Omega} \times \mathbf{r}_p + \dot{\mathbf{r}}_p))] \times \boldsymbol{\Omega} + (\mathbf{M}\mathbf{v} \times \mathbf{v}) + \mathbf{T}_{ext} \\ & + (\boldsymbol{\Omega} \times \mathbf{r}_p) \times (\bar{m}(\mathbf{v} + \boldsymbol{\Omega} \times \mathbf{r}_p + \dot{\mathbf{r}}_p)) + \bar{m}\hat{\mathbf{r}}_p g \mathbf{R}^T \mathbf{k}] \times \mathbf{r}_p \\ \tilde{\mathbf{Z}}_{b_{sm}} = & -\mathbf{M}^{-1}[(\mathbf{M} + m_b \mathcal{I})\mathbf{v} + \bar{m}(\mathbf{v} + \boldsymbol{\Omega} \times \mathbf{r}_p + \dot{\mathbf{r}}_p)] \times \boldsymbol{\Omega} \\ & + m_0 g \mathbf{R}^T \mathbf{k} + \mathbf{F}_{ext}] - \boldsymbol{\Omega} \times \dot{\mathbf{r}}_p\end{aligned}$$

The constraint forces $\bar{\mathbf{u}}$, \mathbf{u}_b on the internal masses \bar{m} and m_b may be computed by differentiating $\dot{\mathbf{r}}$ with respect to time, writing the result in the form of (3.34), and setting

$\ddot{\mathbf{r}}_{\mathbf{b}} = 0$. This gives

$$\begin{pmatrix} \ddot{\mathbf{r}}_{\mathbf{p}} \\ 0 \end{pmatrix} = \begin{pmatrix} \tilde{\mathbf{Z}}_{\mathbf{p}_{sm}} \\ \tilde{\mathbf{Z}}_{\mathbf{b}_{sm}} \end{pmatrix} + \mathbf{F}_{sm} \begin{pmatrix} \bar{\mathbf{u}} \\ \mathbf{u}_{\mathbf{b}} \end{pmatrix}. \quad (3.43)$$

Where

$$\mathbf{F}_{sm} = \begin{pmatrix} M^{-1} - \hat{\mathbf{r}}_{\mathbf{p}} \mathbf{J}^{-1} \hat{\mathbf{r}}_{\mathbf{p}} + \frac{1}{m} \mathcal{I} & M^{-1} \\ M^{-1} & M^{-1} + \frac{1}{m_{\mathbf{b}}} \mathcal{I} \end{pmatrix}. \quad (3.44)$$

When the sliding internal mass is also fixed in place, by setting $\mathbf{w}_{\mathbf{p}} = 0$, then the constraint forces $\bar{\mathbf{u}}$ and $\mathbf{u}_{\mathbf{b}}$ on the internal masses are

$$\begin{pmatrix} \bar{\mathbf{u}} \\ \mathbf{u}_{\mathbf{b}} \end{pmatrix} = -\mathbf{F}_{sm}^{-1} \begin{pmatrix} \tilde{\mathbf{Z}}_{\mathbf{p}_{sm}} \\ \tilde{\mathbf{Z}}_{\mathbf{b}_{sm}} \end{pmatrix}. \quad (3.45)$$

Physical Description of Model Terms

This section will explain what some of the glider model terms represent physically.

It is helpful to consider the derivation from Equation (3.6) to Equations (3.9)-(3.10). Certain terms appear because the glider dynamic equations are written in the non-inertial body frame. These include terms $\mathbf{P} \times \boldsymbol{\Omega}$ and $\boldsymbol{\Pi} \times \boldsymbol{\Omega}$ in (3.9)-(3.10). If we disregard the dynamics of the internal point masses, set external forces and torques to zero, and consider a glider in free space instead of a fluid, then Equations (3.9) and (3.10) reduce to Euler's equations for a free rigid body. $(m_h \mathcal{I}) \mathbf{v} \times \boldsymbol{\Omega}$ and $\mathbf{J}_s \boldsymbol{\Omega} \times \boldsymbol{\Omega}$ are torques and forces that appear when tracking the dynamics of a rigid body in a rotating, non-inertial frame. These terms commonly appear in vehicle dynamics, where it is standard to write the dynamic equations in the body-fixed frame [17, 15].

Terms containing $\mathbf{M}_{\mathbf{f}}$ and $\mathbf{J}_{\mathbf{f}}$ are forces and torques due to the added mass and inertia

of the vehicle moving through an inviscid fluid. These include $\mathbf{M}_f \mathbf{v} \times \mathbf{v}$ and $\mathbf{J}_f \boldsymbol{\Omega} \times \boldsymbol{\Omega}$. These terms appear in Kirchhoff's equations for a rigid body in an inviscid fluid, [39, 37].

Each set of glider dynamic equations contains terms representing forces on the point masses and the associated forces and torques on the vehicle. The terms corresponding to the three internal point masses are similar. These terms appear in groups of three, representing the same physical mechanisms acting on each of the three point masses. Explanations below for forces on \bar{m} also apply to corresponding forces on the other point masses.

Keep in mind Equations (3.21)-(3.22) for the point mass momenta \mathbf{P}_p , \mathbf{P}_w , and \mathbf{P}_b . These terms appear differently after the state transformation of Section 3.2.4 but represent the same forces. For example, the force on the point mass in the rotating frame, $\mathbf{P}_p \times \boldsymbol{\Omega}$ in Equation (3.31), is $\bar{m}(\mathbf{v} + \boldsymbol{\Omega} \times \mathbf{r}_p + \dot{\mathbf{r}}_p) \times \boldsymbol{\Omega}$ in Equation (3.38). Similar terms appear for the other internal masses.

Consider terms representing forces that appear in \mathbf{F} , $\tilde{\mathbf{F}}$, and $\tilde{\mathbf{F}}_{sm}$ in Equations (3.31),(3.38), (3.42).

- $(\mathbf{M} \mathbf{v} \times \boldsymbol{\Omega})$ is equal to, from the definition of \mathbf{M} , $(m_h \mathcal{I} \mathbf{v} \times \boldsymbol{\Omega} + \mathbf{M}_f \mathbf{v} \times \boldsymbol{\Omega})$. This is the sum of the inertial force on the vehicle in the rotating frame and the added mass forces due to the rotation of the body in a fluid.
- $\mathbf{P}_p \times \boldsymbol{\Omega}$ is the inertial force from the internal mass dynamics in the rotating body frame.
- $m_0 g \mathbf{R}^T \mathbf{k}$ is the net buoyant force on the vehicle, the sum of the buoyant and gravitational forces. Terms representing gravitational and buoyancy forces have been explained previously.
- $\bar{\mathbf{u}}$ is the control force on the moving point mass \bar{m} .

Now consider moments appearing in \mathbf{T} , $\tilde{\mathbf{T}}$, and $\tilde{\mathbf{T}}_{sm}$

- $\mathbf{M}\mathbf{v} \times \mathbf{v}$ is a moment on the vehicle from added mass effects. Substituting for \mathbf{M} using the definition of \mathbf{M} gives $(m_h \mathcal{I}\mathbf{v} \times \mathbf{v} + \mathbf{M}_f \mathbf{v} \times \mathbf{v}) = (\mathbf{M}_f \mathbf{v} \times \mathbf{v})$. This added mass moment is zero when \mathbf{M}_f is a multiple of I (a symmetrical vehicle, for example a sphere or a cube) or when \mathbf{v} coincides with a principal axis of \mathbf{M} .
- $\mathbf{J}\boldsymbol{\Omega} \times \boldsymbol{\Omega}$ is the moment on the solid body in the rotating body frame plus the moment due to the added inertias and rotation of the vehicle. Substituting the definition of \mathbf{J} gives two terms, $\mathbf{J}_s \boldsymbol{\Omega} \times \boldsymbol{\Omega}$ which is the torque in the body frame due to the spinning of the solid body, and $\mathbf{J}_f \boldsymbol{\Omega} \times \boldsymbol{\Omega}$, which is the added mass torque due to the spinning of the vehicle in a fluid.
- $\bar{m} \hat{\mathbf{r}}_p g \mathbf{R}^T \mathbf{k}$ is a moment on the vehicle from the weight of the moving mass at position \mathbf{r}_p from the center of the body frame.
- $\hat{\mathbf{r}}_p \bar{\mathbf{u}}$ is a moment on the body from the force on the point mass (other than $\bar{m}g$). The glider body and the internal masses are coupled - forces $\bar{\mathbf{u}}$ exerted on the internal masses result in (equal and opposite) forces and associated moments on the body.

Gliders are buoyancy driven. Therefore, the net buoyancy force m_0g determines the order of magnitude of the forces acting on the glider. In a steady glide, the lift and drag forces are of the same order of magnitude as the net buoyancy. The magnitude of the lift is less than the net buoyancy, and drag is equal to or less than the net buoyancy, depending on the glide path angle (see Chapter 4). At glide path angles near 45 degrees, the magnitudes of lift and drag are about half that of m_0g .

In a straight, steady glide $\boldsymbol{\Omega}$ is zero, so many of the above terms may be small. For existing oceanographic gliders, $\boldsymbol{\Omega}$ is small for most flight operations, so many of these terms

may be small in comparison to the buoyancy force. In these gliders $\dot{\mathbf{r}}_{\mathbf{p}}$ generally small due to the design of the mass actuators ($\dot{\mathbf{r}}_{\mathbf{p}}$ is zero at equilibrium). The forces acting on a glider are discussed further in Chapter 5 and Chapter 7.

3.2.7 Glider Model Hydrodynamic Terms: Lift, Drag, Moment

Here we will introduce the form of the hydrodynamic terms in the glider dynamic equations. Determination of hydrodynamic forces for a specific vehicle is discussed later in Chapter 5.

The external forces and moments on the glider, \mathbf{F}_{ext} and \mathbf{T}_{ext} , include hydrodynamic forces \mathbf{F}_{hydro} and moments \mathbf{M}_{hydro} due to the glider's motion through the water. These hydrodynamic forces and moments arise from both viscous and inviscid effects. Forces and moments due to added mass and inertia are included separately in the glider model as shown above. The full unsteady hydrodynamic of a body moving in a fluid are extremely complex. Therefore it is necessary to adopt a model of manageable complexity that sufficiently represents the hydrodynamic forces on the glider.

Hydrodynamic forces on the glider may be expressed in the wind frame as lift, drag and sideforce. Hydrodynamic moments are also expressed in the wind frame. This follows standard aerospace conventions, [15, 66]. Hydrodynamic forces and moments are written in the wind frame as

$$\mathbf{F}_{hydro} = \begin{pmatrix} -D \\ SF \\ -L \end{pmatrix}, \quad \mathbf{M}_{hydro} = \begin{pmatrix} M_{DL1} \\ M_{DL2} \\ M_{DL3} \end{pmatrix},$$

where L, D, SF are lift, drag and sideforce and M_{DLi} is the hydrodynamic moment about the i^{th} wind axis. These are expressed in the body frame as $\mathbf{R}_{WB}\mathbf{F}_{hydro}$ and $\mathbf{R}_{WB}\mathbf{M}_{hydro}$.

as described in Section 3.1.3.

The hydrodynamic forces on the glider are complicated functions of the vehicle geometry and vehicle motion through the water. If a glider has external control surfaces such as a rudder, elevators or ailerons, their positions and settings will influence the hydrodynamic forces and moments.

Standard aerospace practice involves use of coefficient-based models for the hydrodynamic forces on a vehicle. Hydrodynamic force coefficients may be determined using a variety of methods including reference data, CFD modelling, and flight tests. Coefficient models may include terms depending on vehicle velocity, acceleration, and angular rates. See [27], [26], [55].

A simple quasi-steady model for the hydrodynamic forces takes the form

$$\mathbf{F}_{hydro} = \begin{pmatrix} -D \\ SF \\ -L \end{pmatrix} = \begin{pmatrix} -\frac{1}{2}\rho V_r^2 AC_D(\alpha, \beta, \boldsymbol{\delta cs}, Re) \\ \frac{1}{2}\rho V_r^2 AC_{SF}(\alpha, \beta, \boldsymbol{\delta cs}, Re) \\ -\frac{1}{2}\rho V_r^2 AC_L(\alpha, \beta, \boldsymbol{\delta cs}, Re) \end{pmatrix} \quad (3.46)$$

C_D, C_{SF}, C_L are the coefficients of drag, sideforce and moment. The quantity $\frac{1}{2}\rho V_r^2$ is the dynamic pressure. A is the characteristic area of the glider by which the coefficients are defined. α and β are the aerodynamic angles as defined in Section 3.1.3. $\boldsymbol{\delta cs}$ is the vector of control surface settings (usually written in degrees from their zero positions) and Re is the Reynolds number of the flow on the vehicle.

To accurately model the vehicle hydrodynamics, some rotational damping must also be included in this model. The exact form of the linear and rotational damping on a vehicle is quite complex. Rotational damping of sub-surface ocean vehicles may be modelled as linear and quadratic with respect to rotational velocity $\boldsymbol{\Omega}$ [17]. The model for the hydrodynamic

moments on the vehicle then takes the form

$$\mathbf{M}_{hydro} = \begin{pmatrix} M_{DL1} \\ M_{DL2} \\ M_{DL3} \end{pmatrix} = \begin{pmatrix} \frac{1}{2}\rho V_r^2 AC_{M1}(\alpha, \beta, \boldsymbol{\delta cs}, Re) \\ \frac{1}{2}\rho V_r^2 AC_{M2}(\alpha, \beta, \boldsymbol{\delta cs}, Re) \\ \frac{1}{2}\rho V_r^2 AC_{M3}(\alpha, \beta, \boldsymbol{\delta cs}, Re) \end{pmatrix} + \mathbf{K}_{\Omega^1}\boldsymbol{\Omega} + \boldsymbol{\Omega}\mathbf{K}_{\Omega^2}\boldsymbol{\Omega}. \quad (3.47)$$

C_{M1}, C_{M2}, C_{M3} are the coefficients of hydrodynamic moment around the wind 1, 2, 3 axes. \mathbf{K}_{Ω^1} and \mathbf{K}_{Ω^2} are the rotational damping matrices for the linear and quadratic damping terms, respectively. The hydrodynamics of a high speed vehicle are highly coupled, but in a first approximation \mathbf{K}_{Ω^1} and \mathbf{K}_{Ω^2} may be modelled as diagonal [17, 59].

Additional damping terms may be added to the glider dynamics model without changing the overall model formulation (i.e., the necessary hydrodynamic terms may simply be added in the above model). Additional force and moment damping terms may depend on V or $\alpha, \beta, \dot{\alpha}, \dot{\beta}$. Such terms appear in aircraft, for example, because changes in the flow over the wings are transported by the flow to the aircraft's tail surfaces. Changes in the downwash over the wing have some transport lag before reaching the tail. The resulting forces and moments are highly dependent on V and the fluid transport time from the wings to the tail. In relatively slow-moving (and often tailless) underwater gliders with a small range of speeds, these terms may be negligible.

Note that in a steady glide, \mathbf{v} is constant, so $\dot{\alpha} = \dot{\beta} = 0$, but $\boldsymbol{\Omega} = 0$ only in a straight steady glide. $\boldsymbol{\Omega} \neq 0$ in a vertical spiral glide.

This model is a standard one, derived using airfoil theory and potential flow calculations and then verified using experimental observations, see for example [15, 43]. Methods for determination of the coefficients are described in Chapter 5. Note that these forces and

moments are written about the center of the wind frame, which is also the body frame center, so care must be taken to account for their points of action when computing the coefficients from various data sources.

The following chapters include analysis of the glider dynamics when confined to the vertical plane. When modelling the glider in the vertical, longitudinal plane, the hydrodynamic forces and moment are modelled as

$$D = \frac{1}{2}\rho C_D(\alpha)AV^2 \approx (K_{D_0} + K_D\alpha^2)(v_1^2 + v_3^2) \quad (3.48)$$

$$L = \frac{1}{2}\rho C_L(\alpha)AV^2 \approx (K_{L_0} + K_L\alpha)(v_1^2 + v_3^2) \quad (3.49)$$

$$M_{DL} = \frac{1}{2}\rho C_M(\alpha)AV^2 \approx (K_{M_0} + K_M\alpha)(v_1^2 + v_3^2) + K_{\Omega_2^1}\Omega_2 + K_{\Omega_2^2}\Omega_2^2 \quad (3.50)$$

where C_D , C_L and C_M are the standard aerodynamic drag, lift and moment coefficients by A , the maximum glider cross sectional area, and ρ is the fluid density. For the longitudinal quasi-steady fluid model, C_D , C_L and C_M are functions of α and the K 's are constant coefficients.

Chapter 4

Glider Dynamics

In this chapter, the glider model derived in Chapter 3 is applied to an analysis of glider dynamics. This analysis makes use of several variations of the glider model. Experimental observations are also discussed. The principal analysis is of the longitudinal dynamics of the glider model. The longitudinal model is derived from the three dimensional glider model and is used to determine equilibria and their stability. A simplified model of the glider vertical plane dynamics is then analyzed. The phugoid mode dynamics of the glider model are studied by applying simplifying assumptions to the vertical plane model. Other sections discuss the lateral and three dimensional dynamics of gliders.

In Section 4.1, the longitudinal dynamics of the glider model are analyzed by confining the model from Chapter 3 to the vertical plane. The vertical plane is an invariant plane of the dynamic equations. This longitudinal model is used to find steady equilibrium glides (Section 5.1.3) in the vertical plane and to perform linear analysis of their stability. This follows work presented earlier in [42, 24, 25]. Analysis of the longitudinal plane model is directly applicable to modern oceanographic gliders because their deployments include many glide sections roughly within a vertical plane. Straight, steady glides are the most

common operational motions of real, oceangoing gliders. The equations of motion in the plane are determined and the equilibria steady glides are found and subjected to linear analysis.

The analysis makes use of the glider model both before and after the control transformation and change of states described in Section 3.2.4. That transformation changes the manner in which the internal masses are controlled, so that the acceleration of the internal sliding mass is a control input. This allows the position of the masses to be fixed inside the hull and results in improved gliding stability, and more accurately models the system in existing gliders. The longitudinal plane is first analyzed using the untransformed equations. A summary of results for the transformed equations follows, along with some discussion of the differences between the two cases. These include some differences in the stability of steady glides and the transition between different steady glides, especially those inflecting from upwards to downwards glides or vice-versa.

Section 4.2 examine the phugoid mode of underwater gliders using a simplified model of the glider longitudinal dynamics. This analysis follows along the lines of the analysis of the phugoid mode for aircraft conducted by Lanchester in 1908 [40, 73].

Section 4.3 discusses gliding in three dimensions. This includes a brief discussion of the lateral dynamics of gliders. Steady straight and spiral glides are examined, including some results from simulations and from in-ocean experiments with full-scale gliders. Other items of interest include deviations from the vertical plane due to static mis-trim and coupling between the rudder and roll angles. The latter was found to couple the Slocum electric glider's roll and yaw steering dynamics.

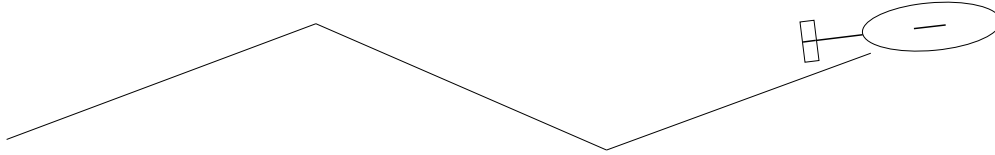


Figure 4.1: Sawtooth Gliding in the Vertical Plane.

4.1 Longitudinal Model

This section analyzes the longitudinal dynamics of underwater gliders, following our work in [42, 24, 25]. The model of the glider longitudinal dynamics is derived by confining the model of Chapter 3 to the vertical plane. Simplifications are made to the internal mass layout from the full glider dynamic model. The resulting vertical plane model is analyzed. Steady glide equilibria are found and a general linearization about these steady glides is determined. This model and linearization may be used to examine the stability of steady glides and has applications in glider design and in design of their control systems.

Existing gliders spend much of their operational time in steady, straight-line glides as modelled in this section, Figure 4.1. The reasons for this include gliding efficiency, low power consumption, and the nature of their scientific sampling missions. Of particular interest are the possible choices of equilibrium steady glides, the stability of those glides as a function of glider design and internal mass positioning, and transitions between glides, particularly between straight, steady glides upwards and downwards in the vertical plane.

As part of the analysis here, the glider model is slightly simplified by restricting the arrangement of the internal masses. This follows the simplified mass arrangement introduced in Section 3.2.6. The offset static point mass m_w is eliminated, and the ballast mass m_b is restricted to a position at the glider centroid such that $\mathbf{r}_b = 0$. This removes the inertial effects of the offset mass and the coupling between pitch moment and ballast mass resulting from a ballast mass offset from the vehicle CB. Useful results are then determined from the

model with this restricted layout. These results remain useful when these restrictions are relaxed. The principal difference in the equilibrium equations when these masses are included is a change in the pitch balance equation. More complex internal mass arrangements may be addressed using the full glider vertical plane model.

The restriction to the vertical plane ignores certain dynamics associated with out-of-plane motion. It may be judged, from simulation and experiment, that the restriction is a reasonable one. Experiments using the Slocum glider show that the vertical plane steady glides are qualitatively consistent with the results of the model (see Chapter 5). The vertical plane is an invariant plane in the dynamic equations. Restriction to the longitudinal plane is a standard method of analysis in aircraft dynamics. Additionally, the design of some gliders, Slocum especially, controls the vertical plane dynamics using separate actuators and control algorithms from those used to control lateral dynamics. In the Slocum electric glider design, for example, gliding in the vertical plane is controlled using the ballast tank and internal sliding mass actuator, while steering out of the plane is controlled using the rudder, without any actuation of the internal masses. In many glides the rudder is used to actively stabilize gliding motion to a straight glide in the vertical plane. For these reasons, study of the vertical plane dynamics is both useful and representative of actual glider operation.

4.1.1 Equations of Motion in the Vertical Plane

This section confines the glider equations of motion to the vertical plane. We first restrict the arrangement of internal masses. Eliminate the offset static mass by setting $m_w = 0$. Fix the ballast mass at the centroid of the glider body, where $\mathbf{r}_b = 0$. The glider with simplified internal masses is shown in Figure 4.2. These changes eliminate the inertial coupling due to the offset static point mass m_w , and the coupling between the ballast state and the vehicle

inertia and pitch moment. In some glider designs, including Slocum, the ballast actuates both the pitch and the buoyancy of the vehicle. The ballast is positioned to produce both the desired ballast state and pitch angle for upwards and downwards glides.

The model used for investigation here is chosen to capture the major elements of glider dynamics without extra complication. In this model, the sliding mass principally actuates the orientation of the glider and the ballast system actuates the buoyancy. The overall dynamics of gliding are similar to the case analyzed here, even when offset masses \mathbf{r}_b and m_w are included. Some small differences have been noted, including the coupling between ballast and pitch resulting from an offset ballast system. Terms corresponding to these internal masses appear in the full dynamic model and may easily be added to the analysis given here. They appear in later sections, for example, when determining the steady glide equilibria and parameters for the Slocum glider in Chapter 5.

We now specialize the model to the vertical plane, the $\mathbf{i}\text{-}\mathbf{k}$ plane in inertial coordinates and the $\mathbf{e}_1\text{-}\mathbf{e}_3$ plane in body coordinates. Accordingly,

$$\mathbf{R} = \begin{pmatrix} \cos \theta & 0 & \sin \theta \\ 0 & 1 & 0 \\ -\sin \theta & 0 & \cos \theta \end{pmatrix}, \quad \mathbf{b} = \begin{pmatrix} x \\ 0 \\ z \end{pmatrix}, \quad \mathbf{v} = \begin{pmatrix} v_1 \\ 0 \\ v_3 \end{pmatrix}, \quad \boldsymbol{\Omega} = \begin{pmatrix} 0 \\ \Omega_2 \\ 0 \end{pmatrix},$$

$$\mathbf{r}_p = \begin{pmatrix} r_{P1} \\ 0 \\ r_{P3} \end{pmatrix}, \quad \mathbf{P}_p = \begin{pmatrix} P_{P1} \\ 0 \\ P_{P3} \end{pmatrix}, \quad \bar{\mathbf{u}} = \begin{pmatrix} u_1 \\ 0 \\ u_3 \end{pmatrix},$$

where θ is pitch angle.

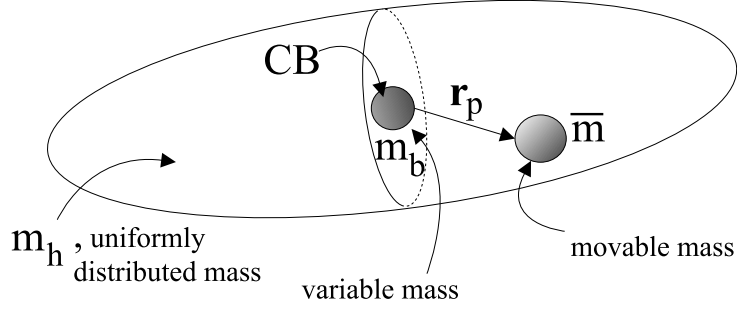


Figure 4.2: Glider with simplified internal masses.

The equations of motion (3.38) for the gliding vehicle restricted to the vertical plane become

$$\dot{x} = v_1 \cos \theta + v_3 \sin \theta \quad (4.1)$$

$$\dot{z} = -v_1 \sin \theta + v_3 \cos \theta \quad (4.2)$$

$$\dot{\theta} = \Omega_2 \quad (4.3)$$

$$\begin{aligned} \dot{\Omega}_2 = & \frac{1}{J_2}((m_3 - m_1)v_1v_3 - (r_{P1}P_{P1} + r_{P3}P_{P3})\Omega_2 \\ & - \bar{m}g(r_{P1} \cos \theta + r_{P3} \sin \theta) + M_{DL} - r_{P3}u_1 + r_{P1}u_3) \end{aligned} \quad (4.4)$$

$$\dot{v}_1 = \frac{1}{m_1}(-m_3v_3\Omega_2 - P_{P3}\Omega_2 - m_0g \sin \theta + L \sin \alpha - D \cos \alpha - u_1) \quad (4.5)$$

$$\dot{v}_3 = \frac{1}{m_3}(m_1v_1\Omega_2 + P_{P1}\Omega_2 + m_0g \cos \theta - L \cos \alpha - D \sin \alpha - u_3) \quad (4.6)$$

$$\dot{r}_{P1} = \frac{1}{\bar{m}}P_{P1} - v_1 - r_{P3}\Omega_2 \quad (4.7)$$

$$\dot{r}_{P3} = \frac{1}{\bar{m}}P_{P3} - v_3 + r_{P1}\Omega_2 \quad (4.8)$$

$$\dot{P}_{P1} = u_1 \quad (4.9)$$

$$\dot{P}_{P3} = u_3 \quad (4.10)$$

$$\dot{m}_b = u_4 \quad (4.11)$$

Here, α is the angle of attack, D is drag, L is lift and M_{DL} is the viscous moment as shown

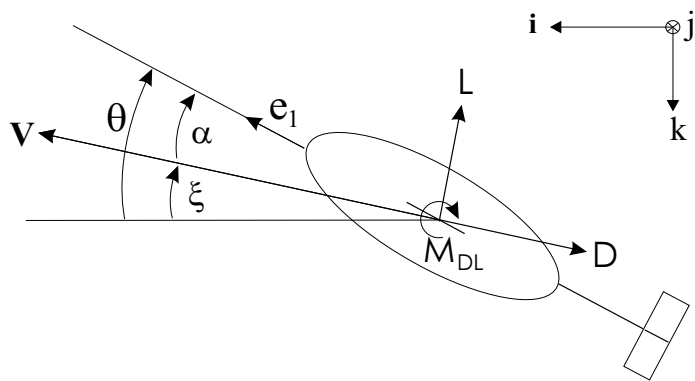


Figure 4.3: Lift and drag on glider confined to the vertical plane.

in Figure 4.3.

These forces and moment are modelled as described in Chapter 3. As shown in Figure 4.3, we denote the glide path angle by ξ where

$$\xi = \theta - \alpha.$$

We also denote the glider speed by V where

$$V = \sqrt{(v_1^2 + v_3^2)}.$$

We will typically specify a glide path by desired glide path angle ξ_d and desired speed V_d .

We define inertial coordinates (x', z') such that x' is the position along the desired path:

$$\begin{pmatrix} x' \\ z' \end{pmatrix} = \begin{pmatrix} \cos \xi_d & -\sin \xi_d \\ \sin \xi_d & \cos \xi_d \end{pmatrix} \begin{pmatrix} x \\ z \end{pmatrix}. \quad (4.12)$$

Then, z' measures the vehicle's position in the direction perpendicular to the desired path.

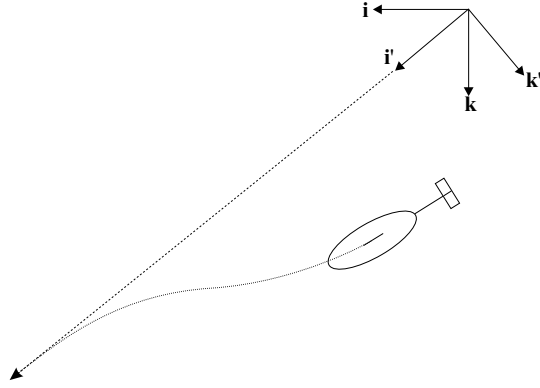


Figure 4.4: Planar gliding controlled to a line.

The dynamics of the z' state are

$$\dot{z}' = \sin \xi_d (v_1 \cos \theta + v_3 \sin \theta) + \cos \xi_d (-v_1 \sin \theta + v_3 \cos \theta). \quad (4.13)$$

Glider control and gliding along a desired line with $z' = 0$ are discussed in Chapter 6.

In the glider model, the movable point mass can be controlled in all directions (2 degrees of freedom in the planar case). However, it may sometimes be the case that control over the CG location is restricted, for example, when a battery may only be shifted in a limited way. For the planar case, this might translate into a movable point mass with only one degree of freedom. This is the case in several existing glider designs. To model this we consider the case in which r_{P3} is fixed ($\dot{r}_{P3} = 0$), i.e., we can only move the point mass \bar{m} in the e_1 direction. Then,

$$P_{P3} = \bar{m}(v_3 - r_{P1}\Omega_2). \quad (4.14)$$

The new equations of motion are Equations (4.1)-(4.11) excluding (4.8) and (4.10). Further, P_{P3} is replaced by (4.14) and u_3 is replaced by \dot{P}_{P3} which is computed by differentiating

(4.14) with respect to time. In particular, Equations (4.4) and (4.6) are replaced with

$$\begin{pmatrix} \dot{\Omega}_2 \\ \dot{v}_3 \end{pmatrix} = \mathbf{Z}^{-1} \begin{pmatrix} \frac{1}{J_2}(f_1 + r_{P1}\bar{m}\Omega_2\dot{r}_{P1}) \\ \frac{1}{m_3}(f_2 - \bar{m}\Omega_2\dot{r}_{P1}) \end{pmatrix},$$

where

$$\begin{aligned} f_1 &= (m_3 - m_1)v_1v_3 - \bar{m}g(r_{P1}\cos\theta + r_{P3}\sin\theta) + M_{DL} - r_{P3}u_1 \\ f_2 &= m_1v_1\Omega_2 + P_{P1}\Omega_2 + m_0g\cos\theta - L\cos\alpha - D\sin\alpha \\ \mathbf{Z} &= \begin{pmatrix} 1 + \frac{\bar{m}r_{P1}^2}{J_2} & -\frac{\bar{m}r_{P1}}{J_2} \\ -\frac{\bar{m}r_{P1}}{m_3} & 1 + \frac{\bar{m}}{m_3} \end{pmatrix}. \end{aligned}$$

4.1.2 Gliding Equilibria

We prescribe a desired straight-line glide path by specifying the desired glide path angle ξ_d and the desired speed V_d . We denote with subscript “ d ” the value of all dynamic variables at the glide equilibria. To get the conditions for such planar gliding equilibria, we set the left hand side of Equations (4.13) and (4.3) through (4.11) to zero. This gives equilibria for the general longitudinal model, and is not limited to the case when r_{p3} fixed. This gives

$$0 = \sin\xi_d(v_{1d}\cos\theta_d + v_{3d}\sin\theta_d) + \cos\xi_d(-v_{1d}\sin\theta_d + v_{3d}\cos\theta_d) \quad (4.15)$$

$$0 = \frac{1}{J_2}((m_{f3} - m_{f1})v_{1d}v_{3d} - \bar{m}g(r_{P1d}\cos\theta_d + r_{P3d}\sin\theta_d) + M_{DLd}) \quad (4.16)$$

$$0 = \frac{1}{m_{1d}}(-m_{0d}g\sin\theta_d + L_d\sin\alpha_d - D_d\cos\alpha_d) \quad (4.17)$$

$$0 = \frac{1}{m_{3d}}(m_{0d}g\cos\theta_d - L_d\cos\alpha_d - D_d\sin\alpha_d) \quad (4.18)$$

$$0 = \frac{1}{\bar{m}}P_{P1d} - v_{1d} \quad (4.19)$$

$$0 = \frac{1}{\bar{m}}P_{P3d} - v_{3d} \quad (4.20)$$

and $z'_d = \Omega_{2_d} = u_{1_d} = u_{3_d} = u_{4_d} = 0$. Note that

$$\begin{aligned} m_{1_d} &= m_{b_d} + m_h + m_{f1}, \\ m_{3_d} &= m_{b_d} + m_h + m_{f3}, \\ m_{0_d} &= m_{b_d} + m_h + \bar{m} - m, \end{aligned}$$

which are all dependent on the equilibrium value of the variable mass m_{b_d} .

Given ξ_d , Equations (4.17) and (4.18) may be solved for α_d , independent of V_d as shown below. This is possible because ξ_d is a function of the glider's lift/drag ratio at the equilibrium. Generally the lift/drag polar of a vehicle, which is a function of its geometry, is unchanged over some range of Reynolds numbers. Therefore we may consider it invariant with respect to V once a given operational speed envelope has been determined. Given this lift/drag polar, the lift/drag ratio is a function only of α , not V . We can then compute

$$\theta_d = \xi_d + \alpha_d, \quad v_{1_d} = V_d \cos \alpha_d, \quad v_{3_d} = V_d \sin \alpha_d,$$

$$P_{P1_d} = \bar{m} v_{1_d}, \quad P_{P3_d} = \bar{m} v_{3_d}.$$

m_{b_d} can then be solved again using (4.17) and (4.18). Finally, Equation (4.16) gives a one-parameter family of solutions for $(r_{P1_d}, r_{P3_d})^T$.

First, we compute α_d from Equations (4.17) and (4.18). Note that these equations reduce to

$$\begin{pmatrix} 0 \\ m_{0_d} g \end{pmatrix} = \begin{pmatrix} \cos \theta_d & \sin \theta_d \\ -\sin \theta_d & \cos \theta_d \end{pmatrix} \begin{pmatrix} \cos \alpha_d & -\sin \alpha_d \\ \sin \alpha_d & \cos \alpha_d \end{pmatrix} \begin{pmatrix} D_d \\ L_d \end{pmatrix}$$

$$= \begin{pmatrix} \cos \xi_d & \sin \xi_d \\ -\sin \xi_d & \cos \xi_d \end{pmatrix} \begin{pmatrix} K_{D_0} + K_D \alpha_d^2 \\ K_{L_0} + K_L \alpha_d \end{pmatrix} V_d^2, \quad (4.21)$$

where we have adopted the quasi-steady hydrodynamic model, Equations (3.48)-(3.49) presented in Section 3.2.7. The first equation of (4.21) is a quadratic equation in α_d . Provided $V_d \neq 0$ and $\xi_d \neq \pm \frac{\pi}{2}$, we have

$$\alpha_d^2 + \frac{K_L}{K_D} \tan \xi_d \alpha_d + \frac{1}{K_D} (K_{D_0} + K_{L_0} \tan \xi_d) = 0. \quad (4.22)$$

Equation (4.22) may be solved for a realizable α_d provided ξ_d satisfies

$$\left(\frac{K_L}{K_D} \tan \xi_d \right)^2 - \frac{4}{K_D} (K_{D_0} + K_{L_0} \tan \xi_d) \geq 0. \quad (4.23)$$

Evaluating condition (4.23) to find admissible values of ξ_d in the range $(-\frac{\pi}{2}, \frac{\pi}{2})$, we see that we must choose

$$\xi_d \in \left(\tan^{-1} \left(2 \frac{K_D}{K_L} \left(\frac{K_{L_0}}{K_L} + \sqrt{\left(\frac{K_{L_0}}{K_L} \right)^2 + \frac{K_{D_0}}{K_D}} \right) \right), \frac{\pi}{2} \right)$$

or

$$\xi_d \in \left(-\frac{\pi}{2}, \tan^{-1} \left(2 \frac{K_D}{K_L} \left(\frac{K_{L_0}}{K_L} - \sqrt{\left(\frac{K_{L_0}}{K_L} \right)^2 + \frac{K_{D_0}}{K_D}} \right) \right) \right).$$

These conditions arise because a steady glide is only possible at a glide path angle corresponding to a realizable lift/drag ratio, given a specific glider's hydrodynamic parameters. Therefore the maximum lift/drag ratio of the glider determines its minimum (magnitude) glide path angle. One condition specifies the shallowest glide path angle when gliding downwards, and the other the smallest glide path angle when gliding upwards.

Here we choose the α_d that is the solution of (4.22) with smaller magnitude. This is desirable from an aerodynamic standpoint because it gives a lower drag than would the larger α_d solution. This may be understood also as choosing the α_d on the better side of the vehicle lift/drag polar, choosing the lower drag for a given lift/drag ratio. Also note that the aerodynamic model is expected to be more accurate at smaller angles of attack. We compute

$$\alpha_d = \frac{1}{2} \frac{K_L}{K_D} \tan \xi_d \times \left(-1 + \sqrt{1 - 4 \frac{K_D}{K_L^2} \cot \xi_d (K_{D_0} \cot \xi_d + K_{L_0})} \right). \quad (4.24)$$

If $\xi_d = \pm \frac{\pi}{2}$, then we simply have

$$\alpha_d = -\frac{K_{L_0}}{K_L}. \quad (4.25)$$

For a vehicle which is symmetric about the body \mathbf{e}_1 - \mathbf{e}_2 plane, $K_{L_0} = 0$. In this case, for equilibria corresponding to vertical flight ($\xi_d = \pm \frac{\pi}{2}$), i.e. straight up or straight down, the desired angle of attack is zero.

We may determine m_{b_d} from the latter equation in (4.21),

$$m_{b_d} = (m - m_h - \bar{m}) + \frac{1}{g} \left(-\sin \xi_d (K_{D_0} + K_D \alpha_d^2) + \cos \xi_d (K_{L_0} + K_L \alpha_d) \right) V_d^2. \quad (4.26)$$

Finally, we may solve for a one-parameter family of sliding mass locations $(r_{P1_d}, r_{P3_d})^T$ which satisfy Equation (4.16). The family of solutions is

$$\mathbf{r}_{P_d} = \mathbf{r}^\perp + \gamma \begin{pmatrix} -\sin \theta_d \\ \cos \theta_d \end{pmatrix} \quad (4.27)$$

where

$$\mathbf{r}^\perp = \frac{1}{\bar{m}g} \left((m_{f3} - m_{f1})v_{1_d}v_{3_d} + (K_{M_0} + K_M\alpha_d)V_d^2 \right) \begin{pmatrix} \cos \theta_d \\ \sin \theta_d \end{pmatrix}$$

and where γ is a real number. The vector \mathbf{r}^\perp is a particular solution of Equation (4.16). The term $(-\sin \theta, \cos \theta)^T = (\mathbf{R}^T \mathbf{k})$ is the direction of gravity in body coordinates. \mathbf{r}^\perp is orthogonal to the direction of gravity and γ measures the vehicle's “bottom-heaviness” as shown in Figure 4.5.

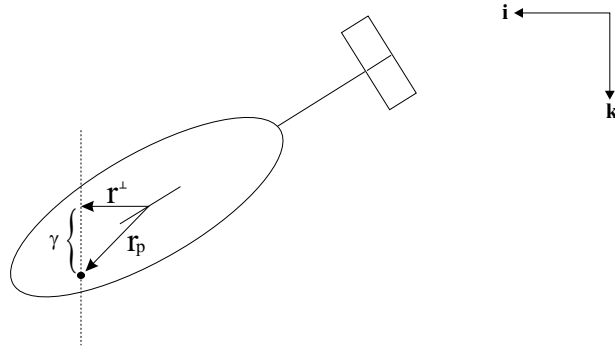


Figure 4.5: Family of possible movable mass locations for a steady glide.

For an experimental vehicle, r_{P3} may be a more physically relevant choice of free design parameter than γ . In several existing gliders, for example Slocum, r_{P3} is fixed. In this case,

$$r_{P1_d} = -r_{P3_d} \tan \theta_d + \frac{1}{\bar{m}g \cos \theta_d} \left((m_{f3} - m_{f1})v_{1_d}v_{3_d} + (K_{M_0} + K_M\alpha_d)V_d^2 \right) \quad (4.28)$$

for a given value of the parameter r_{P3_d} , provided $\theta_d \neq \pm \frac{\pi}{2}$. If $\theta_d = \pm \frac{\pi}{2}$, there is an equilibrium of the desired form if and only if the parameter r_{P3_d} satisfies

$$r_{P3_d} = \frac{1}{\bar{m}g \sin \theta_d} \left((m_{f3} - m_{f1})v_{1_d}v_{3_d} + (K_{M_0} + K_M\alpha_d)V_d^2 \right). \quad (4.29)$$

If (4.29) is satisfied, r_{P1_d} is a free parameter, and the choice of r_{P1_d} will affect the glider's "bottom heaviness" and the stability of the glide by changing γ . In fact, we should not choose r_{P3_d} to satisfy condition (4.29) in general because this will require that r_{P3_d} be small. Since r_{P3_d} contributes to the vehicle's "bottom-heaviness" at shallower glide path angles, designing a glider to satisfy condition (4.29) in straight up or down glides will affect stability of these other equilibria. (For a vehicle symmetric about the body \mathbf{e}_1 - \mathbf{e}_2 plane, $\theta_d = \pm \frac{\pi}{2}$ implies that $K_{M_0} = 0$ and $\alpha_d = 0$. In this case, condition (4.29) requires that $r_{P3_d} = 0$.)

4.1.3 Linearization

We now determine the linearization for the planar glider about a steady glide path.

Let $\mathbf{z} = (z', \theta, \Omega_2, v_1, v_3, r_{p_1}, r_{p_3}, P_{P_1}, P_{P_3}, m_b)^T$ and let $\mathbf{u} = (u_1, u_3, u_4)^T$, where (u_1, u_3) is the control force on the internal moving mass as described in Section 3.2.3. Computing the linearization for the glider equations with pointmass acceleration control (Section 3.2.5) follows the same procedure. Define

$$\begin{aligned}\delta \mathbf{z} &= \mathbf{z} - \mathbf{z}_d \\ \delta \mathbf{u} &= \mathbf{u} - \mathbf{u}_d, \text{ where } \mathbf{u}_d = \mathbf{0}.\end{aligned}$$

Then the linearized system is

$$\delta \dot{\mathbf{z}} = \mathbf{A} \delta \mathbf{z} + \mathbf{B} \delta \mathbf{u} \tag{4.30}$$

where

$$\mathbf{A} = \begin{bmatrix}
 0 & -V_d & 0 & -\sin \alpha_d & \cos \alpha_d & 0 & 0 & 0 & 0 & 0 \\
 0 & 0 & 1 & 0 & 0 & 0 & 0 & 0 & 0 & 0 \\
 0 & a_{32} & a_{33} & a_{34} & a_{35} & -\frac{\bar{m}g \cos \theta_d}{J_2} & -\frac{\bar{m}g \sin \theta_d}{J_2} & 0 & 0 & 0 \\
 0 & a_{42} & a_{43} & a_{44} & a_{45} & 0 & 0 & 0 & 0 & a_{410} \\
 0 & a_{52} & a_{53} & a_{54} & a_{55} & 0 & 0 & 0 & 0 & a_{510} \\
 0 & 0 & -r_{P3} & -1 & 0 & 0 & 0 & \frac{1}{m} & 0 & 0 \\
 0 & 0 & r_{P1} & 0 & -1 & 0 & 0 & 0 & \frac{1}{m} & 0 \\
 0 & 0 & 0 & 0 & 0 & 0 & 0 & 0 & 0 & 0 \\
 0 & 0 & 0 & 0 & 0 & 0 & 0 & 0 & 0 & 0 \\
 0 & 0 & 0 & 0 & 0 & 0 & 0 & 0 & 0 & 0
 \end{bmatrix} \tag{4.31}$$

and

$$\mathbf{B} = \begin{bmatrix}
 0 & 0 & 0 \\
 0 & 0 & 0 \\
 -\frac{r_{P3_d}}{J_2} & \frac{r_{P1_d}}{J_2} & 0 \\
 -\frac{1}{m_{b_d}+m_h+m_{f1}} & 0 & 0 \\
 0 & -\frac{1}{m_{b_d}+m_h+m_{f3}} & 0 \\
 0 & 0 & 0 \\
 0 & 0 & 0 \\
 1 & 0 & 0 \\
 0 & 1 & 0 \\
 0 & 0 & 1
 \end{bmatrix}. \tag{4.32}$$

Here,

$$\begin{aligned}
\alpha_{v_1} &= -\frac{v_{3d}}{V_d^2} \\
\alpha_{v_3} &= \frac{v_{1d}}{V_d^2} \\
D_{v_1} &= (K_{D_0} + K_D \alpha_d^2)(2v_{1d}) - 2K_D \alpha_d v_{3d} \\
D_{v_3} &= (K_{D_0} + K_D \alpha_d^2)(2v_{3d}) + 2K_D \alpha_d v_{1d} \\
L_{v_1} &= (K_{L_0} + K_L \alpha_d)(2v_{1d}) - K_L v_{3d} \\
L_{v_3} &= (K_{L_0} + K_L \alpha_d)(2v_{3d}) + K_L v_{1d} \\
M_{v_1} &= (K_{M_0} + K_M \alpha_d)(2v_{1d}) - K_M v_{3d} \\
M_{v_3} &= (K_{M_0} + K_M \alpha_d)(2v_{3d}) + K_M v_{1d}
\end{aligned}$$

where we have abbreviated $\frac{\partial \alpha}{\partial v_1}$ as α_{v_1} , etc. and

$$\begin{aligned}
a_{32} &= \frac{\bar{m}g}{J_2}(r_{P1d} \sin \theta_d - r_{P3d} \cos \theta_d) = \frac{\bar{m}g}{J_2}(-\gamma_d) \\
a_{33} &= -\bar{m}(r_{P1d} v_{1d} + r_{P3d} v_{3d}) \\
a_{34} &= \frac{1}{J_2}((m_{f3} - m_{f1})v_{3d} + M_{v_1}|_{eq}) \\
a_{35} &= \frac{1}{J_2}((m_{f3} - m_{f1})v_{1d} + M_{v_3}|_{eq}) \\
a_{42} &= -\frac{m_{0d}}{m_{1d}}g \cos \theta_d \\
a_{43} &= -\frac{m_{3d} + \bar{m}}{m_{1d}}v_{3d} \\
a_{44} &= \frac{1}{m_{1d}}(L_{v_1} \sin \alpha_d + L \cos \alpha_d \alpha_{v_1} - D_{v_1} \cos \alpha_d + D \sin \alpha_d \alpha_{v_1})|_{eq} \\
a_{45} &= \frac{1}{m_{1d}}(L_{v_3} \sin \alpha_d + L \cos \alpha_d \alpha_{v_3} - D_{v_3} \cos \alpha_d + D \sin \alpha_d \alpha_{v_3})|_{eq} \\
a_{410} &= -\frac{g \sin \theta_d}{m_{1d}} + \frac{(m_{0d})g \sin \theta_d}{(m_{1d})^2} - \frac{1}{(m_{1d})^2}(L \sin \alpha_d - D \cos \alpha_d)|_{eq} \\
a_{52} &= -\frac{m_{0d}}{m_{3d}}g \sin \theta_d
\end{aligned}$$

$$\begin{aligned}
a_{53} &= \frac{m_{1_d} + \bar{m}}{m_{3_d}} v_{1_d} \\
a_{54} &= \frac{1}{m_{3_d}} (-L_{v_1} \cos \alpha_d + L \sin \alpha_d \alpha_{v_1} - D_{v_1} \sin \alpha_d - D \cos \alpha_d \alpha_{v_1})|_{eq} \\
a_{55} &= \frac{1}{m_{3_d}} (-L_{v_3} \cos \alpha_d + L \sin \alpha_d \alpha_{v_3} - D_{v_3} \sin \alpha_d - D \cos \alpha_d \alpha_{v_3})|_{eq} \\
a_{510} &= \frac{g \cos \theta_d}{m_{3_d}} - \frac{(m_{0_d}) g \cos \theta_d}{(m_{3_d})^2} - \frac{1}{(m_{3_d})^2} (-L \cos \alpha_d - D \sin \alpha_d)|_{eq}.
\end{aligned}$$

The notation $(\cdot)|_{eq}$ indicates that the quantity is to be evaluated at the desired equilibrium.

This linearization can be used to check features of a given vehicle design, e.g., to check stability or controllability of a desired glide path given a choice of vehicle design parameters. One can also use this linearization to help automate the design procedure. For example, consider a vehicle that has been fully designed but for a choice of the position of the movable mass for a given glide path. Application of the Routh criterion to the characteristic polynomial of the matrix \mathbf{A} gives conditions for stability of the glide path. These conditions can be written in terms of the free variable r_{P3} . r_{P3} would then be chosen for behavior with desired stability and r_{P1} would then be computed according to (4.28).

4.1.4 Equilibrium Glides for ROGUE

Given a set of parameters describing a glider like ROGUE, we may compute steady glides for that vehicle. Mass and inertia properties of ROGUE were measured directly. Added mass and inertia properties can be found, for example, in [37]. Lift and drag for the body were found experimentally as described in [25]. Lift and drag for the wings were taken from the data in [62]. Lift for the body plus wings was then computed using Schrenk's method [61], and drag was computed as the sum of the drag on the wing and the body. The pitch moment was approximated using reference data, taking into account the tail. The vehicle model parameters are given as follows: $m = 11.22$ kg, $m_h = 8.22$ kg, $\bar{m} = 2.0$ kg, $m_{f1} =$

2 kg, $m_{f3} = 14$ kg, $J_2 = 0.1$ Nm², $K_{D_0} = 18$ N(s/m)², $K_D = 109$ N(s/m)², $K_L = 306$ N(s/m)², $K_M = -36.5$ Nm(s/m)². Masses m , m_h and \bar{m} were measured directly, with a high degree of accuracy. The other parameters have less precision because they are based on look-up tables and approximation methods.

Four steady glide paths are calculated, at glide angles ($\xi = \theta - \alpha$) of -30° , -45° , 30° and 45° , using the method of Section 4.1.2. We compute the glide path at -30° by choosing a desired glide speed $V_d = 0.30$ m/s and a desired vertical location of the movable mass given by $r_{P3_d} = 4$ cm. This results in an equilibrium variable mass given by $m_{b_d} = 1.36$ kg. The glide path at -45° is computed for these same values of r_{P3_d} and m_{b_d} . The corresponding equilibrium speed for this glide is computed as $V_d = .37$ m/s. Similarly, we computed the two steady upward glide paths, for the same value of r_{P3_d} and the same buoyant force magnitude, i.e., the value of $|m_{0_d}|$ is held constant. Recall that m_0 is the mass of the vehicle m_v less the mass of the displaced fluid m . The full description of each of the four glide paths is given in Table 4.1.

Variable	Down 30°	Down 45°	Up 30°	Up 45°
ξ_d (deg)	-30	-45	30	45
θ_d (deg)	-23.7	-41.5	23.7	41.5
α_d (deg)	6.3	3.5	-6.3	-3.5
V_d (m/s)	0.30	0.37	0.30	0.37
v_{1_d} (m/s)	0.29	0.36	0.29	0.36
v_{3_d} (m/s)	0.03	0.02	-0.03	-0.02
r_{P1_d} (cm)	0.41	2.20	-0.41	-2.20
r_{P3_d} (cm)	4.0	4.0	4.0	4.0
P_{P1_d} (kg-m/s)	0.60	0.73	0.60	0.73
P_{P3_d} (kg-m/s)	0.07	0.04	-0.07	-0.04
m_{b_d} (kg)	1.36	1.36	0.64	0.64
m_{0_d} (kg)	0.36	0.36	-0.36	-0.36

Table 4.1: Four Steady Glide Paths for ROGUE

4.1.5 Stability of Equilibrium Glides

Local properties of steady glide paths can be studied using the linearization of Section 4.1.3. Linear stability of the equilibria was investigated for a number of steady glides, both upwards and downwards. Model parameters were chosen to represent a typical glider design. Steady glides and their stability were also examined using parameters for the ROGUE laboratory glider.

Using the original glider dynamic equations, detailed in Section 3.2.1 and before application of the control transformation in Section 3.2.4, gives the linearization presented in Section 4.1.3. When parameter values for a “typical” oceanographic glider and for the ROGUE glider were used, the linearized equations were found to have some unstable eigenvalues. This instability arises from the coupling between the vehicle dynamics and the internal sliding mass. In the model formulation using the force on the internal mass as a control, the mass is free to move inside the vehicle. This makes it possible for the internal mass position \mathbf{r}_p to change from the equilibrium \mathbf{r}_{pd} in response to vehicle motions. This instability is analogous to the instability problems associated with fuel slosh in space vehicles, [51]. As discussed below and presented in [5], the control transformation of Section 3.2.4 effectively provides a suspension system for the moving internal mass and eliminates this instability. Note that this instability is a result of the glider model, not an instability present in real gliders, whose internal masses are held in place by their actuators. The feedback transformation described here fixes an instability in the glider model (thereby correcting an inaccuracy of the model), not a physical instability present in a real glider with actuator controlled internal masses.

In the untransformed case, where force on the point mass is a control and the shifting mass moves freely inside the vehicle, the instability can be easily resolved through use of

linear state feedback such as an LQR controller, as described in Chapter 6. The LQR controller stabilizes the steady glide paths, and simulations show it provides adequate disturbance rejection. This control also provides adequate performance when used to switch between different glides that are both in the upwards or both in the downwards direction, but performs poorly when switching between upwards and downwards glides or the reverse. A switch from glide equilibrium A to glide equilibrium B refers to the application of the LQR controller designed for glide equilibrium B to initial conditions corresponding to glide equilibrium A.

The instability of the steady glides and the performance problems in switching between downwards and upwards glides stem from the manner in which the control of the internal sliding mass is represented in the equations of motion. In Equations (3.31), the control input \mathbf{u} corresponds to the force on the internal moving mass. These equations accurately describe the physical coupling between the glider and internal mass with the point mass free to move around inside the vehicle. Even when the control \mathbf{u} is zero, the shifting point mass can move in response to the motion of the vehicle. Adding feedback to control the point mass position is sufficient to stabilize steady glides but has shortcomings in performance as just described. However, it is perhaps more effective and more practical to consider the nonlinear control law and change of states, described in Section 3.2.4, that models the shifting point mass as constrained to a suspension system inside the vehicle and makes the control \mathbf{w} the acceleration of the point mass. The resulting equations still accurately model the coupling between the internal mass and the vehicle and more accurately model the control used in actual gliders. The transformation yields a stable system.

The transformed glider dynamics are given by Equations (3.38). These may be simplified and confined to the plane as described above. The equilibria steady glides, including

the position of the internal sliding mass, are unchanged by the control transformation. Linearization of the transformed equations gives a stable system with eigenvalues all in the left half-plane. This is an improvement over the untransformed equations. The new equations also exhibit significantly improved performance in switching between steady glides, including allowing switching between upwards and downwards glides. From investigation using a number of simulations, it appears that the controlled system using state feedback and the new equations has a significantly larger region of attraction than the untransformed system.

Pitch stability in gliders is provided by the arrangement of the internal masses and the distance between the CG and the CB. This distance is given by γ as noted before. Many glider designs have no horizontal tail for pitch stability or control. Gliders are often hydrodynamically designed for stability in order to operate for long periods at steady glides with controls fixed, that is, with fixed ballast and internal mass positions. Setting the point mass acceleration \boldsymbol{w} to zero fixes it in place. This is equivalent to stick-fixed or controls-fixed stability in aircraft.

While these results are determined by simulation, it is expected that they will apply to a range of glider designs. The simulations used parameters typical for existing gliders. The results may remain valid given some variation in those parameters. Consider that existing gliders are all designed for gliding efficiency, low power consumption, and extended deployments. They are all designed for stable steady gliding with controls fixed. They have similar body and wing arrangements and their hydrodynamic properties are similar. These designs, as well as future glider designs with similar mission and geometry, may be expected to have model parameters within some reasonable range of each other.

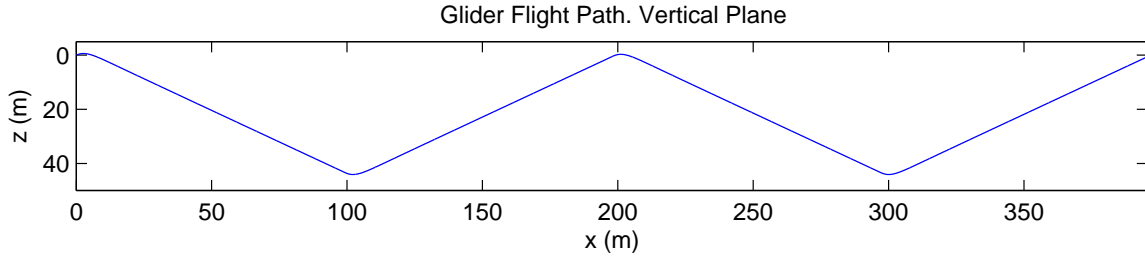


Figure 4.6: Glide path in the vertical plane. From simulation.

4.1.6 Example: Sawtooth Gliding in The Vertical Plane

Figure 4.6 shows the glide path in the vertical plane of an underwater glider simulated using the glider dynamic model. The glider modelled here is similar in size to existing gliders such as Slocum. The simulation shows four steady glide segments and three stable inflections between upwards and downwards glides. Other vertical plane states and V and α are shown in Figure 4.7. The states converge to their desired equilibrium values, shown in Table 4.3. Figure 4.8 shows the internal mass states and control inputs for the simulation. The control inputs are physically reasonable. They appear as spikes on the plot because of the length of time of simulation and the relative scaling of the plot axes.

At each inflection the internal mass position and the ballast mass are changed to match the next equilibrium glide. The only control used is feedback control of the internal mass states. External disturbances are neglected. Upon adjustment of the internal masses the glider transitions smoothly to the new equilibrium glide.

In this glider r_{p1} and m_b are controlled and r_{p3} is fixed. The internal actuators and controls in this simulation are configured to take about ten seconds to move the sliding mass to its new position and to pump ballast. This does not model any particular vehicle's actuators. Fully open-loop control of the internal masses was also simulated, without feedback of the mass position. With this method small errors in numerical integration may

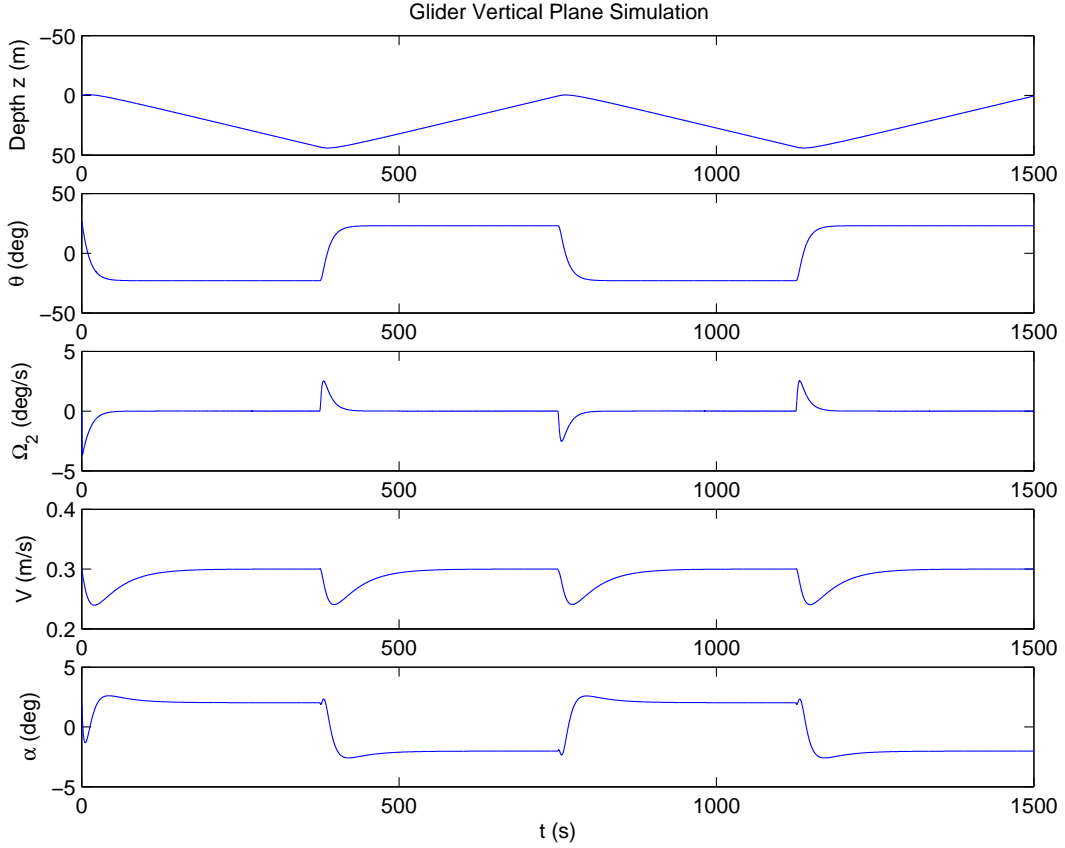


Figure 4.7: Vertical Plane States.

lead to nonzero errors in position \mathbf{r}_p or velocity $\dot{\mathbf{r}}_p$. Feedback is therefore desirable even in simulations. Note that existing gliders use servo motors with feedback to control mass and ballast positions.

Simulations with faster and slower actuation than shown here also gives stable transitions, although care should be taken with very slow actuators or those which move the internal mass and ballast at very different speeds. For example, a very fast ballast adjustment with a slow \mathbf{r}_p adjustment may lead to poor performance in transitions.

The parameters used in the simulation are given in Table 4.2. This glider has a stabilizing hydrodynamic pitch moment, $\frac{\partial}{\partial \alpha} C_{M_{total}}(\alpha)|_{eq} < 0$, $\frac{\partial}{\partial \alpha} ((m_{f3} - m_{f1}) \sin \alpha_{eq} \cos \alpha_{eq} + M_{DL_{eq}}) < 0$. A range of pitch moment parameters giving $\frac{\partial}{\partial \alpha} C_{M_{total}}(\alpha)|_{eq} > 0$ are also

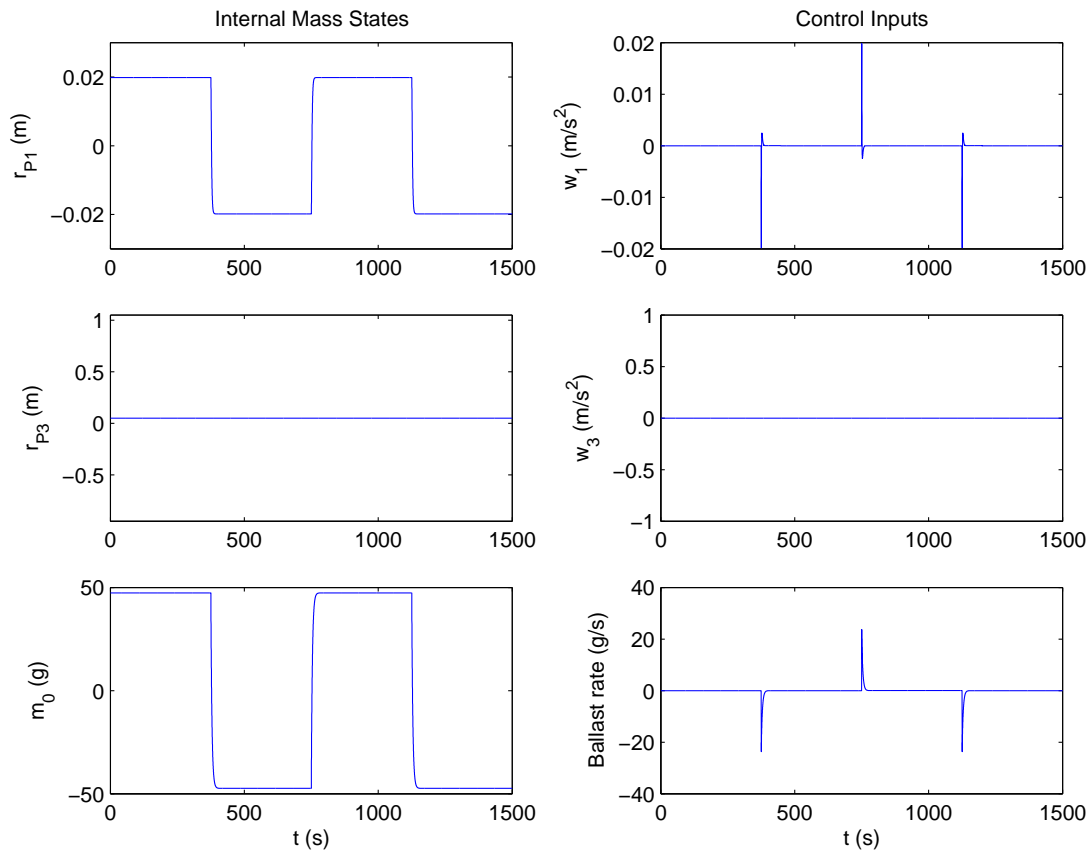


Figure 4.8: Internal mass position, accelerations, and net buoyancy and pumping rate.

stable, given sufficient bottom-heaviness of the glider. Stability can be analyzed using the linearization presented above and in simulation.

Note that the full three dimensional dynamics of the glider were simulated with initial conditions in the vertical plane invariant subspace. Given a stable glider configuration and hydrodynamic parameters, simulations beginning out of the planar subspace converge to planar motion.

Body length (m)	1.5	K_{L_0}	0
radius (m)	0.11	K_L	132.5
displacement m (kg)	50	K_{D_0}	2.15
sliding mass \bar{m} (kg)	9	K_D	25
hull mass m_h (kg)	40	K_{M_0}	0
$m_{f1,2,3}$ (kg)	5,60,70	K_M	-100
$J_{1,2,3}$ (kg · m ²)	4,12,11	$K_{\Omega_{2_1}}$	50
		$K_{\Omega_{2_2}}$	50

Table 4.2: Glider Simulation Parameter Values.

Variable	Down	Up
ξ_d (deg)	-25	25
θ_d (deg)	-23	23
α_d (deg)	2	-2
V_d (m/s)	0.30	0.30
v_{1_d} (m/s)	0.3	0.3
v_{3_d} (m/s)	0.02	-0.02
r_{P1_d} (cm)	1.98	-1.98
r_{P3_d} (cm)	5.00	5.00
m_{b_d} (kg)	1.047	.9526
m_{0_d} (kg)	0.047	-0.47

Table 4.3: Simulation Steady Glides.

4.2 The Phugoid Mode for Underwater Gliders

In this section we derive a simplified model of underwater glider flight dynamics in the vertical plane, following Lanchester’s original work on aircraft flight dynamics and the phugoid mode [40, 73]. The glider phugoid model is derived by confining the three dimensional glider model to the vertical plane and applying Lanchester’s phugoid assumptions. This yields a system of four equations, specifying the glider position, orientation and speed. The flight paths of the phugoid glider model are qualitatively similar to those of aircraft or underwater gliders. The underwater glider phugoid equations are shown to take two forms, one fully integrable and one not, depending on the whether the angle of attack is fixed at zero or a nonzero value. In the integrable case the glider phugoid dynamics and flightpath may be

scaled to match Lanchester’s solutions using a similarity factor. In the non-integrable case, the level flight equilibrium becomes a stable (unstable) center when the angle of attack is fixed at a positive (negative) value.

In 1908, F.W. Lanchester derived a simplified model of the longitudinal dynamics of an aircraft [40, 73]. He named this model and the resulting trajectories the phugoid motion of the aircraft (Von Mises [73] humorously notes that this name derives from the Greek for “to fly” in the sense of fleeing from something, not flying through the air). By applying three simplifying assumptions to the aircraft equations of motion, Lanchester developed a simple system which exhibits gliding motions including level flight, wavy flight and flight in loops. Lanchester’s assumptions include cancelling drag on the vehicle and fixing the angle of attack. They are described in Section 4.2.1.

In this section we apply Lanchester’s assumptions to the model of the underwater glider in the vertical plane. Several cases are examined, including gliding motion when added mass and buoyancy effects are significant due to the density of the fluid. When the glider’s angle of attack α is fixed at zero, or when the glider’s added masses m_{f1} and m_{f3} are equal, the equations are fully integrable. If added mass and buoyancy are zero, we recover Lanchester’s equations for the phugoid motion and the system is integrable. When added mass and buoyancy are significant but the vehicle angle of attack is fixed at zero, the system is still integrable and has dynamics similar to Lanchester’s system, within a similarity factor.

When the added masses m_{f1} and m_{f3} are unequal and the angle of attack is fixed and nonzero, the system is no longer conservative (and is not hamiltonian and integrable). The resulting dynamics, phase portrait and vehicle trajectories are examined through simulation. It is also shown that applying the small angle assumption to the angle of attack makes it possible to write the equations of motion as the integrable system plus perturbation terms.

4.2.1 Lanchester's Assumptions and the Phugoid Equations

We now apply Lanchester's assumptions to the glider vertical, longitudinal plane equations of motion and examine several cases, including phugoid motion when $\alpha = 0$ and $\alpha \neq 0$, with and without added mass and buoyancy. The longitudinal dynamics of an underwater glider are given by Equations (4.1)-(4.11). Lanchester detailed his phugoid assumptions in [40], where he applied three simplifying assumptions to the aircraft longitudinal equations of motion:

1. Drag on the aircraft is cancelled out by an equal and opposite thrust. An equivalent assumption is that drag and thrust are both zero. Note that this is the case for a vehicle in a two dimensional inviscid flow.
2. The moment of inertia J is very small, or equivalently the pitching moment M_{DL} is much larger than J . M_{DL} is assumed to be stabilizing towards a constant α , so the body will equilibrate very quickly to a constant angle of attack α at which M_{DL} is zero.
3. The angle of attack α is fixed. This is consistent with the previous assumption. Given this and the relation $\xi = \theta - \alpha$, the difference between the pitch angle and glide path angle is fixed.

Lanchester examined the case of an aircraft moving in a fluid with no added mass or buoyancy effects. To derive the phugoid equations for an underwater glider, consider the case of a glider whose ballast mass m_b is fixed and disregard the sliding internal mass. Lanchester's assumptions would, in any case, severely limit any action of the sliding mass on the glider motion. Apply assumptions one through three to Equations (4.1) through (4.6). Assumptions two and three fix the angle of attack α at a value to be chosen. Consider first

the case where we fix $\alpha = 0$. This requires that $v_3 = \dot{v}_3 = 0$. Then $\dot{V} = \dot{v}_1$, and Equation (4.5) becomes Equation (4.35). Equations (4.1) and (4.2), which track the position of the glider, may then be written as (4.33) and (4.34). Applying Lanchester's second and third assumptions, disregard Equation (4.4). Equation (4.6) may be solved for $\dot{\theta} = \Omega_2$, giving Equation (4.36). The equations of motion are then

$$\dot{x} = V \cos \theta \quad (4.33)$$

$$\dot{z} = -V \sin \theta \quad (4.34)$$

$$\dot{V} = \frac{1}{m_1}(-m_0 g \sin \theta) \quad (4.35)$$

$$\dot{\theta} = \frac{1}{m_1 V}(L - m_0 g \cos \theta) \quad (4.36)$$

where $L = \frac{1}{2}\rho C_L(\alpha)ArV^2$ (here Ar is the characteristic area of the glider).

Equations (4.33) and (4.34) simply track the position of the glider in the vertical plane. The energy of the glider is independent of x and z appears only in the potential energy of the glider. Note that m_3 does not appear in the equations of motion for the $\alpha = 0$ case. Setting $m_{f1} = 0$ and $m_0 = m_v = m_1$ gives Lanchester's original phugoid equations.

The system for $\alpha = 0$, Equations (4.33)-(4.36), has one equilibrium (modulus 2π). It corresponds to level flight at velocity $V = V_L$ and $\theta = 0$ where

$$V_L = \left(\frac{2m_0 g}{\rho C_L Ar} \right)^{\frac{1}{2}}. \quad (4.37)$$

The system of equations has two conserved quantities, E and A . E is the total energy of the system. A is a function of velocity V and pitch angle θ .

$$E = \frac{1}{2}m_1 V^2 - m_0 g z \quad (4.38)$$

$$A = \frac{V}{V_L} \cos \theta - \frac{1}{3} \left(\frac{V}{V_L} \right)^3. \quad (4.39)$$

Conservation of energy E gives

$$V^2 = 2 \frac{m_0}{m_1} g z + C$$

We may choose constant $C = 0$ to make $z = 0$ the maximum height of the flight path (recall that z is positive down). This gives all flight paths with the same energy level $E = 0$. Note that the lift force on the glider is perpendicular to the velocity vector at all times and does no work. There are no other hydrodynamic forces on the glider when $\alpha = 0$.

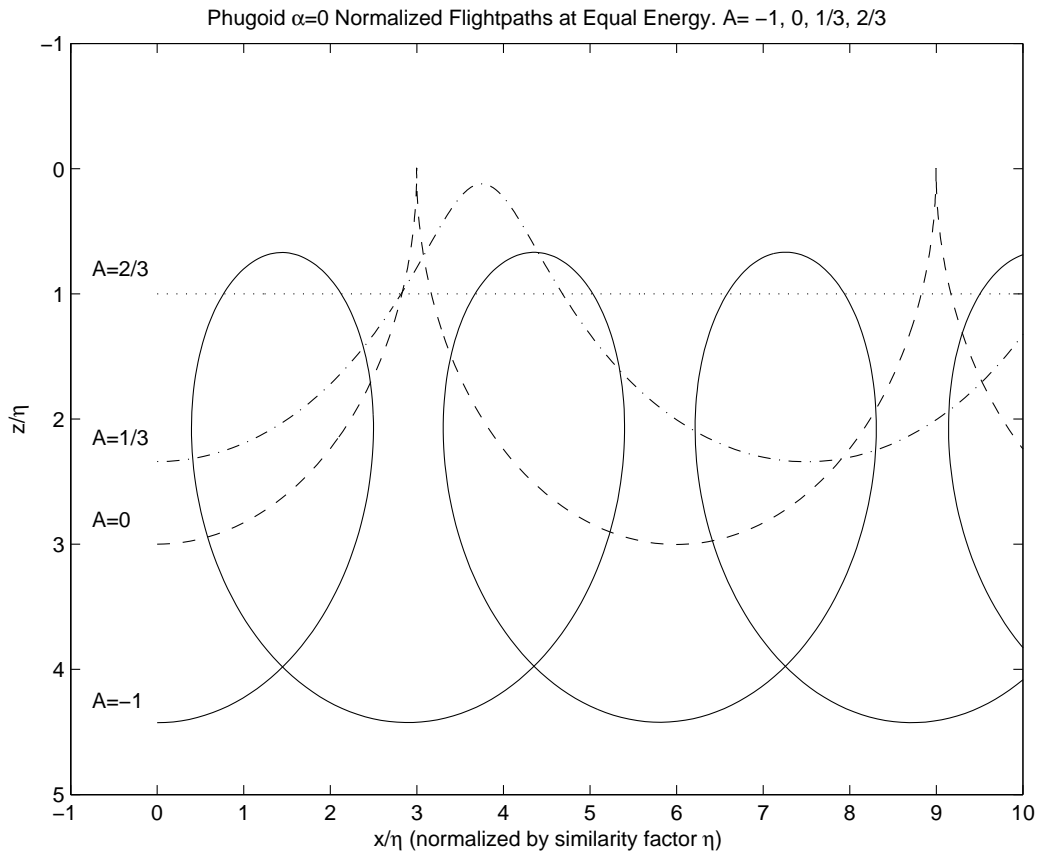


Figure 4.9: Phugoid Flight Paths.

Figure 4.9 shows flight paths in the $x - z$ plane for four initial conditions at equal energy and different values of A . The axes are normalized by similarity factor $\eta = (2 \frac{m_0}{m_1} g) / (V_L^2)$.

The characteristics of the flight path depend on conserved quantity A . The flight paths shown were generated by integrating the equations of motion for initial conditions $\theta(0) = 0$ and $A = \frac{2}{3}, \frac{1}{3}, 0$ and -1 . $A = \frac{2}{3}$ corresponds to level flight at the equilibrium and is the maximum A corresponding to a physical solution of the system. $\frac{2}{3} > A > 0$ corresponds to wavy flight about the level flight path. Along the $A = 0$ path, the glider reaches $\theta = \frac{\pi}{2}$ with $V = 0$ at $z = 0$, then rotates to $\theta = -\frac{\pi}{2}$ and glides downwards with increasing V . The $A = 0$ glide paths show a sharp cusp at points where $V = 0$. $A < 0$ gives looping flight paths.

Lanchester's results on phugoid motion for the aircraft address the fully integrable case $m_0 = m_1 = m_v$. The phugoid dynamics with added mass and buoyancy and $\alpha = 0$ are also fully integrable and the flight paths are identical to Lanchester's (with similarity factor η). The equations are also integrable for nonzero α and equal added masses.

Figure 4.10 shows levels sets of A in the phase plane for the underwater glider phugoid system, Equations (4.33)-(4.36). Trajectories remain on a level set of A and move clockwise or towards increasing θ . An equivalent phase portrait was generated by integrating the equations of motion forward and backwards in time from a set of initial conditions. The equilibrium is a center and $A = 0$ is the separatrix between solutions circling the equilibrium $V = V_L, \theta = 0$ and solutions moving with increasing θ through $\theta = \pi$, whose flight paths are loops.

The phase portrait of the phugoid system exhibits similarities to the phase plane of a pendulum. These include equilibria that are centers spaced 2π apart and a separatrix dividing two regions in the phase plane; one region of solutions where θ increases continually and one region of solutions which oscillate about the equilibria. These systems are characterized by the exchange of potential and kinetic energy as the glider or pendulum falls and speeds

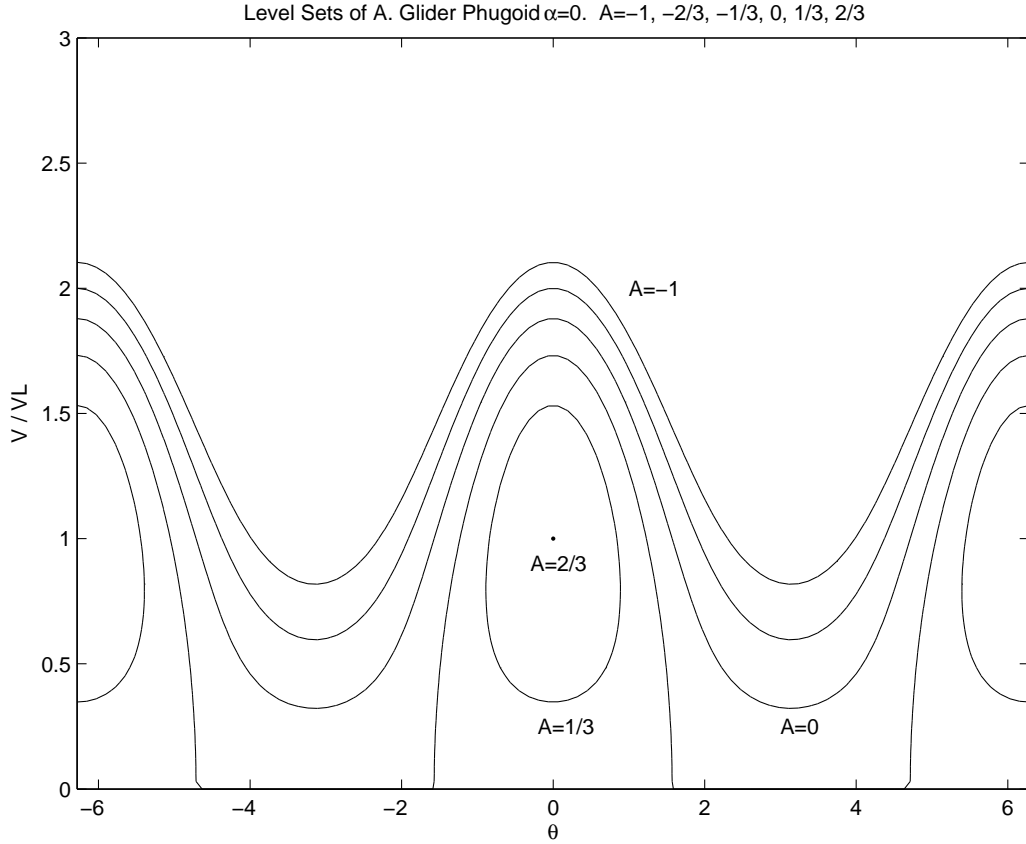


Figure 4.10: Phugoid Phase Plane. Level Sets of A.

up or rises and slows.

4.2.2 Phugoid Dynamics for $\alpha \neq 0$

We now examine the glider phugoid equations when α is fixed at a nonzero value. This corresponds to fixing $\tan \alpha = \frac{v_1}{v_3}$. We use Equation (4.17) to find \dot{V} and then use the relation $\dot{v}_1 \tan \alpha = \dot{v}_3$ and equations (4.17) and (4.18) to solve for $\dot{\theta}$. The resulting equations are

$$\dot{x} = V \cos(\theta - \alpha) \quad (4.40)$$

$$\dot{z} = -V \sin(\theta - \alpha) \quad (4.41)$$

$$\dot{V} = \frac{1}{m_1 \cos \alpha} \left(-m_3 V \dot{\theta} \sin \alpha - m_0 g \sin \theta + L \sin \alpha \right) \quad (4.42)$$

$$\dot{\theta} = \frac{-m_0g \left(\frac{1}{m_1} \tan \alpha \sin \theta + \frac{1}{m_3} \cos \theta \right) + L \left(\frac{1}{m_1} \tan \alpha \sin \alpha + \frac{1}{m_3} \cos \alpha \right)}{V \left(\frac{m_1}{m_3} \cos \alpha + \frac{m_3}{m_1} \tan \alpha \sin \alpha \right)} \quad (4.43)$$

Note that $\dot{\theta}$ appears in equation (4.42) in order to conserve space. Setting $\alpha = 0$ in the above equations yields Equations (4.33)-(4.36). If $m_{f1} = m_{f3}$, Equations (4.42)-(4.43) become

$$\dot{V} = \frac{1}{m_1}(-m_0g \sin(\theta - \alpha)), \quad (4.44)$$

$$\dot{\theta} = \frac{1}{m_1 V}(L - m_0g \cos(\theta - \alpha)), \quad (4.45)$$

which are identical to the $\alpha = 0$ case with a simple phase shift by α .

The equilibrium for the $\alpha \neq 0$ system (4.40)-(4.43) is $\theta = \alpha, V = V_L$ where V_L is the same as (4.37), for the $\alpha = 0$ case. This equilibrium corresponds to level flight, where the glider velocity vector is horizontal and the glider e_1 axis is inclined by angle α with respect to it. V no longer lies along the glider e_1 axis as it did in the $\alpha = 0$ case. In the general case $m_{f1} \neq m_{f3}$, E and A , where

$$E = \frac{1}{2}m_1v_1^2 + \frac{1}{2}m_3v_3^2 - m_0gz, \quad (4.46)$$

and A is defined by (4.39), are no longer conserved quantities of the motion, although lift is still perpendicular to velocity and does no work. This may be interpreted as the constraint holding the angle of attack constant doing work on the system.

Figure 4.11 shows four flight paths for the phugoid dynamics with fixed $\alpha = 5^\circ$, generated by numerically integrating Equations (4.40) - (4.43). The added masses used are shown in the figure. The initial conditions are $\theta = \alpha$ with the same V and z initial conditions used for Figure 4.9 for the $\alpha = 0$ case. The equilibrium level flight path remains straight. Other

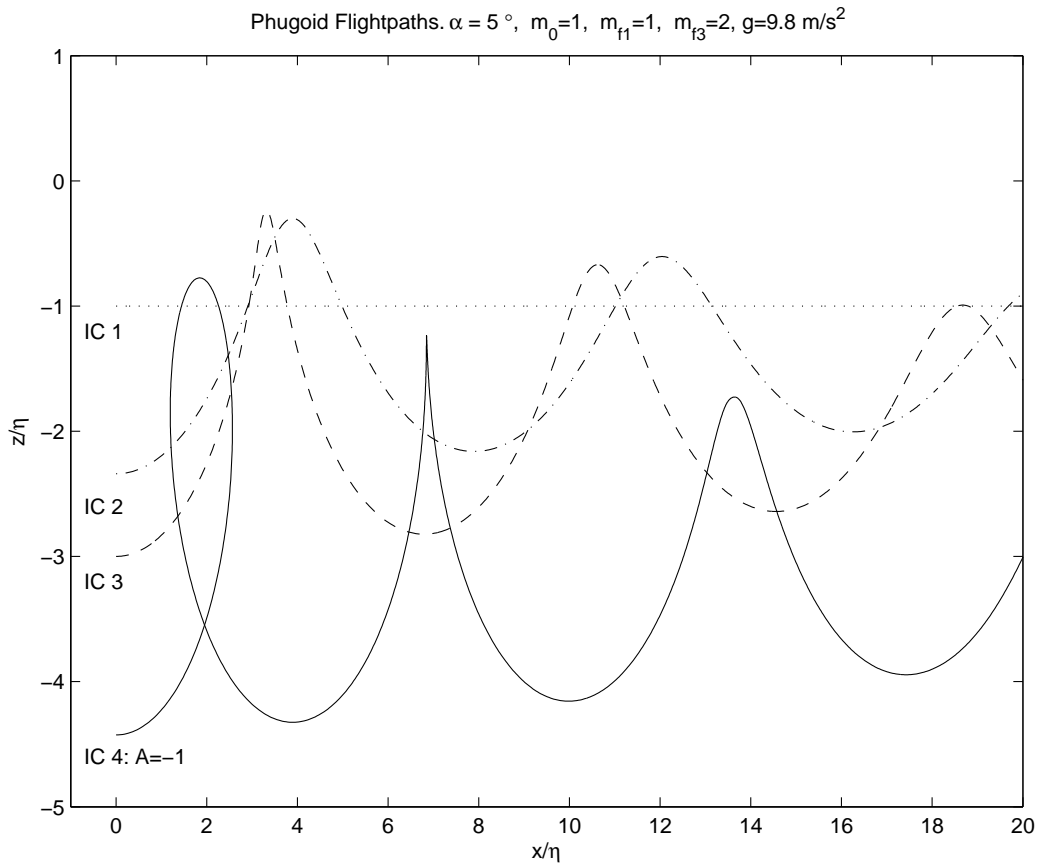


Figure 4.11: Flight Paths for $\alpha = 5$.

flight paths progress from looping to wavy to level flight.

Figure 4.12 plots solutions on the phase plane from the same initial conditions. Setting $\alpha > 0$ makes the level flight equilibrium (α, V_L) a stable focus, with solutions spiralling inwards in the clockwise direction. The flight path from IC 4, which in the $\alpha = 0$ case performed loops, now performs one loop and progresses to wavy, then level flight. Setting $\alpha < 0$ makes the equilibrium an unstable focus, with solutions spiralling away in the clockwise direction.

Figures 4.13 and 4.14 show A and energy versus time for the same set of initial conditions. Trajectories move to higher levels of A until reaching the equilibrium value. Note that A does not increase monotonically. The energies of the trajectories decrease on average as

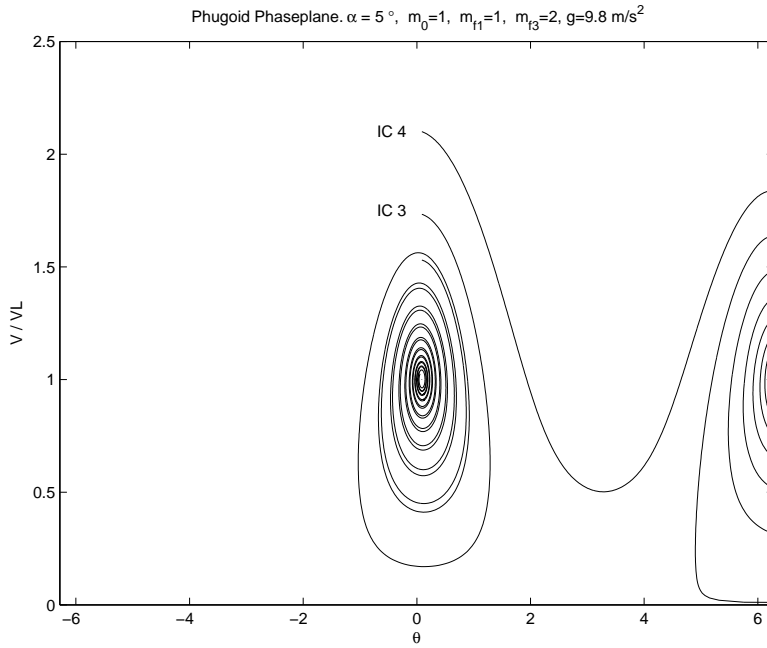


Figure 4.12: Phase Trajectories for $\alpha = 5$, Same Initial Conditions.

they move towards equilibrium glides, but do not decrease monotonically.

The $\alpha \neq 0$ case may be examined as a perturbation to the conservative (hamiltonian and integrable) case. This involves applying the small angle assumption to α and grouping the equations as $\mathbf{f} + \alpha \mathbf{g}$, where \mathbf{f} represents the integrable equations of motion and \mathbf{g} contains the perturbation terms. Taking (4.42) and (4.43) and setting $\cos \alpha = 1$, $\sin \alpha = \alpha$, and $\tan \alpha = \alpha$, multiplying and substituting, and discarding terms of order α^2 and α^3 , gives

$$\dot{V} = \frac{1}{m_1}(-m_0 g \sin \theta) + \alpha \left(\frac{L}{m_1} \right) \left(1 - \frac{m_3}{m_1^2} \right) + \alpha \left(\frac{m_3}{m_1^2} \right) (m_0 g \cos \theta) \quad (4.47)$$

$$\dot{\theta} = \frac{1}{m_1 V} (L - m_0 g \cos \theta) - \alpha \left(\frac{m_3}{m_1^2 V} \right) (m_0 g \sin \theta). \quad (4.48)$$

Setting $m_1 = m_3$, these equations simplify to

$$\dot{V} = \frac{1}{m_1}(-m_0 g \sin \theta) + \alpha \left(\frac{1}{m_1} \right) \left(L \left(1 - \frac{1}{m_1} \right) + m_0 g \cos \theta \right) \quad (4.49)$$

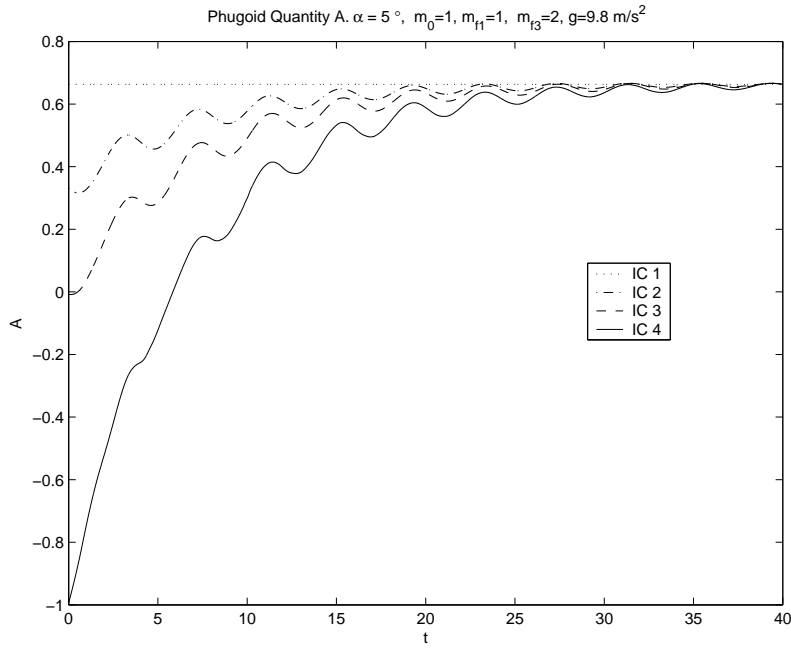


Figure 4.13: A vs. Time along Phugoid Trajectories. $\alpha = 5$, Same Initial Conditions.

$$\dot{\theta} = \frac{1}{m_1 V} (L - m_0 g \cos \theta) - \alpha \left(\frac{m_0 g \sin \theta}{m_1 V} \right). \quad (4.50)$$

Note that setting $m_1 = m_3$ before applying the small angle approximation simplifies the phugoid $\alpha \neq 0$ equations to (4.45).

Related work in [6] presents a singular perturbation theory analysis of the phugoid equations and the glider equations in the vertical plane, using the phugoid mode conservation laws to derive a Lyapunov function to prove stability of gliding.

4.2.3 Lateral Dynamics

The lateral dynamics of underwater gliders are of interest for navigation, stability analysis, and underwater glider design. “Lateral dynamics” is standard aerospace terminology referring to the vehicle \mathbf{e}_1 - \mathbf{e}_2 plane and the yaw, sideslip and roll dynamics of the vehicle (Figure 4.15). This section briefly discusses modelling the lateral dynamics of underwater gliders.

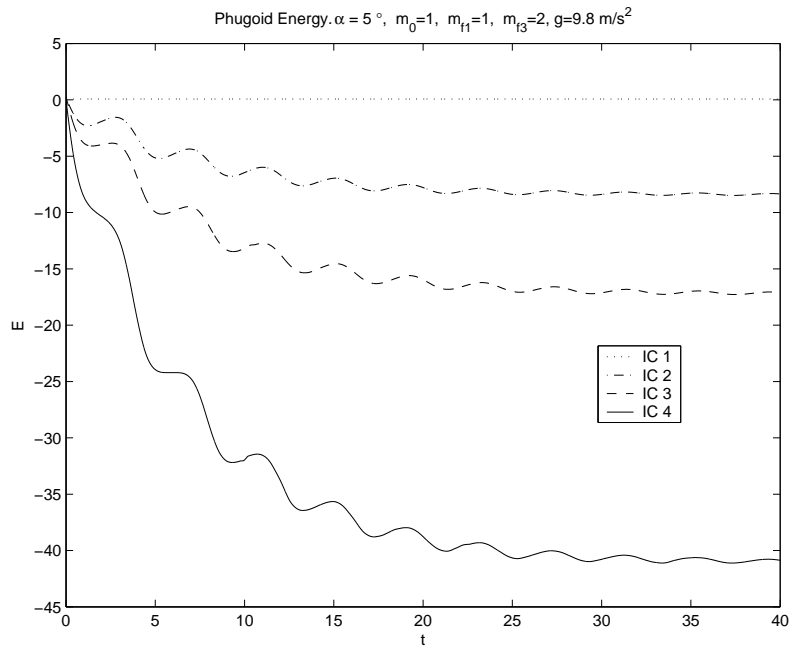


Figure 4.14: Energy vs. Time along Phugoid Trajectories. $\alpha = 5$, Same Initial Conditions.

Of particular interest are turning controlled by rolling or rudder, yaw resulting from static mis-trim of the glider CG, and rudder-roll coupling. These are discussed further as three dimensional effects in Section 4.3.

In aircraft literature it is standard to examine separately the longitudinal and lateral dynamics of an airplane [15, 43]. Simplifications are made to the highly coupled full aircraft dynamic equations. The six dynamic equations governing the linear and angular velocities of the aircraft are broken into two sets of three equations and analyzed separately, usually with a linear analysis about the equilibrium. Standard aircraft lateral analysis includes yaw, sideslip and roll dynamics to analyze control of roll and heading actuated with ailerons and rudder. Linear analysis of underwater glider dynamics follows a similar approach. The three dimensional equations can be linearized about the gliding equilibria and assumptions analogous to those for aircraft applied to decouple the longitudinal and lateral dynamics.

Aircraft lateral models and linear analysis reveal important dynamic phenomena, in-

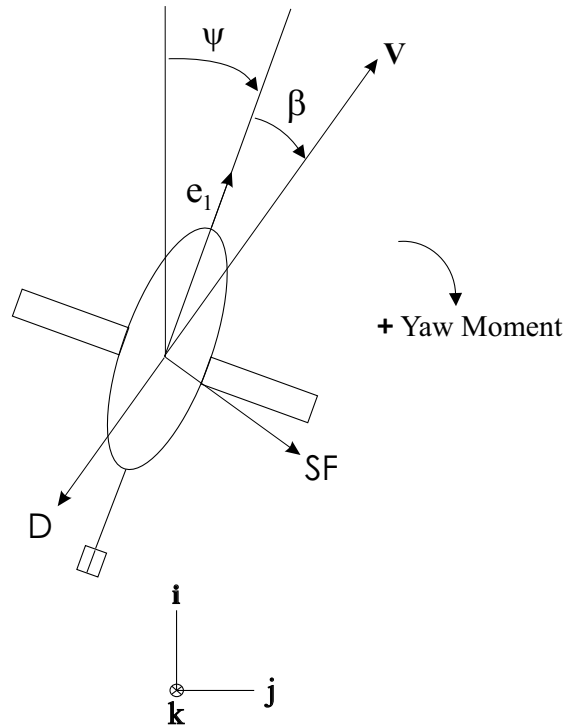


Figure 4.15: Lateral forces and states (shown with glider in xy plane).

cluding the Dutch roll mode, roll damping, and the spiral mode. See, for example, [66]. These depend on the hydrodynamic model used in the analysis, specifically the degree of coupling included between yaw and roll rates and moments.

The lateral dynamics of underwater gliders differ from those of aircraft. Differences include the righting moment due to the separation of the underwater glider's CG and CB. The propulsive force on an underwater glider is proportionally much smaller than for aircraft and sailplanes. Equilibrium steady glides of underwater gliders are much steeper than those of aircraft and sailplanes.

There is no lateral invariant plane in the underwater glider dynamic equations. It is not possible to choose some inclined plane in which the glider will stay as it glides. Therefore a lateral nonlinear analysis confined to an invariant plane, as was performed for the underwater glider vertical plane dynamics, is not possible. Therefore it is difficult

to model the lateral dynamics of underwater gliders as uncoupled from the longitudinal dynamics without significant simplifications.

There is similarly no lateral invariant plane for aircraft. For example, the following changes will move an aircraft out of the lateral, horizontal plane. Changes in speed change the lift force and lead to vertical accelerations. Changes in speed may also change the pitch balance of the aircraft. Rolling motion may move the lift vector away from vertical so that it does not balance the aircraft's weight, producing a vertical acceleration. Depending on the design of the aircraft and the detail of the hydrodynamic model, coupling between yaw, roll, and pitch may cause deviation from the plane.

It is possible to argue that analysis using uncoupled lateral equations is more applicable to aircraft than to underwater gliders. An aircraft is capable of maintaining a small glide path angle and small pitch angle, staying somewhat close to the horizontal plane. Underwater gliders generally do not. Powered aircraft can balance drag with thrust to move horizontally. Sailplanes are capable of close-to-level flight. Underwater gliders must move vertically to glide, and existing gliders have large glide path and pitch angles compared to sailplanes and aircraft.

To model and analyze the lateral dynamics of underwater gliders, we considered several different models, from simplified 'toy' models of a glider in the horizontal plane to the full three dimensional dynamic equations. The dynamics of these lateral 'toy' models were restricted to the lateral plane through an imposed constraint. It is difficult to say how accurately these restricted models approximate underwater glider lateral dynamics in three dimensions. They are formulated to exhibit the qualitative phenomena of three dimensional gliding such as yaw control through rudder and roll and rudder-roll coupling. The details of their dynamics may be quite different than those of the three dimensional model.

The yaw dynamics of the Slocum Electric Glider were examined using a lateral model derived by restricting the full three dimensional underwater glider model, with simplified internal masses, to the horizontal plane. A first version of this toy model confines the glider pitch and roll to be zero, so the glider body e_1 - e_2 plane coincides with the inertial x - y horizontal plane. Yaw is controlled using a rudder. Drag may be counteracted by setting the drag coefficient to zero or by adding a thrust force with a fixed direction in the body frame to cancel the drag at some equilibrium speed. If roll is not included, this model has dynamics in the horizontal plane similar to those of a ship.

In this model, when thrust is fixed in the body frame, stability of a forward steady motion depends on the placement of the internal moving mass, which influences the glider CG position. Some positions are unstable and others stable, depending on whether the CG position along the e_1 axis is ahead of or behind the centroid of the body and the yaw moment on the body. This is probably an artifact of the ‘toy’ model, not applicable to the full glider dynamics. Such an instability has not been observed during in-ocean experiments with gliders, nor in simulations with the three dimensional glider model.

An alternate restricted lateral model confines the underwater glider to motion in the horizontal plane but allows the glider to roll. This allows steering and yaw using the internal mass to actuate the roll of the glider, and shows the effects of static mis-trim and rudder-roll coupling in a simple model. While the model exhibits similar qualitative phenomena, it is difficult to say how relevant these results are to the three dimensional glider dynamics. These restricted longitudinal models give insight into the lateral dynamics of interest. It is probably necessary to use the full three dimensional equations to analyze these phenomena accurately.

Underwater glider yaw and roll dynamics differ from those of aircraft. The principal

difference is the static stability due to the glider's CG-CB separation. Aircraft are generally neutrally stable in a roll. There is no restoring force to move an aircraft at a nonzero roll angle to the upright position. In an underwater glider, the distance between the CB and CG, $\Delta CB - CG$, provides a stabilizing (righting) moment in the pitch and roll directions. Consider one example of how this affects the lateral dynamics. The spiral mode in aircraft is reduced or eliminated in sufficiently bottom-heavy gliders. In the spiral divergent mode, an initial roll angle causes the (stick-fixed) aircraft to yaw and roll further into a steady turn or tightening spiral, possibly resulting in an uncontrollable spin. In gliders with a large enough $\Delta CB - CG$ the static moment stabilizes the roll dynamics. This depends on the glider static moment, hydrodynamic design, and the degree of hydrodynamic coupling between yaw and roll. The same mechanism changes the Dutch roll mode and the overall roll dynamics of the glider. This is discussed further in the next section.

Other differences between gliders and aircraft arise due to the use of controlled internal masses, the effects of added mass and inertia, and the resulting coupling in the glider dynamics. See Section 7.1 for further discussion.

4.3 Gliding in Three Dimensions

4.3.1 Steady Glides

Three types of steady glides are of interest:

1. Straight, steady glides with zero sideslip, $\beta = 0$.
2. Straight, steady glides with nonzero sideslip, $\beta \neq 0$.
3. Spiral, steady, turning glides, both coordinated turns ($\beta = 0$) and others.

These exist in the glider model of Chapter 3 and have also been observed in the operation of gliders such as Slocum and Seaglider. Existence of these types of equilibria is expected because the glider dynamics are invariant with respect to translations in x and y and rotations about the direction of gravity, z . If water density ρ is taken to be uniform with depth, and surface and bottom effects are disregarded, the equilibria do not vary with depth. As always, these equilibria and their stability depend on the glider's hydrodynamics and internal mass configuration.

Straight Glides

Steady glides in the longitudinal plane have already been discussed. These glides are also equilibria in the three dimensional equations, as the longitudinal plane is an invariant plane of the full glider dynamics.

Straight line glides with some small sideslip angle are similar to those shown in the longitudinal model. Consider a glider with stable hydrodynamics and sufficiently bottom-heavy internal mass distribution. A small static roll offset will cause a turning glide, but this may be offset with some rudder angle, resulting in a straight glide with nonzero roll and sideslip angles. The glide path angle is determined by the glider lift/drag ratio at the steady flight condition. Flight with a nonzero sideslip angle generally decreases the lift/drag ratio of a glider or aircraft, producing a steeper or slower glide (generally an undesirable effect). The detail of the hydrodynamic model determines the extent to which this appears in the three dimensional model dynamics. See [26].

Existing gliders operate predominantly in straight, steady glides as shown in the longitudinal model section and in Chapter 5. Straight glides are desirable for power conservation. Existing gliders (Slocum, Spray, Seaglider) are designed to be statically stable and to glide

with minimal control application.

Gliders may stabilize the longitudinal plane statically, with a design including a vertical tail, wing sweep or dihedral. Gliders can also stabilize straight glides actively, using their turning actuators. Turns between straight glides may be steady or unsteady motions.

Example: Converging to a Stable, Steady Planar Glide.

The following plots show simulation output for a glider with the same parameters as in Section 4.1 and with $K_\beta = 90$. Figure 4.16 shows the simulation output of Euler angles and Figure 4.17 shows the glider velocity and aerodynamic angles. The glider simulated here has high directional stability, with stabilizing K_M and K_β . This could represent a glider with wings and tail far aft on the glider, as with Seaglider.

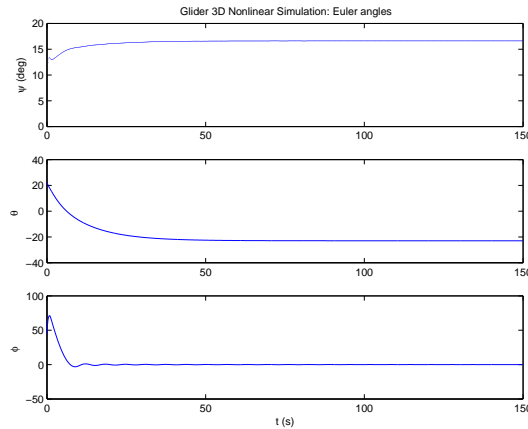


Figure 4.16: Simulation Euler Angles.

The internal mass and ballast are positioned to give the same \mathbf{x}_d , a downwards straight glide, as in Section 4.1, Table 4.3. The glider’s initial condition is offset from \mathbf{x}_d in pitch, roll, angular velocity, and velocity: $\theta_0 = 22^\circ$, $\phi_0 = 45^\circ$, $\boldsymbol{\Omega}_0 = (1, 1, 1)^T$ (rad/s), $\mathbf{v}_0 = (0.2, .10, .11)^T$ (m/s). The states converge to the desired straight glide. Heading is not controlled. Lowering the hydrodynamic angular damping produces a more oscillatory convergence.

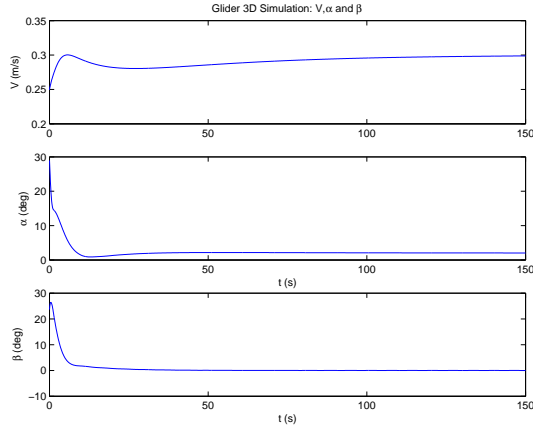


Figure 4.17: Simulation Aerodynamic Angles.

4.3.2 Spiral Glides

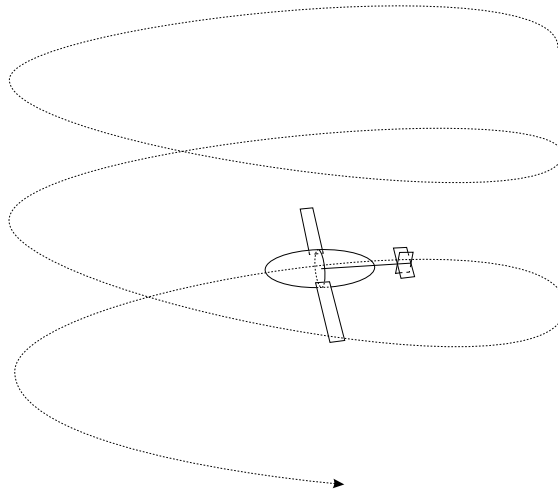


Figure 4.18: A steady spiral glide.

Gliding equilibria are solutions of the glider three dimensional dynamic equations with $\dot{\Omega} = \dot{v} = \dot{r}_p = \dot{r}_b = \dot{m}_b = 0$. Figure 4.18 shows a steady spiral glide. In a steady spiral, $\Omega = R^T k \omega_3$, where $k \omega_3$ is the inertial angular velocity and ω_3 the glider heading rate. Substituting these conditions into the simplified internal mass case, (3.42), gives $\tilde{T}_{sm} = 0$ and $\tilde{F}_{sm} = 0$, where \tilde{T}_{sm} and \tilde{F}_{sm} are the torques and forces in the ‘simplified masses’ model as defined in Section 3.2.6. The glider three dimensional equilibria equations are

then

$$0 = \mathbf{J}\boldsymbol{\Omega} \times \boldsymbol{\Omega} + \mathbf{M}\mathbf{v} \times \mathbf{v} - \mathbf{r}_p \times [\bar{m}(\mathbf{v} + \boldsymbol{\Omega} \times \mathbf{r}_p) \times \boldsymbol{\Omega}] + \bar{m}\hat{\mathbf{r}}_p g \mathbf{R}^T \mathbf{k} + \mathbf{T}_{ext}, \quad (4.51)$$

$$0 = [(\mathbf{M} + m_b \mathcal{I})\mathbf{v} + \bar{m}(\mathbf{v} + \boldsymbol{\Omega} \times \mathbf{r}_p)] \times \boldsymbol{\Omega} + m_0 g \mathbf{R}^T \mathbf{k} + \mathbf{F}_{ext}. \quad (4.52)$$

where spiral glides have $\boldsymbol{\Omega} = \mathbf{R}^T \mathbf{k} \omega_3$. Setting $\omega_3 = 0$ gives straight glides.

Spiral equilibria were found by solving these equations numerically for a given \mathbf{r}_p and m_b . One method for finding spiral glides is to choose \mathbf{r}_p and m_b using the vertical plane equilibrium equations, for some desired planar glide. Some mass offset Δr_{p2} may then be introduced and the corresponding 3D equilibria found numerically.

If the glider is configured such that it is hydrodynamically stable and bottom-heavy, the resulting spiral glide will be stable and simulations will converge to that glide. Stability may be examined through linearization about the steady glide. Numerical linearization and nonlinear simulations were used to study a variety of steady spiral and straight glides.

Multiple equilibria are possible for some choices of \mathbf{r}_p and m_b , depending on the glider hydrodynamics. This also true for degenerate cases such as $\mathbf{r}_p = 0$, $m_b = 0$, or for strange sets of hydrodynamic parameters (that correspond to a bizarre vehicle geometry). Picture, for example, a glider with some \mathbf{r}_p , $m_b > 0$, such that it is bottom-heavy and stable gliding downwards. Another equilibrium may exist for the same \mathbf{r}_p , m_b where the glider is inverted and the CG is above the CB. This will likely be unstable, depending on the relative magnitudes of the glider internal mass and hydrodynamic forces.

Glidern designed such that there is one stable equilibria for a given internal mass configuration are desirable in low-power applications like ocean sensing, since minimal control action is required and the onboard CPU can ‘sleep’ for periods of steady gliding. The ap-

pearance of multiple equilibria appears to be only a small concern when modelling existing gliders. For parameters representing a glider like Slocum or Seaglider, one stable equilibria was found for the $\mathbf{r}_p \neq 0$, $m_b \neq 0$ tested. Other equilibria found (in a brief examination) were unstable. If more unusual designs are considered, some sets of parameters and internal mass states may have multiple stable glides.

The number and stability of the equilibria is important when considering control and navigation by switching between stable glides. To switch from glide A to B, it is necessary for glide A to lie within the region of attraction of glide B, given the switching control used and any control used to stabilize glide B. For the glider configurations considered in simulation, with no control other than the movement of the point mass to position B, the steady glides were found to have significant regions of attraction. Initial conditions at multiple other steady glides in the upwards and downwards directions and a range of other initial conditions were found to converge to the single steady glide corresponding to the \mathbf{r}_p and $m_b = 0$ chosen. The region of attraction of the stable equilibria may be examined using nonlinear simulations and following the methods of [36].

When evaluating equilibria, keep in mind that the hydrodynamic model used here is valid only for attached flow at low angles of attack and sideslip and in some linear and (low) angular velocity range. This limits the domain of interest when finding equilibria. Model variation, for example, modelling the hydrodynamic moment as cubic in alpha instead of linear, may introduce new equilibria.

Stability of a steady glide confined to the vertical plane does not guarantee three dimensional stability of the corresponding straight, steady glide. A glider with hydrodynamics that give stable 3D motions will generally have stable planar glides (with the proper corresponding mass positions), but it is possible for a glider stable in 2D to have, for example,

yaw characteristics such that a disturbance out of the vertical or a small Δr_{p2} will produce a steep nose-down dive instead of a steady spiral turn. This was demonstrated in simulations, especially when $\Delta CB - CG$ is small. Therefore both pitch and yaw stability should be considered in glider design and choice of r_p . Gliders designed for static (controls-fixed) stability may use steady turns for efficient gliding.

A Steady Spiral Glide

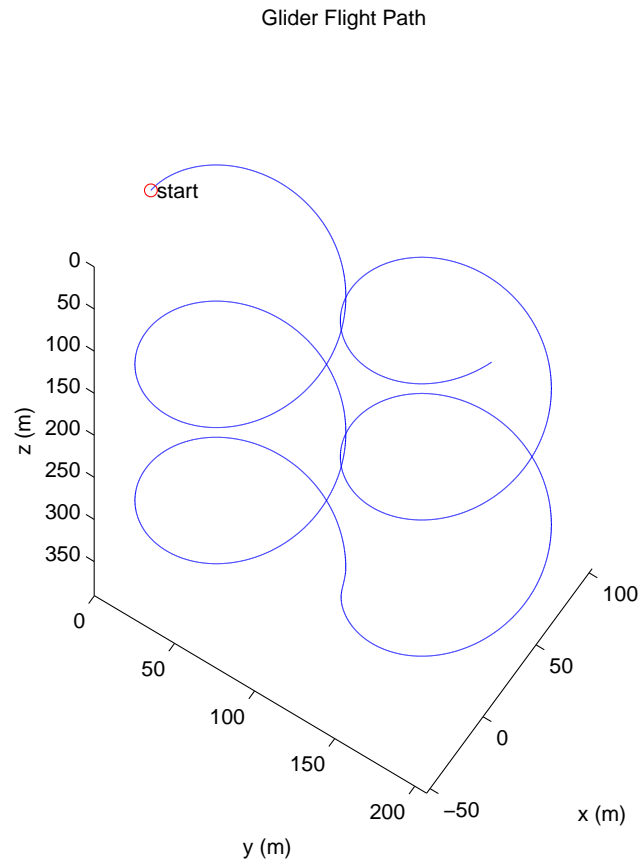


Figure 4.19: Steady Spiral Simulation. Glider inflects at maximum depth.

Figures 4.19-4.23 show simulation output for example steady spiral glides downwards and then upwards. The simulation uses the same glider parameters as in the previous examples. The internal mass is positioned to give a downwards glide with a 45° roll angle.

r_{p3} is fixed. r_{p1} and m_b are set for the downwards and upwards glides as in the previous examples. Note that the resulting pitch angle is steeper here than in the planar case because the roll and sidlip angles are nonzero and the lateral characteristics of the glider affect the pitch equilibrium of the glide. The spiral glides shown here are both stable.

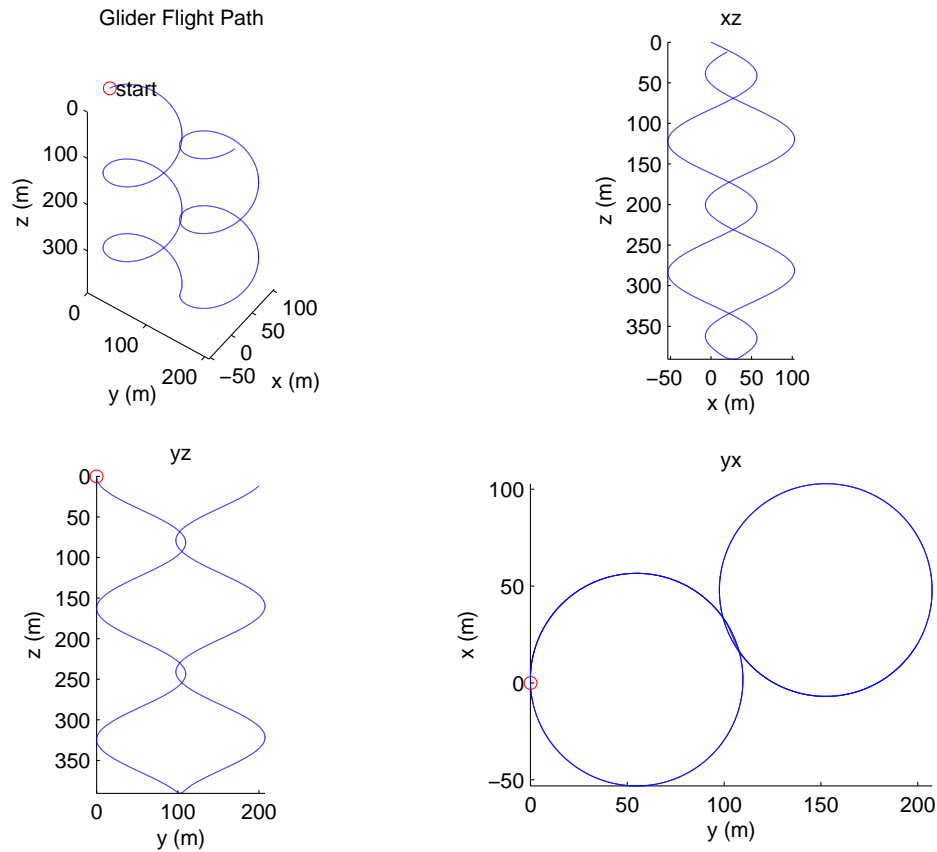


Figure 4.20: Glider path projected onto xz , yz and xy planes.

Figures 4.19 and 4.20 show the path of the glider in space. The glider begins at the origin of the inertial coordinate system in a steady spiral glide downwards. In this glide the glider is rolled 45° to the right and has a positive heading rate (turns to the right) when gliding downwards, demonstrating that this glider has a positive roll-yaw coupling (described in the following sections). After 3000 s the glider moves the internal mass and ballast to the position corresponding to the upwards glide, as shown in Figure 4.23. This

changes r_{p1} and m_b , but not r_{p2} or r_{p3} . When gliding upwards, the same roll angle produces a negative heading rate and turns to the left.

The position and orientation of the glider versus time are shown in Figure 4.21. Angular and linear velocities are shown in Figure 4.22. Because the glider pitch and roll angles are nonzero, no element of $\mathbf{\Omega}$ is zero. If a glider's roll angle is zero in a steady spiral, perhaps in a glider turning using a rudder instead of roll, then $\omega_2 = 0$ in the spiral. Here, because $\phi = 45^\circ$, $\omega_2 = \omega_3$. This follows from $\mathbf{\Omega} = \mathbf{R}^T \mathbf{k} \omega_3$.

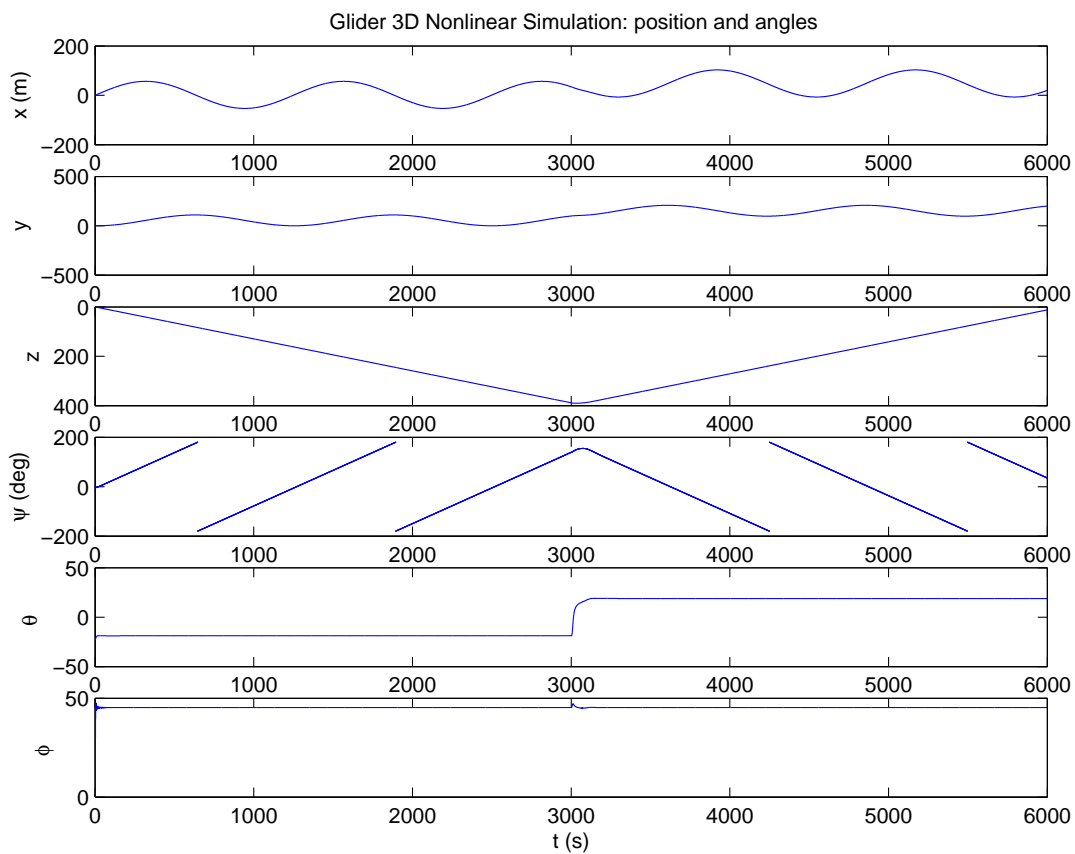


Figure 4.21: Position and orientation. Heading, pitch, roll in Euler angles.

The sliding mass and ballast positions are shown in Figure 4.23. In this simulation the maximum control inputs are limited. The maximum sliding mass acceleration (in the body frame) is 1 (mm/s^2) and the maximum ballast pumping rate is 1 (g/s^2). The pumping is

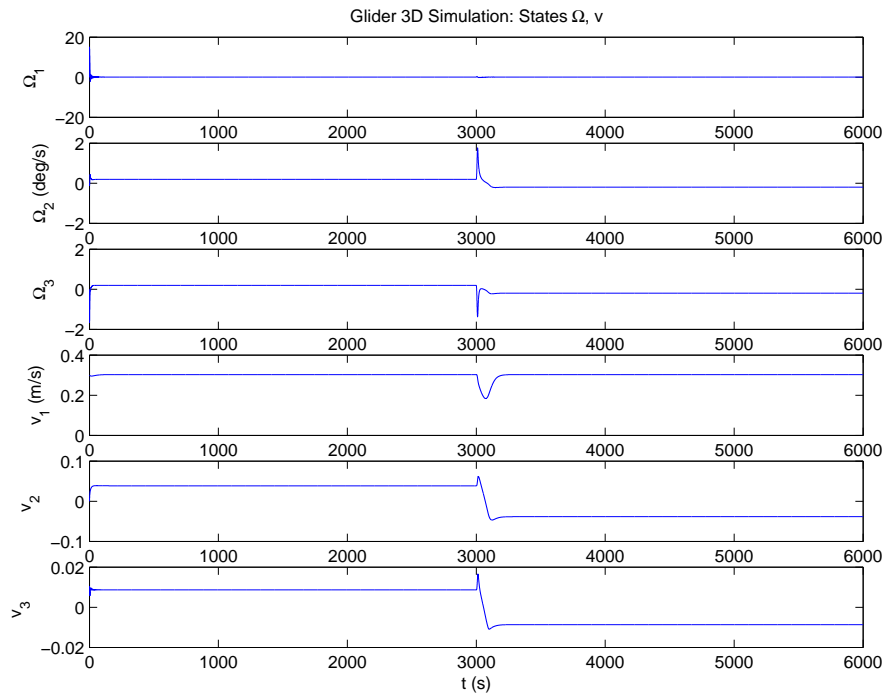


Figure 4.22: Angular and linear velocities expressed in the glider body frame.

completed in about 100 s and the inflection to the upwards steady glide takes about 150 seconds.

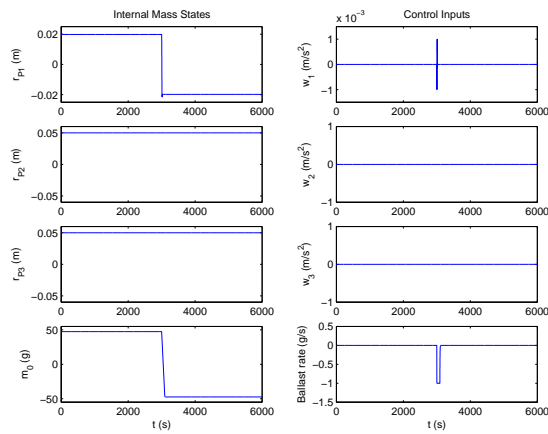


Figure 4.23: Internal mass positions and controls.

4.3.3 Turning

Gliders may turn using steady or unsteady turning glides. Gliders can actuate their heading and yaw using two methods:

1. Rolling to cause a banked turn. This rotates the lift vector and pitch moment on the glider so they have a component out of the vertical plane. Seaglider and Spray use this method to turn. Their internal mass actuators have a degree of freedom in the roll direction, so the internal point mass can be used to change the glider's roll angle.
2. Using a rudder or other moving hydrodynamic surfaces. This produces a turning moment on the glider. The Slocum Electric glider design uses a rudder to turn. Differential spoilers on a tailless glider or flying wing are another example.

Gliders with roll actuation may glide in banked, coordinated turns with zero sideslip angle. Gliders whose roll is statically stabilized by their internal mass arrangement will probably use unbanked turns with some sideslip angle. Gliders using a combination of hydrodynamic surfaces to actuate roll and yaw may fly in banked turns without internal actuation.

Design choice of a glider's yaw control and actuation should take into account the frequency of inflections in the glider's operations. If roll is used to control the glider's yaw rate, then the roll must be changed in direction each time the glider inflects from an upwards to a downwards glide. In shallow water operations involving many inflections, this may be undesirable. In a design using a rudder, the relationship between the rudder angle and yaw rate is independent of the glide direction (up or down). Therefore use of a rudder is desirable for some operations, for example in littoral areas. This is the motivation for the use of a rudder in the Slocum electric glider. Because the Slocum electric is designed

for shallow gliding and frequent inflections, the rudder is used to control yaw and roll is statically stabilized, not actuated.

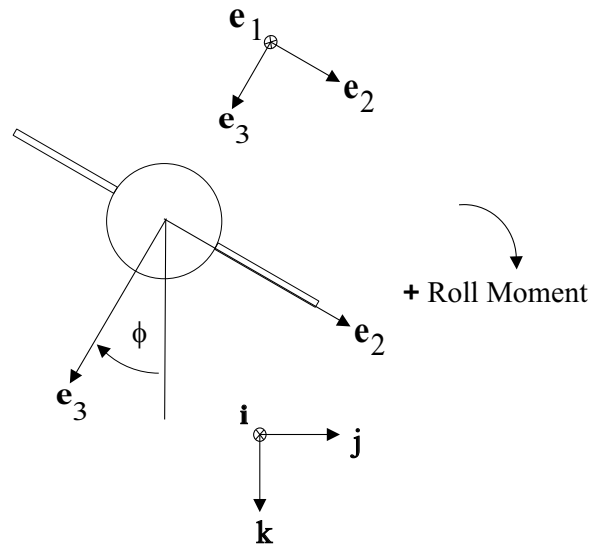


Figure 4.24: Roll and roll moment, viewed from rear. Shown with e_1 aligned with i .

The relationship between roll (Figure 4.24) and yaw (Figure 4.15) at equilibrium depends on the hydrodynamics of a given glider. The hydrodynamic moment on the glider is a function of the glider body geometry and wing position and the position of its tail and control surfaces. A major factor in the pitching moment on the glider is the design of its wings and their position relative to the glider's CG. This affects the location of the vehicle's hydrodynamic center of pressure (CP) relative to its CG. The CP is the point on the vehicle at which the hydrodynamic force (i.e., lift and drag) effectively acts. This influences the moment due to the lift and drag forces. A glider whose CP is forwards of its CG will have a positive hydrodynamic pitching moment at equilibrium. The moment on the body alone is generally destabilizing ($\frac{\partial}{\partial \alpha} M_{body} > 0$), so for negative pitching moment slope ($\frac{\partial}{\partial \alpha} M_{total} < 0$) the wing must be far enough aft to overcome this. Consider, for example, a glider with its CP forward of its CG and $\frac{\partial}{\partial \alpha} M_{total} > 0$ moving in a steady, straight glide at a downwards glide path angle. A small positive roll angle will produce a positive yaw rate. The roll angle

rotates the lift vector and other hydrodynamic force vectors to the right (in the positive direction). Because they act at the CP forwards of the CG, the glider yaws right (positive yaw direction).

Glider pitch dynamics are stabilized principally by their internal mass and buoyancy torques. Because of the design and slow speeds of the average existing glider, the maximum control moment from the internal mass is generally much greater than the hydrodynamic torques. This gives some leeway in the designer's choice of the glider's wing position and the resulting hydrodynamics and center of pressure.

There is significant variation in the pitch moment profiles of existing gliders. In an aircraft, one typically expects a positive roll/yaw relationship, where a roll to the right produces a yaw to the right when gliding downwards. Existing oceanographic gliders provide examples of both positive and negative roll/yaw relations. In the case of the Seaglider, the wings and the net center of pressure are located aft of the vehicle's center of gravity. This results in a roll-yaw coupling opposite that normally found in aircraft. When the Seaglider is gliding downwards and rolls to the right, the location and direction of the lift vector produces a yaw to the left.

The glider orientation may be parameterized using heading ψ , pitch θ , and roll ϕ Euler angles. The heading rate is

$$\dot{\psi} = \frac{\sin \phi}{\cos \theta} \Omega_2 + \frac{\cos \phi}{\cos \theta} \Omega_3.$$

Consider a glider in a straight, steady glide with $\beta = 0, \phi = 0, \mathbf{\Omega} = 0$. The heading response to a small roll angle is

$$\begin{aligned} \frac{\partial}{\partial \phi} \ddot{\psi}|_{eq} &= \left(\frac{1}{\cos \theta} \frac{\partial}{\partial \phi} \dot{\Omega}_3 \right) |_{eq} \\ &= \frac{1}{J_3 \cos \theta_{eq}} \left[((m_{f3} - m_{f1}) \sin \alpha_{eq} \cos \alpha_{eq} + K_{M_0} + K_M \alpha_{eq}) V_{eq}^2 \right]. \end{aligned}$$

The quantity in square brackets is the total hydrodynamic pitching moment on the glider at equilibrium, including the added mass moment. At this equilibrium this moment is countered by the internal mass moment.

The hydrodynamic parameters of Slocum and Seaglider have been estimated using reference methods. CFD analysis of their hydrodynamics appears in [32], including estimates of their pitch moment. For both Slocum and Seaglider, $K_{M_0} = 0$ because of their top-to-bottom symmetry, so the total hydrodynamic moment at $\alpha = 0$ is zero. For Slocum, $\frac{\partial}{\partial \alpha} M_{total} > 0$ at small angles of attack, so $\left[((m_{f3} - m_{f1}) \sin \alpha_{eq} \cos \alpha_{eq} + K_{M_0} + K_M \alpha_{eq}) V_{eq}^2 \right] > 0$ for downwards glides ($\alpha > 0$). Therefore, Slocum has positive roll-yaw coupling. Seaglider's hydrodynamics give it negative roll-yaw coupling. This is also demonstrated by simulations of the equations of motion and has been observed in experiments at sea with Slocum (Chapter 5) and Seaglider [14].

In a glide with some sideslip angle, such as steady spiral with some roll angle, a glider's roll-yaw coupling is determined by the relative magnitudes and directions of the pitch and yaw moments on the glider. Because of this a variety of positive and negative moment parameters may give a positive roll-yaw relationship. In existing gliders the yaw moment is stabilizing (towards $\beta = 0$), due to their vertical tail designs. This produces a yaw moment consistent with a positive roll-yaw coupling. Gliders such as Slocum, with $K_M > 0$, have a

positive roll-yaw coupling. Seaglider’s wing position at the rear of the glider gives a large negative K_M , producing the glider’s negative roll-yaw coupling.

Because gliders glide both upwards and downwards, they exhibit a slightly more complex relationship between banking and turns than is usually seen in aircraft. Because the direction of the lift vector, and typically the angle of attack, is reversed between upwards and downwards glides, the direction of the yaw-roll coupling is reversed. Consider the example in Section 4.3.2, which shows a glider with a positive roll/yaw relationship. When it is gliding downwards, a roll to the right produces a positive yaw rate (it turns to the right). When it is gliding upwards, it produces negative yaw rate (it turns left) with a roll to the right.

4.3.4 Static Mis-trim

Some misalignments of a glider’s CG may occur while ballasting a glider before deployment, or as a result of damage or fouling during operation. Depending on the individual glider design and actuation, this may result in a static roll angle and a yaw moment on the glider. In a glider with sufficient degrees of freedom in the actuation of its moving internal mass, the misalignment may be corrected simply by adjusting r_p . In a glider with a restricted internal mass, for example, one actuated only in the e_1 direction, a mis-trim Δr_{p2} will result in a roll.

Existing gliders have few or no moving external surfaces for attitude control. Roll and pitch may be controlled using internal actuators alone, so it is possible to design a glider with no external control surfaces. Seaglider, for example, has no moving control surfaces. Gliders may also use a combination of internal and external actuators. The Slocum electric glider uses a rudder to actuate yaw and internal masses to control pitch. Roll is set by the

static trim balance of the vehicle.

Consider a case where a Slocum electric glider is deployed with some static roll mis-trim, i.e., a nonzero static roll angle resulting from an off-centerline CG position. The sliding internal mass is not actuated in the roll direction, so the mis-trim cannot be removed while the glider is deployed. This roll angle produces a yaw moment on the glider by rotating the lift vector out of the vertical plane. To produce a straight glide, this yaw moment must be counteracted by the rudder, resulting in a steady glide with nonzero roll angle and nonzero sideslip angle. These both tend to increase the drag and reduce the lift on the glider, which is undesirable from a performance standpoint.

This situation also produces an interesting coupling between control of the glider's yaw, roll and depth rate. The yaw moment due to the roll mis-trim changes direction between upwards and downwards glides because the lift vector points up when gliding down, and down when gliding up. Therefore, the rudder angle necessary to counteract the mis-trim yaw moment will change between upwards and downwards glides. The magnitude of the mis-trim yaw moment may also change, depending on the glider geometry, requiring a corresponding adjustment of the rudder angle.

One can imagine other situations that may arise when using a mixed combination of internal and external actuators. Another interesting effect occurs in a glider design with mixed internal and external actuators. The forces generated by internal mass actuators are independent of glide speed. This is one of the factors that makes them attractive in a low speed glider. The forces on the external actuators depend on the dynamic pressure, $(1/2)\rho V^2$. In high speed gliders the relative magnitude of the static and hydrodynamic forces may require special consideration.

Similar situations, where an asymmetry in the glider is counteracted with an actuator,

may also occur in gliders with other combinations of actuators. A glider design with internal mass actuation in the roll direction, such as the Seaglider, Spray and the Slocum Thermal designs, can adjust the roll trim of the vehicle using an internal actuator. Cases are possible which would result in these gliders also making straight line glides with nonzero roll and sideslip angles. Consider, for example, the case where one wing of the glider becomes fouled with seaweed, or some other case results in a higher drag on one side of the glider. The resulting yaw moment would need to be counteracted with some roll angle for the glider to travel in a straight line.

It is also possible for a roll to be generated dynamically in a glider due to some asymmetry in its external geometry. If, for example, the wings of a glider are slightly misaligned or twisted relative to one another, they produce a rolling or yawing moment. Some moments may also be produced by asymmetrically placed instruments, such as a CTD mounting. The moment may change with different glide directions and must be countered by some actuator use.

Systems may be incorporated in a glider design to reduce these problems. The mis-trim problem may be countered by making it easier to trim the vehicle for zero roll. Internal mass trimming devices may be incorporated into the glider, for example, an internal roll mass that may be trimmed manually or automatically during an initial deployment or in a trim tank without removing the vehicle from the water. A small internal mass roll actuator may be built into the vehicle, not for purposes of active roll control but only to counter small changes in the CG location over the course of a long deployment, for example, due to barnacle formation. Use of ailerons and other external surfaces may also be considered, although these may reduce the durability of the vehicle and increase its complexity.

An Example from Flight Tests

Experiments were performed with a Slocum glider with some static roll angle to determine the required rudder angle to counteract the yaw due to roll. Figures 4.25-4.26 show experimental data from glider tests at sea using a Slocum electric glider. These tests are described further in Chapter 5. The figures here show data from test Vert 18. In this test, Slocum WE01 glides with fixed sliding mass position and ballast in between inflections. Static mis-trim of the glider results in some positive roll angle and yaw moment. There are other yaw moments on the glider, probably due to lateral asymmetry of the CTD location. The rudder is fixed at 3.5° to counteract this moment.

Figure 4.25 shows the heading, depth, pitch and roll of the glider. The glider has a positive roll angle throughout the test. When gliding downwards, the glider has a positive heading rate. It has a negative heading rate when gliding upwards. (This matches turning behavior predicted using the glider model with hydrodynamic parameters for Slocum estimated using hydrodynamic references). The internal mass is fixed during steady glides and the glider pitch is stable at the equilibrium steady glides. The internal mass position and ballast are shown in Figure 4.26.

4.3.5 Rudder-roll coupling

Because of its high tail, the electric Slocum shows some coupling between rudder and roll. This produces different heading control qualities when gliding upwards than when gliding downwards. The tail and rudder are located at the rear of the glider and are above the glider's CG. Because of its position, deflection of the rudder from its zero position produces both a yaw and a roll moment on the glider. A (positive) deflection of the rudder produces a (positive) yaw moment and a (positive) rolling moment. This results in a coupling between

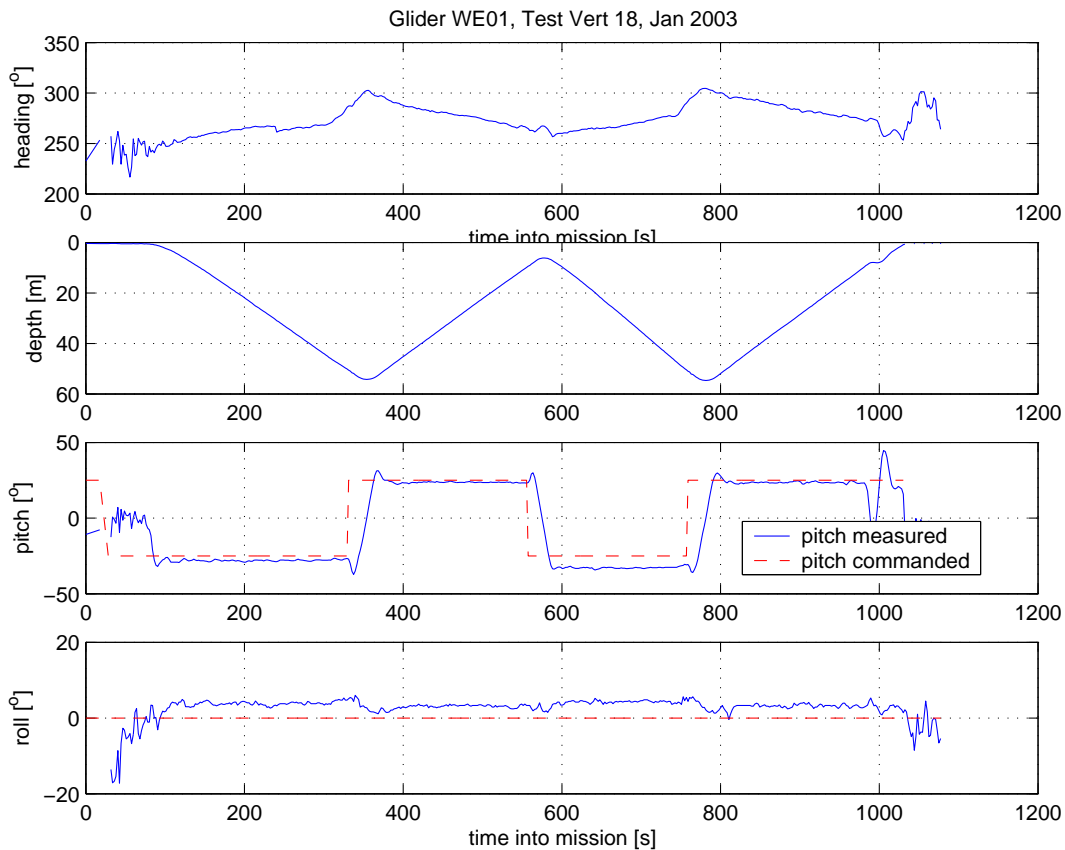


Figure 4.25: Slocum Glider Test Vert 18. Heading, depth, pitch and roll.

the yaw and roll actuation of the glider. The direction of these moments is the same whether the glider is gliding up or down, although it is conceivable that the force on the rudder may change due to some interference from the flow off the glider body and wings.

The direction of the yaw moment due to a roll mis-trim changes between up and down glides, as described in previous sections. Because of this, the effect of the rudder on the yaw dynamics of the glider will change between upwards and downwards glides. The high rudder produces a rolling moment on the glider, which changes the roll angle. Depending on the roll/yaw relationship of the glider and whether it is gliding upwards or downwards, this additional roll will produce a yaw moment on the glider acting either against or with the rudder yaw moment. This effectively decreases or increases the control authority of the

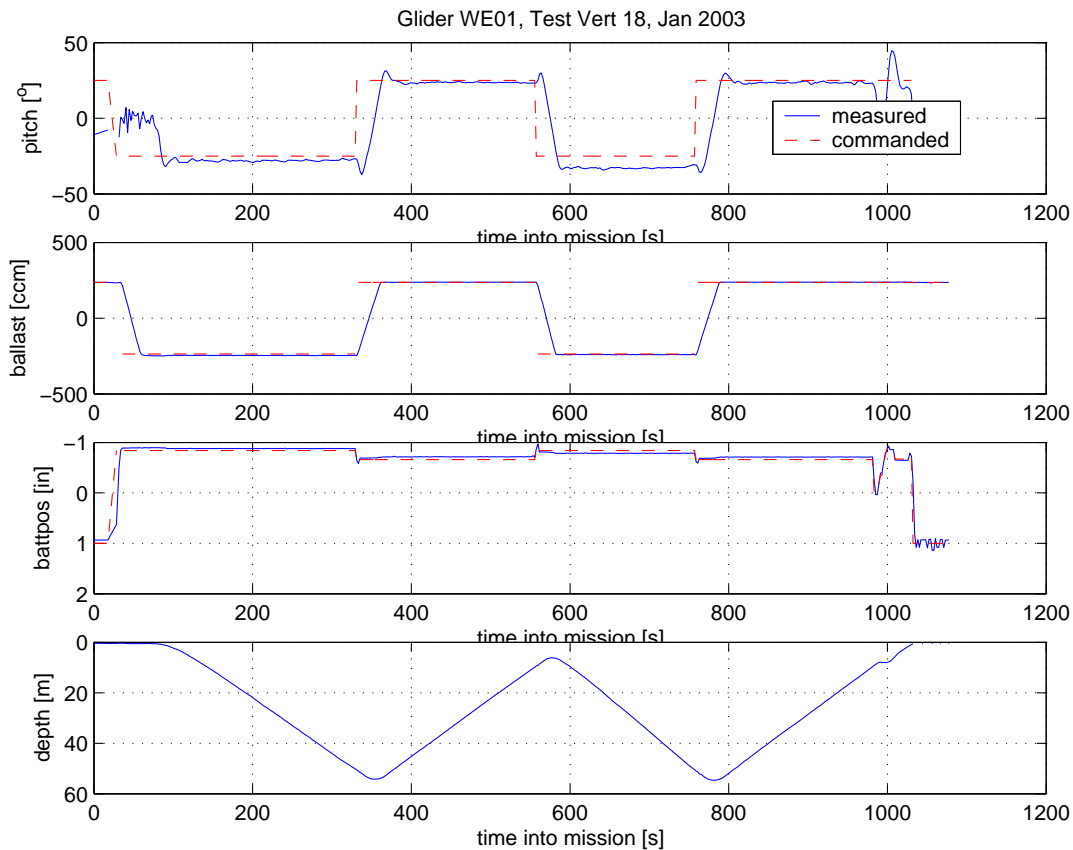


Figure 4.26: Slocum Glider Test Vert 18. Pitch, ballast, mass position, and depth.

rudder. Depending on the magnitude of this effect, it may be necessary for the glider control system to take this into account and to use different gains for the rudder for upwards and downwards glides. We have observed this phenomenon during in-ocean trials of the Slocum vehicle.

4.4 Chapter Summary

In this chapter glider dynamics, including steady glide equilibria, their stability, and switching between steady glides, are analyzed using the glider dynamic model of Chapter 3. The analysis makes use of several versions of the glider model, including a model confined to the longitudinal plane, a simplified phugoid model, and the full three dimensional glider model.

First, the glider model is confined to the longitudinal plane the the steady glide equilibria are found. The steady glide equilibria have some interesting properties. The speed V and glide path angle ξ of a steady glide may be chosen separately, within the bounds of possible m_0 and \mathbf{r}_p . A choice of (V, ξ) admits a family of \mathbf{r}_p sliding mass positions, allowing some choice of the glider's bottom-heaviness. Possible mass positions in an operational glider will depend on its internal mass actuator's range. If \mathbf{r}_{p3} is fixed, then one mass position will satisfy a given choice of (V, ξ) .

The stability of the gliding equilibria are studied through linearization and through simulation. It is shown that it is possible to design a statically stable underwater glider, using the hydrodynamic design and the static forces on the glider and internal masses. This is consistent with experimental results. Steady glides and transition between steady glides are demonstrated. In the longitudinal plane, stable switching between straight glides is demonstrated. In the three dimensional model, stable switching between both straight and vertical spiral glides is demonstrated.

The phugoid model for an underwater glider is derived by applying Lanchester's phugoid assumptions to the glider longitudinal dynamic model. It is shown that, in the conservative $\alpha = 0$ case, the underwater glider phugoid case is identical to the Lanchester phugoid within a similarity factor that depends on the added mass and net buoyancy of the glider. The $\alpha \neq 0$ case is shown to be non-conservative, due the constraint forces imposed in this case.

Three-dimensional glider dynamics are studied using the glider model. Straight and spiral equilibrium glides are identified. Their stability is analyzed using linearization, simulation, and experiments (also see Chapter 5). It is shown that stable equilibrium glides are possible given a stable hydrodynamic and static design of the glider. A properly designed and trimmed glider will converge to a stable straight glide in the longitudinal plane

without use of its actuators. Turning and heading control using rudder and roll is also examined. It is shown that the direction of a glider's roll-yaw coupling depends on the glider's hydrodynamics and the location of its hydrodynamic center in relation to its center of gravity.

The effects of static mis-trim on glider heading are also shown. A static mis-trim creates a steady roll angle and a yaw moment on the glider. To maintain a desired heading this yaw moment must be counteracted with the glider's rudder or through roll actuation. Examples are shown in simulation and from experimental data. Flight test data from oceanographic gliders are shown with similar qualitative behavior to the glider model. Rudder-roll coupling and roll mis-trim are both shown in experimental data.

Note that Chapter 7 includes a comparison of the dynamics of gliders and sailplanes.

Chapter 5

Modelling The Slocum Glider and Parameter Identification from Experiments at Sea

This chapter details how the glider model of Chapter 3 may be adapted to model the Slocum Glider, including its geometry, rudder, ballast pump and internal sliding mass. We identify the vertical plane model parameters for the Slocum glider in two steps. First, parameters are determined to match the set of steady glides in new flight test data from the Slocum Glider. Existing estimates of the glider hydrodynamic parameters are taken into account and used in determining the glider lift and drag coefficients. Second, we propose a method for determining the parameters that appear in the dynamic equations but not in the steady state equations. Parts of this work appeared in [22].

In the process of performing the identification, we also identify the buoyancy trim offset of the glider used in the flight tests. This buoyancy trim offset was likely the result of an original mis-trim; the glider was not perfectly trimmed and ballasted before launch. Our

approach to computing the mis-trim has potentially far-reaching application. For instance, the method we describe here could be adapted as a means for updating trim measurements upon deployment or as a remote diagnostic tool. In the latter case, the method would be used to detect changes in the glider behavior resulting from fouling from seaweed, a slow leak in the hull or a problem with the ballast system, for example. Problems of these types have occurred during deployments of existing gliders; it is suspected that a slow leak played a role in the loss of one glider in 2003. This concept for identifying the buoyancy trim offset of the glider provides an excellent illustration of the advantages of having a model.

Existing glider designs are described in Chapter 2. Operational ocean going gliders include the Slocum glider [80], the Spray glider [63] and Seaglider [14]. The Slocum glider is described further in Section 5.1.1. These operational gliders are similar in size and geometry, each measuring about two meters long and weighing around fifty kilograms. Each has a cylindrical hull, two fixed wings and a tail. They are all buoyancy-propelled, fixed-winged gliders which shift internal ballast to control attitude. All are designed to be statically stable in a glide. In the electric Slocum, designed for dives from five to 200 meters, roll is set by the glider's static CG position and pitch is controlled by moving internal mass. Yaw and heading are controlled using the rudder mounted on the vertical tail of the glider.

In this chapter we describe model parameter identification for the Slocum using experimental flight test data from a test cruise in the Bahamas in January 2003 (described in Section 5.1.2). We adapt the glider model of Chapter 3 to the Slocum electric glider, modelling the location of the ballast system, the properties of the moving pitch mass, and the rudder. The resulting equilibrium equations appear in Section 5.1.3. In Section 5.2 we determine parameter values such that the model will match the data set of equilibria for the glider. This determines the coefficients for our quasi-steady hydrodynamic model and

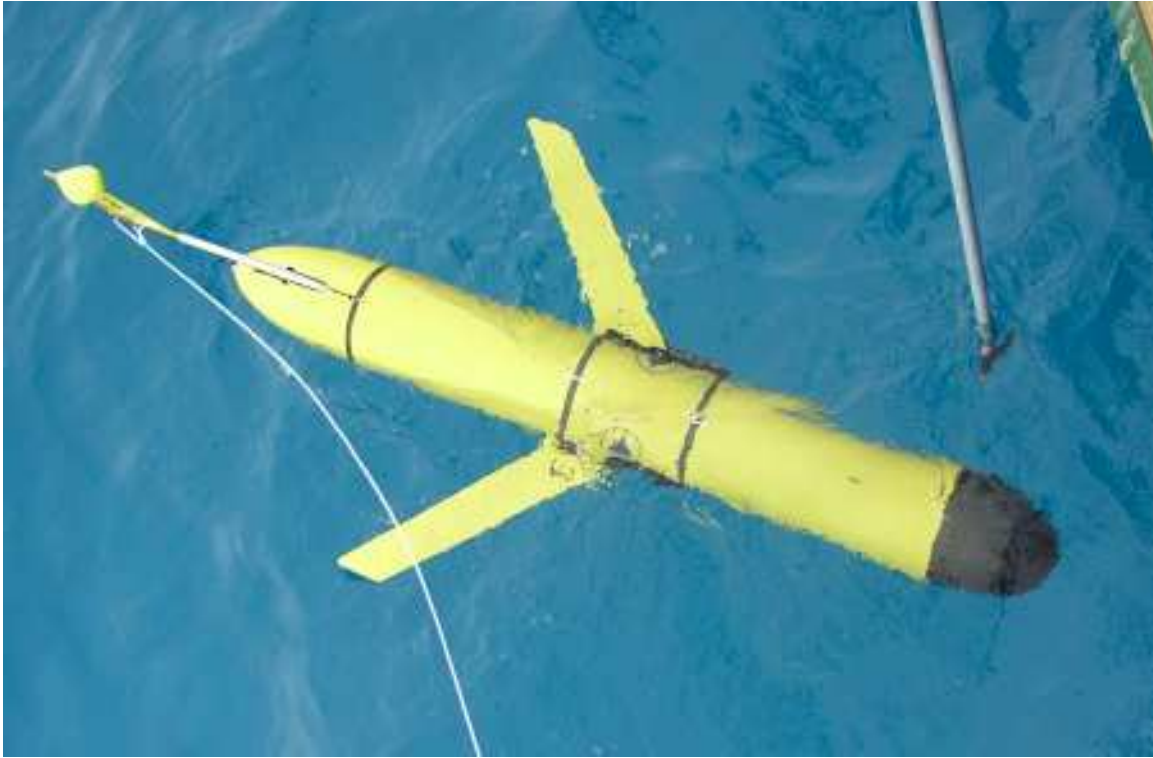


Figure 5.1: A Slocum Glider.

parameters representing the trim and buoyancy of the glider. We discuss ideas for future work and include some remarks in Section 5.3.

5.1 Slocum Glider Model

5.1.1 Slocum Glider

The Slocum Glider design was briefly described in Chapter 2. We now provide a more detailed description, especially of the elements important to the vehicle flight testing.

The Slocum glider is manufactured by Webb Research Inc., Falmouth, MA. It is a buoyancy-driven, autonomous underwater vehicle [76, 80]. The operational envelope of the glider includes a 200 m depth capability and a projected 30 day endurance, which translates

into approximately 1000 km operational range with a 0.4 m/s fixed horizontal and 0.2 m/s vertical speed. The glider has an overall length of 1.5 m and a mass of 50 kg. The buoyancy engine is an electrically powered piston drive, located in the nose section of the glider. See Figure 5.1. The drive allows the glider to take in and expel water, thereby changing its overall buoyancy. The mechanism allows a close to neutrally buoyant trimmed glider to change its displacement in water by ± 250 ccm, which corresponds to approximately $\pm 0.5\%$ of the total volume displaced. This change in buoyancy generates a vertical force which is translated through two swept wings into a combined forward and up/downward motion. Due to the location of the piston drive, also called buoyancy engine, the change in direction of the buoyant force also creates the main pitching moment for the glider. Besides the buoyancy engine the glider possesses two more control actuators, a 9.1 kg battery pack, referred to as the *sliding mass*, that can be linearly translated along the main axis of the glider and a rudder attached to the vehicle tail fin structure. The sliding mass is used for fine tuning the pitch angle.

The glider has two onboard computers, a control computer and a science computer. Navigation sensors on the glider measure heading, pitch, roll, depth, sliding mass position and the piston drive position. These readings are recorded and processed by the control computer. Vehicle position at the surface is determined by a GPS receiver, with the antenna located on the rear fin. Note that while submerged, the glider velocity and horizontal position are not sensed because of the difficulty in measuring these states.

While underwater, the glider navigates using a deduced reckoning algorithm. At present, the pitch angle and depth rate measurements and an assumed angle of attack are used by the onboard computer to estimate the horizontal speed of the glider. Pitch control, using

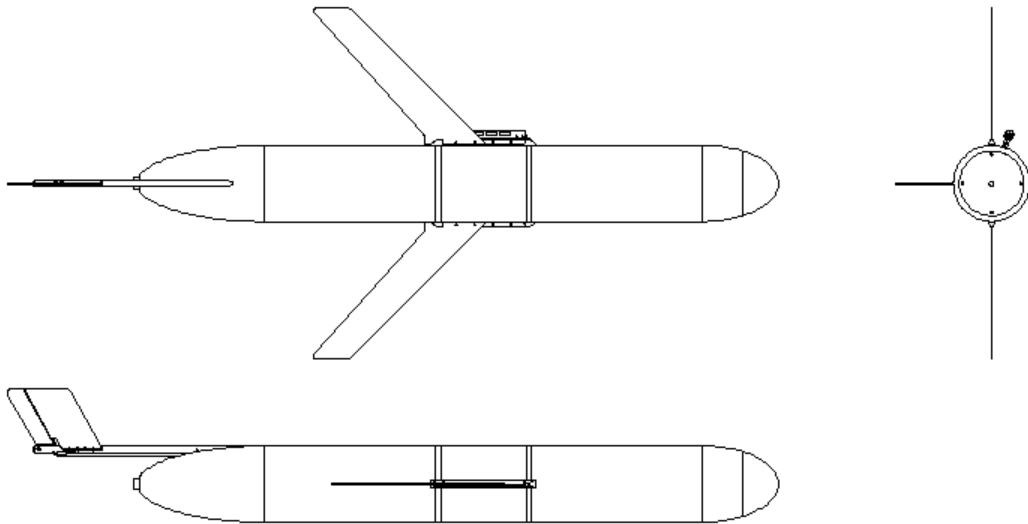


Figure 5.2: Slocum Electric Glider Layout [77].

the sliding mass, and heading control, using the rudder, use proportional feedback loops with deadbands and variable timing. The control is activated on a variable timing schedule depending on the heading and pitch error relative to the specified deadband.

The Slocum glider can be programmed to navigate in various ways. For a typical mission scenario the glider navigates to a set of preprogrammed waypoints specified by the operator. A mission file with these waypoints, desired glide path angles and speeds, control gains, deadbands, and other parameters, may be transmitted to the glider before the start of the mission. The glider is then capable of operating autonomously and navigating with dead reckoning and closed-loop pitch and heading control. A mission is composed of yos and segments. A yo is a single down/up cycle, while a segment can be composed of several yos and starts with a dive from the surface and ends with a surfacing. At all surfacings the glider tries to acquire its GPS location.

Other available modes of operation include gliding at a given compass heading, fixed

rudder angle or fixed battery position. A variety of operational modes were used in the work presented in this chapter, including gliding with fixed actuators and with full feedback and navigation.

5.1.2 Experiments with Slocum

We conducted glider in-water flight tests during January 2003 near Chub Key, Bahamas, using Slocum Glider WE01, owned and operated by Woods Hole Oceanographic Institution (WHOI), Woods Hole, MA. The principal investigator on this research cruise was Dr. David Fratantoni (WHOI). Operations were conducted from the RV Walton Smith of the University of Miami. Using glider WE01, we conducted a series of test glides including both steady and unsteady straight glides and steady and unsteady turning glides. The series of glides included glides with fixed internal mass and rudder positions and glides under feedback control. Glides with more dynamic behavior included controlled glides using waypoint navigation or fixed compass heading and controlled glides with a variety of feedback gains and deadbands.

The glider experiments conducted on the cruise were designed in advance for model verification and parameter identification. The hydrodynamic properties of the Slocum glider were estimated in advance using theoretical calculations and standard aerodynamic reference data. In order to collect the necessary data, we performed a set of glides including (1) steady glides at different pitch angles, and (2) glides that exhibit rich dynamic behavior such as unsteady turning and pitching with large actuator excursions. The design and schedule of the tests was intended to explore the full range of motions possible within the confines of the existing glider control system.

Table 5.1 shows the flight tests conducted, all using glider WE01. A typical flight test

Test	z (m)	Description
Vert 01	25	Test pitch performance. Adjust controller. Rudder ($\delta R = 0$).
Vert 02	50	Pitch test. Adjust pitch gain. Fixed ($\delta R = 0$).
Vert 03	50	Pitch with tuned gains. Fixed ($\delta R = 0$). Steady glide and turn.
Vert 04	50	Steeper pitch dive. Fixed \mathbf{r}_p and ($\delta R = 0$). Steady glide, turn.
Vert 05	50	Steep pitch dive. Different \mathbf{r}_p . Steady glide, turn.
06 to 11	0	Omitted because of operational constraints
Vert 12	50	Tuned pitch gains, \mathbf{r}_p lookup function. Controlled heading.
Vert 14	15	Repeat mission of Vert 04.
Vert 15	50	Controlled heading, pitch with tuned gains and lookup function.
Vert 16	50	Controlled pitch with tuned controller, fixed ($\delta R = 0$)
Vert 17	50	Pitch, heading with tuned gains. Steady turning glides.
Vert 18	50	Fixed \mathbf{r}_p and ($\delta R = 3.5^\circ$). Steady glides.
Vert 19	50	Fixed \mathbf{r}_p and ($\delta R = 2^\circ$). Steady glides.
Vert 20	50	Shallower pitch. Fixed \mathbf{r}_p . Controlled heading. Steady glides.
Vert 21	50	Fixed \mathbf{r}_p and ($\delta R = 4^\circ$). Steady glides.
Vert 22	50	Multi-segment mission. Waypoint following, tuned gains.

Table 5.1: Flight Tests at Sea with Slocum electric WE01. January 2003.

mission consisted of two glides to fifty meters depth, enough depth to reach equilibrium glides. The glider surfaced at the beginning and end of the mission for a GPS position fix and data transfer. Both fixed control glides and glides using pitch and heading feedback were conducted. During fixed control glides, the rudder and sliding pitch mass were held at pre-determined positions for the duration of each downwards and upwards glide. This resulted in the glider reaching a steady glide equilibrium corresponding to those control settings.

Although there are some disturbances and measurement noise in the data, the steady glides stand out plainly (see Figures 5.3 and 5.4). Automated scripts were used to select periods of steady gliding in the test data and compute the average values, over those intervals, of the navigational states and their derivatives. Only directly measured sensor data is used in computing the steady glides. Navigational states estimated by the vehicle dead reckoning navigation system are not used. As an example, time-averaged state values for

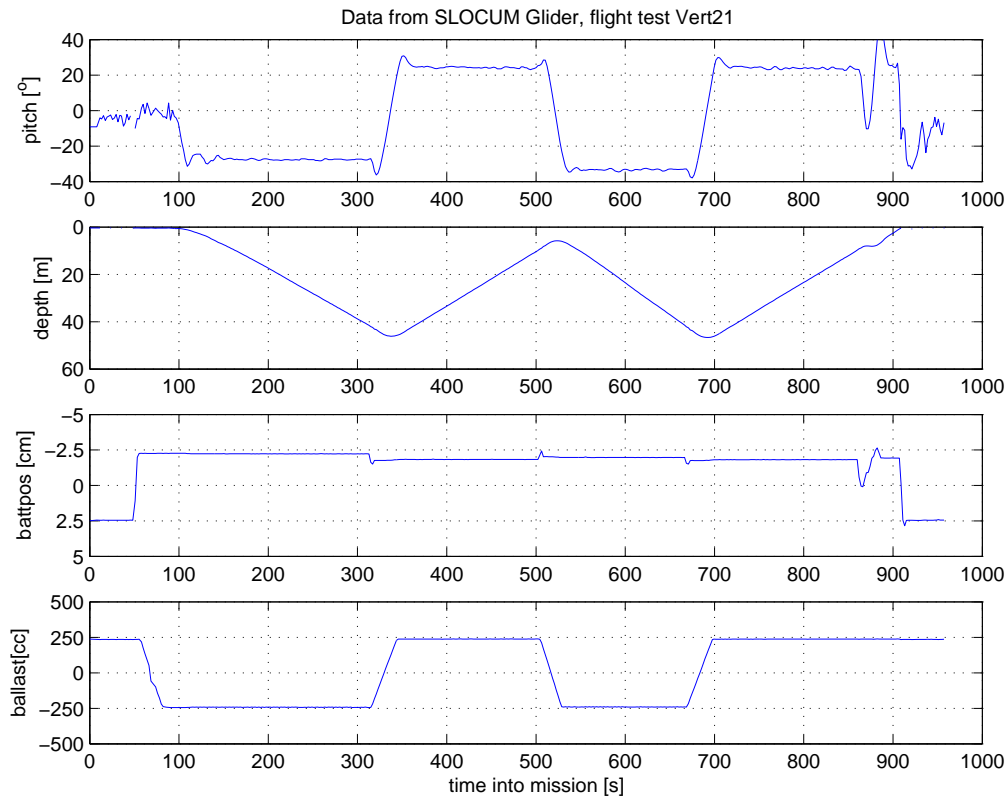


Figure 5.3: Slocum Data from Flight Test Vert 21.

four steady glides are shown in Table 5.2, as are values for α , V and drag coefficient $C_D(\alpha_{eq})$ by frontal area computed using methods described in Section 5.2.

There are a number of sources of uncertainty in the flight test data. As noted, the glider velocity and horizontal position are not measured. The currents in the area of operation are unknown. Estimates of the currents may be made using the model of the glider dynamics, but this cannot be used to determine the model parameters. Glider velocity and current are important because the hydrodynamic forces on the glider depend on the glider's speed relative to the water. Other sources of uncertainty in the glider data include the trim condition of the glider and the CG position. Some static roll offset appears in the data, i.e., the CG and static trim of the glider induced some static roll. Because of operational considerations during the cruise it was not possible to correct this trim or to obtain completely accurate

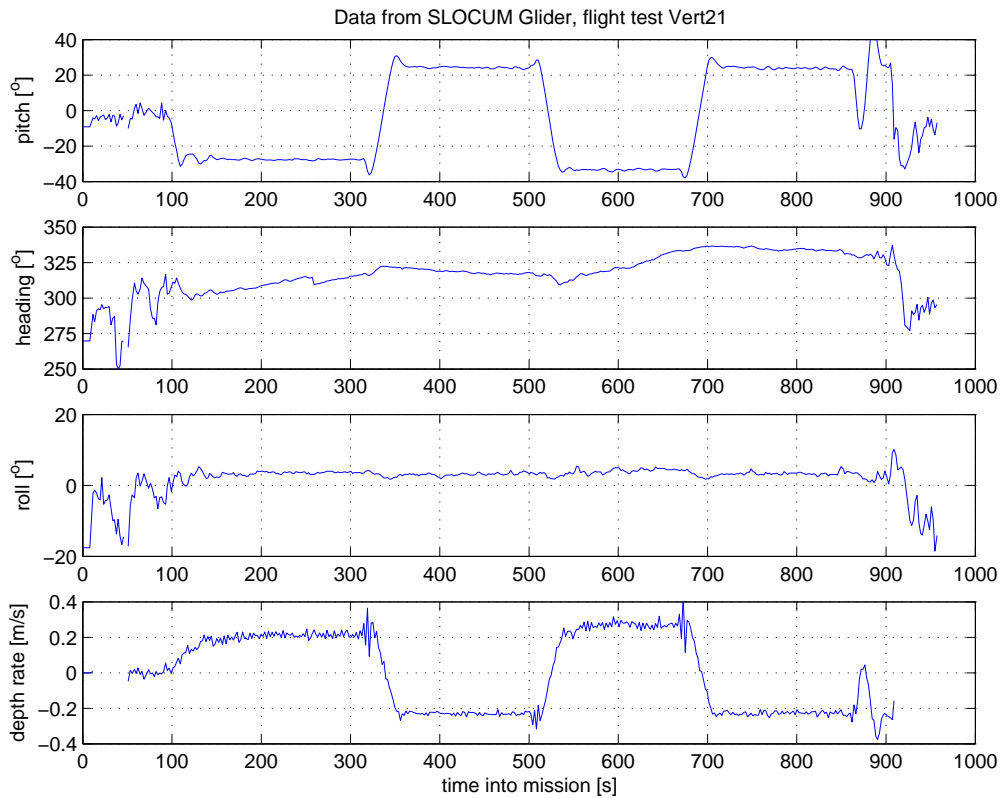


Figure 5.4: Slocum Data from Flight Test Vert 21.

static mass and trim measurements (in Section 5.2 a novel method is used to identify the glider buoyancy offset). The wings are made of a thin composite material which may deflect during flight and change the glider’s hydrodynamic performance. When at the surface to determine GPS position, the glider is subject to wind and current-driven drifting, and this leads to some uncertainty in the glider’s surfacing position (GPS position is not used for parameter estimation).

As mentioned above, the glider used in experiments had a slight static roll due to mis-trim. Because of this, the glider was slightly out of the longitudinal plane in flight. This is another possible source of error in the experimental analysis. The static roll produces a small yaw moment which is offset by a small rudder angle. This probably results in the glider flying with some sideslip angle. This could result in additional drag on the glider and

Avg. Value	Glide 1	Glide 2	Glide 3	Glide 4
Pitch θ (deg)	-22.77	23.74	-25.78	24.03
Depth rate \dot{z} (m/s)	0.168	-0.224	0.200	-0.228
Battery pos. (cm)	-2.4	-1.8	-2.3	-1.8
Ballast m_b (cc)	-244.4	237.3	-247.7	237.5
Rudder δR (deg)	2	4	2	5
Roll ϕ (deg)	3.34	3.23	3.81	3.38
Heading ψ (deg)	334	333	333	334
AoA α (deg)	2.7	-2.9	2.3	-2.9
Speed V (m/s)	0.388	0.499	0.425	0.503
Drag Coeff. $C_D(\alpha_{eq})$	0.27	0.31	0.25	0.31

Table 5.2: Example of Steady Glide Data. Flight Vert22_4 on Slocum Glider WE01.

possibly change the lift and moment on the glider in comparison with fully longitudinal, zero-sideslip flight (effects of sideslip angle are discussed further in the following section). These problems could be reduced in future flight tests by correcting the roll trim of the glider. Other asymmetries in the glider geometry also appear in the data. The glider is not laterally symmetrical. For example, the CTD located on the left side of the glider is a significant source of drag, resulting in some yaw moment on the glider. This is supported by the data from tests Vert 16 through Vert 21 using fixed rudder angles.

5.1.3 Slocum Model Planar Equilibrium Equations

In this section the glider model derived in Chapter 3 is adapted to model the Slocum glider design. This involves adjusting the parameters corresponding to the internal masses and the vehicle geometry.

The model parameters are adjusted to match the Slocum body and wing shape. In the electric Slocum design, control is applied to two masses inside the vehicle, the ballast mass and the sliding battery pack. We model this with control applied to two masses inside the vehicle: we control the mass of a point with fixed position in the body, representing

the ballast tank, and control the position of a mass with varying position within the body, representing the moving battery pack. The model describes the nonlinear coupling between the vehicle and the shifting and changing masses. The major forces on a glider are all incorporated into the model, including buoyancy, the moments and forces due to the internal moving mass, and quasi-steady hydrodynamic forces. Beginning with the Glider Equations (3.38), we set terms in the model for the Slocum ballast system location, the sliding mass range of travel, and the rudder. The aim of the model is to adequately match the dynamic performance of the glider while maintaining a level of simplicity in the model that allows for analytical work and design insight.

The internal masses used to model the Slocum design are the variable ballast mass m_b , the movable mass \bar{m} and a fixed mass m_w . These are shown in Figure 5.5 (and in Figure 3.4). In the Slocum design all three of these masses are confined to the glider $\mathbf{e}_1 - \mathbf{e}_3$ plane. The ballast system is located just behind the nose of the glider. The sliding battery pack mass moves in the fore-aft direction only, so r_{P3} and r_{P2} are fixed. The offset mass m_w is located behind the CB of the glider in order to provide the proper trim balance. The Slocum gliders are normally trimmed such that their pitch is level when the ballast and sliding mass are at the midpoints of their travel. This requires m_w to be aft of the CB. r_{w3} is determined by the static trim and bottom-heaviness of the glider.

Now consider this model specialized to the longitudinal plane (assumed invariant), as in Chapter 4, and solve for the equilibrium steady glides in the equations of motion. The resulting Slocum vertical plane equilibrium equations are

$$\dot{x} = v_1 \cos \theta + v_3 \sin \theta \tag{5.1}$$

$$\dot{z} = -v_1 \sin \theta + v_3 \cos \theta \tag{5.2}$$

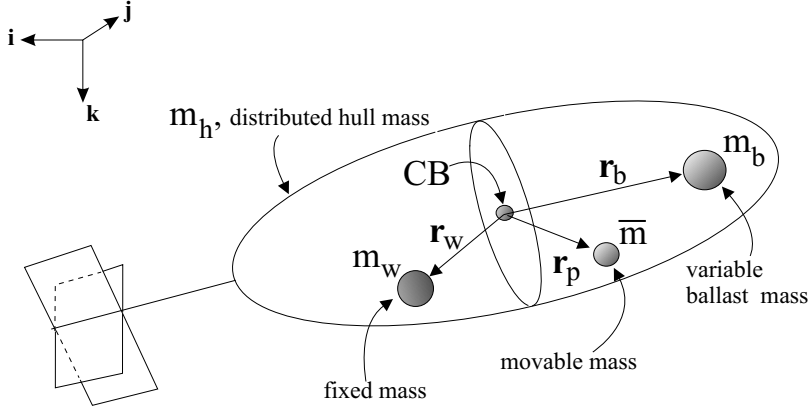


Figure 5.5: Glider mass definitions.

$$\begin{aligned}
0 &= (m_{f3} - m_{f1})v_{1eq}v_{3eq} - \bar{m}g(r_{P1eq} \cos \theta_{eq} + r_{P3eq} \sin \theta_{eq}) \\
&\quad - m_{beq}g(r_{b1} \cos \theta_{eq} + r_{b3} \sin \theta_{eq}) - m_w g(r_{w1} \cos \theta_{eq} + r_{w3} \sin \theta_{eq}) \\
&\quad + M_{DL_{eq}}
\end{aligned} \tag{5.3}$$

$$0 = L_{eq} \sin \alpha_{eq} - D_{eq} \cos \alpha_{eq} - m_{0eq}g \sin \theta_{eq} \tag{5.4}$$

$$0 = L_{eq} \cos \alpha_{eq} + D_{eq} \sin \alpha_{eq} - m_{0eq}g \cos \theta_{eq} \tag{5.5}$$

where the subscript eq denotes the state at equilibrium steady glide. v_1 and v_3 are the components of the glider velocity in the \mathbf{e}_1 and \mathbf{e}_3 directions, respectively, as shown in Figure 3.1. Here, θ is pitch angle, α is the angle of attack, D is drag, L is lift and M_{DL} is the viscous moment as shown in Figure 4.3. m_{f3} and m_{f1} are the added mass terms corresponding to the \mathbf{e}_1 and \mathbf{e}_3 directions, as derived by Kirchhoff [39]. In these equations, as in [42], we take the added mass cross terms to be zero. We note that equilibrium terms corresponding to the offset mass m_w and the location \mathbf{r}_b of the ballast mass m_b do not appear in [42].

As presented in Chapter 3 and shown in Figure 5.6, we denote the glide path angle by ξ where $\xi = \theta - \alpha$. At equilibrium, it may be shown that $\xi_{eq} = -\tan^{-1} \left(\frac{D_{eq}}{L_{eq}} \right)$. We also

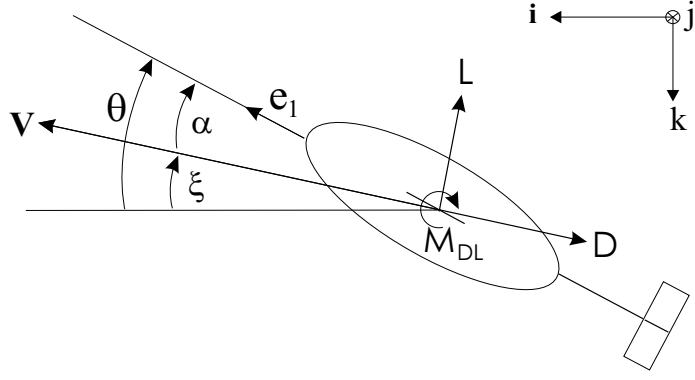


Figure 5.6: Lift and drag on glider.

denote the glider speed by V where $V = \sqrt{(v_1^2 + v_3^2)}$. Using equation (4.2) and our angle definition in Figure 5.6, we can write the glider depth rate as

$$\dot{z} = -V \sin(\xi) = -V \sin(\theta - \alpha). \quad (5.6)$$

The quasi-steady hydrodynamic forces and moment in the vertical plane are modelled as

$$D = \frac{1}{2} \rho C_D(\alpha) A V^2 \approx (K_{D_0} + K_D \alpha^2)(v_1^2 + v_3^2) \quad (5.7)$$

$$L = \frac{1}{2} \rho C_L(\alpha) A V^2 \approx (K_{L_0} + K_L \alpha)(v_1^2 + v_3^2) \quad (5.8)$$

$$M_{DL} = \frac{1}{2} \rho C_M(\alpha) A V^2 \approx (K_{M_0} + K_M \alpha)(v_1^2 + v_3^2) \quad (5.9)$$

as described in Section 3.2.7. A method for determination of the coefficients from flight data is described in Section 5.2.

Determining a model for moment on the vehicle body is challenging. Different sources of reference data may predict significantly different moments on the vehicle. This results in part from the sensitivity of the moment to small changes in the vehicle geometry and to small differences in the flow on the fore and aft of the body. Other coefficient models for the moment could be used, for example one depending on α^3 . Some latitude is available

when choosing the moment model to fit experimental data.

This quasi-steady hydrodynamic model is expected to be accurate for equilibrium steady glides. It may be less accurate away from equilibrium glides and when the glider experiences high accelerations or angular rates. The hydrodynamics of the flow about the glider are much more complex during such motions, requiring a more complex hydrodynamic model. In the case of our initial analysis and the standard mission use of the Slocum glider, the majority of the operational time is spent at steady glides. Transitions and inflections between steady glide equilibria are relatively slow. Because of this, the quasi-steady hydrodynamic model may prove satisfactory for our analysis. Incorporating a more complex hydrodynamic model involves adding terms to the lift, drag and moment model. Experimental data and results of simulations using the glider model suggest that some angular damping should be included in analysis of dynamic motions. This does not affect the planar equilibria.

Chapter 4 included an analysis of the equilibrium steady glide equations for a generic glide. One interesting property of the equilibrium steady glide equations is that the glide path angle is independent of the glide speed. Glide path angle depends only on the equilibrium angle of attack. When choosing an equilibrium glide, it is possible to specify the glide path angle and glide speed V independently. The glide speed can be set by fixing the net buoyancy of the glider.

Determining the steady glides for a glider such as the Slocum requires finding the set of model parameters that describe the glider mass and hydrodynamic characteristics. This is described in Section 5.2. Using one method, the hydrodynamic coefficients of the glider are estimated using reference data for ships, submarines and standard shapes. With these estimated coefficients, the equilibrium equations may be used to compute the set of steady glide conditions for the Slocum glider. Figure 5.7 shows the steady glide angles given the

estimated lift and drag parameters. Figure 5.8 shows the steady glide speeds given the same estimated parameters. The estimated hydrodynamic coefficients are $c_L(\alpha) = 7.55\alpha$ and $c_D(\alpha) = 1.4 + 0.12\alpha^2$, by area. The cross sectional area is $A = 0.0355\text{m}^2$ and $\rho = 1000\text{kg/m}^3$, giving parameters $K_{D_0} = 2.15 \text{ kg/m}$, $K_D = 24.95 \text{ kg/m}$, $K_{L_0} = 0 \text{ kg/m}$, $K_L = 132.55 \text{ kg/m}$, used to generate these figures. The maximum net buoyancy is $m_0 = 250 \text{ g}$.

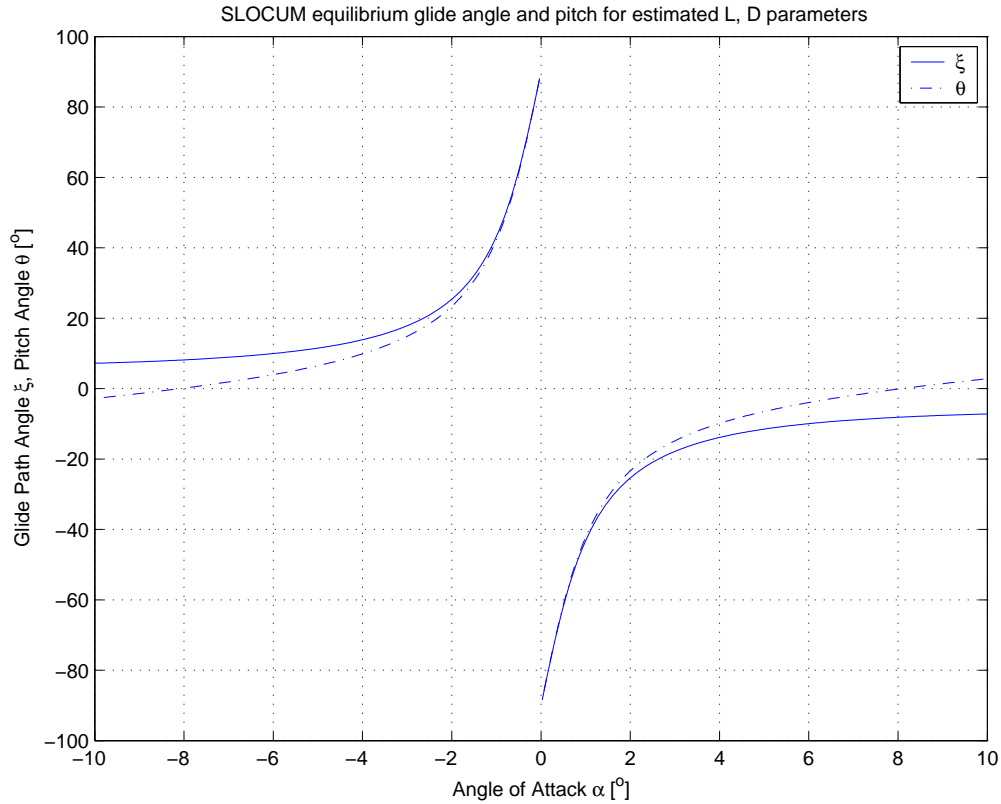


Figure 5.7: Equilibrium glides using lift and drag estimated from reference data.

5.2 Parameter Identification

We wish to determine the model parameters matching the Slocum model equilibria Equations (4.1)-(5.5) to the steady glides from experimental data. These parameters represent the physical variables corresponding to the glider's mass, inertia and hydrodynamic characteristics. The parameters that appear in the steady glide equations are the displacement

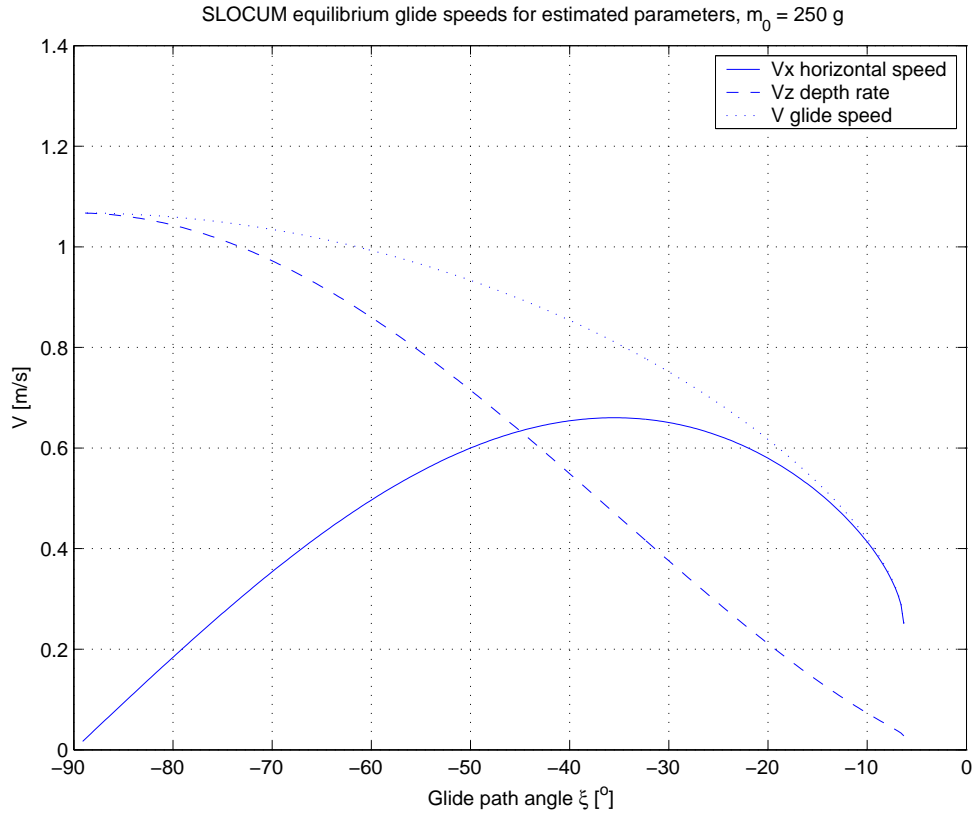


Figure 5.8: Equilibrium speed using lift, drag, estimated from reference data.

m , the masses m_h , m_w , and \bar{m} , the positions \mathbf{r}_b and \mathbf{r}_w of the ballast mass and offset mass, and the hydrodynamic parameters K_{D_0} , K_D , K_{L_0} , K_L , K_{M_0} , K_M , m_{f3} and m_{f1} .

Parameters corresponding to mass and inertia may be measured directly. The mass and buoyancy trim of the glider can be measured by weighing the glider in air and in water. The position of the glider CG may be determined through direct experimental measurement. The position of the CB is the centroid of the displaced volume of water, and can be computed from direct measurements or from the glider geometry. Other mass parameters can be determined using similar methods. The inertia characteristics of the glider can be measured several ways; one way is the bifilar pendulum method, which measures the glider's frequency of oscillation in a pendulum apparatus. Note that the moment of inertia does not appear in the equilibrium equations.

If direct measurement is not possible, for example when a glider is already at sea, it may be possible to determine some of these parameters through analysis of glider data and by comparison of several equilibria. For example, in Section 5.2.2 we describe a method to identify a glider’s buoyancy trim offset from flight test data, and in Section 5.2.3 we use an analogous method to identify the glider static pitch trim.

A variety of methods were used to determine the model hydrodynamic parameters, including reference hydrodynamic data for generic shapes, aircraft, ships and submarines, computational fluid dynamics (CFD) analysis, wind tunnel data, and flight test data. An extensive selection of references is available, including [26, 27, 39, 55]. Because the hydrodynamic parameters are sensitive to small changes in the vehicle geometry, it is challenging to determine these parameters so that they accurately match flight data.

We first estimated hydrodynamic parameters for lift, drag and moment for the Slocum geometry using reference data. This involved calculating the hydrodynamic forces on each of the glider components using theoretically and experimentally determined reference data. These parameters were compared to the results of preliminary wind tunnel tests conducted at Princeton [4]. More accurate wind tunnel tests were also designed using the methods of [49]. These may be conducted as part of future research. In addition, calculations of glider hydrodynamic characteristics using CFD analysis appear in [32].

Solving Equation (5.6) for V gives

$$V = \left| \frac{\dot{z}}{\sin(\theta - \alpha)} \right|. \quad (5.10)$$

Substituting Equation (5.10) and the hydrodynamic coefficients (5.7), (5.8), and (5.9)

into Equations (5.4) and (5.5) gives us

$$0 = \frac{1}{2}\rho C_L(\alpha_{eq})A \left(\frac{\dot{z}_{eq}}{\sin(\theta_{eq} - \alpha_{eq})} \right)^2 \sin \alpha_{eq} - \frac{1}{2}\rho C_D(\alpha_{eq})A \left(\frac{\dot{z}_{eq}}{\sin(\theta_{eq} - \alpha_{eq})} \right)^2 \cos \alpha_{eq} - m_{0_{eq}}g \sin \theta_{eq} \quad (5.11)$$

$$0 = \frac{1}{2}\rho C_L(\alpha_{eq})A \left(\frac{\dot{z}_{eq}}{\sin(\theta_{eq} - \alpha_{eq})} \right)^2 \cos \alpha_{eq} + \frac{1}{2}\rho C_D(\alpha_{eq})A \left(\frac{\dot{z}_{eq}}{\sin(\theta_{eq} - \alpha_{eq})} \right)^2 \sin \alpha_{eq} - m_{0_{eq}}g \cos \theta_{eq}. \quad (5.12)$$

These equations include measured quantities \dot{z} , θ and m_0 . Angle of attack α is a function of v_1 and v_3 and is not sensed. Hydrodynamic coefficients $C_L(\alpha)$ and $C_D(\alpha)$ have been estimated but are not known exactly. These estimates, however, do yield forces in the form (5.7) and (5.8). Substituting (5.7) and (5.8) into (5.11) and (5.12) gives two equations with four parameters K_{D_0} , K_D , K_{L_0} , K_L and unknown α .

In the following, we use an existing estimate of the value of lift parameters and then determine drag parameter values consistent with the flight test data. This is necessary because of the limited number of states available from the glider sensor suite. Angle of attack or velocity data would allow us to determine more parameters from experimental data, as discussed in Section 5.3.

5.2.1 Lift

The Slocum glider body is symmetric from top to bottom and the wings are symmetrical flat plates. From this, the reference methods show that lift should be zero at angle of attack $\alpha = 0$ and should be antisymmetric about $\alpha = 0$. We compared estimates of the lift coefficient of the glider from three sources: aerodynamic reference data, CFD analysis from [32], and preliminary wind tunnel data. These estimates are reasonably close to one

another. The lift coefficient from [32] was computed using the most advanced methods, so we use this estimate for $C_L(\alpha)$ by frontal area:

$$C_L(\alpha) = 11.76 \alpha + 4.6 \alpha|\alpha| \quad (5.13)$$

where α is in radians. Note that this is close to, but not exactly, linear in α as modelled in (5.8).

Equations (5.11) and (5.12) may be rearranged, given glider lift coefficient (5.13) and the steady-glide-test sensor data described in Section 5.1.2. Solving (5.12) for drag D_{eq} and substituting into (5.11) gives

$$0 = L_{eq} \sin \alpha_{eq} - m_{0_{eq}} g \sin \theta_{eq} - \left(\frac{L_{eq} \cos \alpha_{eq} - m_{0_{eq}} g \cos \theta_{eq}}{\sin \alpha_{eq}} \right) (\cos \alpha_{eq}),$$

$$\text{where } L_{eq} = \frac{1}{2} \rho C_L(\alpha_{eq}) A \left(\frac{\dot{z}_{eq}}{\sin(\theta_{eq} - \alpha_{eq})} \right)^2.$$

Given the steady glide data from flight tests, determined in Section 5.1.2, this equation may be solved for the equilibrium angle of attack α_{eq} for each steady glide (using time averaged steady glide states like those shown in Table 5.2).

5.2.2 Drag

In this section we determine a drag coefficient for the glider given the lift estimate (5.13), such that steady glides computed with the equilibrium equations are consistent with flight test data. Because of the limited sensor data available from flight tests, it is not possible to estimate the glider's lift and drag coefficients independently from the flight data alone. Instead, a method is adopted which takes the lift estimate (5.13) to be the best available

lift estimate and then uses flight test data to determine the drag estimate. We describe first an analysis using the buoyancy tank ballast m_b as the glider net buoyancy m_0 . This yields a $C_D(\alpha)$ that is inconsistent with our expected drag in both form and magnitude, as discussed below. We then describe a method used to identify a static buoyancy trim offset in the test glider. The buoyancy trim offset is then used to compute a $C_D(\alpha)$ that is more consistent with theoretical and other predictions.

Drag estimates calculated using aerodynamic reference methods or preliminary wind tunnel tests each predict that glider drag coefficient $C_D(\alpha)$ will have the form given in equation (5.7). Because of the glider's symmetrical design, drag should be symmetrical (an even function) with respect to angle of attack, with the minimum (profile) drag at zero angle of attack.

Using Equation (5.11) or (5.12), one can solve for $C_D(\alpha_{eq})$ given data for a steady glide and the lift and angle of attack from Section 5.2.1. Figure 5.9 shows the drag coefficient determined using this method for ten of the steady glides in data from tests Vert 18 through Vert 22. Each point on the plot corresponds to the coefficient of drag calculated for one steady glide.

Note that glides with positive angle of attack α , which are glides downwards, appear to have much higher coefficients of drag than the group of glides upwards glides with negative angles of attack. This result is not consistent with any of the estimates for the glider drag dependence on α . Our reference calculation of drag predicts a parabolic drag dependence on angle of attack. The drag shown is also higher than the predicted drag.

One possible explanation for the differences between upwards and downwards glide is that the glider actually has an asymmetrical drag curve. Some elements of the glider geometry are asymmetrical from top to bottom, including the CTD sensor located below

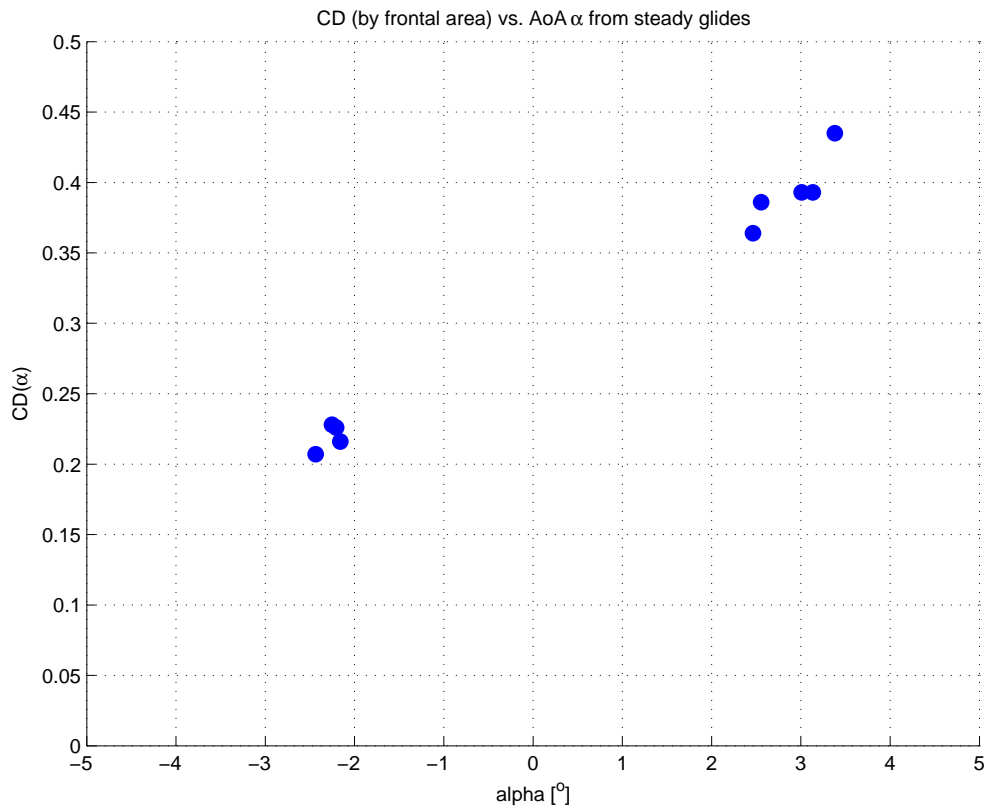


Figure 5.9: C_D computed from equilibrium glide data assuming no buoyancy trim offset.

one of the wings and the vertical tail. However, these items are small compared to the glider body and wings, both of which are symmetrical, so it is not expected that these small differences would account for such a large difference in the drag. Regardless of this asymmetry, drag is still expected to be close to minimum at zero angle of attack.

The simplest and the most obvious explanation for the difference between the upwards and downwards glides is an offset in the glider buoyancy trim. This is consistent with a difference in depth rate between upwards and downwards glides in the flight test data. This buoyancy offset can be found using the symmetry of the glider and lift coefficient to compare upwards and downwards glides at the same magnitude pitch angles. As noted, because of the symmetrical design of the glider, the lift curve is an odd function with respect to angle of attack and the drag curve is expected to be an even function (see Figure 5.7).

Glides conducted at the same magnitude pitch angle upwards and downwards should have the same magnitude glide path angle ξ_{eq} and angle of attack α_{eq} . Given the symmetry in lift and drag, and our approximation to the longitudinal plane, differences in velocity between these glides are caused by differences in the driving buoyant force. By comparing such glides in the flight test data, we estimate the trim offset in the glider buoyancy.

First we substitute $m_{0_{eq}} = m_{b_{eq}} + \Delta m_0$ into equation (5.14). Using the steady glide data, we estimate the buoyancy trim offset Δm_0 by requiring glides with the same $|\theta_{eq}|$ to have the same $|\alpha_{eq}|$. This involves solving for α_{eq} for each of the symmetrical glides as a function of Δm_0 and determining the Δm_0 for equal $|\alpha_{eq}|$. Using the available data, we estimate the buoyancy trim offset to be $\Delta m_0 = -73$ grams. This means that, for the water density and the weight of the glider WE01 during these tests, the glider is 73 grams light (positively buoyant) when the ballast tank is set at the half full “zero buoyancy” point. This corresponds to ballast = 0 in the glider data and to $m_b = 250$ in the glider dynamic model. When this buoyancy trim offset is not accounted for, as shown in Figure 5.9, it appears that there is more drag going down (i.e., it is harder to go down) and less drag going up (i.e., easier).

Substituting $m_{0_{eq}} = m_{b_{eq}} + \Delta m_0$ into equations (5.11) or (5.12), $C_D(\alpha_{eq})$ may be computed for each steady test glide (see Figure 5.10).

A least-square fit of the data, assuming drag of the form (5.7), gives drag parameter

$$C_D(\alpha) = 0.214 + 32.3 \alpha^2. \quad (5.14)$$

where α is in radians. As shown in Figure 5.10, the steady-glide data points are close to a parabolic function of angle of attack α and are symmetrical about $\alpha = 0$. These properties

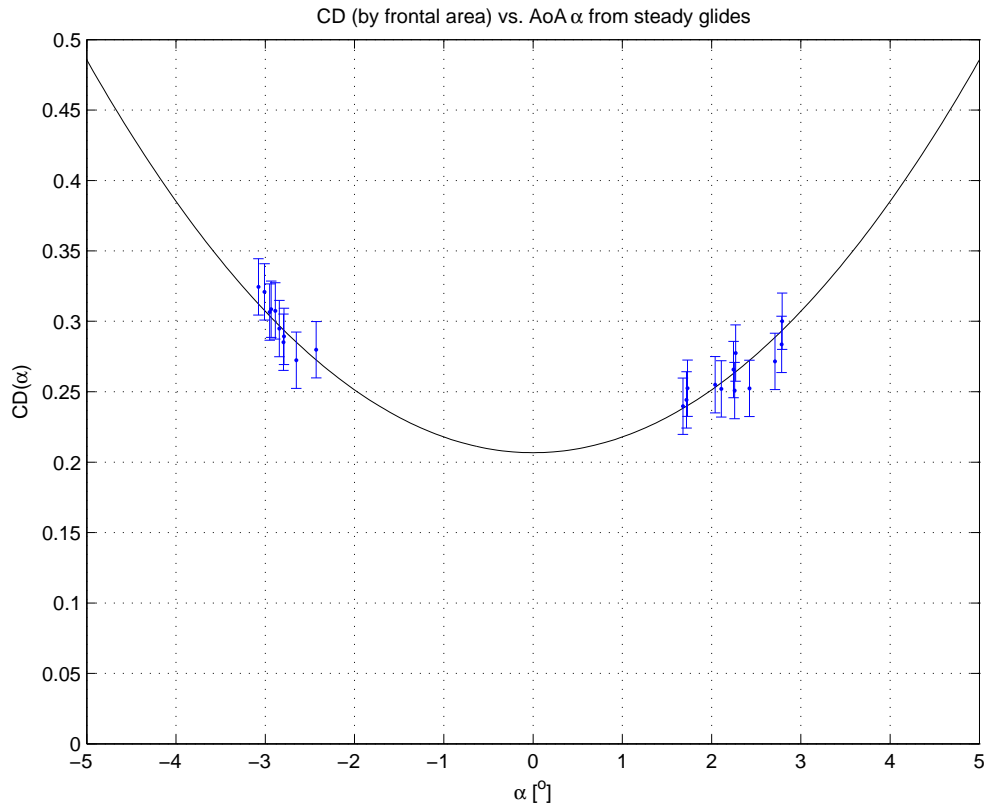


Figure 5.10: C_D computed from equilibrium glide data assuming buoyancy trim offset of -73 grams.

are consistent with the expectations from our reference calculations for drag.

The magnitude of the drag least-squares fit (5.14) is about 75% greater, at $\alpha = 0$, than the drag calculated from references, and as much as 150% greater at $\alpha = -3^\circ$. This suggests that the drag estimates from reference data and CFD analysis are too low. This is not unusual when comparing drag estimates to experimental data.

There are several possible explanations for the difference between the drag found here and the drag predictions using reference calculations. One explanation is that the drag model is based on an ideal geometric model and does not include variations in the geometry (e.g., surface roughness, wing deformation, small protrusions, etc.). The model therefore provides a drag estimate that is lower than the measured drag. It is also difficult to accurately predict drag on the Slocum's CTD sensor because of its complex geometry and

position on the hull. Wind tunnel experiments performed during design of Seaglider [14] indicate that a toroidal conductivity sensor with “about 2% of the frontal cross sectional area of the [glider body] accounted for more than 25% of the total drag”. It is unlikely that variation in the drag on the CTD sensor alone should produce the differences between the predicted and observed drag profiles for Slocum, but this illustrates the sensitivity of the drag to small variations in geometry. The Reynolds number range in which the gliders operate may also play a role in this sensitivity.

Another explanation for the high drag shown in the data is that the steady glides measured in the flight data deviate from the longitudinal plane. This is highly probable because of the glider static roll mis-trim and other asymmetries in the glider geometry. These produce a yawing moment on the glider. Data from flight tests with fixed rudder angle $\delta R = 0$, for example Vert 16, show small heading rates in steady glides (less than twenty degrees over 100 s). This suggests that these steady glides are at some small sideslip angle and that the effects of the small roll and sideslip angles and of the glider’s lateral asymmetries on the glider yaw rate are small. Because the glider has no sideslip and angle of attack sensors, the order of the sideslip angle must be estimated from other sensor data. It is possible that this sideslip angle due to the static roll is of the same order of magnitude as the angle of attack, and may account for the differences between the expected and estimated drag. The difference may also be explained by a combination of these factors. This is a continuing subject of analysis.

In other test glides, including Vert 18, 19 and 21, the rudder was fixed at a small angle to counteract the yaw moment on the glider due to roll and asymmetries. Because of rudder-roll interaction and asymmetries in the yaw moment on the glider between up and down glides, a different rudder angle is needed to maintain a constant heading in upwards glides than

is needed in downwards glides. In tests Vert 20 and Vert 22, rudder control with feedback gains, determined using the results of previous flight tests, was used to stabilize a fixed heading glide (Vert 20) and as part of waypoint following navigation (Vert 22). This gave acceptable heading performance and demonstrated differences in rudder actuation between upwards and downwards glides.

Differences in the sideslip and roll angles and other asymmetries in the glider and the resulting out-of-plane motion may also account for the differences in the distribution of the drag data points shown in Figure 5.10. The cluster of data points at negative angles of attack is more tightly clustered and covers a smaller range in α than those at positive α . Other variables including the glider pitch control system determined the α of different steady glides.

Using the hydrodynamic coefficients determined from the data, the equilibrium equations may be used to compute a new set of steady glide conditions, analogous to those computed for Figures 5.7 and 5.8 using the estimated parameters. Figure 5.11 shows the steady glide angles given the parameters identified from the data. Figure 5.12 shows the steady glide speeds given the same identified parameters. For a 25° glide angle, the identified parameters yield a depth rate of 20 cm/s and a horizontal speed of 42 cm/s, as can be seen from Figure 5.12. This is consistent with estimates from glider operations conducted by Webb Research Corporation and WHOI.

5.2.3 Pitch Moment

To compute the hydrodynamic moment on the glider during steady flight, we use Equation (5.3). The moments due to the internal mass, the ballast tank and the offset mass may be computed from the steady-glide sensor data. The term $(m_{f3} - m_{f1})v_{1eq}v_{3eq}$ represents

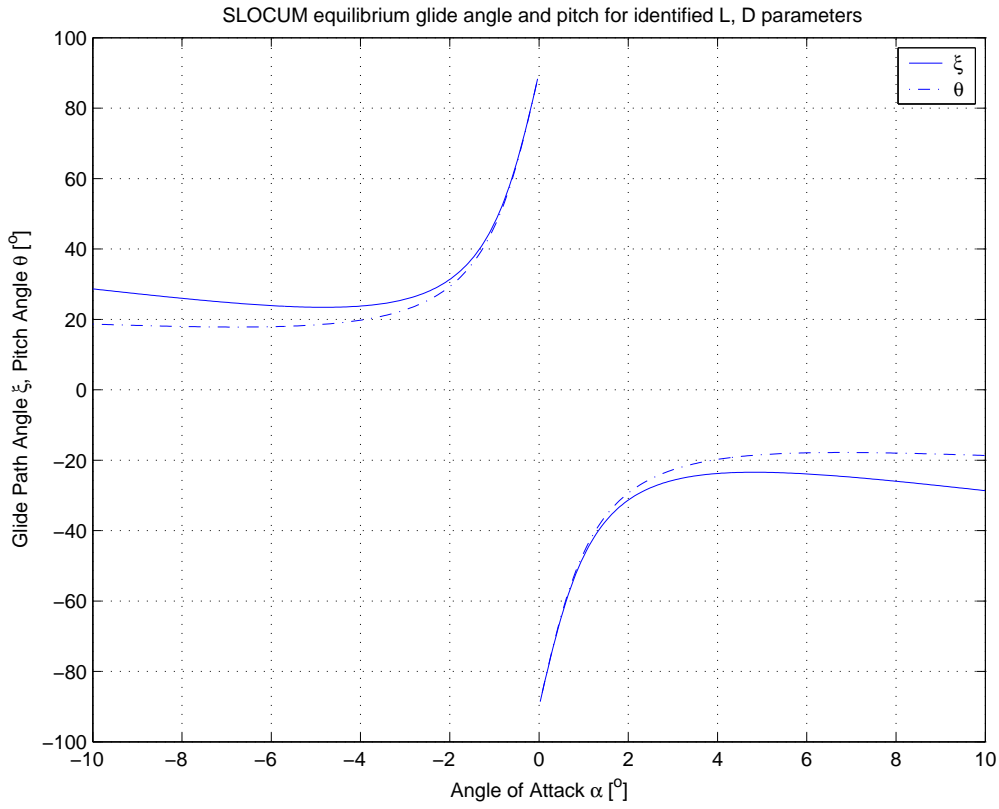


Figure 5.11: Equilibrium glides using Lift, Drag fit to glide data

the moment due to the glider's added mass at equilibrium and $M_{DL_{eq}}$ is the remainder of the total hydrodynamic moment on the glider. For the steady-state analysis, we will group these terms together in $C_{M_{total}}(\alpha)$ as

$$\frac{1}{2}\rho AV^2 C_{M_{total}}(\alpha) = (m_{f3} - m_{f1})v_{1_{eq}}v_{3_{eq}} + M_{DL_{eq}}. \quad (5.15)$$

Substituting (5.15) into Equation (5.3) and rearranging gives

$$\begin{aligned} \frac{1}{2}\rho AV^2 C_{M_{total}}(\alpha) &= (\bar{m}g(r_{P1_{eq}} \cos \theta_{eq} + r_{P3_{eq}} \sin \theta_{eq}) + m_{b_{eq}}g(r_{b1} \cos \theta_{eq} + r_{b3} \sin \theta_{eq}) \\ &\quad + m_w g(r_{w1} \cos \theta_{eq} + r_{w3} \sin \theta_{eq})) \end{aligned} \quad (5.16)$$

which may be solved for $C_{M_{total}}(\alpha)$ given the steady glide flight data.

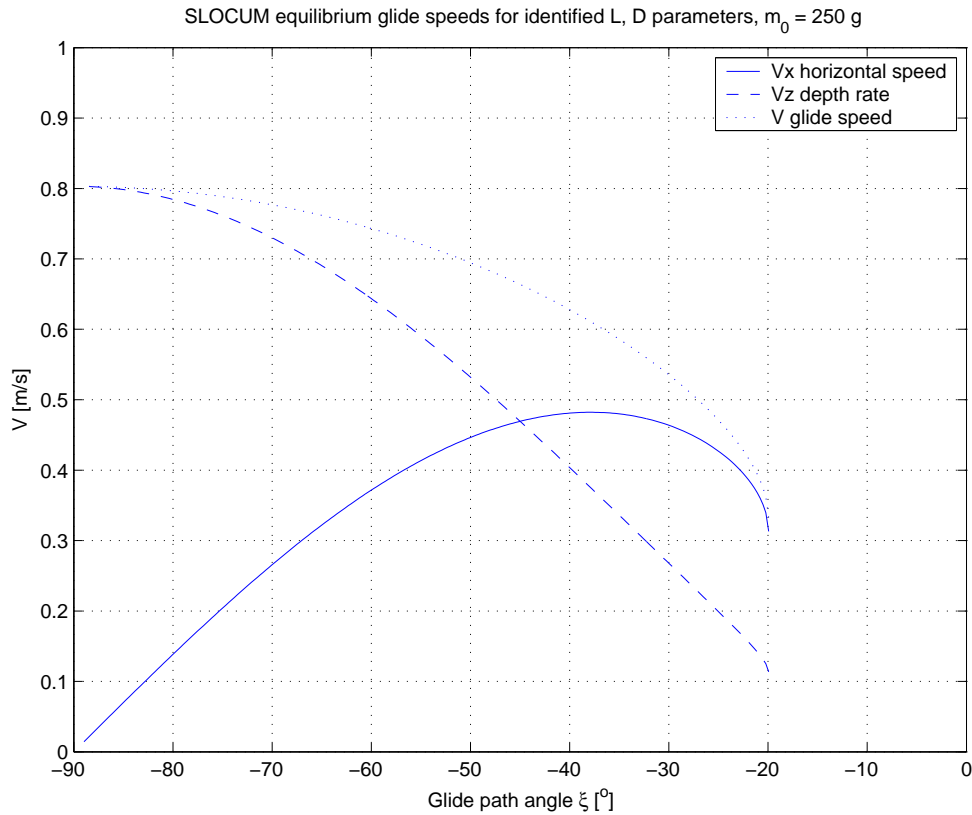


Figure 5.12: Equilibrium speed using Lift, Drag fit to glide data.

Before a glider is deployed in the ocean, instruments may be installed or moved and static trim weights may be manually positioned within the hull to adjust the glider's trim. This changes the mass and trim of the glider. In the model, the uniformly distributed hull mass m_h and the offset mass m_w are used to represent the distribution of fixed components in the glider. The position of the offset mass may be determined using static measurements during trimming of the glider before launch, or calculated from flight test data. Before launch the Slocum gliders are trimmed manually using a static buoyancy tank. The glider ballast tank is set to half-full and weights are adjusted within the hull to make the glider neutrally buoyant and level. Using data from the static trim process, we may determine m_w and r_w by solving Equation (5.3) with $v_1 = 0$ and $v_3 = 0$. The mass and position of the ballast and sliding mass are determined from flight test sensor data.

In some cases, as discussed in Section 5.2.2, it may not be possible to measure the static trim of the glider. In this case it is possible to determine the mass offset r_{w1} , given r_{w3} and a set of data from symmetrical steady glides up and down. Using a method of comparison analogous to that in Section 5.2.2, we use the symmetry of the glider to compare upwards and downwards glides at the same pitch angle. To estimate r_{w1} we use the sensor state data from these glides and first compute the moment due to internal masses (as a function of unknown r_{w1}) for each glide. This is set equal to the hydrodynamic moment according to (5.3) for each glider. We then equate the magnitude of the moment coefficients for an upward glide and a downward glide corresponding to the same pitch angle magnitude and solve for r_{w1} . For Glider WE01 as trimmed in these tests, this analysis gives $r_{w1} = -0.093$ m.

Once we have determined the internal masses and positions, we may solve for $C_M(\alpha)$ for each glide in our set of steady glides. The result and a least squares fit are shown in Figure 5.13.

The least-square linear fit of this data, with $C_{M_{total}}(\alpha = 0) = 0$ because of the symmetry of the glider, is

$$C_{M_{total}}(\alpha) = 0.63 \alpha,$$

where α is in radians.

The hydrodynamic moment on the glider is small compared to the moments due to the internal masses. The moment due to the ballast and sliding mass together is around 35 N·m in the nose-down direction. The offset mass, located behind the vehicle CB, provides a countering nose-up moment. At equilibrium, the hydrodynamic moment is the difference

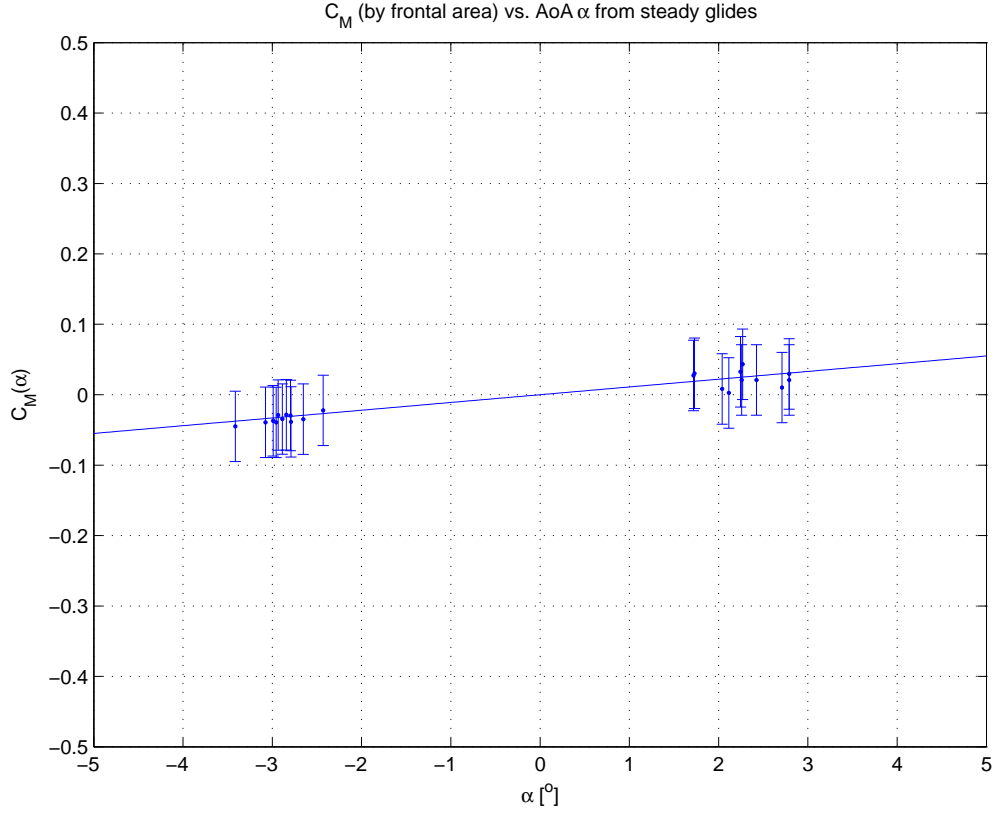


Figure 5.13: $C_{M_{total}}$ computed from equilibrium glide data.

between these moments, as shown in Equation (5.16). We estimate the hydrodynamic moment to be of the order 0.1 N·m or less. Because this moment is small in magnitude compared to the static mass moments, small uncertainties in the positions of the internal masses result in relatively large uncertainties in the moment coefficient. Note that variation in $C_{M_{total}}(\alpha)$ could still yield plots lying within the error bounds shown in Figure 5.13. These include variations in the form of $M_{DL_{eq}}$, for example, modelling it as cubic in α . The data may also be fit with a $C_{M_{total}}(\alpha)$ of the form in Equation (5.15), which may be rearranged to give

$$C_{M_{total}}(\alpha) = \frac{2}{\rho A}((m_{f3} - m_{f1}) \cos \alpha_{eq} \sin \alpha_{eq} + M_{DL_{eq}}).$$

This still gives a $C_{M_{total}}(\alpha)$ that is close to linear with respect to α about $\alpha = 0$.

Effects due to glider motion out of the longitudinal plane in some flight tests will also influence the accuracy of the analysis, as noted in Section 5.2.2. In order to determine the glider coefficient of moment more accurately, other methods such as wind tunnel tests and CFD analysis may be employed. Flight tests with more complete instrumentation should also be useful. The relatively small hydrodynamic moment means that, for gliders like Slocum travelling at low velocities, the pitching effect of the internal mass controls can easily overcome the vehicle hydrodynamic moment.

5.2.4 Identifying Unsteady Parameters

Once the equilibrium steady glides are matched, a set of parameters in the dynamic equations remains to be identified. The remaining unknown parameters are those that are not uniquely identified by matching the equilibrium steady glides, and those parameters that appear only in the dynamic equations of the vehicle and not at the equilibria. These include m_{f1} , m_{f3} , J_{f2} , and any hydrodynamic forces depending on Ω or $\dot{\alpha}$, for example, damping terms in moment M_{DL} .

One possible approach for identifying these parameters makes use of the nonlinear parameter estimation methods described in [65]. This makes use of an iterative numerical search procedure. The cost function to be minimized is a function of the square of the difference between the flight test data and the glider model output given the known control inputs and the measured states. An initial trial point for the search is the unsteady parameter values estimated using reference data or CFD analysis. The search direction may be determined by a direct search or gradient search procedure. Criteria for termination of the search may be based on the change in the cost function, magnitude of the gradient, or the change in the trial point between iterations. The search should be limited to reason-

able values of the glider parameters, for example, positive added masses and inertias within some range of existing estimates. The analysis is work in progress. It is limited by the experimental data available. It is possible that improved experimental data is required for this method to accurately identify the model parameters.

One concern when using this method is determining the correct set of parameters, i.e., those corresponding to their real physical values, as opposed to a set of parameters that only match a given set of experimental data. The iterative methods used are not guaranteed to give a unique solution for the set of parameters. The accuracy of the solution may depend on the quality and variety of experimental data matched. Flight tests data including the full range of glider dynamic motions and more comprehensive sensor data are desirable.

The range of possible motions in the flight tests was constrained by the glider control system, which is designed to stabilize a specific range of steady gliding motions. It is not possible for this system to provide persistent excitation or any significant variety of control inputs. In the case of oceanographic gliders this may be a minor concern. If the glider operation will consist almost entirely of a few specific gliding motions it may be sufficient, for that application, to identify the model parameters by matching data from those types of motions.

5.3 Remarks on These Methods

The method, in Section 5.2.2, for determining the static buoyancy trim offset of the glider could possibly be adapted to trim the glider at the beginning of a deployment and to detect system changes in the glider during deployment. Possible system faults in the glider that could occur during a mission include (1) fouling by seaweed, (2) taking on water through a small leak in the hull, and (3) a problem with the ballast system. These faults could be

detected and distinguished using the methods described here by comparing upwards and downwards glides.

Given an accurate set of model parameters, such faults may also be detected using a variety of other methods. These could make use of the glider model with nominal parameter values and compare the glider's performance to its nominal performance. Experience during flight tests suggests that certain problems, such as decreasing ascent speeds in sequential dives, indicate a problem with the glider buoyancy that could lead to loss of the vehicle. Even given the limited sensor suite available during normal deployments, it should be possible to monitor the vehicle with on-board software to detect such problems. Some faults, such as fouling by seaweed, could possibly be corrected without retrieval of the vehicle, for example, by maneuvering the glider to glide backwards or in an unsteady manner that shakes the seaweed loose. Other problems may require retrieval of the glider. In this case the glider may be required to stay on the surface and its motion limited to drifting with the current. Software on the Slocum glider already monitors the battery power and prevents a dive when low power would jeopardize its safe return to the surface.

Recommendations for Future Flight Tests

The results and analysis of the flight data used in this chapter suggest benefits to making use of additional sensors and methods for future flight tests. Moorings or fixed sensors located off the glider but in the flight test area could be used to measure the current conditions at the operational depths. For the purpose of flight tests, sensors could be temporarily installed on the glider to measure its velocity, angle of attack, and sideslip angle. Such sensors are standard in aircraft flight tests but would require adaptation for use on the glider, both because it is underwater and travels at a low velocity. Angle of attack and sideslip angle

could be measured using a simple vane system attached to the nose of the vehicle. Velocity could be measured in a number of ways, depending on the speed of gliding. Because gliders generally travel at low speeds, a pitot tube is probably unsuitable. A propeller type velocity meter may work, provided the glider speed is high enough. An acoustic doppler velocimeter (ADV) could be mounted in the glider science section and used to measure glide speed and the aerodynamic angles. This would measure the velocity of the water relative to the glider acoustically. Because of its size and power consumption, this instrument may only be suitable for flight tests, not for standard deployments, although plans exist to outfit the Spray gliders with ADVs with a twenty meter range.

During flight testing, position and velocity could both be measured by an acoustic ranging system with transponders and receivers on the glider and fixed to the ocean floor. Measuring data with high enough accuracy may require a purpose-built acoustic range, the use of an existing naval test range or the like. It would also be necessary to measure the ocean currents along the test range. This could also be done using existing acoustic doppler current profilers (ADCPs) such as those on fixed moorings in Monterey Bay. Some acoustic systems are already in the process of being adapted for use on the Slocum glider, and these could provide a useful estimate of the glider position and velocity during tests. These sensor systems vary in size and expense, with the use of an existing doppler current measuring installation being relatively inexpensive. It would not be necessary to add these flight test sensors permanently to the glider, but rather install them temporarily for the duration of flight tests. These types of data would allow more accurate measurement of the glider dynamics and hydrodynamic characteristics.

Some experiments using an acoustic system have been conducted using the Seaglider (see [14]). These tests involved tracking the horizontal position of the Seaglider using an acoustic

array and tracking its vertical using the glider's depth sensor. Currents were measured with an ship-board ADCP. The Seaglider hydrodynamic parameters were then determined using a regression over data from hundreds of dives.

Flight tests with an acoustic positioning system on the glider and on fixed moorings, an ADV mounted on the glider and an ADV mounted on a fixed mooring to measure ocean currents in the test range should provide good test data.

The operational limitations involved in the ocean flight tests detailed here and the lack of a comprehensive sensor suite placed severe limitations on our identification efforts. However, such limitations are to be expected when operating a relatively new vehicle platform and when operating in the ocean. The nature of the gliders themselves places a limit on the available instrumentation and power during standard operation. Even with these limitations, significant analysis is possible. The relatively basic sensor improvements described above would allow for an expanded data set for evaluation. Additional sensor data should prove especially useful for determining the parameters corresponding to unsteady motions of the glider, such as the glider added masses. It should be noted that the experimental results for the drag on the glider were greater than those predicted by reference data and computational analysis. This suggests that there is an important role for experimental testing, in combination with other methods, in evaluating glider performance.

Chapter 6

Glider Controller Design and Analysis

Full use of the capabilities and advantages of underwater gliders in ocean sampling and other applications requires an accurate and reliable control system. Accurate navigation is required both for travel and to correlate recorded scientific sampling data to spatial locations. Control is essential for efficient gliding, so gliders operate with maximum range or speed. Improvements in glider control should add to their utility in scientific missions. Most importantly, feedback control systems provide a measure of robustness to disturbances and uncertainty. This includes changes in a glider's performance over time, a significant concern when gliders are to be deployed in extended missions at sea. Therefore, glider control systems should be of interest both to the technically inclined engineer and to scientists using gliders in their work.

Our work aims to develop a model-based feedback control design methodology. Sections of this chapter have been presented in [42, 25, 24, 50, 2]. The intent of our work is to allow improvement upon currently implemented glider control strategies. A systematic design methodology that provides control in the full state-space is expected to make possible the design of glider controllers that require less experimentation and tuning and

provide more robustness to fouling, payload changes and other uncertainties as compared to current techniques. Additionally, using a model-based approach, a dynamic observer can be designed to estimate states such as glider velocity. These estimated states could then be used to determine horizontal glider motion instead of the current navigation methods which rely on assumptions of constant angle of attack. A model-based approach is also useful in determining optimal glider motions and in glider design (Chapter 7).

Section 6.1 analyzes control of gliding in the vertical, longitudinal plane, including controllability and observability of steady glides in the vertical plane. Control design with an observer is performed for the dynamics specialized to the vertical plane. Continuous feedback laws are developed. When energy is at a premium, we envision a scenario in which one might occasionally and temporarily turn off the active feedback control routine (including sensors), e.g., during periods of relative calm or when tight control is less critical. This type of energy saving method is used in several existing gliders, where the control system and feedback loops are “turned on” intermittently. Some gliders also use deadbands to reduce the power used by control application. Section 6.3.4 presents a method for analyzing deadband and saturation control features using describing function analysis.

Our glider model captures the essential dynamic features of underwater gliding. Versions of the model with varying complexity may be used in control analysis. For example, the detail and number of terms in the hydrodynamic model, and the number of internal masses may be varied, and these models confined to the longitudinal or lateral planes (Chapter 4). Simplicity allows for development of general control design strategies. These strategies, along with insights gained from their development, are expected to be relevant to the design of control laws for the more complex models of operational gliders. Feedback provides robustness to uncertainty, and this uncertainty may include unmodelled dynamics. Control

has been investigated using several versions of the model with varying complexity.

Because of power constraints, limited available volume, and the difficulties of underwater sensing, many operational gliders do not carry the sensors necessary to determine the full glider dynamic state. In particular, glider x and y position and velocity are costly to measure directly when submerged. Similarly, aerodynamic angles α and β are not measured.

In cases when some states cannot be directly measured, such as with oceangoing gliders, the design of an observer offers possible improvements over current glider control methods. Section 6.1 presents a controller design that uses a linear observer. We design a dynamic observer to estimate the glider state from a limited set of measurements.

Section 6.2 discusses features of the control systems of existing oceanographic gliders Slocum, Seaglider and Spray. Features of the Slocum glider control system include proportional feedback for pitch and heading control, use of deduced reckoning to navigate underwater, variable timing of the controls, and use of a deadband to reduce the energy used for control. Section 6.2.2 describes control experiments conducted using a Slocum glider during the operations at sea described in Chapter 5. Control gains, timing, deadband and sliding mass placement parameters were modified and tuned to improve the glider's performance. This improved controller was implemented on the glider during subsequent oceanographic operations.

Section 6.3 briefly discusses other application of the glider model in controller design, including on-line parameter identification and controller adaptation, efficient gliding using intermittent control and deadbands, and inflection control. Section 6.3.4 presents a describing function analysis of controlled gliding. This includes analysis of the stability of controlled gliding with nonlinear control elements (deadbands and saturation) and analysis of the existence and stability of limit cycles in the controlled system.

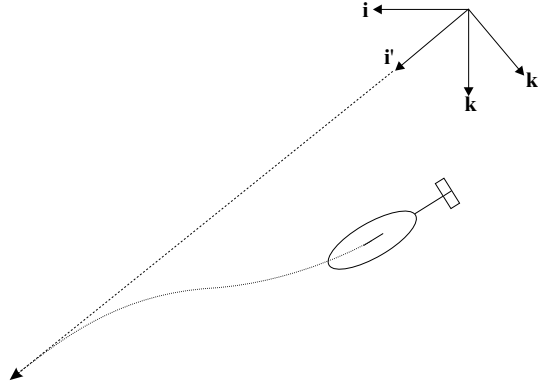


Figure 6.1: Planar gliding controlled to a line.

6.1 Controlled Planar Gliding

In this section we evaluate linear controllability and observability of the longitudinal glider system about steady vertical plane glides. We then design linear controllers and observers and demonstrate their application in simulations.

In controlled gliding in the vertical plane, a glide path is typically specified by the desired glide path angle ξ_d and desired speed V_d . Equation (4.12) defines inertial coordinates (x', z') such that x' coincides with the desired path and z' measures the vehicle's perpendicular distance to the desired path. We define two gliding objectives:

GO1 The objective is to control only the direction and speed of the vehicle's glide path.

In this case we need not consider x and z at all.

GO2 The objective is to control gliding along a prescribed line (see Figure 4.4). In this case we will include z' (but exclude x') in our analysis and we aim to make $z' = 0$.

The dynamics of the z' state are given by Equation (4.13), $\dot{z}' = \sin \xi_d (v_1 \cos \theta + v_3 \sin \theta) + \cos \xi_d (-v_1 \sin \theta + v_3 \cos \theta)$.

In the glider model of Chapter 3 the movable point mass can be controlled in all directions (2 degrees of freedom in the planar case). In some designs control of the CG and

sliding mass locations may be restricted. For example, a sliding mass (typically a battery) may be actuated in one direction. This may be modelled in the planar case as a movable point mass with only one degree of freedom. We consider the case in which r_{p3} is fixed and r_{p1} is controlled. Bounds on r_{p1} depend on a given glider’s design and actuators.

6.1.1 Controllability

We now examine controllability of steady glide paths for the steady planar glides of Section 4.1. Linear controllability is evaluated for a model of our experimental vehicle ROGUE, described in Section 2.2.7. The same procedure is applicable to other glider designs, including Slocum.

The planar glider model of Section 4.1 is locally (linearly) controllable for the four glide paths listed in Table 4.1. That is, \mathbf{A} and \mathbf{B} as given by (4.31) and (4.32), when evaluated at any of the four equilibria, satisfy the controllability rank condition. Note that the linearization includes the state z' , meaning that controllability extends to the variable z' . Accordingly, we can successfully design a linear controller that will locally accomplish not only glide objective **GO1** but also **GO2**.

It is of interest to check the controllability rank condition in the case that the movable mass \bar{m} can only move in one direction (i.e., r_{P3} is fixed). To do this we have linearized the equations of motion for the single degree-of-freedom moving mass derived in [42]. Again the new \mathbf{A} and \mathbf{B} matrices for this case, when evaluated at any of the above four glide paths, satisfy the controllability rank condition. Thus, it seems that at least for linear type control action, not much is lost in restricting the degrees of freedom of the movable mass from two to one. Several operational gliders have moving masses that translate in the vehicle long axis and rotate in the roll direction, corresponding to a design with one degree of freedom

when considering only the vertical plane.

On the other hand, for large motions such as switching from an upward to a downward glide path, care needs to be taken if restricting the degrees of freedom of the movable mass. For instance, while motion of the movable mass restricted to the r_{P1} direction would be sufficient for sawtooth maneuvers, motion restricted to the r_{P3} direction would probably not allow for both upward and downward glide motions. In the typical glider body shape, with long axis along e_1 , mass motion restricted to the r_{P3} direction will have more limited travel as compared to motion in the r_{P1} direction. The change in pitch moment due to an offset ballast mass must also be accounted for, as described for the Slocum glider in Chapters 3 and 5.

The movable mass \bar{m} for ROGUE is approximately 1/6 of the vehicle displacement m . This is a similar proportion of the total glider mass as the movable mass in the gliders Slocum, Spray and Seaglider. Variations in this mass or its location will not in principle affect local controllability of a steady glide path.

In practice, there are tradeoffs associated with moving a large mass a short distance versus moving a small mass a large distance. The power and energy required to move the sliding mass and the required actuator accuracy should be considered. A large moving mass requires a shorter travel and a smaller portion of the vehicle volume. Variation in mass and location also affect the range of feasible glide paths and performance when switching between them.

The variable mass m_{b_a} in ROGUE at the equilibrium shown above is a larger fraction of the vehicle displacement than in other gliders. This mass controls glide speed; thus, designing a smaller variable mass would reduce maximum glide speed (see Chapter 7).

6.1.2 Observability

Observability of the linearized model about the four glide paths listed in Table 4.1 was also investigated. If **GO1** is our objective, i.e., if we are interested in controlling only the direction and speed of the vehicle's glide path, then we need not measure z' . The nine-dimensional dynamic model (which excludes z') is completely observable with measurements limited to movable mass position r_{p1} , r_{p3} and variable mass m_b . In this case, pitch angle θ , pitch rate Ω_2 , linear velocity components v_1 and v_3 and the momentum of the movable mass P_{p1} , P_{p3} need not be sensed. Observability means that with the measurements of r_{p1} , r_{p3} and m_b , a dynamic observer could be designed to give an estimate of the unmeasured states θ , Ω_2 , v_1 , v_3 , P_{p1} and P_{p3} . Of course, θ is typically already measured and Ω_2 is not so hard to measure, so the real advantage is in the estimation of v_1 , v_3 , P_{p1} and P_{p3} which are more difficult to measure. The nine-dimensional dynamic model is also completely observable with measurements limited to θ , r_{p1} (or r_{p3}) and m_b . Again, this means that using these three measurement signals, an observer could be designed to estimate the rest of the states.

We note that the use of a dynamic observer to estimate the glider states has the potential to improve the accuracy of horizontal motion determination over presently implemented methods which are based on assumptions of constant angle of attack, etc. For example, on Slocum, the horizontal motion of the glider during the glide is estimated from GPS fixes taken at the surface, measured pitch angle θ , an assumed angle of attack and vertical speed computed from depth measurements [76]. On Spray, horizontal flight distance is similarly calculated based on a constant pitch, heading and angle of attack to which the vehicle is being controlled [63].

If **GO2** is our objective, i.e., if we want to control the glider to a prescribed line in the plane, then we need a measurement of z' . Recall from (4.12) that z' depends on both depth

z , which is easily measured, and horizontal position x , which is not so easily measured. The measurements r_{p1} , r_{p3} and m_b , together with a measurement of z (or alternatively θ , r_{p1} , m_b and z), do not render x observable. This means that without an initial condition measurement $x(0)$, the trajectory $x(t)$ cannot be computed, and so z' is not observable. That is, using any combination of the other nine states, it is not possible to design a dynamic observer to estimate the z' state. However, with an initial measurement of x , given say from a GPS fix taken when the glider is at the surface, the horizontal motion of the glider can be dead reckoned using velocity estimates from the observer. This introduces some error $z' - z'_{ded}$ into the estimate of the z' state. Using the deduced z'_{ded} in the feedback control, the glider can perform **GO2**, gliding along or parallel to the desired glide path with some offset in the z' direction due to dead reckoning error.

The dead reckoning approach involves calculating horizontal velocity \dot{x}_{ded} , then integrating to obtain a deduced x_{ded} . We have that

$$\dot{x}_{ded} = v_{1est} \cos \theta + v_{3est} \sin \theta. \quad (6.1)$$

This can then be used to calculate z'_{ded} . The pitch angle θ and depth z can be measured directly. Estimates of the velocities, v_{1est} and v_{3est} , are provided by the observer, while ξ_d is determined by the desired glide. The equation for the dead reckoned z'_{ded} is then

$$z'_{ded} = \sin \xi_d(x_{ded}) + \cos \xi_d(z). \quad (6.2)$$

The nine observable states include v_1 and v_3 , so our observer estimates v_{1est} and v_{3est} will converge to the actual states when we are close enough to the equilibrium glide path for the linearization to be valid. When there is some error in the observer estimate of the velocities,

integrating (6.1) to find x_{ded} and using (6.2) will result in some error $z' - z'_{ded} \neq 0$. This error depends on the observer state estimate error, which will vary with different state trajectories and disturbances.

6.1.3 Design of a Controller with Observer

In this section we demonstrate, in simulation, controlled gliding in the vertical plane by designing and testing a linear controller and observer for the glide path moving 30° downward as described in Table 4.1. Since the controller is linear, we expect that it should take initial conditions nearby to the 30° downward glide path. This example uses the glider dynamic equations in the vertical plane, (4.1)-(4.11), where the control acts on the momenta of the point mass \bar{m} . Another example below demonstrates control of the transformed equations, (3.42), under the control transformation of Section 3.2.4, where the control is the acceleration of the internal mass.

We demonstrate this result by starting the glider at the 45° downward steady glide and using the linear controller to move it to the 30° downward glide solely by feedback.

Controller Design

We address the case where only a limited set of the states are measured, depending on the sensors on the glider. We design the controller and then, given the limited set of state measurements, design a dynamic observer to determine the full state of the glider. The controller is designed for the linearization (4.31), of the vertical plane glider Equations (4.13) and (4.3)-(4.11), about the 30° downward glide using the LQR (linear quadratic regulator) method. This is a standard linear optimal control design method which produces a stabilizing control law that minimizes a cost function that is a weighted sum of the squares

of the states and input variables.

The cost function to be minimized is defined as

$$J = \int_0^{\infty} \delta \mathbf{x}^T \mathbf{Q} \delta \mathbf{x} + \delta \mathbf{u}^T \mathbf{R} \delta \mathbf{u} dt$$

where \mathbf{Q} and \mathbf{R} are state and control penalty matrices. \mathbf{Q} and \mathbf{R} were chosen to ensure well-behaved dynamics and to prevent large motions in the movable mass position and variable mass that would exceed physical limitations. Taking into account real or desirable maximum state values, the states associated with vehicle and movable mass velocity and variable mass and pitch angle were weighted most heavily. No significant tuning was performed. The weight selections are given by

$$\mathbf{Q} = \text{diag}(.05, .5, 1, 2, 2, .1, .1, 1, 1, .5),$$

$$\mathbf{R} = \text{diag}(1, 1, 1).$$

The corresponding control law is $\mathbf{u} = -\mathbf{K} \delta \mathbf{x}$ where \mathbf{K} is computed using MATLAB as the solution to the Riccati equation given $\mathbf{A}, \mathbf{B}, \mathbf{Q}, \mathbf{R}$.

Observer Design

In the case that some states are not provided by sensor data, as is likely to be the case with the horizontal positions and velocities of an autonomous glider, it is possible to construct a linear optimal observer to estimate the unavailable states. As described in Section 6.1.1, the nine dimensional dynamic model excluding z' is completely observable. If z' is not directly sensed, it is an unobservable state but can be dead reckoned. The construction of an optimal linear observer for the nine dimensional system proceeds in a similar manner to

the construction of the LQR controller.

Our linear system is described by \mathbf{A} and \mathbf{B} , defined above. The system output is $\mathbf{y} = \mathbf{C}\mathbf{x} + \mathbf{v}$, where \mathbf{C} is the system output matrix determined by the available sensors and \mathbf{v} is noise. Given a linear time invariant system subject to additive process disturbance $\mathbf{w}(t)$ and measurement noise $\mathbf{v}(t)$ which are zero mean, gaussian, white noise processes, an observer which minimizes variance in the estimate error is derived in a manner similar to the LQR. The cost function to be minimized is

$$J_0 = \int_0^{\infty} [\tilde{z}_w(t)^2 + \tilde{z}_v(t)^2] dt$$

where $\tilde{z}_w(t) = e^{(\mathbf{A}-\mathbf{L}\mathbf{C})t}\mathbf{w}_0$ is the system zero-state response to plant disturbance $\mathbf{w}(t)$ and $\tilde{z}_v(t) = -e^{(\mathbf{A}-\mathbf{L}\mathbf{C})t}\mathbf{L}\mathbf{v}_0$ is the zero-state response to measurement noise $\mathbf{v}(t)$. Let $\mathbf{w}(t) = \mathbf{w}_0\delta(t)$ and $\mathbf{v}(t) = \mathbf{v}_0\delta(t)$ represent the white-noise processes $\mathbf{w}(t)$ and $\mathbf{v}(t)$, where the Dirac delta Function $\delta(t)$ represents the fact that white noise is uncorrelated in time. Let $\mathbf{W} = \mathbf{w}_0\mathbf{w}_0^T$ and $\mathbf{V} = \mathbf{v}_0\mathbf{v}_0^T$ be the disturbance and noise covariance matrices. Then choosing observer feedback $\mathbf{L} = \mathbf{P}\mathbf{C}^T\mathbf{V}^{-1}$ minimizes the cost function J_0 , where \mathbf{P} is the solution to the observer matrix Riccati equation given $\mathbf{A}, \mathbf{C}, \mathbf{W}, \mathbf{V}$, [47].

In this observer design the \mathbf{W} and \mathbf{V} matrices are chosen according to reasonable estimates of the disturbances and noise. The covariance matrix \mathbf{W} is a diagonal matrix whose elements are the square of the standard deviation of the state disturbances. The standard deviation is taken to be ten percent of the desired value at the equilibrium glide for each state. In the cases where a state \mathbf{x}_i has desired value zero, we determined a maximum deviation $\Delta\mathbf{x}_i$ from equilibrium by simulating several switches between equilibrium glides under full state feedback control. Ten percent of $\Delta\mathbf{x}_i$ is then used as the standard deviation

for the i^{th} state. The noise covariance matrix \mathbf{V} depends on the noise properties of the sensors used in the vehicle. In this design they are taken to be of the same or smaller order of magnitude as \mathbf{W} :

$$\mathbf{W} = \text{diag}(17, 4, 9, 1, 1, 1, 6, 0, 5),$$

$$\mathbf{V} = \text{diag}(1, 1, 1, 1, 1).$$

When determining the cost function to be minimized, if \mathbf{V} is large then computed gain \mathbf{L} will be small, so direct measurements have smaller impact on the state estimate. A large \mathbf{W} implies disturbances dominate the plant dynamics. In that case, computed gain \mathbf{L} is large, resulting in an observer state estimate which depends more heavily on sensor measurements than the plant model.

6.1.4 Simulation: Controlled Planar Gliding

In Figures 6.2-6.4 we show a MATLAB simulation of the (ROGUE-sized) glider switching from a 45° downward glide to a 30° downward glide path. This is accomplished by turning off the controller for the first glide at $t = 5$ seconds and turning on the linear controller for the second glide. In each figure we show results using full state feedback and using an observer to estimate the state used in the control law.

When calculating the controller gain matrix \mathbf{K} and the observer gain matrix \mathbf{L} , some plant parameter error is incorporated into the design. That is, when calculating the gain matrices using the respective Riccati equations, the parameters which determine the \mathbf{A} and \mathbf{B} matrices are varied by up to ten percent. Changing the \mathbf{A} and \mathbf{B} matrices used as the system model in the controller and observer design represents imperfect knowledge of the

glider dynamic coefficients (note that this simulation includes plant parameter variation but no added measurement noise).

In Figure 6.2 we show the glide path before and after the switch. In Figure 6.3 we show plots of position, pitch, linear and angular velocity as functions of time and in Figure 6.4 we show the position of the movable mass, the net buoyant force, and the control inputs as functions of time. Note that this example does not include limits on the control inputs, for example, a maximum pumping rate. The control gains in the example produce a high pumping rate as shown. This is not required for stable behavior. Examples in Chapter 4 and below show switching between glides with other feedback controls and gains.

The figures show that the 45° downward glide path is in the region of attraction of the linear controller designed for the 30° downward glide path. Furthermore, the transient is well behaved. Larger switches between glides are possible and are demonstrated in other examples.

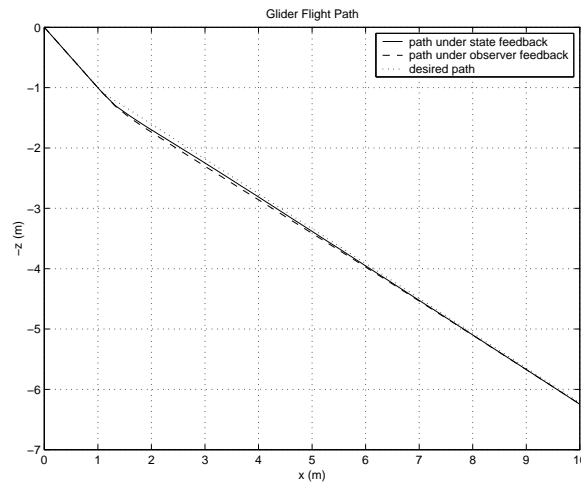


Figure 6.2: Simulation of glide path from 45° downward to 30° downward.

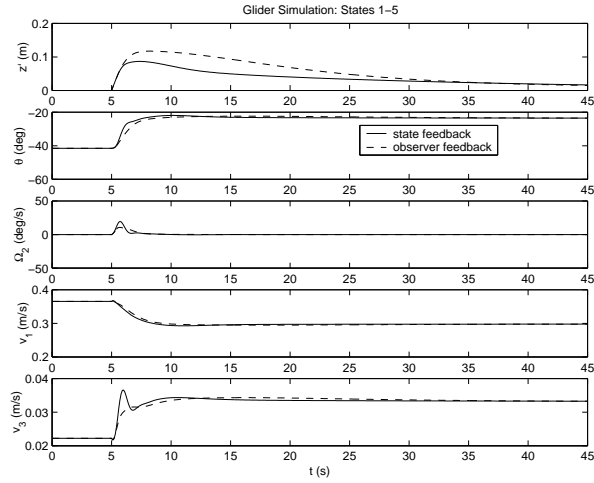


Figure 6.3: Simulation of position and velocity variables.

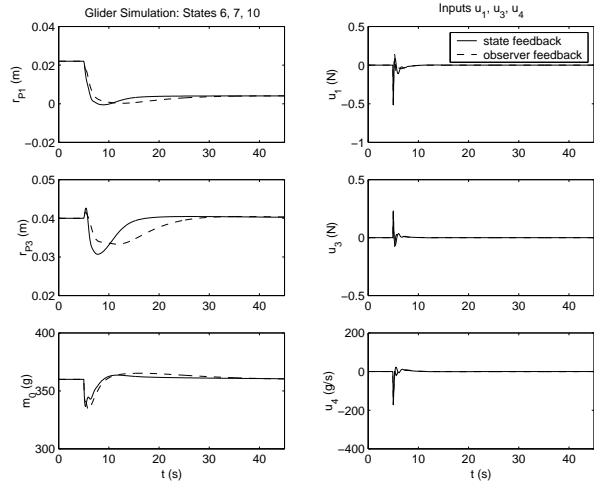


Figure 6.4: Simulation of movable mass, variable mass and control inputs.

6.1.5 Simulation: Controlled Gliding with Inflections

In this section we describe a simulation that demonstrates control of the transformed glider equation with simplified internal masses (3.42), under the control transformation of Section 3.2.4. The control \mathbf{w}_p is the acceleration of the internal mass. The glider modelled here is similar in size to existing gliders such as Slocum. Parameters of the glider simulated are shown in Table 4.2. These are the same parameters as used in the examples in Chapter 4. r_{p1} and m_b are controlled and r_{p3} is fixed.

Figure 6.5 shows the glide path, vertical plane states and V and α from the simulation. The simulation shows four steady glide segments and three stable inflections between upwards and downwards glides. Figure 6.6 shows the internal mass states and the corresponding controls. The states converge to their desired equilibrium values, shown in Table 4.3.

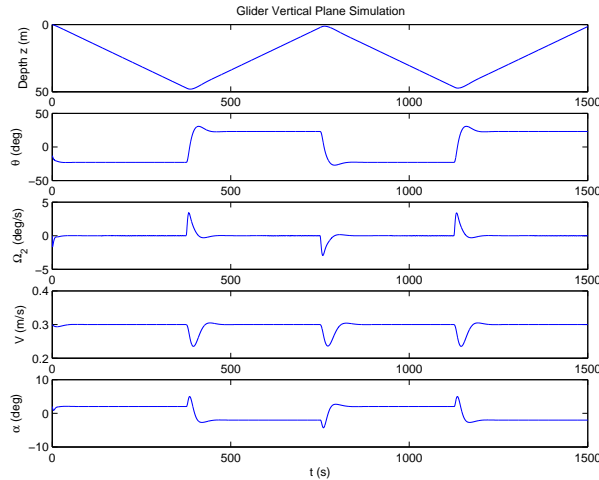


Figure 6.5: Vertical Plane States.

Stable planar gliding and inflections between glides were demonstrated in Chapter 4. In these examples feedback is used only to control the internal mass position and buoyancy to a desired value. Ω and \mathbf{v} , for example, are not sensed or used in computing the feedback. Those examples could be described as “open loop” with respect to the glider’s position and velocity. Parameter uncertainty or variation will produce steady state errors from the desired equilibrium.

This example shows controlled inflection and steady gliding with state feedback and model parameter uncertainties. A linearization is computed for each steady glide and used to compute a linear controller for that glide. Switching between glides is performed by switching on the controller for the desired glide, as described above.

The state is $\mathbf{x} = (\theta, \Omega_2, v_1, v_2, r_{p1}, r_{p2}, \dot{r}_{p1}, \dot{r}_{p2}, m_b)^T$. An LQR controller is computed

with $\mathbf{Q} = \text{diag}(.5, 1, 2, 2, .1, .1, 1, 1, .5)$ and $\mathbf{R} = \text{diag}(100, 1000)$. The steady glides are stable and the control transform results in stable inflections in the open loop case. Therefore the weights on the controls may be chosen to reduce the control actuation and unnecessary energy use. The \mathbf{R} used here is for demonstration, but future choices of the control weights may make use of some analytical method to minimize energy use. In this simulation the control inputs are limited as in the examples of Chapter 4, although the controls do not reach their limits during the simulation.

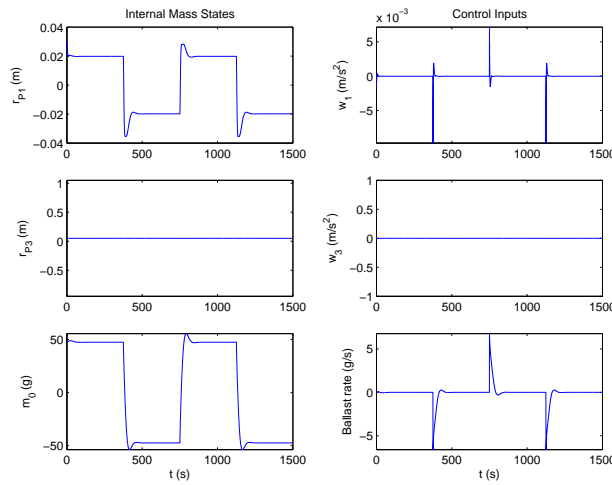


Figure 6.6: Internal mass position, accelerations, and net buoyancy and pumping rate.

To model the parameter uncertainty, all nonzero elements of the \mathbf{A} and \mathbf{B} matrices of the linearization are randomly varied by up to 25% before computing the LQR controller for each glide.

6.2 Control Systems on Operational Gliders

The principal control task on operational gliders is accurate navigation with minimum energy use. The control system must make use of the limited actuation and control authority available while navigating accurately with limited position and velocity sensors. It is nec-

essary to minimize energy use in order to maximize glider range and endurance.

6.2.1 Existing Glider Pitch and Heading Control Systems

Existing oceanographic gliders use linear controllers for pitch and heading. The separate control loops use different actuators to change internal mass position for pitch control and internal mass roll or rudder angle to control heading. The controllers are proportional, PD or PID loops. The gains are designed and tuned from experience or from some linear analysis. The model and work presented above provides a systematic method to develop model-based controllers.

Existing gliders such as Slocum make use of several interesting nonlinear control elements intended to reduce energy use by the control actuators. These include deadbands, variable control update timing, and limits on control actuator step size. The glider controllers can turn off, or “sleep”, for intervals to conserve energy.

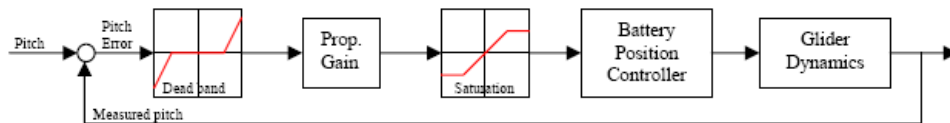


Figure 6.7: Typical controller block diagram. Pitch shown as example, [2].

Figure 6.7 shows the block diagram of a typical glider control loop, the pitch control on the Slocum electric. The steady glide pitch angle is set by the ballast load and sliding mass. Switching between downwards and upwards glides is performed open loop, i.e., the ballast is changed and the sliding mass is moved to a new position. The steady glide linear controller uses proportional feedback and actuates the sliding mass (alone) to adjust the pitch angle. Pitch is measured directly by an inclinometer.

The controller has several nonlinearities, including a deadband, limits on the actuator

step size, and variable control update timing. These are intended to reduce energy use by the control actuators. There are also physical limits on the actuator range. The Slocum controller uses a deadband that sets the control to zero when the error is below a set magnitude. Above this threshold the deadband has no effect on the error signal (i.e., multiplies it by one). A more conventional deadband arrangement, shown in Figure 6.7, has zero gain inside the deadband and output $K(\theta_{error} - \delta)$ above the deadband threshold δ .

Because the error and control are computed only at set time steps, the Slocum controller is actually a discrete controller. The variable control update timing may be a function of the state error history, for example, whether it is within the deadband. Maximum and minimum update intervals are set as control parameters. If the update interval is much faster than the glider dynamics, the controller may be approximated as a continuous controller. The actuator step size limit is the maximum change Δr_{p1} of the sliding mass position permitted per control cycle. For large errors and update intervals this effectively limits the proportional gain of the controller.

Other glider controllers are similar. Spray performs active control of pitch and roll every 40 s using measured pitch and heading errors [63]. “The pitch control algorithm is a straight proportional loop, with low gain to produce an over-damped response toward the desired pitch angle.” The heading control uses a proportional-integral controller (to eliminate steady state heading errors).

6.2.2 Slocum Control Experiments at Sea

Our in-ocean tests of the Slocum glider in January 2003, described in Chapter 5, included experimentation with the tuning of the the glider pitch and heading controllers and inflection

control parameters. We conducted additional tests, described in [2], with a different Slocum glider in Spring 2003 during a cruise conducted under principal investigator Joe Rice on the Canadian Forces Auxiliary Vessel Quest (CFAV *Quest*) in collaboration with SPAWAR System Center, San Diego and DRDC Atlantic, Halifax, Canada. The experiments included varying the controller gains and parameters, the deadband size, control update timing, and inflection mass placement parameters. Because of operational considerations, the overall structure of the controller was not changed, although in some tests the nonlinear control elements were removed. Examples of stable glides and transitions are shown in Chapter 5. Examples of controlled gliding experiments are shown below and in [2].

Pitch Control

Figure 6.8 shows a test glide using Slocum WE01 under controlled gliding with controller gains and parameters before experimental modification. This data is from the January 2003 Bahamas Glider Cruise conducted with WHOI, described in Chapter 5. The glider takes about 100 s to reach the desired pitch angle after the completion of ballast pumping. This is due in part to the incremental adjustments of the sliding mass position. The change in the battery position is clipped to a maximum value per cycle by the controller, giving the ‘battpos’ plot a staircase appearance. Other test glides show this to even greater degrees. The combination of maximum sliding mass adjustment and intermittent control update timing limits the effective gain of the pitch controller, resulting in a slow response.

There is also significant overshoot in pitch. This is caused in part by a mis-trim in the glider e_1 direction. In this test the pitch and battery position lookup function does not match the actual trim condition of the glider. The controller’s parameters are configured for a glider trimmed for zero pitch at neutral buoyancy with the sliding mass at ‘battpos’

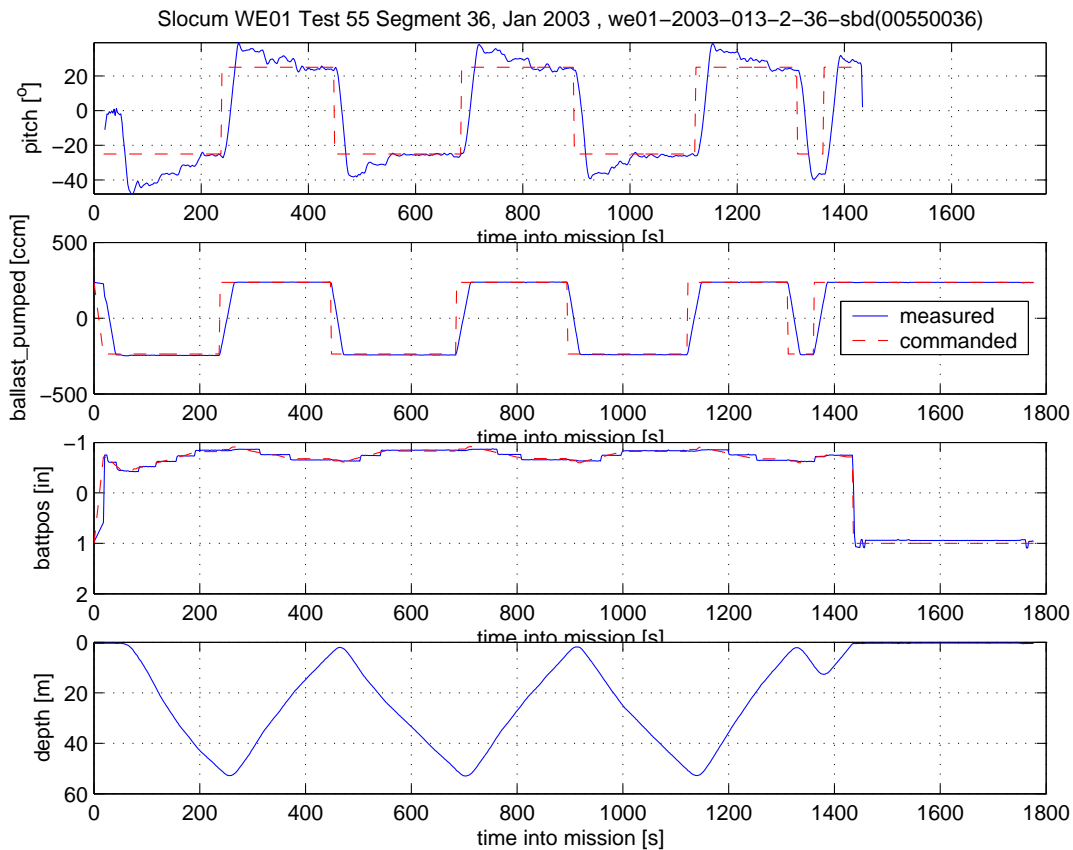


Figure 6.8: Glider WE01 test run before control modifications. Bahamas, January 2003 (see Chapter 5).

zero. This glider is trimmed for that condition with ‘battpos’ near -0.75 inches. This results in a pitch error during the open-loop inflection. The control clipping then limits the pitch controller’s correction of this error. This is repeated at each inflection.

The controller variable update timing and deadband are implemented in this test. The update timing is varied according to the error performance, with maximum 20 s intervals and minimum 2 s. Periods of gliding within the deadband appear as flat portions in the mass position plot.

Subsequent experiments eliminate the control clipping by setting the maximum step size to a very large value. This results in a dramatic increase in actuator use, a reduced rise time to the desired pitch angle, and significant oscillations in mass position and pitch angle

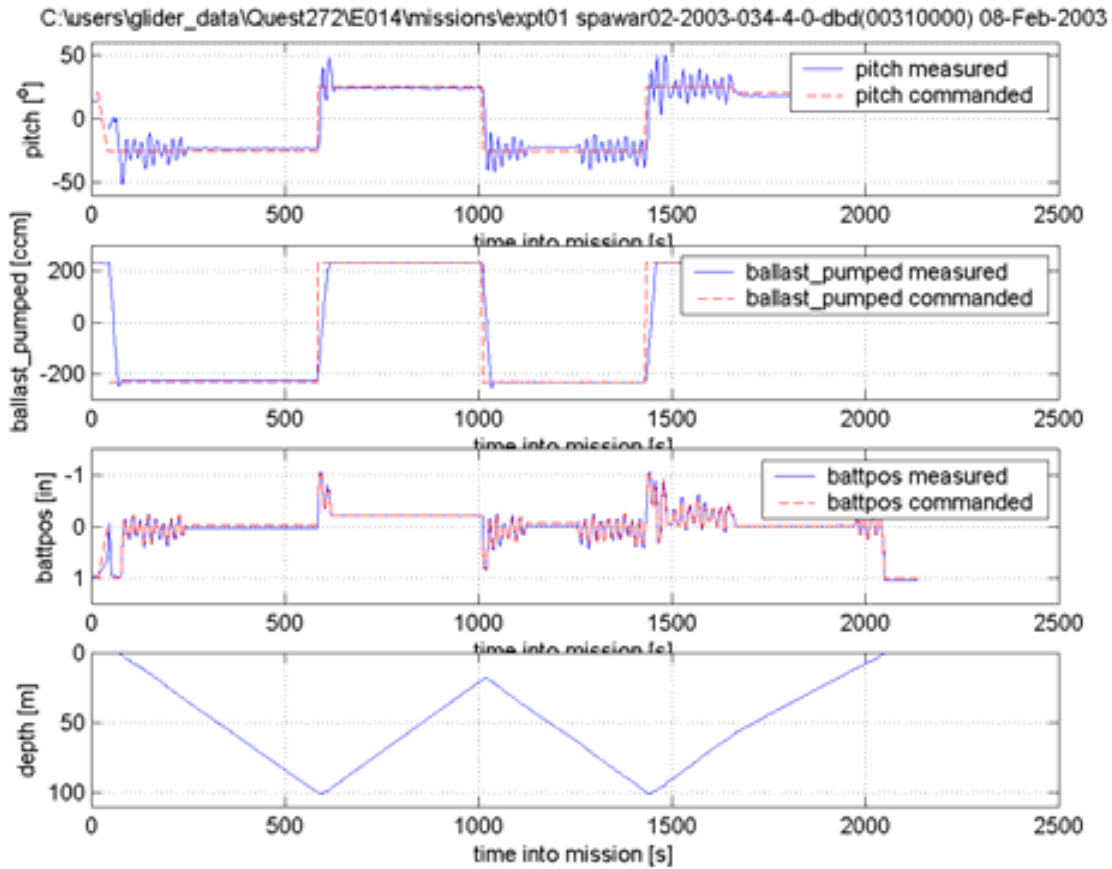


Figure 6.9: Slocum pitch response with high gain, no sliding mass clipping. Spring 2003, glider deployment from CFAV Quest, [2].

before settling to a steady pitch angle. Without clipping, the gain of the controller is too high, producing oscillations. This results in an increased settling time and reduces time spent in the deadband. Figure 6.9 shows an example of this behavior from a later set of tests with another Slocum glider, [2]. There are extended periods of oscillation. Note that around 1250 s into the mission the glider is at equilibrium inside the deadband for a period and is then disturbed out of the deadband, producing another period of controller induced oscillation.

Figure 6.10 shows test glide VERT 22, Segment 5, using Slocum WE01 after tuning of the pitch gains and parameters. The control update timing is fixed at 2 s, the deadband at 3°.

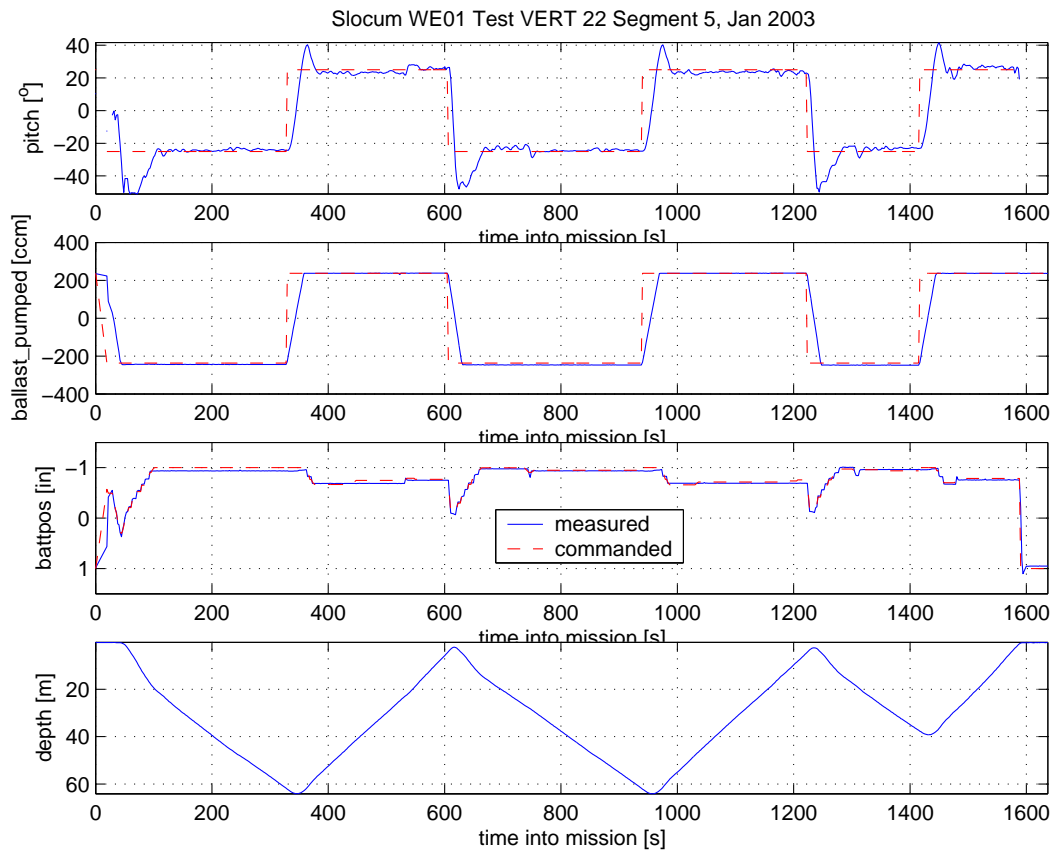


Figure 6.10: Slocum WE01 pitch response after controller tuning. Bahamas, January 2003 (see Chapter 5).

The open-loop mass placement parameters are adjusted to match the glider’s trim condition more accurately using the equilibrium Equations (5.3). The controller lookup function assumes a linear relationship between pitch and battery position, but (5.3) shows that the lookup function should take into account the change in the ballast moment between upwards and downwards glides. For this test a best approximation was made using parameters within the existing controller.

Figure 6.10 shows improved pitch performance compared to the tests before controller tuning. The response time has decreased and there is no oscillation about the equilibrium. Once both actuators are in the equilibrium position, the glider settles to the desired pitch and remains within the deadband. There is still some overshoot in pitch. This is due in

part to the glider's inflection behavior. The ballast is pumped fully to the desired state at glide B before the sliding mass is moved to the new equilibrium position. Also note that because of the glider's mass trim in this series of tests, the sliding mass must move forward when gliding up and backwards when gliding down. This is contrary to what one might intuitively expect and opposite to what occurs in the glider model with simplified masses.

The controller tuning here combined iterative gain and parameter adjustments with analysis using the glider equilibrium equations. This was conducted simultaneously with preliminary glider parameter estimation from test data. If the glider hydrodynamic parameters and trim condition are estimated in advance, the glider model can be used to design and tune the controller with minimal flight test.

The performance improvements observed during this brief series of tests show that, given some knowledge of the glider dynamics developed through analysis of the glider model, even small improvements to the control system and parameters can result in noticeable performance gains.

Heading Control

While a properly designed and trimmed glider's pitch and roll are stable with fixed controls, a glider's heading (compass angle) is generally neutrally stable. Therefore some control is necessary to stabilize a desired heading angle and to reject environmental and plant disturbances. Heading controllers on existing oceanographic gliders make use of linear controllers as described above. Our experiments and analysis address the use of intermittent control updates, deadbands, and heading disturbances and coupling inherent to glider dynamics.

Accurate heading control and navigation is important for glider energy conservation, because small average errors in heading may become, over long glides, large errors in po-

sition. The pumping work for gliding to correct this error may be significant compared to the energy necessary to control heading.

Turning glides are described in Section 4.3. Glider heading dynamics are affected by roll-yaw coupling, rudder-roll coupling, and static mis-trim. In addition, the geometry of a real glider may be asymmetrical, such that the moment on the glider is nonzero at sideslip angle $\beta = 0$. This is the case on the Slocum glider, for example, where the position of the CTD instrument on the port side of the vehicle creates a yaw moment.

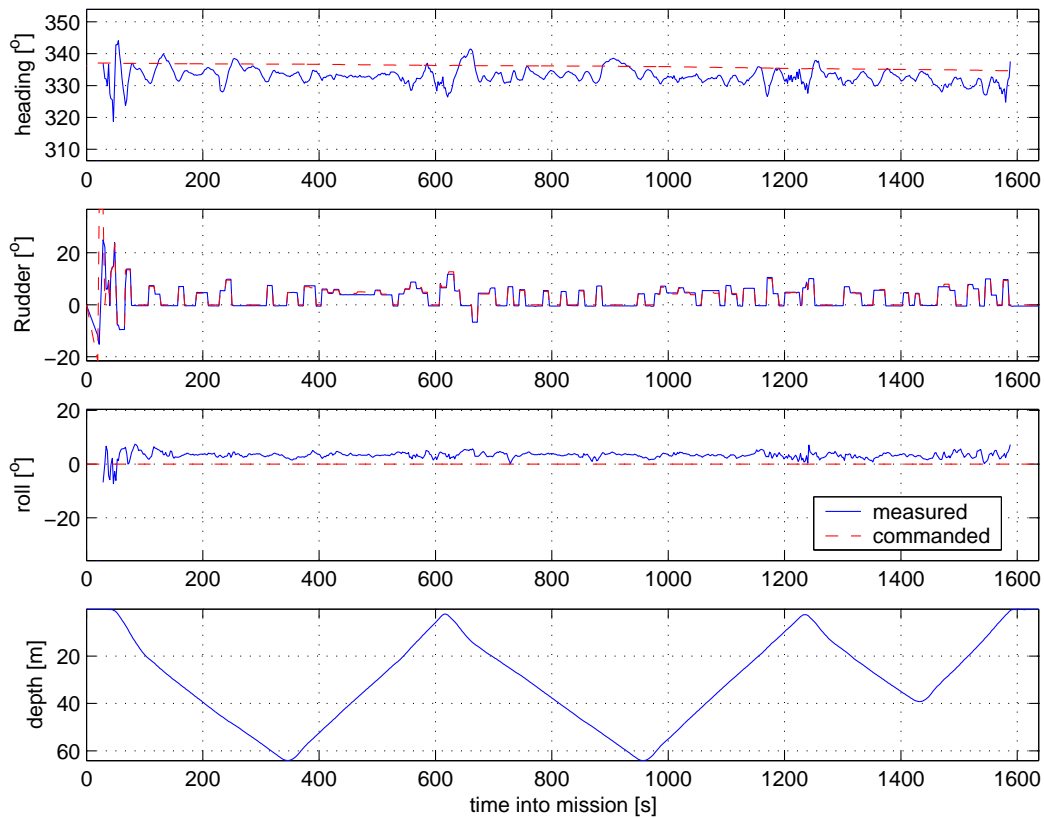


Figure 6.11: Slocum WE01 heading performance, test VERT 22 Segment 5. Bahamas, January 2003 (see Chapter 5).

Figure 6.11 shows experiment Vert 22, Segment 5. The pitch and vertical plane states for this test are shown in the previous section. Heading is controlled by a proportional controller with 2 s to 10 s updates and a 3 degree deadband. There is significant cycling

or chatter by the rudder. This is due to the controller deadband and intermittent timing. This produces an average heading error of about 4 degrees, close to the magnitude of the deadband.

Yaw moments due to the glider geometry and trim affect the glider's heading rate. Drag on the CTD creates a negative yaw moment, and the static roll of the glider creates a positive yaw moment gliding downwards and a negative yaw moment gliding upwards. In this glider the net yaw moment is negative in both upwards and downwards glides. This was determined in previous VERT series experiments, where a positive rudder angle (and yaw moment) was required to offset the net moment from the mass trim and geometry.

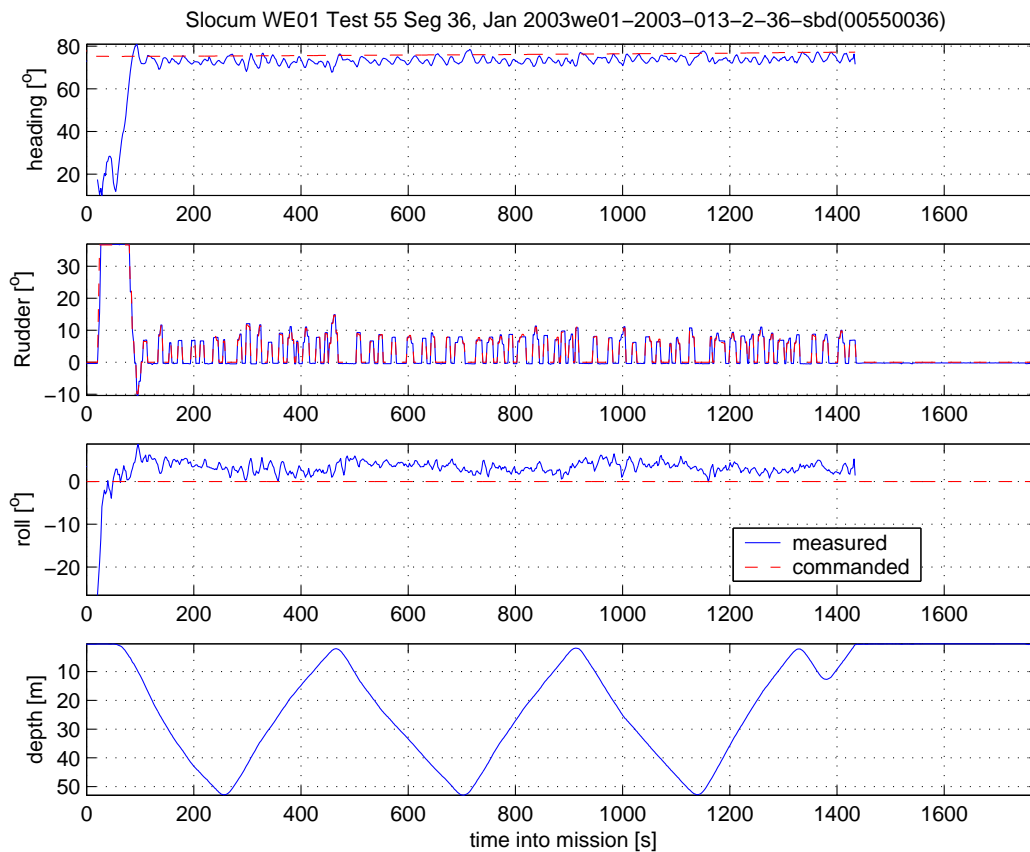


Figure 6.12: Slocum WE01 heading performance, test 55 Segment 36. Bahamas, January 2003 (see Chapter 5).

Figure 6.12 shows data from another test run with WE01, test mission 55, segment 36,

from the same group of experiments. In both examples, the heading error is predominantly negative and the rudder angle cycles between zero and positive values. In test Vert 22 (Figure 6.11) the deadband is $\sim 3^\circ$ and the rudder gain is 2. The rudder tends to switch between zero and $\sim 6^\circ$, the position corresponding to the edge of the deadband. When the rudder is set to zero, the other moments on the glider create a negative yaw rate. Once the deadband threshold is reached the rudder is set to $\sim 6^\circ$, bringing the heading error back into the deadband. Other tests in the Vert series were conducted to determine that $\sim 3.5^\circ$ is the average of the fixed rudder angles to give straight gliding flight in upwards and downwards glides (a smaller set value is required for straight downwards glides and a larger value for straight upwards glides). Therefore, neither zero nor $\sim 6^\circ$ rudder will give a straight glide. Control chattering and limit cycling are discussed further below.

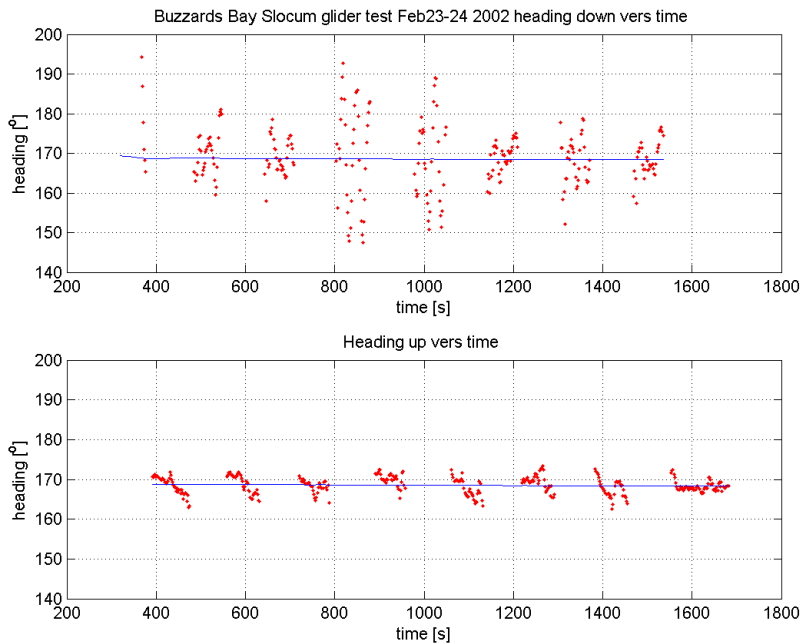


Figure 6.13: Slocum heading in upwards vs. downwards glides, Buzzards Bay 2/23/02. [1]. Data courtesy of David Fratantoni, WHOI.

Data from a different set of glides exhibits differences in heading performance control

when gliding upwards or downwards. Figure 6.13 shows heading versus time for a series of shallow glides with a Slocum glider operated by WHOI in Buzzards Bay, February 23-24, 2002. This data is courtesy of David Fratantoni, WHOI. The heading performance shown is not typical of other tests conducted, including the Slocum tests in January 2003. This test shows significant rudder-roll coupling and heading errors, more than appear in the Vert series of tests, perhaps because the glider in this case is insufficiently bottom-heavy. It is also gliding in shallow water (15 m) with frequent inflections using ballast gearing designed for deeper and slower inflections, while the Vert tests generally used deeper glides. There is a significant difference between the heading performance in upwards and downwards glides. This may occur because of rudder-roll coupling in the Slocum design. Slocum has positive roll-yaw coupling and a high rudder. Therefore, rudder-roll coupling causes a roll and yaw moment that acts against the rudder gliding downwards and with the rudder when gliding upwards. Rudder-roll coupling would be reduced by increasing the bottom-heaviness of the glider or changing the rudder location.

Figure 6.14 shows heading, roll and rudder plots for the same test. Data corresponding to glides downwards are on the left, data for glides upwards on the right. The rudder angle is scaled (divided by six) for comparison with the roll angle. Heading performance is better when gliding up; the heading data points are clustered more closely to the desired value and most are within the 5° deadband. The rudder angle is zero at most points when gliding upwards. The heading data points gliding downwards are more scattered, there is more actuation of the rudder, and the average roll angle is greater. The rudder moves to larger angles when gliding downwards. This is a product of the poor heading performance. It also creates a greater rolling moment on the glider, increasing the incidence of roll-yaw coupling.

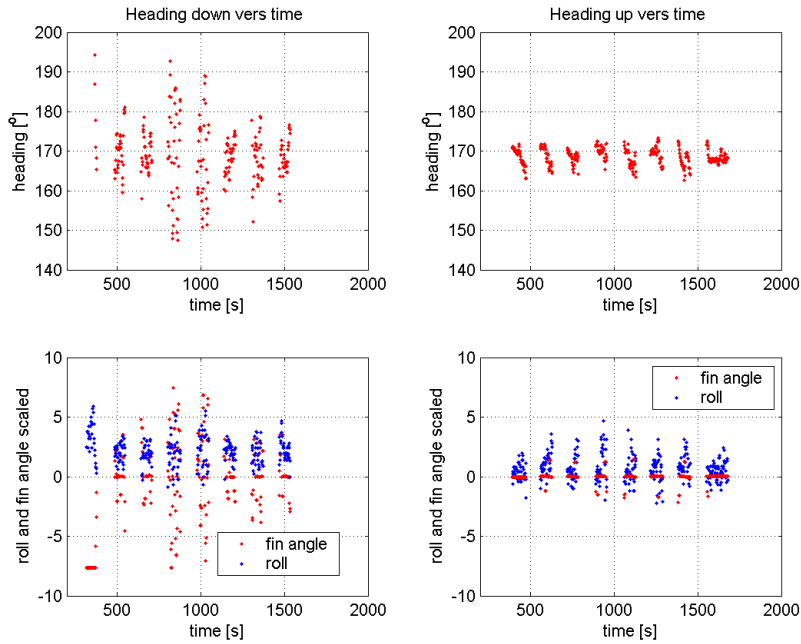


Figure 6.14: Heading, roll and rudder ($\div 6$) in upwards vs. downwards glides, Buzzards Bay 2/23/02. [1]. Data courtesy of David Fratantoni, WHOI.

Recommendations for Glider Control Systems

Modification of the controller structure, deadband, and timing would improve gliding performance and reduce control energy use. An initial step may be use of a more conventional, continuous, deadband function. Combined with changes to the control update timing, this could eliminate chattering or limit cycling in heading and pitch. An analysis of this subject using describing functions appears below. Other improvements are possible within the existing controller structure. For example, the heading control loop uses the same gain for upwards and downwards glides. In configurations with rudder-roll coupling, use of different gains for upwards and downwards glides would improve performance (see Section 4.3). Straight-flight rudder conditions for a given glider's static trim should also be determined for upwards and downwards glides and incorporated into the control system. Use of state feedback controller or proportional-integral controller would improve heading performance

and eliminate steady heading error.

6.3 Other Control Applications of the Glider Model

6.3.1 Adaptation and Parameter Identification

Incorporation of adaptive elements into glider control systems may produce significant performance improvements. Oceanographic gliders are deployed for extended periods, during which they perform similar or identical sawtooth glides and inflections hundreds or thousands of times. Durability and endurance are principle aims of their design. Even a simple system for identifying changes over time in a glider's performance, model parameters, and trim condition could be effective.

Gliders are propelled by relatively small differences in buoyancy (compared to their mass and volume) and their dynamics are sensitive to small changes in their buoyancy, static trim, and hydrodynamics. Changes in the glider's static trim and hydrodynamics are likely to persist for extended periods. For example, bio-fouling, or growth of marine organisms on the glider, was observed during Slocum glider deployments of only a few weeks in the Monterey Bay (during the AOSN II experiments). This is a significant problem for extended deployments of future glider designs. In other experiments, changes in a glider's upwards and downwards glide speed and trim over many dive cycles was determined to be due to gradual and intermittent intake of water into the glider body through a leak. Plant changes of these types could easily be accounted for using a simple adaptive controller system.

A simple adaptive control system could do the following:

- Perform a check-out dive after initial deployment and periodically thereafter, to iden-

tify the glider static and hydrodynamic trim conditions.

- Periodically or continuously identify and update the glider parameters and the control positions for a variety of steady glides.
- Adapt to changes in water density. This could use the glider dynamic model and the CTD sensor (to determine the water density).
- Adjust controller parameters such as control update timing and deadband size. For example, dive performance and the average properties of environmental disturbances in past dives may be used to adjust the control update interval.
- Identify gradual changes in performance that may lead to loss of the vehicle (for example, changes in buoyancy due to a slow leak or bio-fouling).

Many of these adaptive elements involve straightforward application of the glider dynamics model, equilibrium equations and parameter identification methods already described. More advanced methods are available in the literature on adaptive control and system identification.

6.3.2 Control of Inflections

Inflections between upwards and downwards glides present a special control task. During these unsteady motions the glider crosses through a region, about the zero pitch and glide path angles, where steady gliding is not possible. This distinguishes inflections from transitions between two glides in the same vertical direction, where the glider may slowly transition through a number of steady glides. Controlled inflections are necessary for accurate navigation and efficient gliding. This requires:

- Maintaining the desired heading,

- Maintaining forward momentum,
- Avoiding large α or β and separation or stall,
- Minimizing actuator energy use.

A variety of controlled inflections, including open-loop and closed-loop controlled inflections, have already been presented in both simulation and in experiment. Existing oceanographic gliders are designed for static stability in steady glides, and experiments and simulation have shown that the regions of attraction of these steady glides are large. Therefore, inflection may be controlled using either open-loop or closed-loop control, or some combination of the two, for example closed-loop control including some ‘feed-forward’ terms moving the actuators to their new positions.

Our experiments with Slocum gliders and anecdotal reports of inflection performance of Seaglider and Spray show that the relative timing and speed of the actuators is significant to a smooth inflection.

Eriksen [14] describes an instance of poor inflection performance during tests of Seaglider. In a test of the Seaglider, when inflecting to an upwards glide, the sliding battery mass was moved to its new position much faster than the ballast pumping. This resulted in the glider pitching up while still moving downwards and negatively buoyant, producing a rise as the glider’s momentum is dissipated, followed by a period of gliding downwards because the glider is still negatively buoyant. “This has the effect of driving the glider slowly backwards, an unstable configuration that causes it to change heading sharply” [14]. The Seaglider researchers corrected this problem by changing the pitch inflection control. “In later deployments, the glider pitches up only partially until [buoyancy] becomes neutral before pitching up to its desired ascent value” [14].

Some problems in inflection were observed first-hand (visually and with sensors) in our January 2003 tests of the Slocum glider, for example, large pitch angles, changes in heading, and periods of stopped motion (for some tests and control gains). One difference in the Slocum glider is the link between its pitch and net buoyancy due to the location of the ballast tank.

Adjustments of the glider controller and timing, and implementation of the inflection controllers described already, are sufficient for inflection control of stable, relatively slow, oceanographic gliders. Their transitions are relatively gradual and the angles of attack shown in simulations are fairly small. The static moments on the gliders are larger or of the same magnitude as the hydrodynamic moments. Their stability during inflections has already been demonstrated

In more aggressive inflection maneuvers, for example, those in much faster gliders, statically unstable gliders, or those with radical body shapes, modelling and control of inflection may require inclusion of additional (and more complicated) terms in the hydrodynamics model. The unsteady hydrodynamics of the glider may be very complex, especially in a glider moving at high speeds.

Another measure of inflection performance is the net change in depth required to perform an inflection or a sawtooth glide. This depends on the glider actuators and inflection controllers. Some applications, such as littoral operations, require a small inflection depth. Fast turnaround depends on maximum pumping speed and high mass actuator speed. Oceanographic applications could also require gliding within a narrow depth band or many crossings of a given depth, perhaps at an interface between ocean layers.

Existing gliders can glide and inflect in only a few meters of water. Slocum Electric is designed for shallow water application; its ballast system may be geared for gliding in as

little as four meters of water (i.e., operate and perform entire sawtooth glides). Other gliders are designed for use at deeper depths, so inflection speed and distance is less critical. Their ballast systems are designed for efficiency and maximum depth, not speed of inflection. For example, the typical inflection depth change for Spray is four meters [63]. That is, when gliding downwards at steady glide condition, the Spray glider will continue downwards for about four meters after it begins its pumping for inflection.

Inflection speed and performance depends on the steady glide path angles and control inputs, so shallower inflections are possible for both gliders with modification of their actuators and control schemes.

6.3.3 Intermittent Control and Deadbands

As described, controllers for oceanographic gliders make use of deadbands and intermittent control updates for the purpose of energy conservation. The effect of these control elements on overall energy conservation depends on the glider's dynamics and the environmental disturbances on the glider. In some cases, frequent controlled use of actuators, moving the internal masses or rudder, may use less energy than would be required to correct errors in heading and position after an extended period of open-loop gliding.

Consider two possible extremes. The first is gliding in completely calm water. With no disturbances and perfect knowledge of the system, the glider can navigate accurately under only open-loop control. Control actuators are used only for inflections and changes between steady glides, and little energy is used for control. The opposite extreme is gliding in an environment under constant and varying environmental disturbances, for example, in a river or littoral area with significant currents, upwellings, variations in density, etc. In this case frequent or continuous control is required for accurate navigation. Without this,

correcting navigation errors accumulated over time may require significant pumping work. In existing oceanographic gliders, pumping accounts for as much as 75% of the total glider energy budget. Therefore, errors in position are energetically expensive.

Because a properly designed oceanographic glider is stable in pitch and approximately neutrally stable in heading, accurate control of heading will likely require more frequent actuation than control of pitch. Experimental examples include tests in the VERT series of experiments with Slocum WE01 with fixed actuators. The glider's pitch is stable, but there is significant accumulated heading error. Published accounts of experiments with the Seaglider [14] give another example. During one Seaglider test glide, with control interval set to five minutes, the heading drifts by forty degrees within this interval, requiring a turn to correct it.

6.3.4 Controller Induced Limit Cycles: Describing Function Analysis

In this section a describing function analysis is used to determine the existence and stability of limit cycles (self-sustained oscillations) in the glider's controlled dynamics.

Nonlinear elements of the control system are approximated, using describing function $N(A, \omega)$ as a linear gain that is a function of input amplitude A and frequency ω . Stability of the equilibrium and existence and stability of limit cycles in the (approximated) nonlinear system are determined using a Nyquist-based analysis [64, 71, 19]. This analysis uses sinusoidal-input describing functions. Limit cycles predicted by this method are solutions of $G(j\omega) = -\frac{1}{N(A, \omega)}$. If this equation has no solution, no limit cycles are predicted.

The describing function method is an approximate method, and it gives only a prediction of the existence of limit cycles. The amplitude and frequency of predicted limit cycles are often inaccurate. The results are also dependent on the validity of the filtering hypothesis.

See [64, 19]. Experiments and simulation of the full nonlinear system may be used in further analysis, to confirm the existence of limit cycles, and to more accurately determine limit cycle amplitude and frequency.

The accuracy of the describing function analysis depends on the angle of intersection of the $G(j\omega)$ locus with the $-\frac{1}{N(A,\omega)}$ locus. In the case of frequency-independent describing functions, “if the $-\frac{1}{N(A)}$ locus intersects the G locus almost perpendicularly, then the results of the describing function are usually good” [64]. The systems analyzed in this section all have locus intersections that are close to perpendicular.

As shown in the previous experimental examples, it is possible for the deadband and intermittent control to generate limit cycles and actuator chatter (that would not occur without these control elements). This is a function of the controller parameters and the vehicle dynamics. These types of limit cycles are highly undesirable because they lead to frequent actuator use, produce errors in tracking the desired glide, and are energetically inefficient. Their existence is directly contrary to the original purpose of the nonlinear controller elements. Here we neglect the intermittent timing to first examine the effect of deadbands and saturation on a continuous controller.

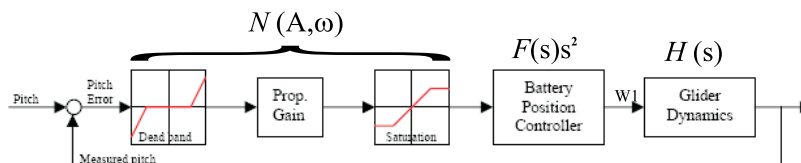


Figure 6.15: System with describing function.

Figure 6.7 shows the glider pitch control loop. Figure 6.15 shows the pitch control loop arranged for the describing function analysis. Linear elements $F(s)$ and $H(s)$ represent the sliding mass actuator and the glider dynamics linearized about the equilibrium. In oceanographic gliders the ballast mass is generally fixed during a steady glide, so here the

glider pitch control dynamics are represented by the transfer function $H(s)$ from input $w_1 = \ddot{r}_{p1}$ to output θ .

Properly designed, a glider is statically stable in pitch (i.e., with fixed internal masses and controls). If the glider parameters are known exactly, open-loop pitch control may be used to reach a desired equilibrium. However, in real-world applications some plant variation and uncertainty are inevitable. Therefore use of feedback is desirable. Feedback may also be used to improve disturbance rejection.

For the glider parameters used in previous examples, and given in Table 4.2, the transfer function from input w_1 to output θ , with linear pitch damping parameter $K_{\Omega^1} = 50$, is

$$H(s) = \frac{-0.006006 s^4 + 0.0006985 s^3 - 4.886 s^2 - 1.759 s - 0.04088}{s^5 + 0.5804 s^4 + 0.2795 s^3 + 0.1177 s^2 + 0.002823 s}. \quad (6.3)$$

Note that the glider pitch is open-loop stable for linear pitch damping coefficient $K_{\Omega^1} > 0$.

The sliding mass actuator may be represented by a second-order transfer function with an electrical and a mechanical time constant. A feedback controller for the actuator may also be included in the system. The sliding mass actuator transfer function, from input to position r_{p1} , is $F(s) = \frac{1}{(T_1 s + 1)(T_2 s + 1)}$. Multiplying $F(s)$ by s^2 gives actuator output \ddot{r}_{p1} . Let $G(s) = F(s) \cdot s^2 \cdot H(s)$ be the forward loop transfer function.

The dynamics of the sliding mass actuator influence the total system stability. Time delays in feedback systems generally contribute to instability. Slower actuator dynamics have a similar effect in this system. To concentrate first on analysis of the nonlinear control elements and the glider dynamics, model the sliding mass actuator as much faster than the glider pitch dynamics, with zero steady error. Setting $T_1 = 0$, $T_2 = 0$, makes the actuator a unity gain. Adopting a slower actuator moves the intersection with the negative real axis

of the Nyquist plot of $G(s)$ to the left (reducing the system gain margin).

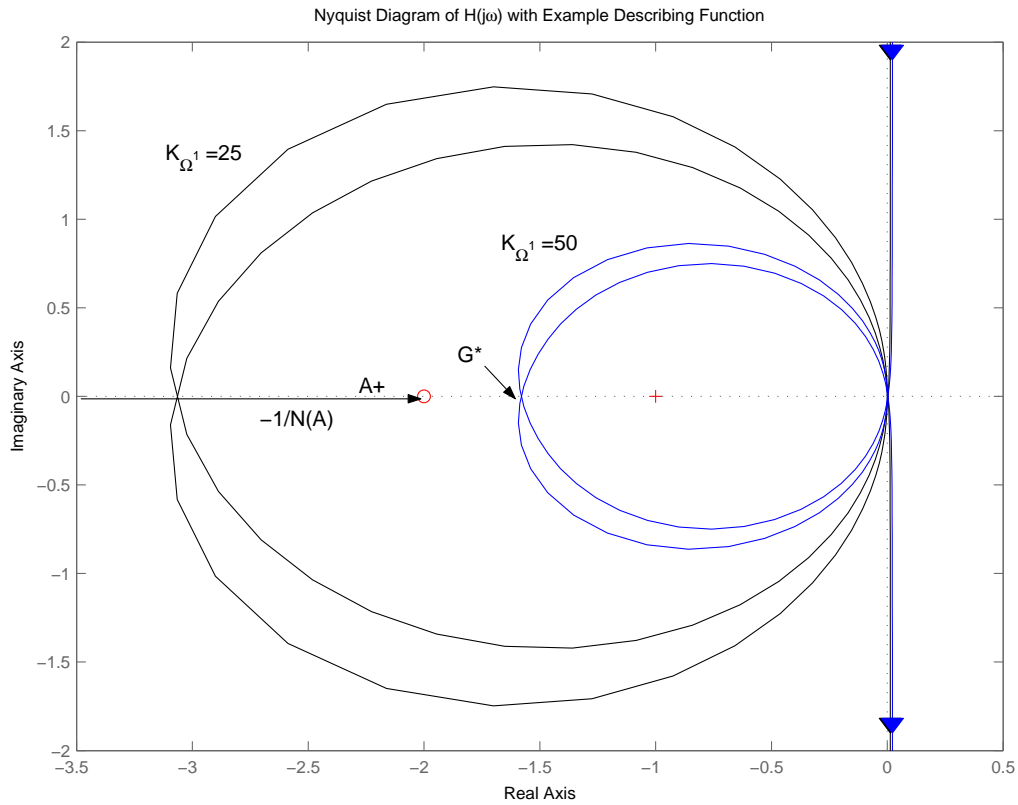


Figure 6.16: Nyquist Diagram.

Figure 6.16 shows the Nyquist plot of $G(s)$ for $K_{\Omega 1} = 25$ and $K_{\Omega 1} = 50$ and $T_1 = 0$, $T_2 = 0$. For convenience, define ω^* and G^* such that $\angle G(j\omega^*) = -180^\circ$ and $G^* = |G(j\omega^*)|$ to specify the point where the Nyquist plot of $G(j\omega)$ crosses the negative real axis. An example plot of $-1/N(A)$ for some frequency-independent describing function (here it could be a deadband) is shown. The direction of increasing A and the maximum value of $-1/N(A)$ are shown. Let $N_{max} = \max(N(A))$. If the Nyquist and describing function plots intersect, define A^* as the amplitude at that point, $G^* = -1/N(A^*)$. For multiple intersections, define A_i^* in increasing order, $A_1^* < A_2^* < \dots$.

Stability of the closed-loop system is determined using the Nyquist criterion, $Z = N + P$, and its extension. The open-loop transfer function has no RHP poles ($N=0$ for $K_{\Omega 1} > 0$).

Therefore, for forward loop proportional gain K , the intersection of the Nyquist plot with the negative real axis determines P , the number of encirclements of the $-\frac{1}{K}$ point. If $P > 0$ then $Z > 0$ and the closed-loop system is unstable. Note that the intersection of the Nyquist plot of $G(s)$ with the real axis moves to the left as linear pitch damping decreases.

For deadbands, saturation, and other frequency-independent describing functions, $-\frac{1}{N(A)}$ lies along the negative real axis, so closed-loop system instability and existence of limit cycles occur under the same conditions. Intersections of the Nyquist plot of $G(s)$ and $\frac{-1}{N(A)}$ predict the existence and stability of limit cycles in the closed-loop system with the non-linear element (within the limitations of the describing function method and assumptions). Each intersection corresponds to a limit cycle. “If points near the intersection and along the increasing- A side of the curve $-1/N(A)$ are not encircled by the curve $G(j\omega)$, then the corresponding limit cycle is stable. Otherwise, the limit cycle is unstable” [64].

Nonlinearity	$f(x)$		$N(A)$	
Deadband (DB)	0	$ x \leq \delta$	0	$A \leq \delta$
	$K(x - \text{sgn}(x)\delta)$	$\delta < x $	$K[1 - \text{satf}(\frac{\delta}{A})]$	$\delta < A$
Slocum DB	0	$ x \leq \delta$	0	$A \leq \delta$
	Kx	$\delta < x $	$\frac{4K\delta}{\pi A} \sqrt{1 - \text{satf}(\frac{\delta^2}{A^2})} + K[1 - \text{satf}(\frac{\delta}{A})]$	$\delta < A$
Saturator	Kx	$ x \leq \delta$	K	$A < \delta$
	$K\delta \cdot \text{sgn}(x)$	$\delta < x $	$K \cdot \text{satf}(\frac{\delta}{A})$	$\delta < A$
DB + Sat.	0	$ x \leq \delta_1$	0	$A \leq \delta_1$
	$K(x - \text{sgn}(x)\delta)$	$\delta_1 < x < \delta_2$	$\frac{K}{\delta_2 - \delta_1} [1 - \text{satf}(\frac{\delta}{A})]$	$\delta_1 \leq A \leq \delta_2$
	$K\delta \cdot \text{sgn}(x)$	$\delta_2 < x $	$K \cdot \text{satf}(\frac{\delta_2}{A} - \frac{\delta_1}{A})$	$\delta_2 < A$

Table 6.1: Controller and actuator nonlinearities and describing functions.

Table 6.1 shows four controller and actuator nonlinearities and their describing functions

$N(A)$. $\text{sgn}(x)$ is the sign function and $\text{satf}(x)$ is the saturation function,

$$\text{satf}(x) = \begin{cases} -1 & x < -1 \\ \frac{2}{\pi}(\sin^{-1} x + x\sqrt{1-x^2}) & |x| \leq 1 \\ 1 & 1 < x. \end{cases}$$

Figure 6.17 show the four nonlinear elements, plots of their describing functions, and sketches of $\frac{-1}{N(A)}$ on the complex plane. The arrow shows the direction of increasing A . For the saturator with deadband, $\frac{-1}{N(A)}$ moves from left to right, then reverses. The saturator with deadband is a reasonable model of a controller with a deadband and a mass actuator with a maximum force or acceleration. Figure 6.18 shows these describing functions for comparison.

Control Element	Case	Eq. Stable?	Limit Cycles (A^*, w^*)
Linear K	$G^* > -1/K$	stable	none
	$G^* < -1/K$	unstable	none
Deadband (DB) and Slocum DB	$G^* > -1/K$	stable	none
	$G^* < -1/K$	unstable for $A > A^*$	one, unstable
Saturator	$G^* > -1/K$	stable	none
	$G^* < -1/K$	unstable ($0 < A < A^*$)	one, stable
Saturator + DB	$G^* > -1/N_{max}$	stable	none
	$G^* < -1/N_{max}$	unstable ($A_1^* < A < A_2^*$)	unstable at (A_1^*, w^*) stable at (A_2^*, w^*)

Table 6.2: Describing function analysis results: stability and limit cycles.

Table 6.2 shows the results of the describing function analysis. For each nonlinearity, the possible cases, their stability and limit cycles are shown. Note that

- Any instability of steady glides is undesirable.
- For the same K and $G^* < -1/K$, the proportional gain controlled system equilibrium is unstable with respect to any disturbance ($A > 0$), the Slocum deadband controlled

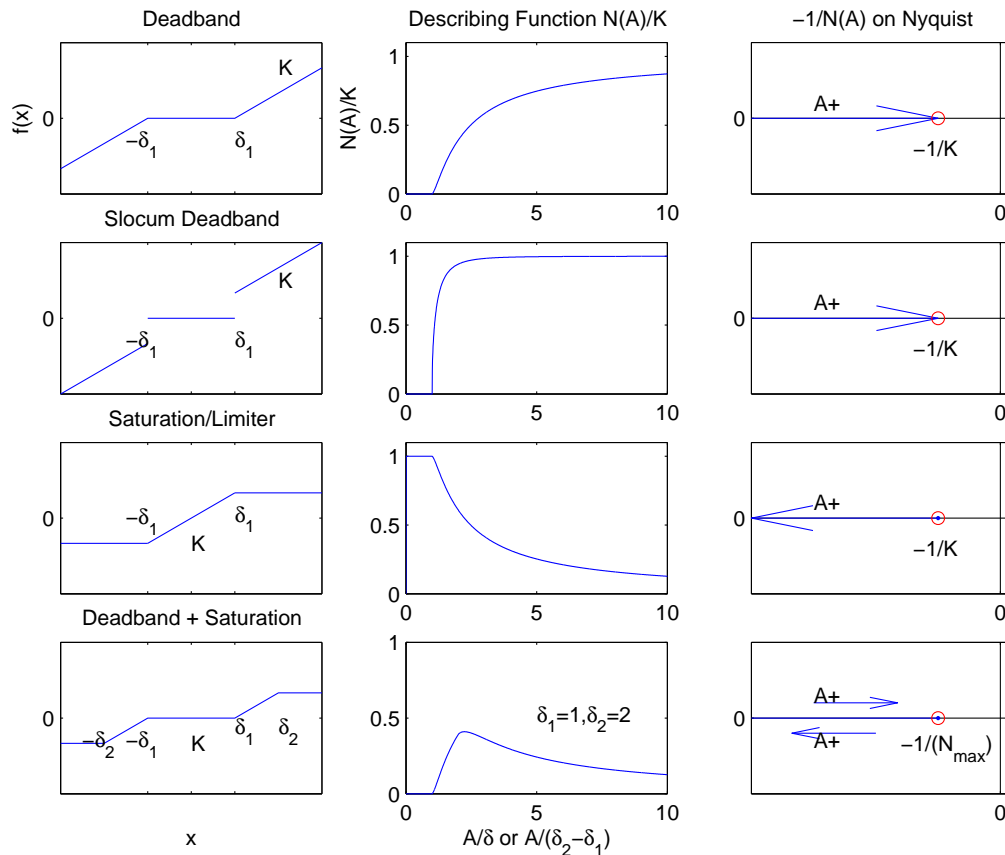


Figure 6.17: Nonlinearities, describing functions, and plots on Nyquist plane.

system equilibrium is unstable for some $A > \delta$, and the conventional deadband is unstable with respect to some larger A .

- For both types of deadbands, A^* is always greater than deadband size δ . If the deadband extended to the full pitch range, the control and mass actuator would never turn on and the (stable) glider pitch dynamics would settle to their equilibrium.
- The deadband nonlinearities alone cannot generate a stable limit cycle.
- In application there is always some disturbance $A > 0$, so if the system with saturator is unstable the disturbance amplitude A has little practical meaning.
- The saturator with deadband can have two limit cycles, one unstable and one stable.

The stable limit cycle occurs at a higher A than the unstable limit cycle. The stable limit cycle appears due to the saturation nonlinearity.

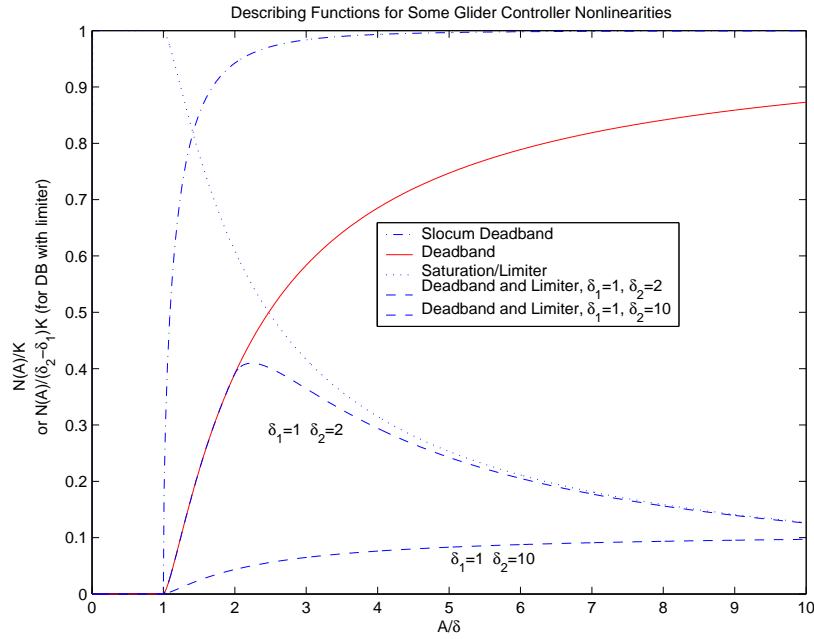


Figure 6.18: Comparison of describing functions. Note scaling of saturator/limiter with DB is different than other describing functions shown.

6.4 Chapter Summary

In this chapter, the glider model is applied to the systematic design and analysis of a glider control system and the control systems of existing oceanographic gliders. It is shown that application of the model and an understanding of glider dynamics can improve glider control, navigation and inflection performance. Improving the glider control system should result in greater glider speed and range and improved scientific utility.

The analysis begins with control of equilibrium steady glides in the glider longitudinal plane model. The steady glides identified in Chapter 4 are shown to be linearly controllable and observable. The steady glides are controllable for two gliding objectives: gliding with a

given direction and speed, and gliding along a prescribed line. Controllability is maintained in the case when r_{p3} of the sliding mass is fixed. If we are interested in controlling only the direction and speed of the glide, the steady glides are shown to be linearly observable, given a limited set of sensors (smaller than that available on oceanographic gliders). If the glider is to be controlled to a prescribed line in the plane, some dead reckoning must be used to track the glider's horizontal position. A method for combining this dead reckoning with a dynamic observer for the other states is presented.

We demonstrate the design of a LQR controller with observer for a steady glide. Controlled planar gliding is demonstrated in simulation. Controlled gliding with inflections is also demonstrated. Inflections are performed by switching from one glide controller to the next. This involved controlling the glider to steady glide A, using the controller for glide A, and then turning off controller A and turning on the controller for glide B. The glider is then controlled to steady glide B.

This chapter also includes an analysis of control systems on operational gliders. A typical oceanographic glider controller is described. These use linear controllers for pitch and heading. They are designed and tuned from experience or from some linear analysis. The glider model presented here provides a method for systematic analysis and improvement of these controllers.

We present results from control experiments at sea using Slocum gliders. Test glides using the existing glider control system under different control gains and parameters demonstrate the importance of properly control gain tuning and control analysis. Test flights are shown which demonstrate slow pitch control response and controller induced pitch oscillations. Using the understanding of glider dynamics developed from the glider model, corrections to the controller timing and gains are made and improved gliding performance

is demonstrated.

Glider heading control is also analyzed. In at-sea experiments, the glider controller's deadband, gain and update timing are shown to produce some control chatter in the rudder when the glider has some mis-trim. Glider static mis-trim and rudder-roll coupling are both shown to have an effect on glider heading control. Modification of the glider deadband function, use of separate heading control gains for upwards and downwards gliding, or application the state feedback controller derived in this chapter are possible steps to improve heading performance.

When designing a glider controller, it is important to take the glider dynamics into account, including the effect of mis-trim, rudder-roll coupling and inflections between upward and downward gliding. The glider model provides a systematic way to do so. Energy conservation is also major concern in controller design. Use of deadbands, intermittent control timing, and other control elements may help conserve energy. It is important to analyze and test these elements so they do not introduce problems that actually increase energy use. Towards this end, the glider model is applied to a describing function analysis of these control system nonlinearities. This analysis shows that, under certain conditions and control gains, the deadband and saturator nonlinearities in the glider control system may destabilize a steady glide or produce a stable limit cycle. Such limit cycles result in significant actuator application and energy consumption and should be avoided.

Chapter 7

Glider Design

This chapter describes application of the glider model to the design of underwater gliders. The glider model, derived in Chapter 3, is applied to the analysis of existing gliders and to the study of possible future glider designs, including tradeoffs in glider design and scaling rules for underwater gliders. The analysis here makes use of the glide equilibria derived in Chapter 4 and the results of subsequent chapters, including the experimental tests of steady glides in Chapter 5. Parts of this Chapter appeared in [32], which provides an analysis of many related topics in glider design.

This chapter is arranged in the following sections:

Section 7.1 compares underwater gliders and sailplanes, with the aim of developing an intuitive understanding of underwater gliders based on an understanding of aircraft.

Section 7.2 analyzes scaling rules for glider steady glide performance, including glide speed versus ballast loading, glide angle, and glider volume.

Section 7.3 provides a general overview of glider design requirements and covers preliminary design of underwater gliders, including sizing, body and wing geometry, and study of

the trade-offs in using alternate glider designs such as flying wings, blended wing/body designs, and gliders with moveable wings and external control surfaces.

Section 7.4 discusses conventional oceanographic glider designs and possible alternative designs, including flying wing configurations. These designs are suited to different glide path angles and mission requirements. Differences between the two are discussed. Flying wing designs offer higher maximum lift/drag ratios, but this is advantageous only at small glide path angles. Existing gliders are designed for steep glide path angles to give maximum speed for a given ballast size. A flying wing configuration is suited to shallower glide path angles, which give greater horizontal travel for a given amount of pumping work and give speeds below the gliders's maximum. The choice of a conventional glider design or a flying wing must take into account the specific requirements of a glider's mission.

References [80, 63, 14] discuss the design and construction of Slocum, Spray and Seaglider. These gliders are all designed for ocean sampling and are similar in size. They will serve as a starting point for an investigation of glider design. Glider design is also discussed in [32] and in Chapter 2. These describe the designs and applications of existing oceanographic gliders.

A principal challenge in the design and operation of underwater gliders is power conservation and management. This must be taken into account in every step of glider design and operation. Because glider missions require extended deployment and long ranges, limited on-board power reserves must be carefully managed. In the case of electrically powered gliders, the on-board batteries must provide all energy for both pumping work and electronic loads, including sensors, computers and communication. Pumping makes up 60 % to 85 % of the total energy budget of existing gliders, depending on the mission use [12].

Examining the existing gliders and their missions allows us to determine some general parameters for glider design. These include size, range, endurance, speed, depth, and payload.

Consider, in preparation for an examination of glider design, some general characteristics of underwater gliders.

1. Gliders glide in a sawtooth pattern. They glide upwards and downwards at negative and positive glide path angles and angles of attack. Existing oceanographic gliders are designed to be top-to-bottom symmetrical because of this gliding motion.
2. Conventional gliders operate at steep glide path angles (about 35 degrees). These are steeper than typical glide path angles for sailplanes (under 5 degrees). This leads to different sizing of the underwater glider body and wings and requires much lower operational lift/drag ratios in underwater gliders than in sailplanes and aircraft. Designing an underwater glider for shallow glidepath angles would similarly require high lift/drag ratios.
3. Gliders control their buoyancy and attitude with internal ballast systems and sliding masses. This provides their propulsion force and also their pitch and roll stability, which results principally from the separation between the glider's centers of gravity and buoyancy. Gliders may also use external moving surfaces including rudder, flaps and ailerons.
4. Gliders are power limited. Range and speed are limited by on-board power stores. This leads to design tradeoffs between range, endurance and speed. Existing oceanographic gliders are designed for long range and endurance and low power use. Efficient gliding is critical to performance.

5. Existing gliders have limited speed. Analysis in this chapter shows that it is possible to design gliders that are significantly faster by increasing the overall size of the glider or by increasing the ballast size relative to the glider's size. Designing faster gliders involves tradeoffs in size and power use, but may be desirable for some applications.
6. Existing gliders are significantly affected by ocean currents. Currents may be of the same order or greater than glider speeds. Operating speeds are designed to overcome expected average currents.
7. Dive depth is important to glider power efficiency (due to existing pumps). Glider maximum depth is limited by structural strength or by ocean bathymetry. The pump systems in Spray and Seaglider, for example, are more efficient at deeper depths.

7.1 Gliders vs. Sailplanes

It is useful to develop an intuitive understanding of the differences between underwater gliders and sailplanes. This comparison facilitates application of existing knowledge of aircraft dynamics and control to underwater gliders.

A principal difference between underwater gliders and sailplanes is that water is much more dense than air - about 800 times more dense. The density of water is 1000 kg/m^3 , while the density of air at sea level is just 1.25 kg/m^3 . Because of this, buoyancy and added mass effects are very important in glider dynamics. These effects are generally neglected in sailplanes, but are significant for lighter-than-air aircraft. The high density of water makes the use of buoyancy and internal mass control possible in underwater gliders.

Some important differences between underwater gliders and sailplanes include:

1. Gliders control their buoyancy. One can imagine flying in a sailplane equipped with

a dial that controls the magnitude of gravity or the density of the sailplane, making it “light as air”.

2. The relative magnitudes of the propulsive forces, as a fraction of the vehicle dry weight, are much smaller in underwater gliders. On sailplanes, the full weight of the sailplane provides the propulsive force. On underwater gliders the controlled buoyant force is relatively small compared to the vehicle dry weight and may be positive or negative. In this aspect, gliders are similar to lighter-than-air craft (such as blimps). Slocum Electric, for example, has a maximum net buoyancy of 250 grams and a mass of 50 kg. Because of this the accelerations and terminal velocities of underwater gliders are smaller (relative to the vehicle weight and size) than in sailplanes.
3. In an underwater glider, the separation between the center of gravity and center of mass provides stability. This makes control of the glider using moving internal masses possible. Static torques can make the glider statically stable in pitch and roll, unlike sailplanes. The stability of a sailplane depends entirely on its aerodynamics. Sailplanes are controlled using moving aerodynamic flaps, ailerons and rudders, while their CG is normally fixed. Underwater gliders are similar to hang gliders, where the CG is moved as the pilot shifts their body.
4. Sailplanes and gliders operate at different glide path angles. Sailplanes are designed for maximum lift/drag performance and minimum glide path angle. Existing gliders are designed for steeper glide path angles and lower lift/drag ratios. This is related to the low speed and relative ballast size of these designs. See Section 7.2.3.
5. Underwater gliders and sailplanes operate in different flight regimes and Reynolds numbers (transitional or below for gliders, turbulent for most sailplanes) and at dif-

ferent glide angles. This leads to different hydrodynamic designs and wing sizing (See Section 7.3).

6. Because they control their buoyancy, gliders can choose their glide path angle and speed separately. Sailplanes have a fixed weight and buoyancy, so glide path and speed have a fixed relationship. This results in sailplane “speed to fly” requirements, since specific airspeeds give minimum sink rate, minimum glide path angle, and so on.
7. Both gliders and sailplanes must carefully manage power and energy. Sailplanes manage speed and height (kinetic and potential energy) and gliders manage power. They may use currents and winds to gain energy from the environment and travel efficiently. Sailplanes make extensive use of updrafts to gain height. In the ocean, vertical velocities are generally smaller than horizontal currents, so instead of using thermal updrafts, gliders may plan their paths to make maximum use of ocean currents.

7.2 Glider Design and Steady Glide Speed

Section 4.1.2 describes the determination of the steady glide equilibria for a glider, given the glider’s hydrodynamic and mass parameters. The design of the glider determines its geometry and these parameters. Because the parameters in the equilibria equations may be chosen during the design process, gliders may be designed differently for optimal performance at different steady glide conditions. For example, operating glide speed must satisfy design requirements given expected currents in the area of operation.

Figure 7.1 shows the minimum possible glide path angle corresponding to a glider’s maximum lift/drag ratio, determined from the glider equilibrium equations (Chapter 4). This figure may also be read as the glide path angle corresponding to a given operational

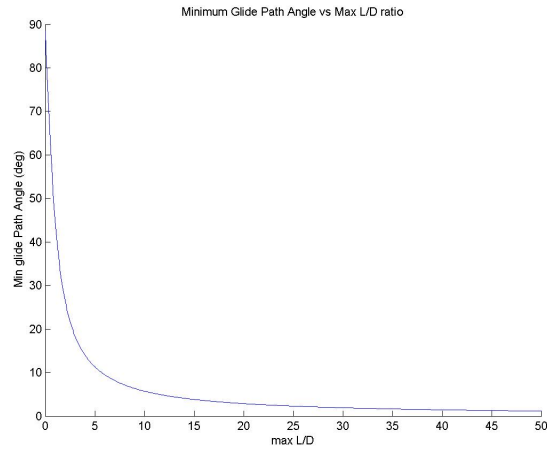


Figure 7.1: Minimum glide path angle vs. maximum lift/drag ratio.

lift/drag ratio. A glider’s maximum lift/drag ratio is determined by its wing and body design. The choice of steady glide path angle determines the lift/drag ratio required in steady flight. Glide path angles steeper than ten degrees require operational lift/drag ratios under five (which would be very low for an aircraft or sailplane). Existing gliding designs fall within this range of lift/drag ratios and glide path angles. If a very small glide path angle is desired, a glider with a very high lift/drag ratio must be designed. Figure 7.1 shows that there is a point of diminishing returns if one is designing a glider with a very high lift/drag ratio in order to attain a very small glide path angle. It will be shown that for maximum glider speed it is more important to minimize the drag on the vehicle than to have a high lift/drag ratio.

Section 4.1.2 reveals a number of interesting properties of steady gliding equilibria. These have some important implications for glider design. First, glide path angle and the speed of the glide may be chosen independently. This is a consequence of the glider’s pitch and buoyancy control. A glider’s range of possible steady glide path angles is a function of its lift/drag profile and the range of its pitch control actuators. The minimum shallowest glide path angle is fixed by the glider’s maximum lift/drag ratio as shown above. The

steepest possible glide is straight down (or up), provided the glider actuators can reach that pitch angle. Maximum glide speed is determined by the balance of the glider's drag and maximum net buoyancy.

Section 4.1.2 shows that a given steady glide corresponds to a range of internal sliding mass positions. The equilibrium mass position balances the hydrodynamic moments on the vehicle. A range of positions along a vertical line is therefore possible, given the limits of travel of the internal mass. The vertical position of the sliding mass affects separation between the glider CB and CG, which affects the glider's stability. In the existing gliders the sliding mass is constrained to travel along the glider's long axis, so one position of the sliding mass will result in one pitch angle. Alternate designs could add degrees of freedom to the internal mass actuator. This could allow the glide stability to be changed in flight. This could be used during transitions between steady glides, for example to reduce the glide stability for faster inflections and to increase it during steady glides.

7.2.1 Glide Speed vs. Ballast Load and Energy

For a given glider geometry and lift/drag distribution, each glide path angle corresponds to a given angle of attack. The speed along the glide path is then a function of the drag on the glider and the buoyant force component along the glide path. We can substitute and re-arrange the glider equilibrium equations (5.1)-(5.5) and substitute in our quasi-steady drag model (Section 3.2.7) to solve for the glider total and horizontal speed:

$$V = \left(\frac{m_0 g \sin \xi}{\frac{1}{2} \rho C_D(\xi(\alpha))} \right)^{\frac{1}{2}} \quad (7.1)$$

$$V_x = \left(\frac{m_0 g \sin \xi}{\frac{1}{2} \rho C_D(\xi(\alpha))} \right)^{\frac{1}{2}} \cos \xi. \quad (7.2)$$

At an equilibrium steady glide, the lift L and drag D balance the glider's net buoyant force m_0g . The glide path angle is a function of the glider lift/drag ratio at the steady flight condition. The glider lift/drag polar and stall angle are determined by its hydrodynamic design.

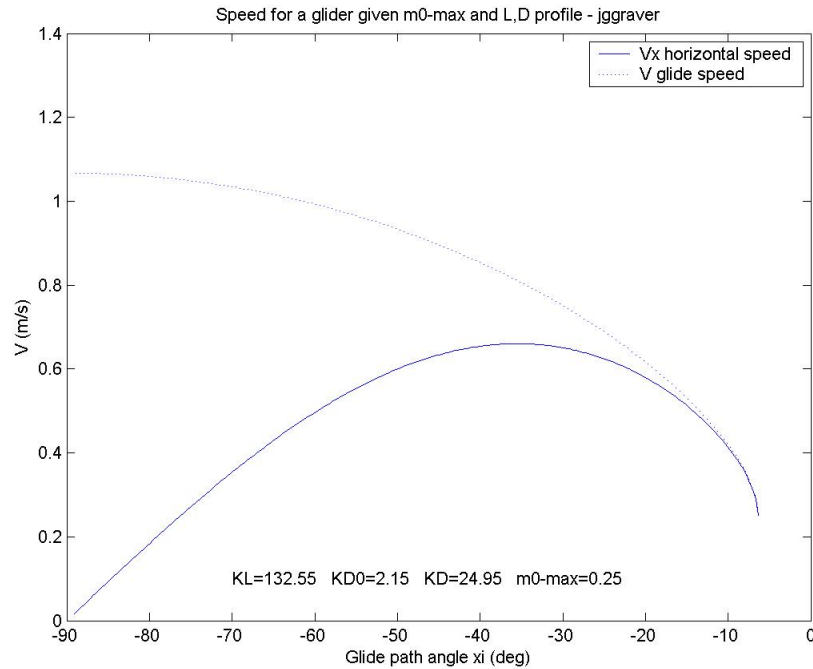


Figure 7.2: Conventional glider design speed vs glide path angle.

Figure 7.2 shows the glide speed and horizontal glide speed versus glide path angle for a glider with 250 g. net buoyancy and hydrodynamic parameters similar to the Slocum gliders. Downward glide path angles are shown. For a symmetrical glider, i.e. one that is symmetrical top to bottom, upwards glides would have the same magnitude glide speeds. A plot of the positive glide path angles would be a mirror of the above plot around the $\xi = 0$ axis.

Stall or separation effects may be taken into account by setting a maximum allowable α and minimum ξ . Stall may occur over the glider wings and body at high angles of attack.

Large angles of attack correspond to glides with small glide path angles. Stall angle of attack for the body and wings could be estimated and the corresponding glide path angles removed from the plot. The glider pitch actuation may also have a limited range, which could reduce the range of possible glide path angles for steady glides.

Two glide path angles, the shallowest possible glide path angle and the glide path angle giving maximum horizontal speed, are of special interest because they are extremes of performance. The shallowest glide path angle gives the greatest horizontal distance for a given depth change (and amount of pumping work). The glide path angle for greatest horizontal glide speed is determined by the glider's drag profile. In Figure 7.2 that angle is about 35 degrees. The shallowest glide path angle gives a relatively slow glide.

The fastest possible glide path angle is steeper, so more pumping work is required to travel a given distance. Maximum horizontal speed requires pumping the maximum ballast load and gliding at a steep glide path angle. Gliding faster will in general require pumping more ballast, both to reach higher ballast loads and because more sawtooth glides are required to travel a given distance. This results in more pumping work.

Choice of a steady glide path for glider operation requires tradeoffs between faster travel and increased pumping work per unit of horizontal travel. Depending on the glider's mission, the tradeoffs between speed and energy conservation will give a desired operational glide path angle. Consider a mission requiring transit between two points with minimum total power use. As time-based costs (for example, the glider hotel load) increase, the optimal travel speed increases. If hotel loads and time based costs dominate the cost of travel, the fastest glide possible is desirable. If pumping work dominates the costs of travel and travel time is not an important factor, gliding at shallower glide angles with smaller ballast amounts and lower speeds is desirable.

7.2.2 Glide Speed vs. Angle

Glider speed is important in many applications. A faster glider may be designed by adjusting the relative size of the internal ballast systems and using low drag geometries. A glider's maximum speed may determine where it is capable of operating and what missions it may perform. The expected currents in an area of operation could provide a design requirement for the glider maximum glide speed. A possible design requirement is that the glider should be able to make progress against the average or the maximum expected currents in the operational area.

Existing gliders, designed for oceanographic sensing, have speeds up to 0.4 m/s. Their design speeds were chosen according to expected average ocean currents, and have given reasonably good sampling capabilities. These gliders travel at relatively low speeds, especially when compared with propeller driven AUVs and ships. In some missions the gliders have had trouble moving against high currents. Other applications may require faster speeds. High speed travel could be important for applications in areas with high currents, such as in littoral areas.

In a steady glide, drag balances the component of the glider's net buoyancy acting along the glide path. The glide path angle determines what component of the buoyant force acts along the glide path. When gliding straight up or down the full buoyant force acts against the drag. This results in the maximum glide speed but provides no horizontal travel. At shallower glide paths, a smaller component of the net buoyancy will act against the drag, but a larger component of the total glider velocity will act in the horizontal direction. This results in a trade-off between glide angle and glider horizontal speed.

Figure 7.3 shows the function $\cos\xi(\sin\xi)^{(1/2)}$, a factor of the glider horizontal speed Equation (7.2), that depends on the glide path angle. This function is at a maximum

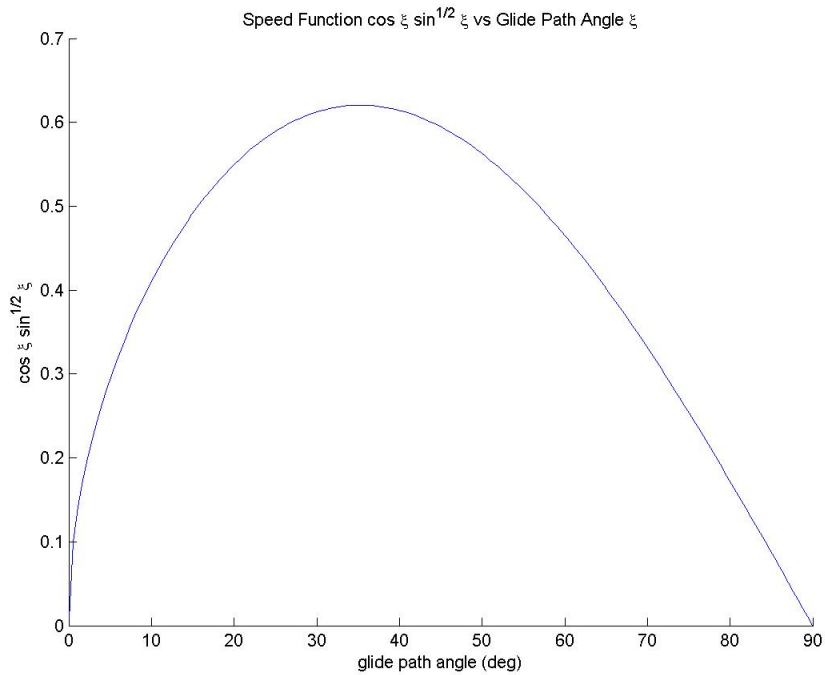


Figure 7.3: Component of Horizontal Glide Speed Equation, $\cos \xi (\sin \xi)^{(1/2)}$

around a glide path angle of 35 degrees and is independent of the glider hydrodynamics. If drag on the glider were independent of ξ , 35 degrees would be the fastest glide path angle. The overall speed of a glider depends on its lift/drag polar and the total drag on the glider as a function of ξ , so the fastest glide path angle for a given glider may be slightly different. A glider design for maximum horizontal speed should minimize drag at a glide angle near 35 degrees.

The equilibrium lift/drag ratio is fixed by the desired glide path angle. Because of the relationship between speed and glide path angle, a glider designed to maximize speed for a given ballast load need not have a high lift/drag ratio. A steeper glide path is necessary for maximum horizontal speed. Therefore, when designing a glider for maximum speed it is more important to minimize drag than to maximize lift. Design for speed requires a glider with minimum possible drag and wings just large enough to provide the required lift/drag

ratio for a given glide path. The fastest glide angle, around thirty-five degrees, requires a lift/drag ratio of only 1.4. This is significantly lower than the lift/drag ratios of sailplanes, which are around 20.

The body produces the majority of the drag on the vehicle, while the wings are much more efficient (lower induced drag) at producing lift. A fast glider design should minimize drag using a low drag body. Efficient, high aspect ratio wings should be sized to provide just enough lift for the fastest (near 35 degree) glide path and minimize the drag at that angle. Increasing the wing area beyond the optimal point increases drag at the desired (low) lift/drag ratio. Designing a glider for maximum speed (for a given ballast size) produces a glider design like Slocum, Spray and Seaglider. These have a streamlined body with relatively small wings and travel (at maximum speed) at glide path angles close to 35 degrees.

7.2.3 Speed vs. Volume and Ballast Fraction

Now consider maximum glider horizontal speed as a function of glider volume, geometry and ballast tank size. In many applications a glider will spend most of its time in steady flight upwards or downwards, so equilibrium speed should give a good idea of the glider's overall speed.

Using Equation (7.2), we can calculate maximum horizontal glide speeds as a function of glider volume (Vol) and ballast capacity. Drag on the glider body can be expressed as a function of volume and shape. $D = C_{D_{Vol}} \times Vol^{\frac{2}{3}}$, where $C_{D_{Vol}}$ is the coefficient of drag by volume determined by the glider body shape. Streamlined bodies such as those in the oceanographic gliders have a $C_{D_{Vol}}$ around 0.03. The maximum value of $(\sin \xi)^{\frac{1}{2}} \cos \xi$ is about 0.6 (see Fig 7.3). Using a glide path angle near that maximum and estimating an

additional twenty percent drag for induced drag, sensors and other additional sources of drag gives the following relation for maximum horizontal speed:

$$V_x = \left(\frac{m_0 g}{\frac{1}{2} \rho (1.2) (0.03) Vol^{\frac{2}{3}}} \right)^{\frac{1}{2}} \quad (0.6).$$

Define ballast fraction $n_b = (m_0)/(\rho Vol)$ as the glider's maximum net buoyancy divided by the glider's total displacement. Slocum Electric, for example, has ballast capacity for 250 grams net buoyancy, positive or negative, and a vehicle displacement of 50 kg. This gives ballast fraction for the Slocum of 0.005. If the ballast fraction is kept constant as glider volume is changed, then maximum horizontal speed scales with $Vol^{\frac{1}{6}}$,

$$V_x = \left(\frac{n_b g Vol^{\frac{1}{3}}}{\frac{1}{2} \rho (1.2) (0.03)} \right)^{\frac{1}{2}} \quad (0.6) \propto Vol^{\frac{1}{6}}.$$

If volume is kept constant and the ballast fraction increased, horizontal speed scales with $n_b^{\frac{1}{2}}$. Figure 7.4 shows glider maximum horizontal velocity versus glider volume for different ballast fractions.

It is therefore possible to design gliders that are much faster than existing gliders by using larger ballast fractions. Note that larger ballast fractions require greater pumping work. A glider need not always operate at maximum net buoyancy. It is possible for a glider to have a large ballast fraction, giving a high maximum speed, and to pump less than the full ballast load in order to reduce pumping work when travelling at slower speeds.

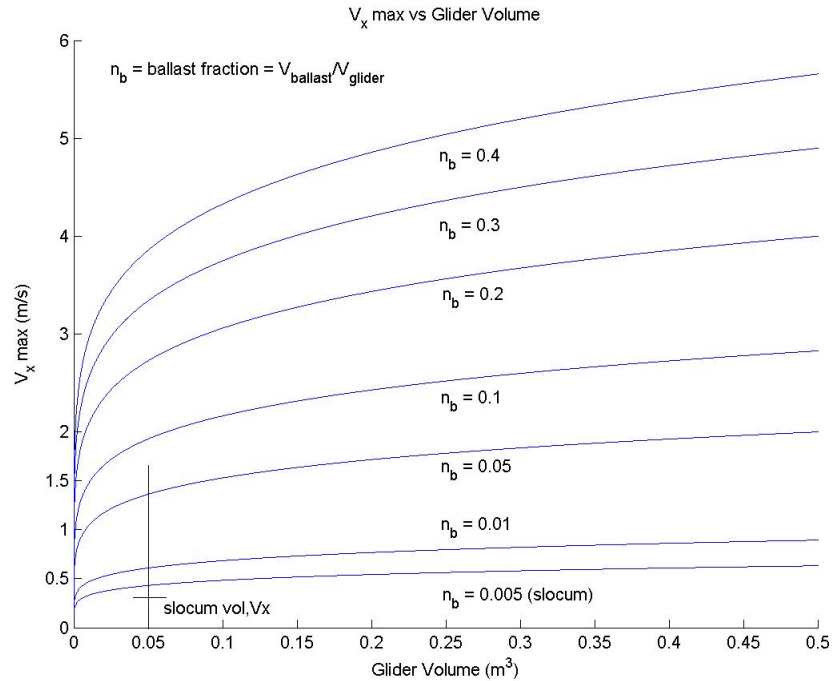


Figure 7.4: Maximum horizontal velocity vs glider size and ballast fraction.

7.3 Preliminary Glider Design

The first steps in designing a glider include determining the mission requirements, sizing the main components, and choosing an initial vehicle geometry. Mission requirements include range, endurance, speed and payload. These will determine the glider's power requirements. Power is frequently the most significant limiting factor in glider performance, so special attention to the power budget is required in all design phases. Power is always a critical factor in AUV design, and is even more so in glider design, given their extended missions. See [63] and [14].

The principal components of an underwater glider include the hull, wings and tail, ballast system, computer, control actuators, power supply (batteries) and payload. Given a set of mission requirements, for example for scientific sensing, the payload may represent a fixed volume, mass and power cost. The vehicle geometry and ballast system may be

determined by the desired steady glide performance. Battery size will be determined by the range and speed requirements and other loads, including the payload. The design process normally requires many iterations and trade-off studies.

The order in which the mission requirements are prioritized and addressed in the design process has a significant effect on the resulting design. For example, the first requirement for a glider may be size and volume. Slocum, Spray and Seaglidern have similar sizes and volumes (in the 50 kg range). Their design specifications required them to be a size that can be handled from a small boat. Determination of a body volume allows sizing of the glider wings and ballast tank. These are chosen according to the desired glide path angle and speed, which in turn are determined by the mission requirements and the expected operating conditions. A specific design limit on the glider volume is a major design parameter that limits the internal volume available for batteries, actuators, payload and other internal components.

In an alternate design process, volume may not be restricted. The design volume may then be varied in trade-off studies. A given mission, speed, range and payload could be specified first, with the glider volume determined that will best satisfy these requirements. Section 7.2.3 indicates that increasing glider size while maintaining the same proportional ballast size increases glide speed. Larger gliders may also accommodate more batteries, but increased ballast size will increase pumping work. The tradeoff between volume and range is a function of glide path, speed, glider volume, and battery size. In general, results presented here and in [32] suggest that larger gliders, with greater volume available for ballast and batteries, are capable of higher speeds and longer ranges. These results also show that the relative sizes of the glider, ballast tank and batteries have a strong influence on glider performance.

Larger gliders are likely to be more expensive and to require more equipment for deployment and retrieval, but a longer range may reduce other operating costs. Existing oceanographic gliders are sized for deployment and retrieval by two people from a small boat, however in many deployments a significantly larger boat and crew is already used. Overall operating costs must take into account the expense of these operations. Because gliders are relatively inexpensive to operate once deployed [13], the cost of frequent deployment and retrieval from a ship may represent a significant portion of total operating cost. Larger gliders with longer range, requiring fewer deployments and therefore less ship time, may have some cost advantages.

Once an initial estimate of the body, wing and ballast size has been determined, design tradeoff studies can compare smaller variations in these parameters and in the glider geometry. An initial design may use a glider layout like that of the existing oceanographic gliders, with some hydrodynamic improvements to the body and wings. The body may be designed to minimize the drag for a given volume. It is then possible to determine operating speed and glide path and to size the ballast system in order to satisfy design requirements. Glide path selection will determine the operational lift/drag ratio required in the design. This will drive the wing design. See, for example, [52, 26, 27]

7.3.1 Glider Hydrodynamic Design

A glider's shape determines its hydrodynamic properties, including lift and drag. Body shape and wing geometry are critical to glider performance. It is always desirable to minimize drag while providing an adequate lift/drag ratio for the desired range of glide path angles.

The drag on a glider may be divided into the profile (non-lifting) drag on the body and

wings and the induced drag from lift production. Lift is produced most efficiently by the wings. The desired operational glide path angle determines the necessary lift/drag ratio and the appropriate sizing of the glider wings relative to the body. The vehicle wetted surface area and wing reference area are important factors in the glider lift/drag ratio [52]. This is because the skin friction drag scales with the surface area of the body and wings while lift production scales with the wing area. Designing an optimal wing planform balances increasing lift/drag ratio with the increased skin drag of a larger wing surface.

Given a desired glider volume or mission requirements, a suitable hydrodynamic design must be chosen. The oceanographic gliders were designed with a fixed volume and a mission of extended range ocean sampling. Slocum, Spray and Seaglider make use of streamlined bodies of revolution and proportionally small wings. Spray and Slocum have bodies that are roughly torpedo shaped cylindrical bodies with smoothly tapered nose and tail sections.

In designs where the body will be at a low or zero angle of attack during flight, relatively simple streamlined bodies of rotation with optimal fineness ratios (length to width) may give the lowest drag shape for a given volume [26]. Proper design of the glider's body and wings can minimize profile drag through use of streamlined shapes and minimize induced drag through use of efficient wing shapes. These methods are well developed from aircraft and ocean vehicle design and are readily applicable to design of underwater gliders.

Existing gliders operate in a relatively low Reynolds number regime (order 10^5 by body length, 10^4 by wing chord). This is close to the transition between laminar and turbulent flow. Each of these flow regimes require specific hydrodynamic designs for the glider wings and body. See [26]. At low Reynolds numbers skin surface drag increases significantly. The formation of laminar separation bubbles over the glider's wing and body may also contribute significantly to drag and may create a net moment on the vehicle. Transition

and separation effects are highly dependent on small aspects of the vehicle geometry and surface features, and are difficult to estimate without experiments and CFD analysis.

Because of these effects, the hydrodynamics of a glider, especially the drag on a glider, depend strongly on the operating Reynolds number. Because the oceanographic gliders operate in this Reynolds number range, relatively small changes in glider speed and size may result in significant changes in the glider's performance. For example, adopting a slightly faster glide path angle and larger ballast load may in some cases reduce the glider's coefficient of drag.

Specialized body shapes for low Reynolds number flow may be considered. The Seaglider body is designed for a low Reynolds number flow. In comparison to a simple body of revolution, specialized bodies of this type may offer lower drag at their design operating condition. These specialized shapes may also have higher drag (in comparison to a simple body of revolution) outside of their design operating conditions (Reynolds number and angle of attack). Reynolds number effects are also of concern in the use of alternate glider designs such as flying wings (discussed below), because these designs may be sensitive to separation effects, especially in designs with large wingspans and high aspect ratios.

In the turbulent flow regime, wing design should maximize aspect ratio to reduce drag [52, 43]. In aircraft the wing span is limited by its structural strength and weight. This is not as significant an issue in gliders because the wing loads are much smaller. Therefore very high aspect ratios are possible. Wing geometry is, however, limited by Reynolds number concerns. In underwater gliders at low Reynolds numbers, increasing wing aspect ratio and reducing wing chord may actually increase the drag on the wing by reducing the Reynolds regime of flow on the wing into the transitional and low Reynolds number regimes. To account for these issues, wing design in the transitional region may require computational

and experimental optimization.

In a conventional glider design, drag on the wings is much smaller than the drag on the body. Therefore the question of wing design optimization may be less of a concern than minimization of the body drag. See [32] for a detailed drag breakdown of operational glider designs. Induced drag is a relatively small fraction of the total drag on the glider. Drag from the CTD or other external sensors may be significant. [14] states that experiments show the CTD may have up to 50 % as much drag as the body.

7.4 Conventional and Alternate Glider Designs

Given an initial design using a conventional glider layout, trade-off studies may optimize the glider hydrodynamics, sizing, speed and other design parameters. Some alternate hydrodynamic designs may also be considered. Possible modifications include the use of movable flaps and surfaces on the wings or all-moving wings. Asymmetrical gliding and wing designs may also be considered. More radical alternate design layouts, such as blended wing/body and flying wing designs, may also be compared. Three types of designs are of special interest:

1. The conventional glider design that is top-to-bottom symmetrical like Slocum, Spray and Seaglider.
2. Conventional designs, with streamlined body and wings, that incorporates moving wings, flaps, and other reconfigurable surfaces. Various combinations of moving aerodynamic surfaces may adjust at each inflection to optimize the glider's hydrodynamics. Also possible is a glider optimized for one angle of attack which rolls over 180 degrees when switching between upwards and downwards glides.

3. Flying wing designs, which maximizes the glider's wetted area ratio and lift/drag ratio. Blended wing-body designs may also be considered.

As shown previously, different glide paths and speeds require different hydrodynamic performance and lift/drag ratios. The different performance envelopes of these designs suggest that different designs are suited to different mission requirements. Operational glide path and speed will probably drive the choice between a conventional glider layout and a flying wing design.

7.4.1 Symmetrical Designs

Because existing oceanographic gliders are designed to glide up and down at the same glide path angle and speed, their bodies and wings are top-to-bottom symmetrical. This is advantageous that gliding performance is the same gliding up or down and no wing actuators are required. But this design limits their hydrodynamic performance and maximum lift/drag ratio. Cambered wing sections are asymmetric but provide better lift/drag performance than symmetrical wing sections.

Designs using moving flaps or wings with adjustable camber or other geometry may give better lift/drag performance than symmetrical designs. The angle of the wing chord relative to the body could be controlled by actuator to keep the body and wings at optimal angles of attack for upwards and downwards glides. The wings angle relative to the body may be adjusted for an optimal lift/drag ratio while keeping the body at zero angle of attack to minimize drag. Because such designs would add actuators and complexity to a glider, durability of additional actuators and moving surfaces must be carefully considered in light of the extended glider missions.

7.4.2 Flying Wing vs. Conventional Glider Designs

Flying wings and blended wing-body designs offer improved lift/drag performance for gliders. They should be considered when design requirements call for shallow glide path angles. In a flying wing, the full volume of the glider is contained within the wing section. By eliminating the body of the glider it is possible to significantly lower the wetted area ratio of the glider and improve its maximum lift/drag ratio. This results in improved gliding performance at shallow glide path angles in comparison to more conventional designs. One problem in the design of flying wing gliders is the internal arrangement of glider components and the construction of a pressurized section within the flying wing.

In a conventional oceanographic glider design, the maximum lift/drag ratio is limited by the constraints of the glider geometry. Drag resulting from flow over the body limits the gliding performance at low glide path angles and high angles of attack. Symmetrical glider designs also limit maximum lift/drag performance. Symmetrical wing sections have lower lift/drag ratios than cambered sections, but are necessary in the symmetrical design to accommodate both up and down gliding. Because of these differences, conventional glider designs may be better suited to steeper glide path angles, and alternative designs including flying wings may perform better at shallow glide path angles.

Figure 7.5 shows an example of maximum lift/drag ratio for a conventional glider with wings of a variable aspect ratio ($AR = 5$ to 50). In a conventional glider design the wings provide the majority of the lift, while the body produces a significant fraction of the drag. Increasing the wing reference area to increase the glider lift/drag ratio gives diminishing returns.

To compare a conventional glider design with a flying wing design, we compare vehicles of the two types with the same useful internal volume. The conventional design, with its

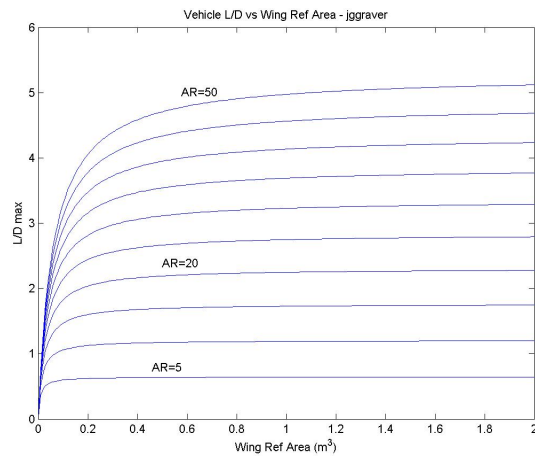


Figure 7.5: Lift/drag ratio vs wing reference area for conventional glider at fixed angle of attack.

cylindrical hull, gives a high internal volume for its wetted surface area. The hull shape is also suited to carrying the internal components. Fitting the payload and components in a flying wing geometry may be more difficult. This is a key concern in adopting a flying wing design, especially because the batteries currently used in gliders must be housed within the pressure hull. Incorporating a pressure hull within a flying wing may be more difficult than in a conventional design and may limit the available volume for battery housing.

Define the packing factor as the fraction of the total vehicle displaced volume that can be used to hold internal components such as payload, computers, and batteries. Packing factor plays an important role in the comparative performance of a flying wing design relative to a conventional design.

As part of a preliminary tradeoff study, we created a general flying wing design with a symmetrical Wortmann airfoil, low wing sweep angle and optimum wing taper ratio. Packing factor was estimated from the flying wing geometry to be about 0.7. This design was then compared to a conventional glider design with the same useful internal volume. Comparison showed:

1. The flying wing design has higher profile (zero lift) drag than the equivalent conventional glider design. This is caused by the larger wetted surface area of the flying wing design, which results in more skin friction drag. Profile drag on the flying wing may be 50 to 100 percent higher than the conventional design, depending on wing packing factor. This means that a conventional glider would be faster at steeper glide path angles where not much lift is required. The packing factor is a dominant factor in this tradeoff and determines the larger surface area of the flying wing.
2. The flying wing design has much higher maximum lift/drag ratio than the conventional design. The flying wing has a maximum lift/drag between 25 and 30, while the symmetrical conventional design has maximum lift/drag around 5 even with high aspect ratio wings.
3. The flying wing design has lower drag at higher lift/drag ratios and shallower glide path angles than the conventional design. This means that a flying wing gliding with a shallow glide path angle would be faster than a conventional glider with equivalent ballast capacity gliding at the same glide path angle. This suggests that flying wing and conventional glider designs are suited to different applications. The conventional glider designs perform better at steeper glide path angles, which provide higher glide speeds. Flying wing designs offer improved performance at shallower glide path angles, which may allow more efficient flight when hotel power loads on the glider are low and the glider power budget is dominated by pumping work. Note that a conventional glider design incorporating cambered airfoils and moving flaps and hydrodynamic surfaces could also offer improved performance.

Chapter 8

Conclusions and Future Work

The principal aim of this work is the comprehensive development and application of a first-principles based nonlinear model of the dynamics of an underwater glider. Underwater gliders have demonstrated enormous potential in oceanographic applications. This potential can be greatly enhanced by the application of the methods and approaches presented here. The glider dynamic model developed in this work, and the analysis conducted using the model, gives significant insight into the physical processes governing the dynamics of gliders. Motivated by interest in this novel vehicle design and by the many useful applications of underwater gliders in oceanography, this work aims to answer the questions of how best to model, control, and design an underwater glider for a given application.

Application of many existing techniques in dynamics and control requires an accurate model of the glider system. This work provides such a model. The glider dynamic model presented here is general and not vehicle specific, and has application in glider design, control, estimation, and optimization. It is applicable to underwater gliders with fixed and moveable external surfaces which can control their buoyancy and center of gravity (CG). It includes the major design elements of underwater gliders, including buoyancy control, wings

and external control surfaces, and the nonlinear coupling between the glider and internal mass actuators. Because this approach is widely applicable rather than vehicle-specific, this work complements the efforts on existing oceanographic gliders such as Slocum, Spray and Seaglider.

This work aims to develop both an intuitive and technical understanding of underwater gliders, and to allow the application of existing methods of engineering analysis for aircraft and submarines to underwater gliders. To do so, a glider dynamic model is developed in Chapter 3 that is complex enough to accurately model the dynamics of an underwater glider, but not so complex as to obstruct insight.

Chapter 4 applies the model to analysis of the dynamics of underwater gliders. We investigate stability and hydrodynamics of gliding and the use of internal mass actuators for control and stabilization, including turning flight and inflection between downwards and upwards glides. It is shown that stable equilibrium steady glides are possible given the proper design of a glider and arrangement of its internal masses. Steady straight glides in the longitudinal plane and steady straight and vertical spiral glides in three dimensions are identified and shown in simulation. The steady glide equilibria in the longitudinal plane have some interesting properties. The speed V and glide path angle ξ of a steady glide may be chosen separately, within the bounds of possible m_0 and \mathbf{r}_p . A choice of velocity and glide path angle (V, ξ) admits a family of \mathbf{r}_p sliding mass positions, allowing some choice of the glider's bottom-heaviness. Stable switching between steady glides is demonstrated in simulations in the longitudinal plane and in three dimensions.

We also derive simpler dynamic models from the full model in order to gain insight into glider dynamics. These include the models of the gliders longitudinal and lateral-directional dynamics and a study of the phugoid mode for underwater gliders. The phugoid model is

derived by applying Lanchester's phugoid assumptions to the glider longitudinal dynamic model. It is shown that, in the angle of attack $\alpha = 0$ case, the underwater glider phugoid model is conservative and is identical to the Lanchester phugoid within a similarity factor that depends on the added mass and net buoyancy of the glider. The angle of attack $\alpha \neq 0$ case is shown to be non-conservative, due to the constraint forces imposed in this case.

Mechanisms for gliders' turning and lateral-directional control are analyzed using the glider model and in at-sea experiments. Oceanographic gliders use rudders and roll-yaw coupling to control their heading. It is shown that a glider's hydrodynamics relative to the position of its center of gravity determine the coupling between roll and turning. It is also shown, using the glider model, simulations, and data from at-sea flight tests, that static mis-trim and rudder-roll coupling have an important effect on the heading control of oceanographic gliders. These coupling mechanisms have opposite effects on glider yaw when gliding upwards compared to gliding downwards. We discuss methods for taking these effects into account in the design of glider actuators and control systems. For example, rudder-roll coupling in upwards and downwards glides should be considered in the design of a glider's vertical tail and in the design of the glider control system.

Methods for tailoring the glider dynamic model to a specific oceanographic glider are demonstrated in Chapter 5. The model is adapted to the Slocum electric glider, including its arrangement of internal moving and ballast masses. We develop methods for parameter identification to determine the model coefficients from measurements of glider geometry and mass and from flight data. Novel techniques are developed to identify the buoyancy offset and hydrodynamic coefficients of the glider using experimental data when static mass and buoyancy measurements taken before launch have significant uncertainty. This work makes use of experimental data from glider trials at sea. Model parameter identification allows the

glider dynamic model to for analysis and control design for operational underwater gliders such as Slocum, Spray and Seaglider. The results of this effort are limited by the quality and amount of available experimental data. Recommendations are made for future glider experiments and instrumentation.

In Chapter 6 the glider model is applied to the design and analysis of underwater glider control systems. Emphasis is placed on control of gliders using buoyancy control, internal actuators, and external surfaces such as a rudder. Steady glides are shown to be controllable and observable when the objective is gliding at a given speed and angle. We demonstrate design of controllers for stabilization of steady glides and demonstrate controlled switching between steady glides and inflections between downwards and upwards glides. We demonstrate the design of a state observer. Combined with the dead reckoning of the glider's horizontal position, use of an observer should improve glider navigation over existing methods in use in oceanographic gliders. Improvements to the control and navigation of underwater gliders should increase their usefulness in scientific applications.

Control features commonly used in existing gliders such as deadbands and intermittent control are also analyzed. This includes features implemented for the purpose of energy conservation, a key design feature in long range oceanographic gliders. Describing function analysis is used to determine the existence and stability of limit cycles due to nonlinearities in the glider's control systems, actuators and dynamics. It is shown that deadband and saturation nonlinearities in the glider control system may, under certain conditions, destabilize stable gliding equilibria or produce controller limit cycling. These undesirable effects may be avoided by the proper choice of a controller and its gains. Simulations and at-sea flight test data is also used in the analysis of the controller and limit cycles. Controller-induced actuator chatter similar to the limit cycles predicted by the describing function analysis

are shown in experimental data. Experiments with an oceanographic glider show that tuning of the glider controller's gains is necessary to avoid slow response, controller induced oscillation, and control chatter.

Recommendations for improvement of glider control systems include: use of different controller gains for upwards and downwards gliding to account for mis-trim and rudder-roll coupling, use of a state feedback controller or proportional-integral controller in heading control, and modification of the deadbands and nonlinear controller elements and gains to avoid control chatter and limit cycling. Other potential applications of the glider model to improving glider control systems include control adaptation and detection of faults and degradations in performance over time. This could be useful given the extended deployments of oceanographic gliders. Inflection control is also discussed and demonstrated and is important to accurate navigation and efficient gliding.

In Chapter 7 the glider model is applied to analysis of glider design and scaling rules for underwater gliders. Differences between underwater gliders and sailplanes are discussed with the aim of developing an intuitive understanding of glider dynamics and design, building on existing knowledge of sailplane and aircraft dynamics. Important differences between underwater gliders and sailplanes include the control of buoyancy, the stabilizing effect of separation between the underwater glider's centers of gravity and buoyancy, and the different relative magnitudes of the propulsive forces on the two types of vehicles. The propulsive force on existing underwater gliders is a small fraction of the glider's (dry) weight, while a sailplane is propelled by its full weight. Because of this, oceanographic underwater gliders glide at much steeper glide path angles than sailplanes.

The glider model is applied to analysis of glider design and the determination of scaling rules for steady glides. Properties of the glide equilibria derived in Chapter 4 are analyzed

with respect to glider design and performance. This includes analysis of the speed of steady glides versus glide path angle, ballast loading, glider hydrodynamics and glider scaling. It is shown that a glider's minimum glide path angle depends on hydrodynamics and maximum lift/drag ratio. Oceanographic gliders, which operate at steep glide path angles, require lift/drag ratios of only one to three. This is significantly lower than the lift/drag ratios of sailplanes, and is reflected in the relatively small wings on oceanographic gliders. At large glide path angles, it is more important to minimize drag than to maximize lift and lift/drag ratio.

Design tradeoffs of speed and efficiency, and design scaling laws are discussed. Existing oceanographic gliders are compared to the possible glider design envelope, and it is shown using the analysis of glider scaling that larger and faster glider designs are possible. Glide speed may be increased by increasing a glider's ballast volume as a fraction of the glider's volume, or by holding the ballast fraction constant and increasing the total size of the glider. Improvements to glider range, scientific usefulness and operating cost may be realized by increasing the glider's size.

Alternate glider designs, including flying wings and gliders with reconfigurable external surfaces, are also discussed. These designs may be better suited to operation at small glide path angles than are existing gliders. The possible drawbacks of alternative designs with moving wings and external surfaces include increased vehicle complexity and reduced durability. The difficulty of incorporating a pressure hull and fitting internal components within a flying wing must also be overcome. The choice of operational glide path angle and speed depends on a glider's mission requirements. Therefore, different designs are better suited to different missions. Conventional glider designs, like Slocum, are suited to steeper glide paths which give faster travel for a given ballast size, while designs with higher

lift/drag ratios, such as flying wings, are shown to be better suited for shallower glide path angles, reducing pumping work for a given horizontal distance travelled.

Future Work

Recommendations for future work include experimental model validation and the further application of the glider model to analysis of glider dynamics, controls and design. Recommendations for glider trials at sea with the purpose of gathering a variety of glider dynamic data are described in Chapter 5. These include trials with a glider specially instrumented to record position, velocity, and hydrodynamic angles while gliding underwater. Improved quality and quantity of glide data would allow the glider model to be compared and validated against experiment. The same experimental data can be used for glider parameter identification and improvement of glider hydrodynamics and performance.

Further improvements in glider capabilities may be gained from use of the natural dynamics of gliders and the ocean. The model may be applied to determine optimal glide equilibria and trajectories for a given mission. Application of the model to glider control and navigation should result in improvements to glider efficiency and scientific utility.

It is expected that the model will match steady glide equilibria and gradual transitions between them well. The model is expected to be less accurate in matching more radical motions, such as very fast transitions, those with high angular rates, bluff body motions, and those with separation. This stems from the nature and limitations of the quasi-steady viscous hydrodynamics model and the added mass model. The added mass model is standard in underwater vehicle dynamics literature and has been the subject of extensive research, but the determination of the added mass terms for a real experimental vehicle and the added mass model's validity for fluid motions where viscous effects are significant are still

the subject of investigation. The model used in this work is expected to be accurate for the analysis included here, including studies of stability of steady glides, but may be augmented in the future by experiments and by the application of more complex hydrodynamic models. Further modelling work may use computational fluid dynamics to model the hydrodynamic forces on a glider in a variety of motions and to determine optimal glider geometries.

The analysis presented here suggests that future glider designs may have significantly greater range, speed, and endurance than existing glider designs. Performance improvements may be achieved through changes in total glider volume and the relative sizes of the internal ballast systems and batteries. Alternate glider geometries are also of interest. The discussion of glider design presented here is schematic. It remains to determine an optimal and algorithmic method for the design of an underwater glider. Design of any aerospace vehicle is subject to numerous tradeoffs and iterations, so the best judgments of the designers may always make up a great part of the design process. The tools and analysis available to them, in glider design and in the design of glider control systems, may be greatly improved. This work is a step towards that goal.

Appendix A

A.1 Rotation Matrices and Parameterizations: Euler Angles and Quaternions

A.1.1 Properties of Rotation Matrices

Transformations between coordinate systems are described mathematically by rotation matrices, written here as \mathbf{R} . Rotation matrices represent rigid body rotations and have the following properties:

1. \mathbf{R} is a 3x3 matrix.
2. \mathbf{R} is orthogonal. $\mathbf{R}^{-1} = \mathbf{R}^T$
3. Determinant(\mathbf{R}) = 1

Note that multiplication of rotation matrices is not commutative.

Orientation may be parameterized using a variety of methods. Two standard methods in aerospace and underwater vehicle dynamics are Euler angles and quaternions. These systems are described in the following subsections.

A.1.2 Euler angles

Euler angles describe the orientation of the vehicle reference frame relative to the inertial frame through a series of three rigid body rotations about specified coordinate axes. The order of axis rotations is fixed by the choice of an Euler angle convention. Permutations of the order of the axes of rotation make twelve different Euler angle conventions possible. The XYZ, or yaw, pitch, roll convention, is the standard convention in aircraft and underwater vehicle dynamics and is utilized here.

The rotation from inertial to body reference frame is parameterized by three angles: yaw ψ , pitch θ and roll ϕ . The XYZ convention defines the rotation from the inertial frame to the body frame as follows:

1. Begin with a reference frame aligned with the inertial frame XYZ.
2. Rotate about the z axis through yaw angle ψ . Positive rotation is defined by the right-hand rule, as is standard. This rotation gives new reference frame X'Y'Z. By X' and Y' we denote that those new axes no longer coincide with the inertial x and y axes, while rotation about the z-axis maintains its direction.
3. From reference frame X'Y'Z, rotate about the Y' axis by pitch angle θ to give frame X''Y'Z'.
4. From X''Y'Z', rotate about the X'' axis by roll angle ϕ . This gives reference frame X''Y''Z''. This completes the rigid body rotation. The orientation of the body-fixed frame of reference $(\mathbf{e}_1, \mathbf{e}_2, \mathbf{e}_3)^T$ is coincident with frame X''Y''Z''.

Note that defining the inertial frame x-axis to be aligned with compass angle zero will make ψ equal to the compass heading angle.

Recall that \mathbf{R} maps vectors expressed with respect to the body frame into inertial frame coordinates. Represent the three Euler angle rotations above by rotation matrices \mathbf{R}_ψ^T , \mathbf{R}_θ^T and \mathbf{R}_ϕ^T , respectively, where

$$\begin{aligned} \mathbf{R}_\psi^T &= \begin{pmatrix} \cos \psi & \sin \psi & 0 \\ -\sin \psi & \cos \psi & 0 \\ 0 & 0 & 1 \end{pmatrix}, \quad \mathbf{R}_\theta^T = \begin{pmatrix} \cos \theta & 0 & -\sin \theta \\ 0 & 1 & 0 \\ \sin \theta & 0 & \cos \theta \end{pmatrix}, \\ \mathbf{R}_\phi^T &= \begin{pmatrix} 1 & 0 & 0 \\ 0 & \cos \phi & \sin \phi \\ 0 & -\sin \phi & \cos \phi \end{pmatrix}. \end{aligned} \quad (\text{A.1})$$

The rotation from inertial to body frame is then

$$\begin{aligned} \mathbf{R}^T &= \mathbf{R}_\phi^T \mathbf{R}_\theta^T \mathbf{R}_\psi^T \\ &= \begin{pmatrix} \cos \psi \cos \theta & \sin \psi \cos \theta & -\sin \theta \\ -\sin \psi \cos \phi + \cos \psi \sin \theta \sin \phi & \cos \psi \cos \phi + \sin \phi \sin \theta \sin \psi & \cos \theta \sin \phi \\ \sin \psi \sin \phi + \cos \psi \cos \phi \sin \theta & -\cos \psi \sin \phi + \sin \theta \sin \psi \cos \phi & \cos \theta \cos \phi \end{pmatrix} \end{aligned} \quad (\text{A.2})$$

And the rotation from the body frame to inertial frame is

$$\begin{aligned} \mathbf{R} &= \mathbf{R}_\psi \mathbf{R}_\theta \mathbf{R}_\phi \\ &= \begin{pmatrix} \cos \psi \cos \theta & -\sin \psi \cos \phi + \cos \psi \sin \theta \sin \phi & \sin \psi \sin \phi + \cos \psi \cos \phi \sin \theta \\ \sin \psi \cos \theta & \cos \psi \cos \phi + \sin \phi \sin \theta \sin \psi & -\cos \psi \sin \phi + \sin \theta \sin \psi \cos \phi \\ -\sin \theta & \cos \theta \sin \phi & \cos \theta \cos \phi \end{pmatrix}. \end{aligned} \quad (\text{A.3})$$

Euler Angle Angular Rates

The glider angular velocity $\boldsymbol{\Omega}$, expressed with respect to the body frame, may be written in terms of the Euler angle rates as

$$\boldsymbol{\Omega} = \begin{pmatrix} \Omega_1 \\ \Omega_2 \\ \Omega_3 \end{pmatrix} = \begin{pmatrix} \dot{\phi} \\ 0 \\ 0 \end{pmatrix} + R_\phi^T \begin{pmatrix} 0 \\ \dot{\theta} \\ 0 \end{pmatrix} + R_\phi^T R_\theta^T \begin{pmatrix} 0 \\ 0 \\ \dot{\psi} \end{pmatrix} \quad (\text{A.4})$$

$$= \begin{pmatrix} 1 & 0 & -\sin \theta \\ 0 & \cos \phi & \cos \theta \sin \phi \\ 0 & -\sin \phi & \cos \theta \cos \phi \end{pmatrix} \begin{pmatrix} \dot{\phi} \\ \dot{\theta} \\ \dot{\psi} \end{pmatrix}. \quad (\text{A.5})$$

Inverting the matrix in Equation (A.5) gives

$$\begin{pmatrix} \dot{\phi} \\ \dot{\theta} \\ \dot{\psi} \end{pmatrix} = \begin{pmatrix} 1 & \sin \phi \tan \theta & \cos \phi \tan \theta \\ 0 & \cos \phi & -\sin \phi \\ 0 & \frac{\sin \phi}{\cos \theta} & \frac{\cos \phi}{\cos \theta} \end{pmatrix} \boldsymbol{\Omega}.$$

This transformation is singular for pitch angles $\theta = \pm 90^\circ$, where $\cos(\theta) = 0$. This phenomenon is known as gimbal lock and arises because there is no one-to-one map between all orientations and \mathbf{R}^3 . Therefore all Euler angle conventions have singularities at some orientations and cannot be used as a global coordinate system to represent orientation. See [20].

In cases when a vehicle will operate close to the singular conditions described, methods exist to avoid gimbal lock. These include tracking orientation using two different sets of Euler angle representations, defined so their singularities do not coincide, or parameterization

of orientation using quaternions.

A.1.3 Quaternions

Quaternions parameterize orientation using four parameters and one constraint. By this method it avoids the gimbal lock singularities that occur with Euler angles. As a result, they may be a better choice for use in simulations and analysis where large angular motions are expected. They have the drawback of adding redundancy, because each orientation is described by two sets of quaternions. Quaternions may be introduced through several mathematical routes. Here we will describe them from a physically intuitive standpoint.

Euler’s theorem of rotation states that “the general displacement of a rigid body with one point fixed is a rotation about some axis” [20]. In other words, any rigid body rotation may be parameterized by specifying an axis of rotation and a rotation angle about that axis. Let $\mathbf{c} = (c_1, c_2, c_3)^T$ be the unit vector along the axis of rotation and let δ be the rotation angle. The corresponding rotation matrix may be written, using the matrix exponential, as $\mathbf{B} = e^{\hat{\mathbf{c}}\delta}$.

To parameterize the rotation in terms of quaternions, define the quaternion vector as

$$\mathbf{q} = \begin{pmatrix} q_0 \\ q_1 \\ q_2 \\ q_3 \end{pmatrix} = \begin{pmatrix} \cos \frac{\delta}{2} \\ c_1 \sin \frac{\delta}{2} \\ c_2 \sin \frac{\delta}{2} \\ c_3 \sin \frac{\delta}{2} \end{pmatrix} = \begin{pmatrix} \cos \frac{\delta}{2} \\ \mathbf{c} \sin \frac{\delta}{2} \end{pmatrix}$$

where \mathbf{q} is subject to the constraint

$$\mathbf{q}^T \mathbf{q} = q_0^2 + q_1^2 + q_2^2 + q_3^2 = 1.$$

The corresponding rotation matrix may then be written as

$$\mathbf{R} = \begin{pmatrix} q_0^2 + q_1^2 - q_2^2 - q_3^2 & 2(q_1q_2 + q_0q_3) & 2(q_1q_3 + q_0q_2) \\ 2(q_1q_2 - q_0q_3) & q_0^2 - q_1^2 + q_2^2 - q_3^2 & 2(q_2q_3 + q_0q_1) \\ 2(q_1q_3 + q_0q_2) & 2(q_2q_3 - q_0q_1) & q_0^2 - q_1^2 - q_2^2 + q_3^2 \end{pmatrix}.$$

The quaternion parameters may be written in terms of the XYZ Euler angles ψ , θ , ϕ as

$$q_0 = \cos\left(\frac{\phi}{2}\right) \cos\left(\frac{\theta}{2}\right) \cos\left(\frac{\psi}{2}\right) + \sin\left(\frac{\phi}{2}\right) \sin\left(\frac{\theta}{2}\right) \sin\left(\frac{\psi}{2}\right) \quad (\text{A.6})$$

$$q_1 = \sin\left(\frac{\phi}{2}\right) \cos\left(\frac{\theta}{2}\right) \cos\left(\frac{\psi}{2}\right) - \cos\left(\frac{\phi}{2}\right) \sin\left(\frac{\theta}{2}\right) \sin\left(\frac{\psi}{2}\right) \quad (\text{A.7})$$

$$q_2 = \cos\left(\frac{\phi}{2}\right) \sin\left(\frac{\theta}{2}\right) \cos\left(\frac{\psi}{2}\right) + \sin\left(\frac{\phi}{2}\right) \cos\left(\frac{\theta}{2}\right) \sin\left(\frac{\psi}{2}\right) \quad (\text{A.8})$$

$$q_3 = \cos\left(\frac{\phi}{2}\right) \cos\left(\frac{\theta}{2}\right) \sin\left(\frac{\psi}{2}\right) - \sin\left(\frac{\phi}{2}\right) \sin\left(\frac{\theta}{2}\right) \cos\left(\frac{\psi}{2}\right). \quad (\text{A.9})$$

Formulas for computing the Euler angles, Euler angle rates and the quaternion rates $\dot{\mathbf{q}}$ in terms of $\boldsymbol{\Omega}$ and \mathbf{q} may be found in [66, 20]. The Euler angles may be found from the quaternion parameters as follows:

$$\tan \phi = \frac{2(q_0q_1 - q_2q_3)}{(q_0^2 - q_1^2 - q_2^2 + q_3^2)} \quad (\text{A.10})$$

$$\tan \theta = \frac{2(q_1q_3 - q_0q_2)}{2(q_0q_1 + q_2q_3) \sin \phi + (q_0^2 - q_1^2)q_2^2 + q_3^2 \cos \phi} \quad (\text{A.11})$$

$$\tan \psi = \frac{2(q_1q_2 + q_0q_3)}{(q_0^2 + q_1^2 - q_2^2 - q_3^2)}. \quad (\text{A.12})$$

The quaternion rates may be written in terms of the body angular velocity $\boldsymbol{\Omega} =$

$(\Omega_1, \Omega_2, \Omega_3)^T$ and the quaternion parameters as

$$\begin{pmatrix} \dot{q}_0 \\ \dot{q}_1 \\ \dot{q}_2 \\ \dot{q}_3 \end{pmatrix} = \frac{1}{2} \begin{pmatrix} 0 & -\Omega_1 & -\Omega_2 & -\Omega_3 \\ \Omega_1 & 0 & \Omega_3 & -\Omega_2 \\ \Omega_2 & -\Omega_3 & 0 & \Omega_1 \\ \Omega_3 & \Omega_2 & -\Omega_1 & 0 \end{pmatrix} \begin{pmatrix} q_0 \\ q_1 \\ q_2 \\ q_3 \end{pmatrix}.$$

The vehicle angular velocity may be written in the body frame as a function of the quaternion rates as

$$\begin{pmatrix} \Omega_1 \\ \Omega_2 \\ \Omega_3 \end{pmatrix} = 2 \begin{pmatrix} -q_1 & q_0 & q_3 & -q_2 \\ -q_2 & -q_3 & q_0 & q_1 \\ -q_3 & q_2 & -q_1 & q_0 \end{pmatrix} \begin{pmatrix} \dot{q}_0 \\ \dot{q}_1 \\ \dot{q}_2 \\ \dot{q}_3 \end{pmatrix}.$$

Note the equations for the angular velocity in terms of the Euler angle rates are nonlinear equations, while angular velocity in terms of the the quaternion parameters are given by a set of linear differential equations. See [66].

Bibliography

- [1] R. Bachmayer. Underwater glider control, 2002. Talk at Institute for Marine Dynamics, St. Johns, Newfoundland, Canada. Presented work with N.E. Leonard and J. G. Graver.
- [2] R. Bachmayer, J.G. Graver, and N. E. Leonard. Glider control: A close look into the current glider controller structure and future developments. In *Proc. IEEE Oceans 2003*, volume 2, pages 951 – 954, 2003.
- [3] A. Baz and A. Seireg. Optimum design and control of underwater gliders. *ASME Transactions*, pages 304–310, February 1974.
- [4] S. Berman. Comparison of the lift, drag and pitch moment coefficients of a slocum glider wind tunnel model with computational results by vehicle control technologies, inc. Technical report, Princeton University Mechanical and Aerospace Engineering Dept., May 2003. Experiments with Graver, J.G.
- [5] P. Bhatta and N. E. Leonard. Stabilization and coordination of underwater gliders. In *Proc. 41st IEEE Conference on Decision and Control*, volume 2, pages 2081–2086, 2002.
- [6] P. Bhatta and N. E. Leonard. A Lyapunov function for vehicles with lift and drag: Stability of gliding. In *Proc. 43rd IEEE Conference on Decision and Control*, pages

4101–4106, 2004.

- [7] J. H. Blakelock. *Automatic Control of Aircraft and Missiles*. John Wiley & Sons, New York, 1965.
- [8] J. P. Campbell and M. O. McKinney. Summary of methods for calculating dynamic lateral stability and response and for estimating lateral stability derivatives. Technical report, NACA R 1098, 1952.
- [9] M. R. Clarke. Buoyancy control as a function of the spermaceti organ in the sperm whale. *Journal of the Marine biology Association, U.K.*, 58:27–71, 1978.
- [10] T. B. Curtin, J. G. Bellingham, J. Catipovic, and D. Webb. Autonomous oceanographic sampling networks. *Oceanography*, 6:86–94, 1989.
- [11] E. Fiorelli, N. E. Leonard, P. Bhatta, D. Paley, R. Bachmayer, and D. Fratantoni. Multi-auv control and adaptive sampling in monterey bay. In *Proc. IEEE Autonomous Underwater Vehicles 2004: Workshop on Multiple AUV Operations (AUV04)*, Sebasco, ME.
- [12] Gwyn Griffiths (Editor). *Technology and Applications of Autonomous Underwater Vehicles*. Taylor & Francis, London, UK, 2003.
- [13] C. C. Eriksen. Autonomous underwater gliders. Technical report, Prepared for the Autonomous and Lagrangian Platforms and Sensors (ALPS) Workshop, Sea Lodge, La Jolla CA, 2003.
- [14] C. C. Eriksen, T. J. Osse, T. Light, R. D. Wen, T. W. Lehmann, P. L. Sabin, J. W. Ballard, and A. M. Chiodi. Seaglider: A long range autonomous underwater vehicle

for oceanographic research. *IEEE Journal of Oceanic Engineering, Special Issue on Autonomous Ocean Sampling Networks*, 26(4), Oct 2001.

- [15] B. Etkin. *Dynamics of Flight*. John Wiley and Sons, New York and London, 1959.
- [16] T. Fossen. *Nonlinear Modelling and Control of Underwater Vehicles*. PhD thesis, Norwegian Institute of Technology (NTH), 1991.
- [17] T. Fossen. *Guidance and Control of Ocean Vehicles*. John Wiley and Sons, New York, NY, 1995.
- [18] Anna M. Galea. *Optimal Path Planning and High Level Control of an Autonomous Gliding Underwater Vehicle*. Master's thesis, Massachusetts Institute of Technology, 1999.
- [19] A. Gelb and W. E. Van der Velde. *Multiple-input Describing Functions and Nonlinear System Design*. McGraw Hill Book Company, New York, 1968.
- [20] H. Goldstein. *Classical Mechanics*. Addison-Wesley, 1980. 2nd edition.
- [21] W. J. Gould. *A brief history of float developments*. Southampton Oceanography Center, Accessed: December 2003. Available at <http://www.soc.soton.ac.uk/JRD/HYDRO/argo/history.php>.
- [22] J. G. Graver, R. Bachmayer, N. E. Leonard, and D. M. Fratantoni. Underwater glider model parameter identification. In *Proc. 13th Int. Symposium on Unmanned Untethered Submersible Tech.*, Durham, NH, 2003.
- [23] J. G. Graver and C. E. Gorbea. Dynamics and control of autonomous underwater gliders. Technical report, Princeton University, 2003. Senior Thesis.

- [24] J. G. Graver and N. E. Leonard. Underwater glider dynamics and control. In *Proc. 12th Int. Symposium on Unmanned Untethered Submersible Tech.*, Durham, NH, 2001.
- [25] J.G. Graver, J. Liu, C. Woolsey, and N. E. Leonard. Design and analysis of an underwater vehicle for controlled gliding. In *Proc. 32nd Conference on Information Sciences and Systems*, pages 801–806, 1998.
- [26] S. F. Hoerner. *Fluid Dynamic Drag*. Published by the author, Midland Park, NJ, 1965.
- [27] S. F. Hoerner and Henry V. Borst. *Fluid Dynamic Lift*. Published by Mrs. Liselotte A. Hoerner, Midland Park, NJ, 1985.
- [28] N. G. Hogg and R. X. Huang (eds). *Collected Works of Henry Stommel*. American Meteorological Society, Boston, 1996.
- [29] P. Holmes, J. Jenkins, and N. E. Leonard. Dynamics of the Kirchhoff equations I: Coincident centers of gravity and buoyancy. *Physica D*, 118:311–342, 1998.
- [30] E. J. Hopkins. A semi-empirical method for calculating the pitching moment of bodies of revolution at low mach number. Technical report, NACA RM A51C14, 1951.
- [31] S. A. Jenkins. Glide optimization for cross country wave flights. *Technical Soaring*, 16(1):3–16, January 1992.
- [32] S. A. Jenkins, D. E. Humphreys, J. Sherman, J. Osse, C. Jones, N. E. Leonard, R. Bachmayer, J. Graver, T. Clem, P. Carroll, P. Davis, J. Berry, P. Worley, and J. Wasyl. Underwater Glider System Study. Technical report, Office of Naval Research, 2003.
- [33] S. A. Jenkins and J. Wasyl. Optimization of glides for constant wind fields and course headings. *Journal of Aircraft*, 27(7):632–638, July 1990.

- [34] C. Jones. Personal communication, 2003.
- [35] Y. Tomoda K. Kawaguchi, T. Ura and H. Kobayashi. Development and sea trials of a shuttle type auv Albac. In *Proc. 8th Int. Symposium on Unmanned Untethered Submersible Tech.*, pages 7–13, Durham, NH, 1993.
- [36] H. Khalil. *Nonlinear Systems*. Prentice Hall, Upper Saddle River, New Jersey, 2nd edition, 1996.
- [37] I. A. Kibel, N. E. Kochen, and N. V. Roze. *Theoretical Hydromechanics*. Wiley, 1964.
- [38] R. Kunzig. A thousand diving robots. *Discover Magazine*, 17(4), April 1996.
- [39] H. Lamb. *Hydrodynamics*. Dover, New York, 6th edition, 1932.
- [40] F.W. Lanchester. *Aerodnetics*. A. Constable and Co., London, 1908.
- [41] N. E. Leonard. Stability of a bottom-heavy underwater vehicle. *Automatica*, 33(3):331–346, 1997.
- [42] N. E. Leonard and J. G. Graver. Model-based feedback control of autonomous underwater gliders. *IEEE Journal of Oceanic Engineering, Special Issue on Autonomous Ocean Sampling Networks*, 26(4):633–645, Oct 2001.
- [43] B. W. McCormick. *Aerodynamics, Aeronautics and Flight Mechanics*. John Wiley, New York and London, 1979.
- [44] D. McRuer, I. Ashkenas, and D. Graham. *Aircraft Dynamics and Automatic Control*. Princeton University Press, Princeton, New Jersey, 1973.

- [45] R. Moitie and N. Seube. Guidance and control of an autonomous underwater glider. In *Proc. 12th Int. Symposium on Unmanned Untethered Submersible Tech.*, Durham, NH, 2001.
- [46] J. N. Newman. *Marine Hydrodynamics*. The MIT Press, Cambridge, Massachusetts, 1977.
- [47] K. Ogata. *Modern Control Engineering*. Prentice Hall, Englewood Cliffs, New Jersey, 1990.
- [48] C. D. Perkins and R. E. Hage. *Airplane Performance, Stability and Control*. John Wiley, New York and London, 1949.
- [49] A. Pope and W. H. Rae Jr. *Low-Speed Wind Tunnel Testing*. John Wiley & Sons, New York, New York, 2nd edition, 1984.
- [50] R. Bachmayer, N.E. Leonard, J. G. Graver, E. Fiorelli, P. Bhatta, and D. Paley . Underwater gliders: Recent developments and future applications. In *Proc. IEEE International Symposium on Underwater Technology (UT'04)*, Tapei, Taiwan.
- [51] B. R. Sturgis, R. D. Robinett, III and S. A. Kerr. Moving mass trim control for aerospace vehicles. *J. Guidance, Control, and Dynamics*, 19(5):1064–1070, 1996.
- [52] D. P. Raymer. *Aircraft Design: A Conceptual Approach*. American Institute of Aeronautics and Astronautics, Washington, DC, 1989.
- [53] F.J. Regan and A.M. Morrison. The planar dynamics of airships. In *5th AIAA Aerodynamic Decelerator Systems Technology Conference*, pages 1375–1395, Albuquerque, NM.

- [54] WHOI Media Relations News Release. Underwater robot makes history crossing the gulf stream. http://www.whoiedu/media2004_Spray_Release.html, November 4, 2004.
- [55] J. Roskam. *Methods for Estimating Stability and Control Derivatives of Conventional Subsonic Airplanes*. Published by the author, Lawrence, KS, 1971.
- [56] J. Roskam. *Flight Dynamics of Rigid and Elastic Airplanes*. Published by the author, Lawrence, KS, 1973.
- [57] J. Roskam. *Airplane Flight Dynamics and Automatic Flight Controls, Part I*. Roskam Aviation and Engineering Corporation, Lawrence, KS, 1979.
- [58] J. Roskam. *Airplane Flight Dynamics and Automatic Flight Controls, Part II*. Roskam Aviation and Engineering Corporation, Lawrence, KS, 1979.
- [59] S.I. Sagatun. *Modelling and Control of Underwater Vehicles: A Lagrangian Approach*. Norwegian Institute of Technology (NTH), Norway, 1992. PhD. Dissertation.
- [60] H. Schlichting and E. Truckenbrodt. *Aerodynamics of The Airplane*. McGraw-Hill International Book Company, New York, New York, 1977. Translated by Heinrich J. Ramm.
- [61] O. Schrenk. A simple approximation method for obtaining spanwise lift distribution naca-tm-948. Technical report, NACA, 1940.
- [62] M. S. Selig, J. F. Donovan, and D. B. Fraser. *Airfoils at Low Speeds*. H. A. Stokely, Virginia Beach, VA, 1989.
- [63] J. Sherman, R. E. Davis, W. B. Owens, and J. Valdes. The autonomous underwater glider ‘Spray’. *IEEE Journal of Oceanic Engineering, Special Issue on Autonomous Ocean Sampling Networks*, 26(4), Oct 2001.

- [64] J. E. Slotine and W. Li. *Applied nonlinear control*. Prentice Hall, Englewood Cliffs, N.J., 1991.
- [65] H. W. Sorenson. *Parameter Estimation*. Marcel Dekker, Inc., New York, 1980.
- [66] Brian L. Stevens and Frank L. Lewis. *Aircraft Control and Simulation*. Wiley, New York, NY, 1992.
- [67] H. Stommel. Direct measurement of subsurface currents. *Deep-Sea Research*, 2(4):284–285, 1955.
- [68] H. Stommel. The Slocum mission. *Oceanography*, 2:22–25, 1989.
- [69] J. C. Swallow. Neutral-buoyancy float for measuring deep currents. *Deep-Sea Research*, 3(1):93–104, 1955.
- [70] F. J. Regan, T. Petsopoulos and J. Barlow. Moving-mass roll control system for fixed-trim re-entry vehicle. *J. Spacecraft and Rockets*, 33(1):54–60, 1996.
- [71] J.H. Taylor. *Describing functions*. In *Electrical Engineering Encyclopedia*. John Wiley & Sons, New York, 1999.
- [72] U. A. Vladimirovich. Optimization criteria and hierarchy of mathematical models of an underwater gliding vehicle. Technical report, St. Petersburg State Marine Technical University, 2002.
- [73] R. Von Mises. *Theory of Flight*. Dover, New York, 1959.
- [74] B. A. Warren and C. Wunsch (eds). *Evolution of Physical Oceanography, Scientific Surveys in Honor of Henry Stommel*. MIT Press, 1981.
- [75] D. Webb. Personal communication, 2005.

- [76] D. Webb and C. Jones. Personal communication, 2001-2004.
- [77] D. Webb and C. Jones. Slocum Three-view. Webb Research Co. Technical Document. Courtesy Webb Research Co., 2002.
- [78] D. C. Webb and P. J. Simonetti. A simplified approach to the prediction and optimization of performance of underwater glider. In *Proc. 10th Int. Symposium on Unmanned Untethered Submersible Tech.*, pages 60–69, Durham, NH, 1996.
- [79] D. C. Webb and P. J. Simonetti. The SLOCUM AUV: An environmentally propelled underwater glider. In *Proc. 11th Int. Symposium on Unmanned Untethered Submersible Tech.*, pages 75–85, Durham, NH, 1999.
- [80] D. C. Webb, P. J. Simonetti, and C.P. Jones. SLOCUM, an underwater glider propelled by environmental energy. *IEEE Journal of Oceanic Engineering, Special Issue on Autonomous Ocean Sampling Networks*, 26(4):447–452, 2001.
- [81] Webpage. *Welcome to the Argo Home page [online]*. Available at: <http://www-argo.ucsd.edu/>, [Accessed: 18. November 2004].
- [82] Joshua Slocum Society International Inc. (Webpage). *Captain Joshua Slocum, The First Man to Sail Around the World Alone*. Accessed: December 2003.
- [83] J. E. White and III R. D. Robinett. Principal axis misalignment control for deconing of spinning spacecraft. *J. Guidance, Control, and Dynamics*, 17(4):823–830, 1994.
- [84] T. M. Williams, R. W. Davis, L. A. Fuiman, J. Francis, B. J. Le Boeuf, M. Horning, J. Calambokidis, and D. A. Croll. Sink or swim: Strategies for cost-efficient diving by marine mammals. *Science*, 288:133–136, April 7, 2001.

- [85] Terrie M. Williams. Intermittent swimming by mammals: A strategy for increasing energetic efficiency during diving. *American Zoologist*, 41(2):166–176, 2001.
- [86] C. Woolsey. *Energy Shaping and Dissipation: Underwater Vehicle Stabilization Using Internal Rotors*. Princeton University, Princeton, NJ, 2001. PhD. Dissertation.
- [87] C. Woolsey and N. E. Leonard. Underwater vehicle stabilization by internal rotors. In *Proceedings of the American Control Conference*, 1999.
- [88] C. A. Woolsey. Hamiltonian attitude dynamics for a spacecraft with a point mass oscillator. In *In Proceedings of the 15th International Symposium on Mathematical Theory of Networks and Systems*, 2002.
- [89] C. A. Woolsey. Aerodynamic transformations. Image courtesy of author., 2003.
- [90] C. A. Woolsey and N. E. Leonard. Moving mass control for underwater vehicles. In *Proceedings of the American Control Conference*, pages 2824–2829, 2002.
- [91] C. A. Woolsey and N. E. Leonard. Stabilizing underwater vehicle motion using internal rotors. *Automatica*, 38(12):2053–2062, 2002.
- [92] Craig A. Woolsey. Reduced hamiltonian dynamics for a rigid body coupled to a moving point mass. *J. Guidance, Control, and Dynamics.*, 2003.
- [93] F. X. Wortmann. Drag reduction in sailplanes. *Soaring*, June and July 1966. and OSTIV Pub. VIII.
- [94] F. X. Wortmann. The sailplane. *Aero-Revue*, June 1971.
- [95] F. X. Wortmann. Some laminar profiles for sailplanes. *Aero-Revue*, pages 14–18, Nov. 1963.

- [96] Carl Wunsch. Biographical memoir of Henry Stommel. *National Academy of Sciences*,
<http://www.nap.edu/readingroom/books/biomems/hstommel.html>. Accessed July 2004.